

Ss. Cyril and Methodius University

Faculty of Civil Engineering

Skopje, Macedonia



**EXPERIMENTAL AND NUMERICAL INVESTIGATION OF CONCRETE COLUMNS
REINFORCED WITH FRP BARS**

Candidate:

MSc. Zijadin GURI, Grad. Civil. Eng.

- Doctoral Dissertation -

Mentor:

Prof. D-r Gjorgji Kokalanov

October, 2018

РЕЗИМЕ

Во предметната докторска дисертација презентирани се оригинални експериментални и нумерички истражувања на однесувањето на бетонски мостовски столбови армирани со обична или стандардна арматура и алтернативно армирани со композитни FRP прачки кои претставуваат нов специфичен композитен материјал.

После воведната Глава-1 во која накратко се изложени предметот и целите на реализираните иновативни експериментални и аналитички истражувања, во наредната Глава-2 се презентирани специфичните физичко-механички карактеристики на FRP прачките кои претставуваат нов специфичен композитен материјал, применет во предметните истражувања како алтернативен материјал за армирање на изградените и експериментално тестираните модели на бетонски мостовски столбови.

Во Глава-3 презентирани се карактеристиките на проектираните и изградените експериментални модели на мостовски столбови армирани алтернативно со класична арматура и со композитни FRP прачки. Освен тоа, презентирана е и применетата интегрална постапка и специфичната експериментална опрема која е користена за реализација на оригиналните експериментални циклични тестови на моделите на мостовските столбови до длабока нелинеарност, вклучувајќи ја и фазата на лом. Сите експериментални тестови беа реализирани под симултано влијание на константни вертикални товари и монотонно растечки циклични хоризонтални товари до лом, со што е овозможена реалистична симулација на сеизмичките сили при реални земјотреси.

Во Глава-4, конзистентно се презентирани добиените оригинални експериментални резултати од сите реализирани експериментални нелинеарни тестови на бетонски мостовски столбови армирани со класична арматура и алтернативно со FRP прачки како специфична композитна арматура. Добиените експериментални резултати покажуваат дека применетата композитна арматура може во иднина да стане сериозна алтернатива за класичната арматура, особено при реализација на специфични технолошки решенија во специфични средини и услови на градење.

Во Глава-5 презентирани е развиениот рафиниран нелинеарен аналитички модел со користење на најнапредните софтверски решенија засновани врз генералниот концепт

на методот на конечни елементи и врз успешната примена на формулираните нелинеарни тродимензионални конечни елементи. Формулираниот детален нелинеарен аналитички модел е успешно верифициран врз основа на оригинални експериментални резултати добиени од реализираните нелинеарни експериментални тестови на моделите на мостовски столбови армирани алтернативно, со класична арматура и со композитна арматура која е формирана со вградување на FRP прачки во улога на подолжна арматура.

Во наредната Глава-6, презентирана е практичната примена на формулираниот рафиниран тродимензионален аналитички модел за анализа на нелинеарен сеизмички одговор на реален мост со средни столбови армирани алтернативно со класична арматура и со арматура формирана од композинти FRP прачки. Резултатите добиени од извршените нелинеарни сеизмички анализи од влијание на реални земјотреси потврдуваат дека формулираните аналитички модели обезбедуваат извонредна генералност и деталност. Потврдено е дека формулираните рафинирани нелинеарни аналитички модели можат да бидат успешно користени за експертски анализи на нелинеарното однесување на мостовски конструкции при многу силни земјотреси во случај кога нивните средни столбови се армирани со новата композитна арматура формирана од FRP прачки.

Во последната Глава-7 дадени се заклучоци произлезени од реализираните интегрални истражувачки активности како и генерални насоки за идни истражувања во предметната специфична истражувачка област.

SUMMARY

Presented in the considered doctoral dissertation are original experimental and numerical comparative investigations of the behavior of concrete bridge piers reinforced by use of plain or standard reinforcement and, alternatively, by use of composite FRP bars representing a new specific composite material.

After the introductory Chapter 1 that provides a brief presentation of the subject and the objectives of the realized specific experimental and analytical investigations, there follows Chapter-2 in which are displayed the specific physical-mechanical characteristics of the FRP bars as a new specific composite material that has been used as an alternative material for reinforcement of the models of the experimentally tested concrete bridge piers.

Chapter 3 shows the characteristics of the designed and built experimental models of bridge piers reinforced by use of classical reinforcement, and alternatively, by use of composite FRP bars. Presented additionally are the applied integral procedure and the specific experimental equipment used for the realization of the original experimental cyclic tests on the models of bridge piers up to deep nonlinearity, including also the failure stage. All experimental tests have been realized under simultaneous effect of constant vertical loads and monotonous incremental cyclic horizontal loads up to failure enabling realistic simulation of seismic forces during real earthquakes.

Chapter 4 provides a consistent presentation of the obtained original experimental results from all realized experimental nonlinear tests on concrete bridge piers reinforced by classical reinforcement and, alternatively, by FRP bars as a specific composite reinforcement. The obtained experimental results show that the applied composite reinforcement may become a sound alternative for the classical reinforcement in future, particularly in realization of specific technological solutions in specific environments and conditions of construction.

Chapter 5 shows the developed refined nonlinear analytical models by use of the most advanced software solutions based on the general concept of the finite element method by successful application of the formulated nonlinear three-dimensional finite elements. The formulated refined nonlinear analytical model has successfully been verified based on the obtained original experimental results from the realized nonlinear experimental tests on

models of bridge piers reinforced with classical reinforcement and composite reinforcement composed of incorporated FRP bars with the role of longitudinal reinforcement.

Presented in the next chapter, Chapter 6, is the practical application of the formulated refined three-dimensional analytical model for analysis of the nonlinear seismic response of a real bridge with central piers reinforced by classical reinforcement and, alternatively, by a reinforcement composed of composite FRP bars. The results obtained from the performed nonlinear seismic analyses under the effect of real earthquakes have confirmed the extraordinary generality and thoroughness of the formulated analytical models. The formulated refined nonlinear analytical models may successfully be used in expert analyses of the nonlinear behavior of bridge structures under very strong earthquakes in case their middle piers are reinforced by the new composite reinforcement composed of FRP bars.

The last, Chapter 7, provides conclusions drawn from the realized integral research activities as well as general directions for future investigations in the considered specific research field.

ACKNOWLEDGEMENT

To successfully realize the integral innovative investigations that have given rise to the original experimental and analytical results presented in the doctoral dissertation, it has been necessary to provide corresponding and very specific research conditions. For me, it was a great privilege to get the opportunity to work on investigations involving development of a new technology in the construction industry that includes development and application of composite materials in the role of a primary reinforcement of concrete elements of engineering structures located in aggressive environments or in world regions characterized by very high seismicity.

I would like to take this opportunity to express my gratitude to the Civil Engineering Faculty, Ss. Cyril and Methodius University and its entire staff for the opportunity that they have given to me to attend doctoral studies.

I am very grateful to Prof. Dr. Gjorgji Kokalanov for the valuable support that he has given to me during the preparation of this dissertation and I am particularly indebted to Prof. Dr. Danilo Ristic for the opportunity that he has given to me to perform, by his advice, extensive original experimental tests in the newly established Regional Seismic Innovation Network Laboratory (ReSIN Laboratory of Industrial science and Technology) located in Skopje, that has been initiated and led by him, following the successful completion of his international long-term innovative NATO Science for Peace project (2010-2013), Brussels, Belgium.

I am also extending my deep gratitude to Prof. Dr. Misin Misini for his continuous assistance and support as well as Prof. Dr. Nebi Pllana, who supported the experimental tests in Skopje and enabled me to realize the experimental tests of materials in his IPE-PROING Institute located in Prishtina.

Finally, deep gratitude is also accorded to my family members for their strong support and understanding that enabled me successful performance of all of my research activities.

M. Sc. Zijadin Guri, grad. Civil eng.

CONTENTS

	РЕЗИМЕ	2
	SUMMARY	4
	ACKNOWLEDGEMENT	6
	TABLE OF CONTENTS	7
	LIST OF FIGURES	11
	LIST OF TABLES	17
1	CHAPTER 1	19
	SUBJECT AND OBJECTIVES OF THE INVESTIGATION	
1.1	Subject of the Investigation	19
1.2	Importance of the Investigation	19
1.3	Objective of the Investigation	20
1.4	State of the Art in the Field of Investigation	20
1.5	Applied Investigation Methods	21
1.6	Brief Description of Investigation Results	21
2	CHAPTER 2	23
	PROPERTIES OF FRP REBARS AS NEW COMPOSITE MATERIAL	
2.1	Types of FRP Rebars	23
2.2	Properties of GFRP Rebars	24
2.2.1	Remarks on Properties of GFRP Rebars	24
2.2.2	Tensile Strength	24
2.2.3	Compressive Strength	27
2.2.4	Shear Properties	29
2.2.5	Bond Behavior of FRP Bars	32
2.3	Example of Tested Square Columns Reinforced With GFRP Rebars	35
2.4	Concluding Remarks on Importance of Present Study	38

3	CHAPTER 3	41
	PROGRAMME OF ORIGINAL CYCLIC TESTS ON BRIDGE COLUMN MODELS WITH STEEL AND GFRP REINFORCEMENT INCLUDING MATERIAL AND BOND BEHAVIOUR TESTING	
3.1	Introduction	41
3.2	Used RESIN Laboratory Testing Facility	42
3.3	Concept of Designed Bridge Column Prototype Models	45
3.4	Testing Program of Constructed Steel-Reinforced Bridge Column Models	46
3.5	Testing Program of Constructed GFRP-Reinforced Bridge Column Models	48
3.6.	Testing of Properties of Materials Used for Prototype Models	48
3.6.1	Concrete Properties	49
3.6.2	Steel Reinforcement Properties	49
3.6.3	GFRP Reinforcement Properties	49
3.7.	Testing of Bond Behavior of GFRP and Steel Rebars	50
3.7.1	Bond Behavior of Steel Rebars	50
3.7.2	Bond Behavior of GFRP Rebars	50
3.8	Test Set Up and Loading of Bridge Column Prototype Models	51
3.9	Concluding Remarks	52
4	CHAPTER 4	73
	ORIGINAL RESULTS OBTAINED FROM NONLINEAR EXPERIMENTAL TESTS OF BRIDGE COLUMN MODELS WITH STEEL AND GFRP REINFORCEMENT	
4.1	Introduction	73
4.2	Results From Cyclic Tests of Steel-Reinforced Bridge Column Models	74
4.2.1	Experimental Hysteretic Curve of Model-M11: Steel Reinforcement Level SRL=1 (12XD12) and Confinement Level CL=1 (t=15.0 cm)	74
4.2.2	Experimental Hysteretic Curve of Model-M12: Steel Reinforcement Level SRL=1 (12XD12) and Confinement Level CL=2 (t=7.5 cm)	75
4.3	Results From Cyclic Tests of GFRP-Reinforced Bridge Column Models	81
4.3.1	Experimental Hysteretic Curve of Model-M21: GFRP Reinforcement Level GFRP-RL=1 (12XD10) and Confinement Level CL=1 (t=15.0 cm)	82
4.3.2	Experimental Hysteretic Curve of Model-M22: GFRP Reinforcement Level GFRP-RL=1 (12XD10) and Confinement Level CL=2 (t=7.5 cm)	83
4.3.3	Experimental Hysteretic Curve of Model-M31: GFRP Reinforcement Level GFRP-RL=2 (12XD8) and Confinement Level CL=1 (t=15.0 cm)	83

4.3.4	Experimental Hysteretic Curve of Model-M32: GFRP Reinforcement Level GFRP-RL=2 (12XD8) and Confinement Level CL=2 (t=7.5 cm)	84
4.4	Concluding Remarks	97
5	CHAPTER 5	101
	ADVANCED REFINED NONLINEAR BEHAVIOUR SIMULATION MODEL OF BRIDGE COLUMN MODELS WITH STEEL AND GFRP REINFORCEMENT	
5.1	General Remarks	101
5.2	Concept of Advanced Refined 3D Analytical Modelling	102
5.3	Refined Modelling of Axial Force-Moment Curves, Push-Over Curves And Moment-Curvature Relations of The Tested Bridge Column Models	104
5.4.	Refined 3D Modelling of Steel-Reinforced Bridge Column Models	116
5.5.	Refined 3D Modelling of GFRP-Reinforced Bridge Column Models	120
5.6	Concluding Remarks	127
6	CHAPTER 6	129
	APPLICATION OF REFINED 3D MODELLING CONCEPT FOR NONLINEAR EARTHQUAKE RESPONSE ANALYSIS OF REAL BRIDGE WITH COLUMNS REINFORCED WITH STEEL AND GFRP REINFORCEMENT	
6.1	Introduction	129
6.2	Refined 3D Modelling Concept Applied for Nonlinear Earthquake Response Analysis of Real Structures	130
6.3	Real Prototype Bridge With Columns Reinforced With Steel and Varying Levels of GFRP Reinforcement Considered For Seismic Response Analysis	137
6.4	Computed Results of Nonlinear Bridge Response For Selected Four Calculation Cases Under Real Petrovac Earthquake Scaled to PGA=0.45 g	142
6.5	Computed Results of Nonlinear Bridge Response For Selected Four Calculation Cases Under Real El-Centro Earthquake Scaled to PGA=0.45 g	163
6.6	Monotonic Push-Over Curves and Hysteretic Curves of Column-1 Used In Computation of Earthquake Responses of Four Prototype Bridges	183
6.7	Concluding Remarks	187

7	CHAPTER 7	189
	CONCLUSIONS AND RECOMMENDATIONS	
7.1	Conclusions	189
7.2	Recommendation for Future Research	191
	LITERATURE	193

LIST OF FIGURES

Chapter 2

Figure 1. Type of FRP rebars.

Figure 2. Stress-strain curves of typical reinforcing fibers: a) carbon (high modulus); b) Carbon (high strength); c) aramid (Kevlar 49); d) S-glass; e) E-glass; f) Basalt B500C – Ordinary steel reinforcement.

Figure 3. Stress-strain diagrams of unidirectional epoxy composites in fiber direction: a) glass/epoxy; b) aramid/epoxy; c) carbon/epoxy.

Figure 4. Shear load applied in FRP rebar.

Figure 5. Off-axis loading of rebar.

Figure 6. Local axis of FRP bar.

Figure 7. Bond modeling of FRP and steel bars.

Figure 8. Tension stiffening behavior of FRP RC element.

Figure 9. Specimen details for columns tested by Tobbi et al. 2012.

Figure 10. Properties of FRP rebars used in calculation.

Figure 11. Normalized moment-axial force interaction diagrams

Chapter 3

Figure 12. Geometry, dimensions and reinforcement details on experimental models.

Figure 13. Geometry, dimensions and reinforcement details on experimental models.

Figure 14. Formwork for columns and reinforcement of columns.

Figure 15. Reinforcement of columns – longitudinal rebars GFRP – Stirrups - 15 cm spacing.

Figure 16. Reinforcement of columns – longitudinal rebars GFRP – stirrups - 7.5 spacing.

Figure 17. Placement of steel pipes for fixing anchors into foundation.

Figure 18. Top plate for application of load.

Figure 19. Concrete columns after concreting.

Figure 20. Concrete cube specimens after testing.

Figure 21. Testing of GFRP rebars under tension.

Figure 22. Properties of used GFRP and steel reinforcement.

Figure 23. Testing of GFRP bars under tension.

Figure 24. Stress-strain diagram for GFRP rebars.

Figure 25. Testing of GFRP rebars under compression.

Figure 26. Devices for shear testing of GFRP rebar.

Figure 27. Results from shear testing of GFRP rebars.

Figure 28. Pullout testing of used GFRP rebars.

Figure 29. Specimens for testing of GFRP and steel rebars – pullout test.

Figure 30. Specimens for testing of GFRP and steel rebars – isolation of bars.

Figure 31. Process of pullout testing.

Figure 32. Pullout experimental results – force – sliding.

Figure 33. Damage on surface of GFRP rebar after pullout testing.

Figure 34. Testing frame with installed column and instrumentation.

Figure 35. Loading protocol.

Chapter 4

Figure 36. Experimental hysteresis of M11 column.

Figure 37. Experimental hysteresis of M12 column

Figure 38. Testing of column M11.

Figure 39. Column M11 – cracking at different stages of loading.

Figure 40. Column M11 – spalling of cover and buckling of longitudinal rebar.

Figure 41. Testing of column M12.

Figure 42. Column M12 – cracking at different stages of loading.

Figure 43. Column M12 – cover spalling.

Figure 44. Experimental hysteresis of M21 column.

Figure 45. Experimental hysteresis of M22 column.

Figure 46. Experimental hysteresis of M31 column.

Figure 47. Experimental hysteresis of M32 column.

Figure 48. Testing of column M21.

Figure 49. Column M21 – cracking at different stages of loading.

Figure 50. Column M21 – maximum displacement of column and cover spalling.

Figure 51. Testing of column M22.

Figure 52. Column M22 – cracking at different stages of loading and displacements.

Figure 53. Column M22 – cover spalling and maximum displacement.

Figure 54. Testing of column M31.

Figure 55. Column M31 – cracking at different stages of loading.
Figure 56. Column M31 – longitudinal bar buckling and bond failure of GFRP rebar.
Figure 57. Column M31 – different cover on the left and the right side of the column.
Figure 58. Testing of column M32.
Figure 59. Column M32 – cracking at different stages of loading.
Figure 60. Column M32 – concrete spalling and maximum displaced column.

Chapter 5

Figure 61. Inelastic models for beams, columns, flexural walls.
Figure 62. Fiber section discretization concept.
Figure 63. 3D volume element modeling.
Figure 64. Degrees-of-freedom and internal forces.
Figure 65. Uniaxial stress-strain relationship for concrete.
Figure 66. Uniaxial stress-strain relationship for steel reinforcement.
Figure 67. Properties of concrete – uniaxial behavior – SOFISTIK.
Figure 68. Uniaxial behavior of concrete under compression – SOFISTIK.
Figure 69. Stress-strain relationship for steel reinforcement.
Figure 70. Properties of steel reinforcement material.
Figure 71. Monotonic force – displacement curves.
Figure 72. FEM model for column. Iteration factor of ultimate loads.
Figure 73. Fiber model for calculations and interaction surface for columns.
Figure 74. M11 – numerical analysis – hysteretic force – displacement.
Figure 75. M11 – numerical vs experimental analysis – hysteresis F-D.
Figure 76. M12 – numerical analysis – hysteresis force – displacement.
Figure 77. M12 – numerical vs experimental analysis – hysteresis F-D.
Figure 78. M21 – numerical analysis – hysteretic force – displacement.
Figure 79. M21 – numerical vs experimental analysis – hysteresis F-D.
Figure 80. M22 – numerical analysis – hysteretic force – displacement.
Figure 81. M22 – numerical vs experimental analysis – hysteresis F-D.
Figure 82. M31 – numerical analysis – hysteresis force – displacement.
Figure 83. M31 – numerical vs experimental analysis – hysteresis F-D.
Figure 84. M32 – numerical analysis – hysteresis force – displacement.

Figure 85. M32 – numerical vs experimental analysis – hysteresis F-D.

Chapter 6

Figure 86. Bridge geometry.

Figure 87. Bridge model – node numbers and element names.

Figure 88. Bridge model – visualization.

Figure 89. Nonlinear stress-strain diagram for steel reinforcement S500.

Figure 90. Nonlinear stress-strain diagram for concrete C30/37.

Figure 91. Cross-section of columns – FEM discretization in fibers.

Figure 92. Petrovac earthquake motion – scaled to $a_g/g = 0.45$.

Figure 93. Calculation 1 – bending moments at the bottom of columns.

Figure 94. Calculation 2 – bending moments at the bottom of columns.

Figure 95. Calculation 3 – bending moments at the bottom of columns.

Figure 96. Calculation 8 – bending moments at the bottom of columns.

Figure 97. Bending moments at the bottom of column 1 – from calc. 1, 2, 3 and 4.

Figure 98. Bending moments at the bottom of column 1 – from calc. 1 and 2.

Figure 99. Bending moments at the bottom of column 1 – from calc. 1 and 3.

Figure 100. Bending moments at the bottom of column 1 – from calc. 1 and 4.

Figure 101. Bending moments at the bottom of column 2 – from calc. 1, 2, 3 and 4.

Figure 102. Bending moments at the bottom of column 2 – from calc. 1 and 2.

Figure 103. Bending moments at the bottom of column 2 – from calc. 1 and 3.

Figure 104. Bending moments at the bottom of column 2 – from calc. 1 and 4.

Figure 105. Bending moments at the bottom of column 3 – from calc. 1, 2, 3 and 4.

Figure 106. Bending moments at the bottom of column 3 – from calc. 1 and 2.

Figure 107. Bending moments at the bottom of column 3 – from calc. 1 and 3.

Figure 108. Bending moments at the bottom of column 3 – from calc. 1 and 4.

Figure 109. Relative displacement of pier 1 from calc. 1, 2, 3 and 4.

Figure 110. Relative displacement of pier 1 from calc. 1 and 2.

Figure 111. Relative displacement of pier 1 from calc. 1 and 3.

Figure 112. Relative displacement of pier 1 from calc. 1 and 4.

Figure 113. Relative displacement of pier 2 from calc. 1, 2, 3 and 4.

Figure 114. Relative displacement of pier 2 from calc. 1 and 2.

Figure 115. Relative displacement of pier 2 from calc. 1 and 3.

Figure 116. Relative displacement of pier 2 from calc. 1 and 4.

Figure 117. Relative displacement of pier 3 from calc. 1, 2, 3 and 4.

Figure 118. Relative displacement of pier 3 from calc. 1 and 2.

Figure 119. Relative displacement of pier 3 from calc. 1 and 3.

Figure 120. Relative displacement of pier 3 from calc. 1 and 4.

Figure 121. Acceleration at node 2 (top of column 1) from calc. 1 and 2.

Figure 122. Acceleration at node 2 (top of column 1) from calc. 1 and 3.

Figure 123. Acceleration at node 2 (top of column 1) from calc. 1 and 4.

Figure 124. Acceleration at node 4 (top of column 2) from calc. 1 and 2.

Figure 125. Acceleration at node 4 (top of column 2) from calc. 1 and 3.

Figure 126. Acceleration at node 4 (top of column 2) from calc. 1 and 4.

Figure 127. Acceleration at node 6 (top of column 3) from calc. 1 and 2.

Figure 128. Acceleration at node 6 (top of column 3) from calc. 1 and 3.

Figure 129. Acceleration at node 6 (top of column 3) from calc. 1 and 4.

Figure 130. El Centro earthquake motion scaled to $a_g/g = 0.45$.

Figure 131. Calculation 5 – bending moments at the bottom of the columns.

Figure 132. Calculation 6 – bending moments at the bottom of the columns.

Figure 133. Calculation 7 – bending moments at the bottom of the columns.

Figure 134. Calculation 8 – bending moments at the bottom of the columns.

Figure 135. Bending moments at the bottom of column 1 – from calc. 5, 6, 7 and 8.

Figure 136. Bending moments at the bottom of column 1 – from calc. 5 and 6.

Figure 137. Bending moments at the bottom of column 1 – from calc. 5 and 7.

Figure 138. Bending moments at the bottom of column 1 – from calc. 5 and 8.

Figure 139. Bending moments at the bottom of column 2 – from calc. 5, 6, 7 and 8.

Figure 140. Bending moments at the bottom of column 2 – from calc. 5 and 6.

Figure 141. Bending moments at the bottom of column 2 – from calc. 5 and 7.

Figure 142. Bending moments at the bottom of column 2 – from calc. 5 and 8.

Figure 143. Bending moments at the bottom of column 3 – from calc. 5, 6, 7 and 8.

Figure 144. Bending moments at the bottom of column 3 – from calc. 5 and 6.

Figure 145. Bending moments at the bottom of column 3 – from calc. 5 and 7.

Figure 146. Bending moments at the bottom of column 3 – from calc. 5 and 8.

Figure 147. Relative displacement of pier 1 from calc. 5, 6, 7 and 8.

Figure 148. Relative displacement of pier 1 from calc. 5 and 6.

Figure 149. Relative displacement of pier 1 from calc. 5 and 7.

Figure 150. Relative displacement of pier 1 from calc. 5 and 8.

Figure 151. Relative displacement of pier 2 from calc. 5, 6, 7 and 8.

Figure 152. Relative displacement of pier 2 from calc. 5 and 6.

Figure 153. Relative displacement of pier 2 from calc. 5 and 7.

Figure 154. Relative displacement of pier 2 from calc. 5 and 8.

Figure 155. Relative displacement of pier 3 from calc. 5, 6, 7 and 8.

Figure 156. Relative displacement of pier 3 from calc. 5 and 6.

Figure 157. Relative displacement of pier 3 from calc. 5 and 7.

Figure 158. Relative displacement of pier 3 from calc. 5 and 8.

Figure 159. Acceleration at node 2 (top of column 1) from calc. 5 and 6.

Figure 160. Acceleration at node 2 (top of column 1) from calc. 5 and 7.

Figure 161. Acceleration at node 2 (top of column 1) from calc. 5 and 8.

Figure 162. Acceleration at node 4 (top of column 2) from calc. 5 and 6.

Figure 163. Acceleration at node 4 (top of column 2) from calc. 5 and 7.

Figure 164. Acceleration at node 4 (top of column 2) from calc. 5 and 8.

Figure 165. Acceleration at node 6 (top of column 3) from calc. 5 and 6.

Figure 166. Acceleration at node 6 (top of column 3) from calc. 5 and 7.

Figure 167. Acceleration at node 6 (top of column 3) from calc. 5 and 8.

Figure 168. Hysteresis and monotonic curve for calc. 1 and calc. 2.

Figure 169. Hysteresis and monotonic curve for calc. 1 and calc. 3.

Figure 170. Hysteresis and monotonic curve for calc. 1 and calc. 3a

Figure 171. Hysteresis and monotonic curve for calc. 1 and calc. 4.

Figure 172. Monotonic (pushover) curve for calc. 1, 2, 3, 3a and 4.

LIST OF TABLES

Table 1. Typical properties of fibers for FRP COMPOSITES.

Table 2. Typical tensile properties of FRP ($V_f = 0.5$ to 0.75) and steel reinforcing bars.

Table 3. Typical mechanical properties of GFRP, CFRP and AFRP.

Table 4. Specimen details and results for columns tested by Tobbi et al. 2012.

Table 5. Results of testing under tension.

Table 6. Results of testing under compression

Table 7. Results of pullout testing

Table 8. Parameters for LADE model of concrete.

Table 9. Model parameters based on concrete class.

Page is intentionally left blank

1. CHAPTER 1

SUBJECT AND OBJECTIVES OF THE INVESTIGATION

1.1. Subject of the Investigation

Fiber reinforced polymer (FRP) bars are an efficient alternative to steel reinforcements for reinforced concrete elements, especially for reinforced concrete bridge elements and other civil engineering structures in aggressive environmental conditions. The primary reason is durability, but other reasons include low weight to strength ratio, electromagnetic neutrality, lightweight and flexibility of FRP bars [1], [4], [6]. In the territory of Kosovo, there are many existing and new structures including bridges, buildings and many other structures that have been degraded by the impact of environmental conditions. The concrete elements reinforced with GFRP (Glass Fiber Reinforced Polymers) rebars are a very good alternative to steel reinforcement as one of the solutions for improving the performance of these structures.

Considering the fact that the Kosovo region and the wider part of Europe are characterized by a high seismicity, it is important and necessary to investigate the actual seismic behavior of the constructed innovative elements reinforced with GFRP rebars.

The investigation of GFRP reinforced concrete elements has never been considered before in this region. It is clear that this research topic and research program represent the first and original attempt as well as a pioneering research effort toward development of a new composite material based technology for reinforced concrete elements applicable in the region and beyond.

1.2. Importance of the Investigation

Earthquakes are one of the most critical and destructive natural phenomena that have recently happened in our region and beyond. Catastrophic consequences and large economic losses have been widely observed. The present study focused on investigation of bridge concrete columns reinforced with the new and innovative material (glass fiber reinforced polymers) is highly important because, up to date, innovative research in this specific field has not been covered sufficiently enough even in the world scale. The present study of concrete elements reinforced with this kind of composite rebars has been performed in order to create advanced structures that are capable of withstanding

earthquake loads and resisting other destructive environmental factors for the purpose of enabling a much better protection of human lives and material properties in future [2], [21], [24].

1.3. Objective of the Investigation

The present research has been directed toward development of a new type of reinforced concrete elements by use of a new material composed of glass fibers as a reinforcement. Numerous earthquakes that have occurred for the last decades have caused severe damages to old and modern structures. The seismic behavior of GFRP reinforced concrete elements and especially bridge and building columns has still not been investigated widely in the world and in the region. In this study, particular emphasis has been put on conducting extensive experimental and numerical investigation of typical models of bridge concrete columns reinforced with GFRP rebars. Concrete columns reinforced with GFRP rebars have been tested under constant axial load and cycling load with increase of horizontal displacements until failure. Observation of the results in terms of hysteresis, bond behavior, buckling of compressed rebars, and many other aspects, has been made. Important specific parameters controlling the specific hysteretic behavior of bridge columns reinforced with GFRP reinforcement and ordinary reinforcement have been experimentally tested, analytically modeled and analyzed.

1.4. State of the Art in the Field of Investigation

For the last decades, fiber reinforced polymer (FRP) composites (a combination of two or more materials) have emerged as an evolutionary link in the development of new materials from conventional materials. Used more often in the defense and aerospace industries, advanced composites are beginning to play the role of conventional materials (commodities) used for load-bearing structural components for infrastructure applications. These unique materials are now being used worldwide for building new structures as well as rehabilitation of in-service structures.

Application of composites in infrastructural systems on a high-volume basis has come about as a result of the many desirable characteristics of composites that are superior to those of conventional materials such as steel, concrete, and wood. The increased use of composites in thousands of applications, industrial, commercial, medical, defense, and construction, has

created a need for researchers and expert professionals dedicated to advancing the theory and design of composites and providing appropriate engineering principles for structural applications in general and concrete structures in particular.

There is a significant volume of literature and research papers on composites, presenting manufacturing of composites as well as analysis and design of composite lamina based on laminated plate theory. Considerable research work has been done over the past several decades, mostly in the U.S., Canada, Japan, and several European countries.

However, the real present need for conducting further specific research, particularly devoted to investigation of the nonlinear behavior of the created new reinforced concrete members reinforced with composite bars under earthquake-like cyclic loads is still evident.

1.5. Applied Investigation Methods

Considering the specificity and the complexity of the investigations realized within the frames of the present doctoral dissertation that have included experimental testing and theoretical modelling of the behaviour of the tested prototype models, the following research methods have been applied: (1) selected appropriate experimental research methods and (2) selected advanced theoretical research methods. In Phase-1, there have been used experimental methods suitable for successful experimental testing of prototype physical bridge column models in laboratory conditions and in accordance with the prepared corresponding experimental research programme. Phase-2 has involved the use of theoretical methods and advanced computer software suitable for successful realization of extensive analytical investigations for simulation of the experimentally obtained results and formulation of verified nonlinear analytical models of the new concrete elements and the selected integral and characteristic bridge structure.

1.6. Brief Description of Investigation Results

Following the introductory Chapter 1 that provides a brief presentation of the subject and the objectives of the realized specific experimental and analytical investigations, in Chapter-2 are displayed the specific physical-mechanical characteristics of the FRP bars as a new composite material that has been used as reinforcement material of the tested models of concrete bridge piers. Presented in Chapter 3 are the characteristics of the designed and built experimental models of bridge piers reinforced by use of classical reinforcement, and

alternatively, by use of composite FRP bars. Presented additionally are the applied integral procedure and the specific experimental equipment used for the realization of the original experimental cyclic tests on the models of bridge piers up to deep nonlinearity, including also the failure stage. All experimental tests have been realized under simultaneous effect of constant vertical loads and monotonous incremental cyclic horizontal loads up to failure enabling realistic simulation of seismic forces during real earthquakes.

Chapter 4 contains a consistent presentation of the obtained original experimental results from all experimental nonlinear tests on concrete bridge piers reinforced by classical reinforcement and, alternatively, by FRP bars as a specific composite reinforcement. The obtained experimental results show that the applied composite reinforcement may become a sound alternative for the classical reinforcement in near future, particularly in realization of specific technological solutions in very specific environments and seismic conditions.

Shown in Chapter 5 are the developed refined nonlinear analytical models by successful use of the most advanced software solutions based on the general concept of the finite element method by successful application of the formulated nonlinear three-dimensional finite elements. The formulated refined nonlinear analytical model has successfully been verified based on the obtained original experimental results from the realized nonlinear experimental tests on models of bridge piers reinforced with classical reinforcement and composite reinforcement composed of incorporated FRP bars with the role of longitudinal reinforcement.

In the following Chapter 6, presented is a method of possible practical application of the formulated refined three-dimensional analytical model for analysis of the nonlinear seismic response of a real bridge with central piers reinforced by classical reinforcement and, alternatively, by a reinforcement composed of composite FRP bars. The results obtained from the performed nonlinear seismic analyses under the effect of real earthquakes have confirmed the extraordinary generality of the formulated analytical models. The formulated refined nonlinear analytical models can be used successfully in expert analyses of the nonlinear behavior of bridge structures under very strong earthquakes in case their middle piers are reinforced by the new composite reinforcement composed of FRP bars. Finally, the last Chapter 7 contains important conclusions drawn from the realized integral research activities along with general directions for future investigations.

2 CHAPTER 2 PROPERTIES OF FRP REBARS AS NEW COMPOSITE MATERIAL

2.1 Types of FRP Rebars

There are many different types of FRP rebars present on the market, Fig. 1. Almost all of them are composed of fibers of aramid, carbon, or glass embedded in epoxy resin (matrix). Glass fiber rebars are mostly used and present on the market and they can vary in respect to many diameters starting from 6 mm up to 25 mm. Glass fibers are made of E-glass, S-glass and Alkali-resistant glass. E-glass has a wide application compared to the other types. S-glass has a higher tensile strength and modulus compared to the E-glass, but is less popular than the E-glass [3], [5], [8], [12], [18]. Depending on the manufacturing process and the producer's specifications, there are many types of bars. Some types of GFRP rebars have a sand coated outer surface and some have helical spiral fiber layer for creation of a rough surface to ensure better adhesion with concrete.



Figure 2. Types of FRP rebars present on the market [16]

2.2 Properties of GFRP Rebars

2.2.1 Remarks on Properties of GFRP Rebars

Glass fiber rebars (GFRP) are anisotropic materials composed of fibers which are embedded in epoxy resin (matrix). The fibers have the role of carrying the load. The role of the epoxy resin is to transfer the load to the fibers, keeping them together and protecting them. Fibers can be from carbon, aramid, glass and other materials. GFRP rebars have shown very good behavior under both tension and compression, even though the behavior under compression has still not been sufficiently investigated. Mechanical properties that are important to be determined are as follows: tensile strength in longitudinal direction (direction of fibers), compressive strength in longitudinal direction (direction of fibers) and shear properties.

Experimental methods are not always the only way of determining the mechanical properties of FRP rebars [7], [13], [17], [31]. For many purposes, some of the presented theoretical expressions can be used for determination of the mechanical properties of FRP rebars.

2.2.2 Tensile Strength

Tensile strength of FRP rebars is one of the most important aspects. There are many factors that affect the tensile strength of FRP rebars. A very important aspect is considered the total fiber volume in relation to the total volume of the rebar. The bar production process, the quality control during the production as well as the composition and the amount of resin content also affect the tensile resistance of the bars in axial direction [6], [12], [13], [16], [19], [20]. The diameter of a rebar is also an important factor due to the fact that fibers that are located closer to the center of the rebar are not subjected to the same strains as those fibers that are closer to the outer surface. It is clear that this effect is more present in bars with a greater diameter and, in this case, bars can fail from some aspects such as tensile rupture of outer fibers, longitudinal splitting of the rebar from the concrete debonding along the interface between the rebar and the concrete) [16], [25], [27], [32], [33]. The tensile behavior of FRP rebars up to failure is represented by a linear elastic stress-strain curve. The

mechanical tensile properties of the FRP rebars and comparison with steel rebars are presented in Fig. 2 and Table 1.

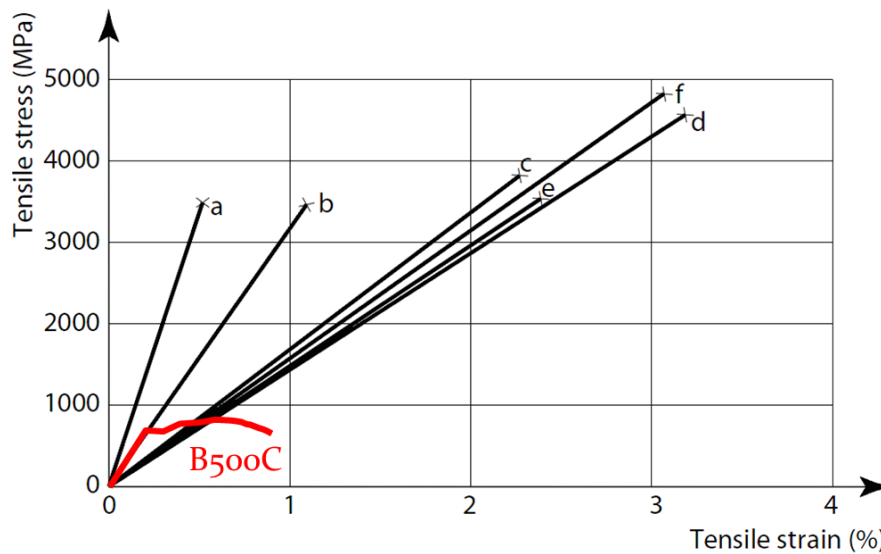


Figure 3. Stress-strain curves of typical reinforcing fibers: a) carbon (high modulus); b) carbon (high strength); c) aramid (Kevlar 49); d) S-glass; e) E-glass; f) Basalt compared with the stress-strain curve of B500C – Ordinary steel Reinforcement [16]

Table 1. Typical properties of fibers for FRP composites [12]

Fibre Type	Density	Tensile strength	Young modulus	Ultimate tensile strain	Thermal expansion coefficient	Poisson's coefficient
	(kg/m ³)	(MPa)	(GPa)	(%)	(10 ⁻⁶ /°C)	
E-glass	2500	3450	72.4	2.4	5	0.22
S-glass	2500	4580	85.5	3.3	2.9	0.22
Alkali resistant glass	2270	1800-3500	70-76	2.0-3.0	-	-
ECR	2620	3500	80.5	4.6	6	0.22
Carbon (high modulus)	1950	2500-4000	350-650	0.5	-1.2...-0.1	0.20
Carbon (high strength)	1750	3500	240	1.1	-0.6...-0.2	0.20
Aramid (Kevlar 29)	1440	2760	62	4.4	-2.0 longitudinal 59 radial	0.35
Aramid (Kevlar 49)	1440	3620	124	2.2	-2.0 longitudinal 59 radial	0.35
Aramid (Kevlar 149)	1440	3450	175	1.4	-2.0 longitudinal 59 radial	0.35
Aramid (Technora H)	1390	3000	70	4.4	-6.0 longitudinal 59 radial	0.35
Aramid (SVM)	1430	3800-4200	130	3.5	-	-
Basalt (Albarrie)	2800	4840	89	3.1	8	-

The theoretical models for determination of the longitudinal modulus E_L and tensile strengths in longitudinal directions (direction of fibers) f_{Lt} are given below (FIB 40), equation 2.1 to 2.3.

$$E_L = E_{fL} V_f + E_m (1 - V_f) \quad (2.1)$$

E_{fL} - Elastic modulus of fibers in longitudinal direction

E_m - Elastic modulus of the isotropic matrix material

Carbon and aramid fibers are orthotropic with different values of longitudinal and transversal modulus E_{fT} . Ratio $E_{fL} / E_{fT} = 24$ for Kevlar, 15.3 for high strength carbon and 65 for high modulus carbon. Where two or more types of fibers are combined in a FRP rebar, the longitudinal modulus is defined by 2.2.

$$E_L = E_{1fL} V_{1f} + E_{2fL} V_{2f} + E_m (1 - V_{1f} - V_{2f}) \quad (2.2)$$

Indexes $1f$, $2f$ refer to the first and the second type of fibers.

Generally, in the FRP rebars, the tensile strain of the fibers is lower than that of the matrix and, in this case, the longitudinal tensile strength is defined by 2.3.

$$f_{Lt} = f_{ft} \left[V_f + \frac{E_m}{E_{fL}} (1 - V_f) \right] \quad (2.3)$$

f_{ft} - Longitudinal tensile strength of fibers

Table 2 and Figure 3 show the typical properties of FRP bars in tension.

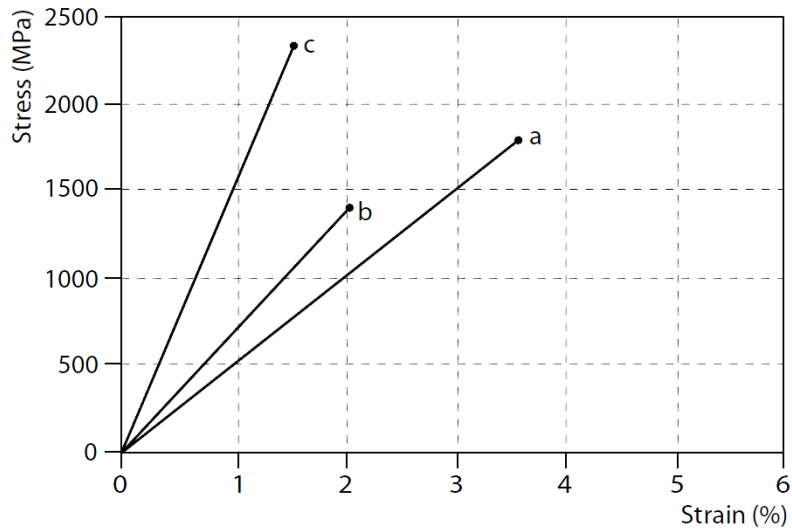


Figure 4. Stress-strain diagrams of unidirectional epoxy composites in fiber direction: a) glass/ epoxy; b) aramid/ epoxy; c) carbon/ epoxy. [12].

Table 2. Typical tensile properties of FRP ($V_f = 0.5$ to 0.75) and steel reinforcing bars

Property	Material			
	Steel	GFRP	CFRP	AFRP
Longitudinal modulus (GPa)	200	35 to 60	100 to 580	40 to 125
Longitudinal tensile strength (MPa)	450 to 700	450 to 1600	600 to 3500	1000 to 2500
Ultimate tensile strain (%)	5 to 20	1.2 to 3.7	0.5 to 1.7	1.9 to 4.4

2.2.3 Compressive Strength

The use of FRP as a compressive reinforcement is not recommended by codes, but the behavior of these rebars under compression is an important aspect to be studied because when bars are used as internal reinforcement in columns, their behavior under compression and tension depends on the type of loading [7], [12], [13], [18], [31]. Many researches have been performed for determination of the mechanical properties, especially the compressive strength of GFRP rebars. It is reported that compressive strength of rebars is between 55 – 65 % of their tensile strength [7], [23], [29]. Many researches have pointed out that the behavior of columns with GFRP rebars is quite similar to the behavior of columns reinforced

with steel rebars (Tobi et al 2012) [32], [33]. Experimental methods are not the best way of determination of compressive strength of FRP rebars. Failure modes depend on the properties of fibers and resin and the volume of fibers in a rebar. The main modes of failure of rebars due to compression are micro buckling of fibers, transverse tensile fracture due to Poisson's ratio and shear failure of a rebar [14], [34], [35]. Theoretical models for determination of compressive strengths in longitudinal directions (direction of fibers) are given in 2.4 through 2.7.

- 1) Micro buckling of fibers in shear mode, when $V_f \geq 0.4$:

$$f_{Lc} = \frac{G_m}{1-V_f} \quad (2.4)$$

f_{Lc} - Compressive stresses in longitudinal direction, G_m -shear modulus of matrix, V_f - Volume of fibers

$$G_m = \frac{E_m}{2(1+\nu_m)} \quad (2.5)$$

- 2) Transverse tensile fracture due to Poisson's strain:

$$f_{Lc} = \frac{[E_f V_f + E_m(1-V_f)](1-V_f^{1/3})\varepsilon_{mu}}{\nu_f V_f + \nu_m(1-V_f)} \quad (2.6)$$

ε_{mu} - Ultimate tensile strain of the matrix

- 3) Failure of fibers under direct shear when V_f is very high:

$$f_{Lc} = 2f_{fs} \left[V_f + (1-V_f) \frac{E_m}{E_f} \right] \quad (2.7)$$

f_{fs} - shear strength of fibers

Table 3. Typical Mechanical properties of GFRP, CFRP and AFRP

Property	E-glass/epoxy	Kevlar 49/epoxy	Carbon/epoxy
Fibre volume fraction	0.55	0.60	0.65
Density (kg/m ³)	2100	1380	1600
Longitudinal modulus (GPa)	39	87	177
Transverse modulus (GPa)	8.6	5.5	10.8
In-plane shear modulus (GPa)	3.8	2.2	7.6
Major Poisson ratio	0.28	0.34	0.27
Minor Poisson ratio	0.06	0.02	0.02
Longitudinal tensile strength (MPa)	1080	1280	2860
Transverse tensile strength (MPa)	39	30	49
In-plane shear strength (MPa)	89	49	83
Ultimate longitudinal tensile strain (%)	2.8	1.5	1.6
Ultimate transverse tensile strain (%)	0.5	0.5	0.5
Longitudinal compressive strength (MPa)	620	335	1875
Transverse compressive strength (MPa)	128	158	246

2.2.4 Shear Properties

Shear behavior of FRP rebars is controlled mainly by the matrix properties and the local distribution of stresses. A shear load applied on a FRP rebar is illustrated in Fig 4.

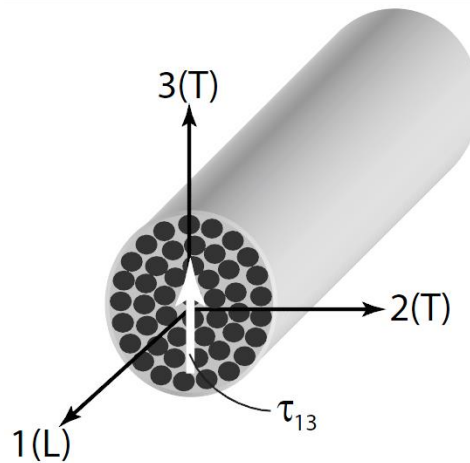


Figure 5. Shear load applied on a FRP rebar

The shear modulus is determined by expression 2.8.

$$G_{13} = G_m \frac{V_f + \eta_{13}(1 - V_f)}{\eta_{13}(1 - V_f) + V_f G_m / G_f} \quad (2.8)$$

$$\eta_{13} = \frac{3 - 4\nu_m + G_m / G_f}{4(1 - \nu_m)} \quad (2.9)$$

G_f - Fiber shear modulus.

When a bar is used as a stirrup, an off-axis strength is required. Formulas for this strength and stiffness are given in Fig. 5 and the expressions given below. The modulus of elasticity along x direction with a rotation angle θ to axis L, where $c = \cos \theta$, $s = \sin \theta$, is:

$$E_{x(\theta)} = \frac{1}{\frac{c^4}{E_L} + \frac{s^4}{E_T} + 2c^2s^2 \left(\frac{1}{2G_{LT}} - \frac{\nu_{LT}}{E_L} \right)} \quad (2.10)$$

E_T - Transverse modulus

G_{LT} - In plane shear modulus

$$E_T = \frac{E_m E_{fT}}{E_m V_f + E_{fT} (1 - V_f)} \quad (2.11)$$

$$G_{LT} = \frac{G_m G_f}{G_m V_f + G_f (1 - V_f)}$$

Ultimate tensile strength for direction θ :

$$f_{x(\theta)t} = \frac{1}{\sqrt{\frac{c^4}{f_{Lt}^2} + \frac{s^4}{f_{Tt}^2} + c^2s^2 \left(\frac{1}{f_{LTs}^2} - \frac{1}{f_{Lt}^2} \right)}} \quad (2.12)$$

f_{Tt} - is transverse tensile strength

f_{LTs} - is in plane shear strength

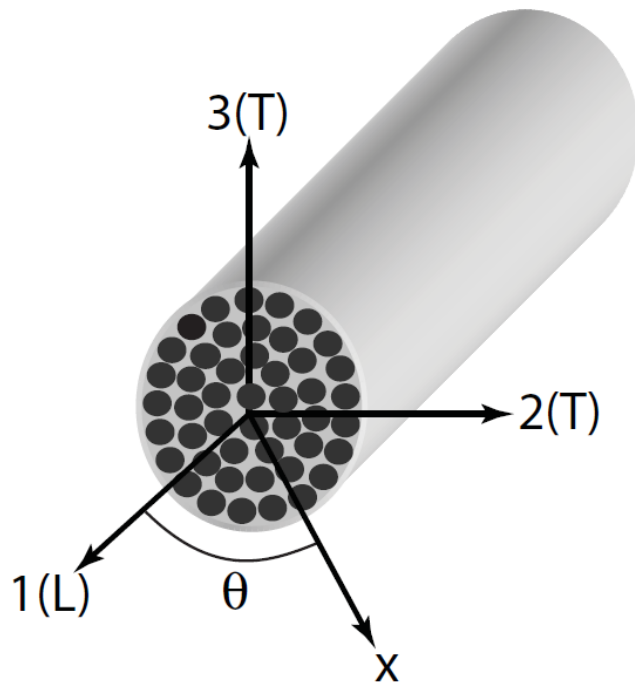


Figure 6, Off-axis loading of a rebar.

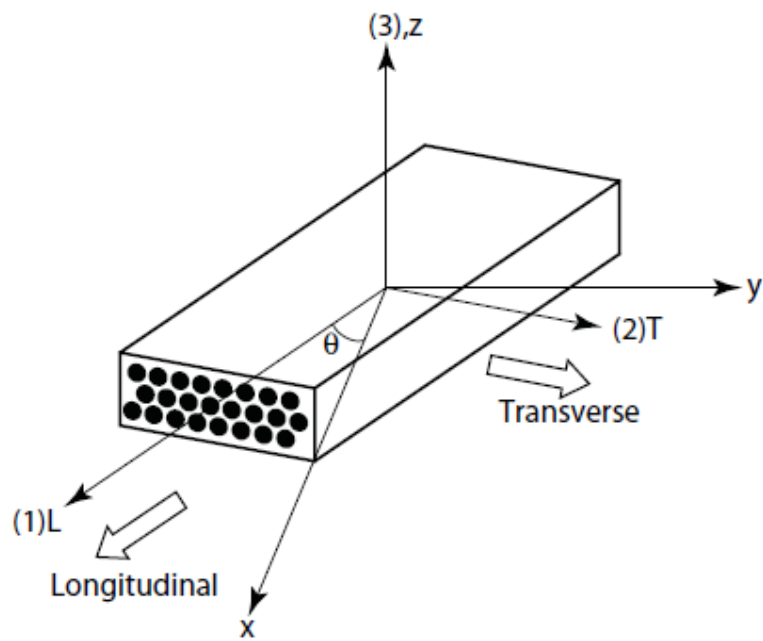


Figure 7. Local Axis of a FRP bar.

$$f_{Tt} = \frac{E_T f_{mt}}{E_m} (1 - V_f^{1/3}) \quad (2.13)$$

f_{mt} - is tensile strength of the matrix

The in plane shear strength of the matrix can be determined from:

$$f_{LIs} = \left[1 + (V_f - V_f^{1/2}) \left(1 - \frac{G_m}{G_f} \right) \right] f_{ms} C_v \quad (2.14)$$

f_{ms} - is the shear strength of the matrix

C_v - is the coefficient of voids

V_v - is the void volume

It is necessary for a FRP rebar to have less than 1% voids.

$$C_v = 1 - \sqrt{\frac{4V_v}{\pi(1-V_f)}} \quad (2.15)$$

2.2.5 Bond Behavior of FRP Bars

The bond between the concrete and the FRP reinforcing bars is an important aspect for developing a composite behavior between the concrete and the FRP bar. To reach composite behavior, sufficient bond must be mobilized between the FRP bar and the concrete to enable transfer of forces between them. The bond interaction of the FRP bar with the concrete is different from the bond between concrete and a profiled steel bar. At the profiled (deformed) steel bar, the interaction with the concrete arises primarily from the mechanical action of the bar lugs against the concrete. When the tensile stress in concrete is exceeded, this mechanical bond action leads to primary cracking extending to the surface. At FRP bars with lower elastic modulus and small surface of undulations, the bond interactions are more of a frictional character. Bond failure in steel bars is mainly

archived by crushing of concrete from the lugs. Bond failure in FRP bars is mainly caused by partial failure of concrete and some surface damage to the FRP [3], [4], [15].

The bond behavior of FRP bars depends on the characteristics of the surface and, for the same type of a surface, it depends on the manufacturing process. It is generally possible to obtain bond strengths of FRP bars of similar or greater magnitude than that of steel. Indented and grain covered bars seem to provide the best results in terms of bond strength. There are three groups of constitutive models for the bond: micro levels, meso levels and macro levels.

In different cases, any of the modeling techniques is used.

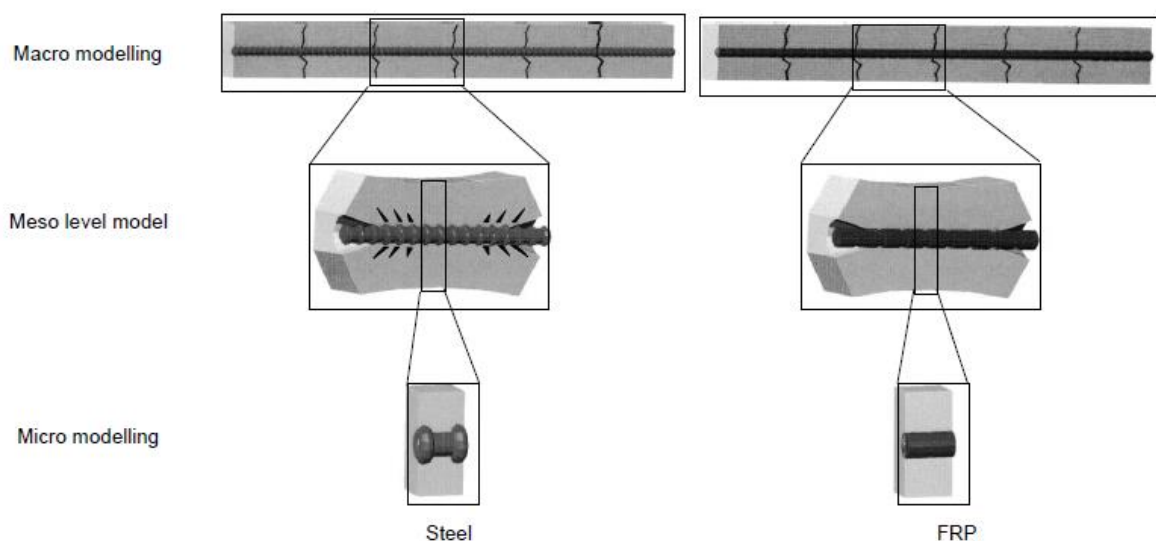


Figure 8. Bond modeling of FRP and steel bars.

a) Macro Modeling - tension stiffening

The contribution of tensioned concrete between cracks in an element by increasing its stiffness is defined as tension stiffening effect of concrete. Tension stiffening is effected by the bond between the reinforcement and the concrete. Fig. 8 shows the concept of tension stiffening of FRP reinforced concrete tensioned element.

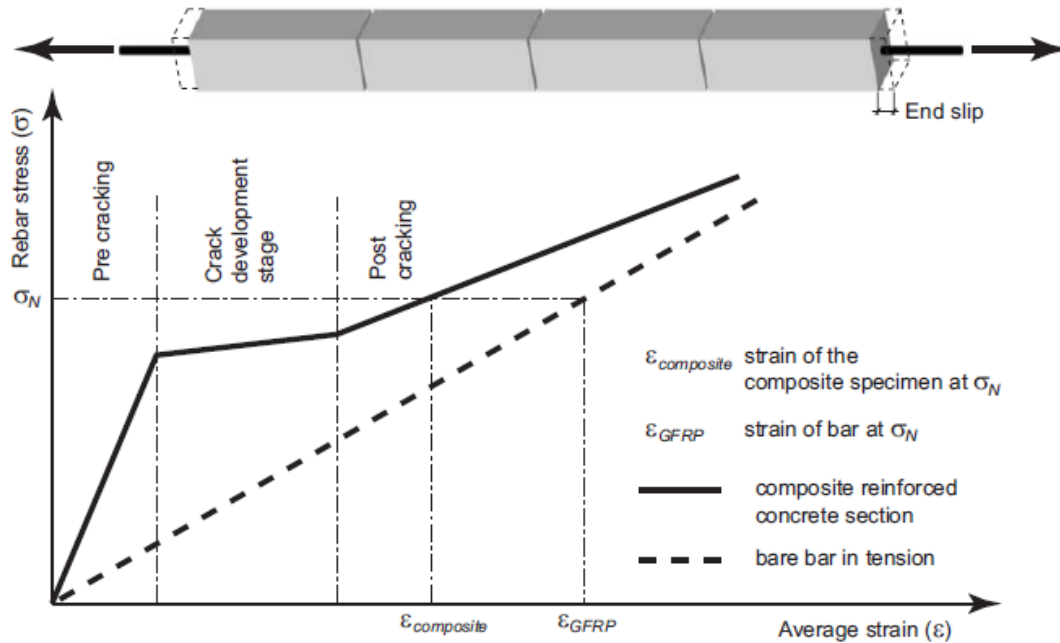


Figure 9. Tension stiffening behavior of FRP RC element.

There are three stages of behavior of a tensioned element: pre-cracking, stage of crack development and post-cracking stage when tension stiffening takes place.

There are many parameters that affect tension stiffening like reinforcement ratio, bar diameters, concrete strength.

b) Bond Modeling

In numerical analysis, the actual bond behavior of FRP rebars has an important role in the response of structural elements.

There are few models for analytical modeling of the bond behavior.

The well-known model of Eligehausen, Popov and Bertero [15] for bond modelling of steel reinforcement can be applied in modeling of the bond behavior of a FRP rebar by using the following expressions:

The ascending branch $s \leq s_m$ is given by:

$$\frac{\tau}{\tau_m} = \left(\frac{s}{s_m} \right)^\alpha \quad (2.16)$$

α - is experimental parameter and is less than 1 ($\alpha = 0.4$ for steel rebars)

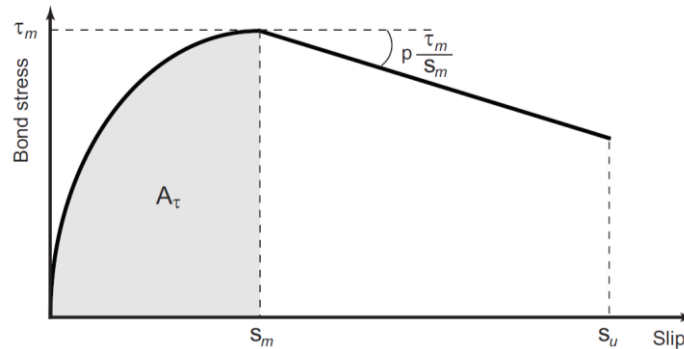


Fig. 5. Modified B.E.P. constitutive law for Bond – Slip [15].

2.3 Example of Tested Square Columns Reinforced with GFRP Rebars

It is known that the use of GFRP rebars as an internal reinforcement in concrete elements is growing worldwide. GFRP reinforcement is mostly used in concrete elements such as columns, beams, slabs, foundation slabs, bridge superstructures and substructures, etc.

Extensive research and experimental tests have been performed by many researchers of the behavior of columns reinforced with GFRP rebars.

Tobbi et al. [32] tested eight columns with a rectangular cross-section, dimensions of 350x350 and height of 1400mm under pure axial compression. Five columns were constructed with GFRP rebars, two columns were reinforced with steel reinforcement and one column was without reinforcement. Table 4 displays the specimen details and some results from the research.

Table 4. Specimen details and results on the columns tested by Tobbi et al. 2012 [32].

Specimen	Bar type	Longitudinal reinforcement	Transverse reinforcement	Tie spacing (mm)	σ_{c1}/f'_c	σ_{cc2}/f'_c
C-P-0-00	---	---	---	---	0.94	---
C-S-1-330	Steel	8 M15	M10 ties	330 (13.0)	0.98	---
C-S-1-120	Steel	8 M15	M10 ties	120 (4.72)	1.05	1.35
C-G-1-120	GFRP	8 No.19	No.13 ties	120 (4.72)	0.98	1.23
C-G-1A-120	GFRP	8 No.19	No.13 ties	120 (4.72)	1.00	1.21
C-G-2-120	GFRP	8 No.19	No.13 ties	120 (4.72)	1.00	1.27
C-G-3-120	GFRP	12 No.16	No.13 ties	120 (4.72)	0.98	1.36
C-G-3-80	GFRP	12 No.16	No.13 ties	80 (3.15)	1.02	1.68

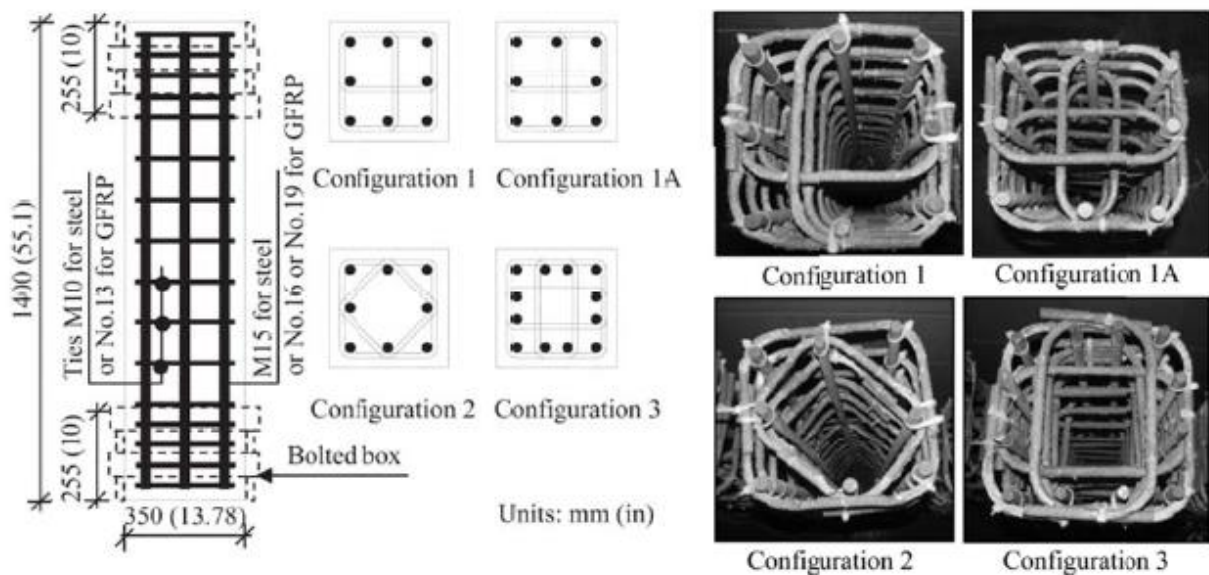


Figure 10. Specimen details on the columns tested by Tobbi et al. 2012 [32].

From the third row of table 4, it is evident that, due to the closer distance of the longitudinal rebars and the arrangement of the stirrups, maximum confinement is reached.

The main conclusions drawn by the authors are:

- The use of GFRP rebars as transverse reinforcement is effective;
- If compressive stresses in the GFRP rebar are taken as 35% of the ultimate tensile strength, the theoretical results are very close to the experimental ones when comparing the theoretical and the experimental results, and
- GFRP rebars can be used as main reinforcement in columns, whereat a smaller stirrup spacing is preferred.

The theoretical research made by Choo [11] has been focused on determination of moment-axial load interaction diagrams for concrete columns by use of different reinforcement ratios and different FRP bar types. The main assumptions used by the author in the analysis have been the following:

- (1) Parabolic and constant diagrams for concrete in compression are used and tensile strength of concrete is ignored;
- (2) A linear stress-strain relationship by using different values of the modulus of elasticity in compression and tension is used for GFRP rebars;
- (3) Bernoulli hypothesis for the section is applied;
- (4) Perfect bond assumption is accepted, and
- (5) Confinement effect is ignored.

The normalization of the moment-axial force interaction diagrams is calculated by using the following expressions:

$$P_n^* = \frac{P}{bh f_c} \quad (2.17)$$

$$M_n^* = \frac{M}{bh^2 f_c} \quad (2.18)$$

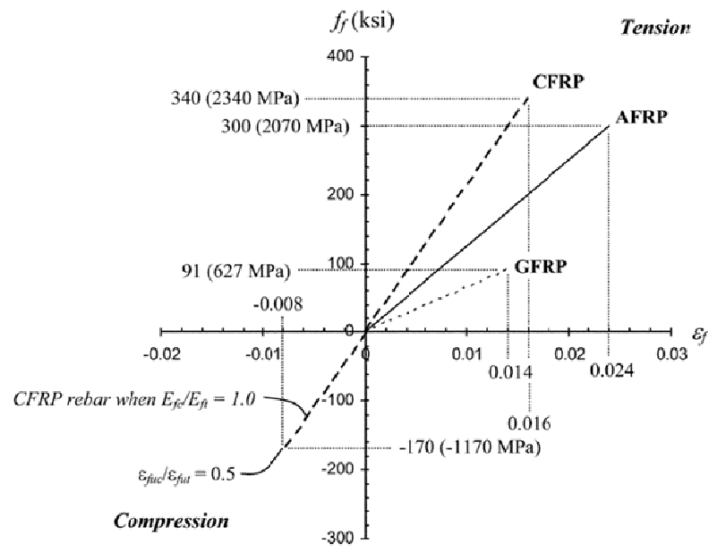


Figure 11. Properties of the FRP rebars used in the calculation [32].

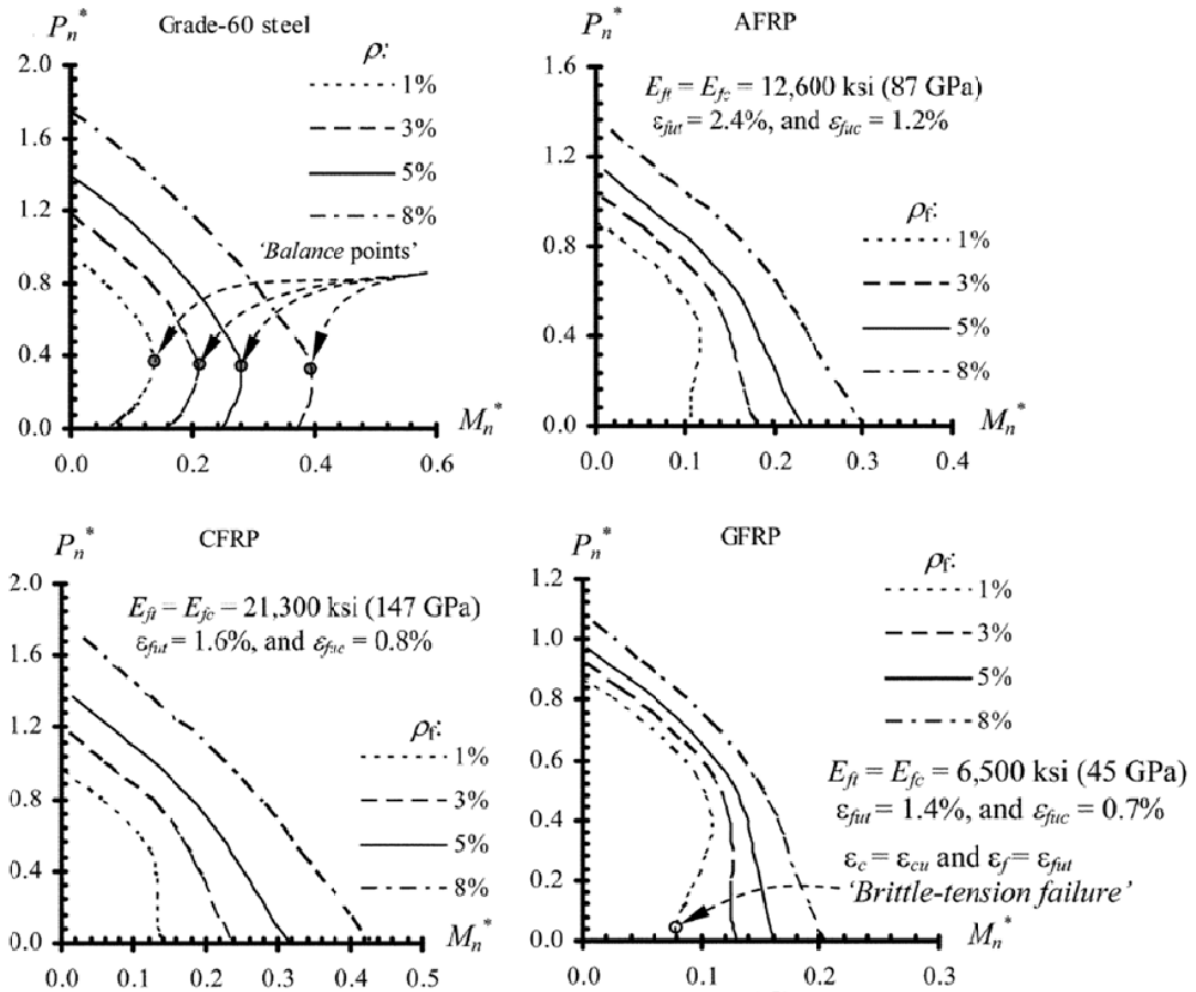


Figure 12. Normalized moment-axial force interaction diagrams [32]

In the case of steel reinforced concrete columns, the balance point occurs when steel reinforcement reaches yielding stresses and concrete reaches peak strain. Columns reinforced with FRP rebars do not show a balance point [11], [12], [13], [18]. For columns reinforced with FRP rebars, with a reinforcement ratio of 3% and greater, the moment resistance increases while the axial load decreases.

2.4 Concluding Remarks on Importance of Present Study

Earthquakes are one of the most critical and destructive natural phenomena that have recently happened in our region and beyond. Catastrophic consequences and large

economic losses have been widely observed. The present study that has been focused on investigation of bridge concrete columns reinforced with the commonly used material and the new innovative material (glass fiber reinforced polymers) is highly important because, up to date, innovative research in this specific field under simulated earthquake-like cyclic loads up to failure, has not been covered sufficiently enough even on a world scale.

The present experimental study of concrete elements reinforced with the implemented new products of composite rebars, produced originally in our region, has been performed with a specific research objective primarily directed toward original creation of advanced structures that are capable of withstanding strong earthquake loads and are efficient in resisting many other destructive environmental factors. The implemented new composite rebars are originally produced in Kragujevac, Serbia by the company „Kompozit Armatura“, the first factory in the Balkan region that produces composite reinforcement GFRP (glass fiber reinforced polymer) rebars.

The general objective of the present extensive experimental and theoretical research represents an original attempt toward development of advanced engineering structures that will provide much better protection of human lives and material properties the future.

Page is intentionally left blank

3 CHAPTER 3 PROGRAMME OF ORIGINAL CYCLIC TESTS ON BRIDGE COLUMN MODELS WITH STEEL AND GFRP REINFORCEMENT INCLUDING MATERIAL AND BOND BEHAVIOUR TESTING

3.1 Introduction

An integral programme for realization of nonlinear cyclic tests of designed bridge column prototype models with steel and GFRP reinforcement has been conceptualized for the purpose of obtaining original experimental results for the needs of the present investigations.

The basic concept of the designed bridge prototype models is briefly presented in item 3.3. It has been harmonized with the set goals of the experimental investigations. In addition, the programme of the experimental studies has also been harmonized with the available experimental conditions in the RESIN Laboratory (briefly presented in item 3.2) applied for realization of the complex experimental tests of the built models. In the RESIN laboratory, conditions have been provided for simultaneous loading of the models with the necessary level of vertical loads and programmed cyclic loads with different magnitudes of displacements in order to enable investigation of the characteristics of nonlinear behavior of the tested models up to deep nonlinearity. A brief description of the testing programs implemented for the constructed steel reinforced bridge column models and GFRP reinforced bridge column models is included in items 3.4 and 3.5, respectively.

The basic mechanical properties of the materials used for the construction of the experimental bridge pier prototype models needed for the formulation of the analytical models have experimentally been defined based on testing of representative material samples, item 3.6.

Very important and specific laboratory tests have also been planned and realized (item 3.7) for the purpose of exploring the bond behavior of GFRP and steel rebars which are of an extraordinary importance for improvement of the accuracy of the formulated analytical models by also including and simulating this specific phenomenon.

Item 3.8 contains a brief presentation of the applied basic concept of the test set-up and loading of the bridge column prototype models used as a basis for successful realization of the original experimental investigations.

Finally, in item 3.9, the most important conclusions drawn from the performed basic material properties tests and the specific bond behavior tests are summarized.

3.2 Used RESIN Laboratory Testing Facility

The planned extensive tests on large scale bridge pier models have been realized in the newly developed and established RESIN Laboratory testing facility (Fig. 34) integrating a total of 15 principal components, including:

- 1) **A laboratory testing frame (LTF).** The laboratory testing frame represents a stiff reinforced concrete structure designed with a specific geometry and conditions to enable successful installation of the test models and the testing equipment. The structure is primarily composed of two identical parallel reinforced concrete frames with external dimensions of length at plan $L = 340.0$ cm and height $h = 330.0$ cm. Each frame is composed of a left and a right column with cross-section proportions $a/b = 60.0 \times 30.0$ cm that are mutually connected in the upper zone by a reinforced concrete horizontal beam of the same proportions. In the lower zone, the reinforced concrete columns are connected by a reinforced concrete base plate with cross-section proportions $a/h = 120.0$ cm \times 40.0 cm, representing the base support for the fixation of the tested experimental models. To provide conditions for application of fixation nuts on the lower side, the reinforced concrete base plate has been elevated from the floor for 10.0 cm. To enable successful fixation of different experimental models and hydraulic actuators, a system of regularly distributed openings formed by built-in metal tubes with external diameter of $\varnothing 42.0$ mm has been made in the base RC plate as well as the vertical and horizontal segments of both RC frames. The laboratory testing frame is specifically conceptualized in this way in order to represent an independent unit that can be removed and mounted on any location according to needs.

- 2) **Model installation system (MIS)**. The model installation system consists of a series of important metal elements with corresponding diameters and different lengths that have corresponding threads and nuts at their ends for fixed fastening (without a gap) of the experimental models in compliance with the expected large forces via the corresponding openings made at suitable locations.
- 3) **Vertical hydraulic actuator (VHA)**. The vertical hydraulic actuator is particularly designed for performance of nonlinear cyclic experimental tests in the earthquake engineering field or in other demanding and specific research fields. From these reasons, a quite large capacity for applied maximum force of $\max F = \pm 300.0$ kN and an exceptionally large stroke (maximum displacement) of the piston of $\max D = \pm 300.0$ mm are provided.
- 4) **Horizontal hydraulic actuator (HHA)**. The horizontal hydraulic actuator is also specifically designed with compatible characteristics for performance of cyclic experimental tests. It is also provided with the same working capacity for maximum force $\max F = \pm 300.0$ kN and an exceptionally large maximum stroke of $\max D = \pm 300.0$ mm.
- 5) **Connecting support of the vertical hydraulic actuator (CVHA)**. The connecting support of the vertical hydraulic actuator represents a specific steel structure which is fixed to both rigid RC beams on two sides. At its risen top, the CVHA structure has a specially designed strong supporting hinge at the formed piston rod. The hinge sustains the reaction forces from the vertical actuator. This hinge enables rotation of the vertical piston with eliminated friction, enabling thus the necessary horizontal displacement of the upper part (the top) of the model which is simultaneously applied by the horizontal piston.
- 6) **Connecting support of the horizontal actuator (CHHA)**. The connecting support of the horizontal hydraulic actuator represents a specific two-part steel structure fixed to both left frame columns, while between the two parts, a specially designed strong supporting hinge is formed to continuously sustain the two-sign reaction forces from the horizontal actuator. Also, this hinge enables adequate rotation of the top of the piston in the case of possible small displacements of its front part during the performance of the complex simultaneous cyclic tests.

- 7) **Vertical actuator oil source reservoir (VASR).** The vertical actuator oil source reservoir is designed as an independent unit with a corresponding capacity to enable realization of the prescribed working conditions of the vertical actuator.
- 8) **Horizontal actuator oil source reservoir (HASR).** The horizontal actuator oil source reservoir is also designed as an independent unit with a corresponding capacity to enable realization of the prescribed working conditions of the horizontal actuator.
- 9) **Vertical actuator controlling system (VACS).** The vertical actuator controlling system represents an electronic (software) control device that provides control of mechanical parameters at each discrete moment throughout an experimental test.
- 10) **Horizontal actuator controlling system (HACS).** The horizontal actuator controlling system represents an electronic device that provides control of mechanical parameters at each discrete moment in the course of an experimental test.
- 11) **Instrumentation system (IS).** The instrumentation system represents installed electronic measuring devices capable of measuring forces, deformations, strains, etc.
- 12) **Experiment execution system (EES).** The experiment execution system actually represents a developed software with a capability of performing experimental tests. In the RESIN Laboratory, there has been applied a developed automated software that has enabled the realization of each experimental test in its entirety and in accordance with the previously prescribed protocol for realization of the test.
- 13) **Data acquisition system (DAS).** The data acquisition system is represented by electronic devices capable of transforming the measured quantities into digital numbers representing the respective mechanical or physical properties.
- 14) **Test data input port (TDIP).** The test data input port represents an specific software part providing conditions for acceptance of input data representing the prescribed protocol of the complete experimental test, and,
- 15) **Laboratory computer (LC).** The laboratory computer is used to install the required software providing control of the experimental tests, data acquisition, data storage, data processing, etc.

To realize the present original experimental tests, RESIN Laboratory has successfully been used since all the designed experimental bridge prototype models have been well harmonized with the existing characteristics of the RESIN laboratory equipment.

The Regional Seismic Innovation Network Laboratory (ReSIN Laboratory of Industrial science and Technology) located in Skopje, has been originally planned to support PhD research and young scientists from the region. With such objectives, the creation of ReSIN Lab was originally initiated, then established and currently led by Prof. Dr. Danilo Ristic. The created ReSIN Lab actually represent well promoted unique open laboratory, following the successful completion of his international long-term innovative NATO Science for Peace project (2010-2013), Brussels, Belgium.

3.3 Concept of Designed Bridge Column Prototype Models

The concept of the designed bridge column prototype models has been established based on optimal consideration of all related parameters, including the geometrical properties of the laboratory testing frame (LTF), Fig. 34, the possible positions of the hydraulic loading actuators, the possible large-scale experimental test models, the location of the connecting openings in the RC base of testing frame, etc.

Optimizing all relevant factors, the scale of $R = 1 : 3$ has been adopted as the most appropriate scale for the design of the test models. The adopted suitable, relatively large scale has enabled the experimental models to be built by use of original materials since the scaling factor in this case does not have greater effect and can be neglected.

The geometrical characteristics of the designed principal prototype model of a bridge pier are presented in Fig. 12. The modeled segment of a bridge pier has been defined to have a circular cross-section with a diameter of $D = 297 \text{ mm} = 29.7 \text{ cm}$ and length $L = 1500 \text{ mm} = 150.0 \text{ cm}$. The lower zone of the bridge pier has been fixed to the designed RC footing with a cross-section $b/h = 60.0 \text{ cm} \times 40.0 \text{ cm}$, in which three openings with $\varnothing = 32 \text{ mm}$ have been designed and made on the left and the right side, respectively, for fixation of the RC footing to the supporting RC plate of the experimental testing frame. The upper part of the RC column of the experimental model ends with a steel plate $400 \times 400 \times 20 \text{ mm}$ fixed

in the concrete by anchors. In this plate, there are four openings $\varnothing 32$ mm for connection with the front plate of the vertical hydraulic actuator.

In addition, fixed to the upper metal plate is also a corresponding horizontal device applied for fixation of the front plate of the horizontal hydraulic actuator used for application of programmed cyclic horizontal loads in the course of each experimental test.

The reinforced concrete footing of all tested models has adequately been reinforced in the upper and the lower zone by longitudinal reinforcement of 7 $\varnothing 12$ mm, with stirrups made of reinforcing steel $\varnothing 8$ mm spaced at distances $e = 15.0$ cm. In this way, the reinforced concrete footings of all tested experimental models have thoroughly satisfied the set condition for column full fixation.

The configuration of the reinforcement of the segment of the model representing the vertical column fixed to the foundation footing itself has been defined to be different for each experimental test for the purpose of exploring the real effect of different specific parameters controlling nonlinear hysteretic behavior of the tested bridge columns under simultaneous effect of constant vertical and simulated cyclic horizontal loads.

3.4 Testing Program of Constructed Steel-Reinforced Bridge Column Models

The first testing programme for the steel-reinforced bridge column models has been planned to include experimental testing of two models designated as experimental model M11 and experimental model M12. The longitudinal reinforcement for both designed experimental models has been anticipated to be composed of common steel reinforcing bars, B500C. Longitudinal reinforcement has been adopted to be identical for both models, composed of 12 $\varnothing 12$ mm steel bars (Fig. 13) ideally fixed to the rigid foundation segment.

The transverse reinforcement has been composed of round stirrups with an overlapping of common steel reinforcing bars with a diameter of $\varnothing 6$ mm. To explore the effect of the actual confinement level, the distance between the stirrups in the first model M11 has been designed to amount to $e = 15.0$ cm, while in the case of the second model M12, the distance has been much smaller, amounting to $e = 7.5$ cm.

For the construction and concreting of all experimental models, an identical formwork has been used. It has been adapted for a multiple use. This procedure has enabled identical construction of all experimental models. However, in each specific experimental model, a corresponding longitudinal and transverse reinforcement has been placed. The different phases of construction of the experimental bridge pier prototype models in the RESIN Laboratory are shown in several characteristic figures (Fig. 14, Fig. 15, Fig. 16, Fig. 17, Fig. 18 and Fig. 19).

3.5 Testing Program of Constructed GFRP-Reinforced Bridge Column Models

The second testing programme included testing of GFRP - reinforced bridge column models and it has been planned to include experimental testing of four designed models designated per pairs as M21, M22 and M31, M32.

The longitudinal reinforcement for the experimental models M21 and M22 has been used identical. The composite reinforcement existed of 12 \varnothing 10mm GFRP reinforcing bars fully anchored to the reinforced concrete footing of the experimental model.

The transverse reinforcement has been composed of round stirrups with an overlap of common steel reinforcing bars with a diameter of \varnothing 6 mm. To explore the effect of the actual confinement level, the distance of the stirrups has been adopted to be different, namely, $e = 15.0$ cm and $e = 7.5$ cm in the experimental model M21 and M22, respectively.

For the experimental models M31 and M32, the longitudinal reinforcement has also been designed to be identical, but in this case, it has been composed of a composite reinforcement with a total of 12 \varnothing 8 mm GFRP-reinforcing bars that have also been fully anchored to the rigid RC foundation of the experimental model.

The transverse reinforcement has been composed of identical round stirrups (with an overlapping) made of common steel with a diameter of \varnothing 6 mm. To also explore the effect of the confinement level, the distance of the stirrups has been used to be different, namely $e = 15.0$ cm and $e = 7.5$ cm in the experimental model M31 and M32, respectively.

3.6 Testing of Properties of Materials Used for Prototype Models

To define the actual characteristics of the built-in materials in the constructed experimental models that have been necessary for the formulation of advanced and experimentally verified analytical models in the second phase of these investigations, experimental testing of taken representative samples of each material has appropriately been performed.

3.6.1 Concrete Properties

Anticipated in the design of the experimental models has been use of concrete with compressive strength of $F_c = 35 \text{ N/mm}^2$ after 28 days. Checking of the concrete used for concreting of the six experimental models has been done through three trial cubes proportioned 150x150x150 mm by use of standard metal formworks.

The trial cubes have been designated as M1, M2 and M3, while their compressive strength has been tested after 28 days of standard curing of concrete, Fig. 20. Testing has been done in PRO-ING Institute in Prishtina by application of an equipment produced by the well known Italian producer CONTROLS. From the performed tests, the following results have been obtained:

- 1) Trial cube M1: $F_c = 35.36 \text{ N/mm}^2$, weight = 8.057 kg;
- 2) Trial cube M2: $F_c = 35.65 \text{ N/mm}^2$, weight = 8.012 kg;
- 3) Trial cube M3: $F_c = 35.13 \text{ N/mm}^2$, weight = 7.863 kg.

The obtained results are confirming the designed compressive concrete strength.

3.6.2 Steel Reinforcement Properties

The defined representative behavior of steel reinforcement B500C used for the columns is given in Fig. 22. The representative yield and the ultimate points are defined as:

- 1) Yield point: $\sigma_y = 500 \text{ N/mm}^2$; $\epsilon_y = 0.2\%$;
- 2) Ultimate point: $\sigma_u = 550 \text{ N/mm}^2$; $\epsilon_u = 5.0\%$.

3.6.3 GFRP Reinforcement Properties

The tensile strength of the implemented GFRP-rebars has been tested by use of 6 specimens with a diameter $d = 8 \text{ mm}$ and a corresponding experimental device, Fig. 21.

From the experimental tests, expected results have been obtained as follows: $F_{t1} = 1108.52 \text{ N/mm}^2$; $F_{t2} = 1110.65 \text{ N/mm}^2$; $F_{t3} = 1101.22 \text{ N/mm}^2$; $F_{t4} = 1117.20 \text{ N/mm}^2$; $F_{t5} = 1104.32 \text{ N/mm}^2$ and $F_{t6} = 1107.72 \text{ N/mm}^2$. From the obtained experimental results, there arises a computational value of $F_t = 1100.00 \text{ N/mm}^2$ which agrees very well with the data

given by the producer presented in Fig. 22, Fig. 23, Fig. 24, Fig. 25, Fig. 26, Fig. 27 and Fig 28 as well as tables Tab. 5, Tab. 6 and Tab. 7.

The presented values obtained from the performed own experimental tests, by which the characteristics specified by the producer have been confirmed, have been used in the next phase, during the formulation of the nonlinear analytical models.

3.7. Testing of Bond Behavior of GFRP and Steel Rebars

The quality of the bond between the built-in ordinary steel reinforcement bars and FRP-reinforcement rebars and the built-in concrete material is a very important mechanical property. Therefore, the own testing of specific bond behavior of GFRP and ordinary steel rebars has also been included in the frames of these investigations.

3.7.1 Bond Behavior of Steel Rebars

For the purpose of bond behavior testing of ordinary steel bars, there have been selected three samples with a diameter of $D = 12$ mm, designated as: 1) B11-SR-d12-1; 2) B12-SR-d12-2 and 3) B13-SR-d12-3. The experimental testing of the bond behavior has been realized in such a way that one end of the steel bar has been built in a concrete block, while the other end has been used for application of tensile force. After 28 days and corresponding curing, the built experimental specimens (Fig. 29 up) have been tested in the PRO-ING Institute in Prishtina. The obtained original experimental relationships between the applied axial tensile force and the manifested sliding are graphically presented in Fig. 32. The relationships shows the achieved satisfying bond between the ordinary steel reinforcing bars and the implemented concrete material for the construction of all the tested bridge column prototype models.

3.7.2 Bond Behavior of GFRP Rebars

For bond behavior testing of the GFRP rebars, three specimens were used from each of the considered three GFRP diameters $D1 = 8$ mm, $D2 = 10$ mm and $D3 = 12$ mm. The experimental testing of the bond behavior has been realized in an analogous way, by building-in of one end of a GFRP bar into a concrete block and using the other end for

application of tensile force. After 28 days and corresponding curing of the built experimental specimens (Fig. 29 down), these have successfully been tested. The obtained original experimental relationships between the tensile force and the manifested sliding are graphically presented in Fig. 32. These relationships have been designated as follows:

- 1) B21-GFRP-d8 = 1 and B22-GFRP-d8-2 – specimens with diameter $D1 = 8$ mm;
- 2) B31-GFRP-d10-1 and B32-GFRP-d10-2 – specimens with diameter $D2 = 10$ mm;
- 3) B41-GFRP-d12-1; B42-GFRP-d12-2; and B43-GFRP-d12-3 – for the tested specimens with diameter $D3 = 12$ mm.

The experimentally defined relationships between the applied axial tensile force and the manifested sliding are graphically and comparatively presented in Fig. 32. The recorded relationships have pointed out the achieved bond between the GFRP-reinforcement bars and the concrete material used for the construction of the bridge column prototype models.

Characteristic details from the realized experimental investigations of the bond behavior of the GFRP rebars are shown in Fig. 30, Fig. 31 and Fig. 33.

In addition to the above statements, from the experimental investigations, it can still be concluded that the bond behavior testing of GFRP rebars represents a very important field of research, particularly in conditions of existence of different classes of GFRP rebars and of different classes concrete with different compressive strength properties.

3.8 Test Set Up and Loading of Bridge Column Prototype Models

Considering the existing conditions at the RESIN laboratory for experimental testing of the representative bridge column prototype models, a successful set up and loading scheme have been defined (Fig. 34). Each tested experimental model has been fixed to the base of the experimental testing frame through a rigid reinforced concrete footing.

Vertical constant (axial) force to the amount of $N = 250$ kN has been applied by means of the appropriately installed vertical hydraulic actuator. Horizontal cyclic force has been applied by means of the suitably installed horizontal hydraulic actuator using a predefined cyclic-displacement history, Fig. 35. Horizontal displacement has been applied by

continuous increase of amplitudes per cycles for 5 mm until reaching of maximum displacement of $\max D = 80$ mm.

3.9 Concluding Remarks

Based on the real insight into the created conditions for the realization of the planned experimental investigations of the bridge column prototype models as well as based on the performed numerous material sample tests, the following conclusions have been drawn:

- (1) For the designed experimental models of bridge columns, there have been selected a convenient scale and an entire testing procedure that have yielded very important original experimental results;
- (2) The characteristics of the built-in concrete completely comply with the designed ones which has been very important for the success of the experimental investigations;
- (3) The quality, i.e., all the characteristics of the built-in ordinary steel reinforcement bars have satisfied all the conditions required with the project;
- (4) The experimental tests have shown that the main strength characteristics as well as the bond behavior characteristics of the used GFRP reinforcement bars have been within the limits prescribed by the producers, guaranteeing achievement of high quality, i.e., reliable, original experimental results;
- (5) The designed experimental models possess optimally harmonized conditions for their regular simultaneous loading with programmed constant axial force and cyclic horizontal force with increasing amplitudes of displacement up to deep nonlinearity and
- (6) The bond behavior characteristics between concrete and GFRP reinforcing bars represent a very complex phenomenon. To provide conditions for improved analytical modeling of this phenomenon, it is necessary to extend the realized experimental tests whereat different classes of built-in concrete and different classes of produced new composite reinforcement are to be included.

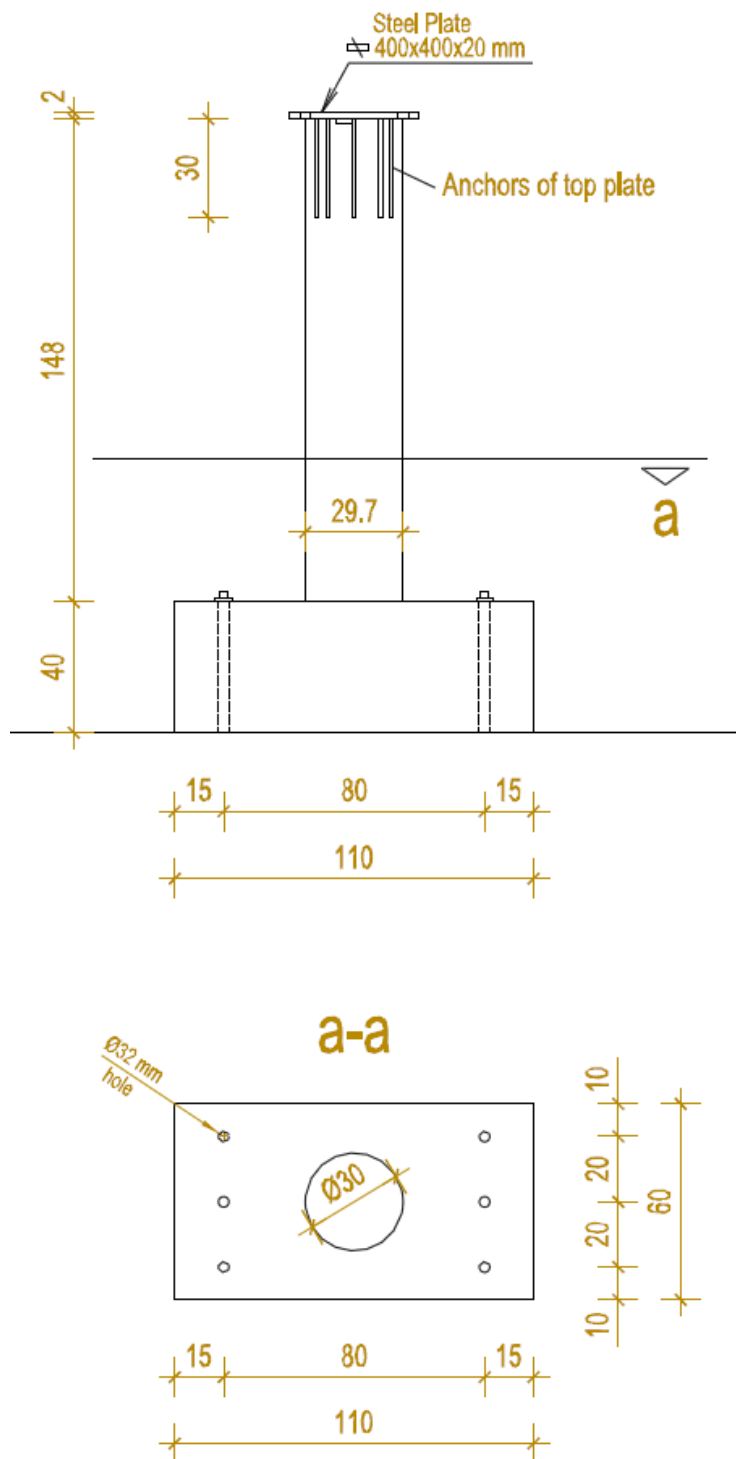


Figure 1 - Geometry, dimensions and reinforcement details for Experimental Models

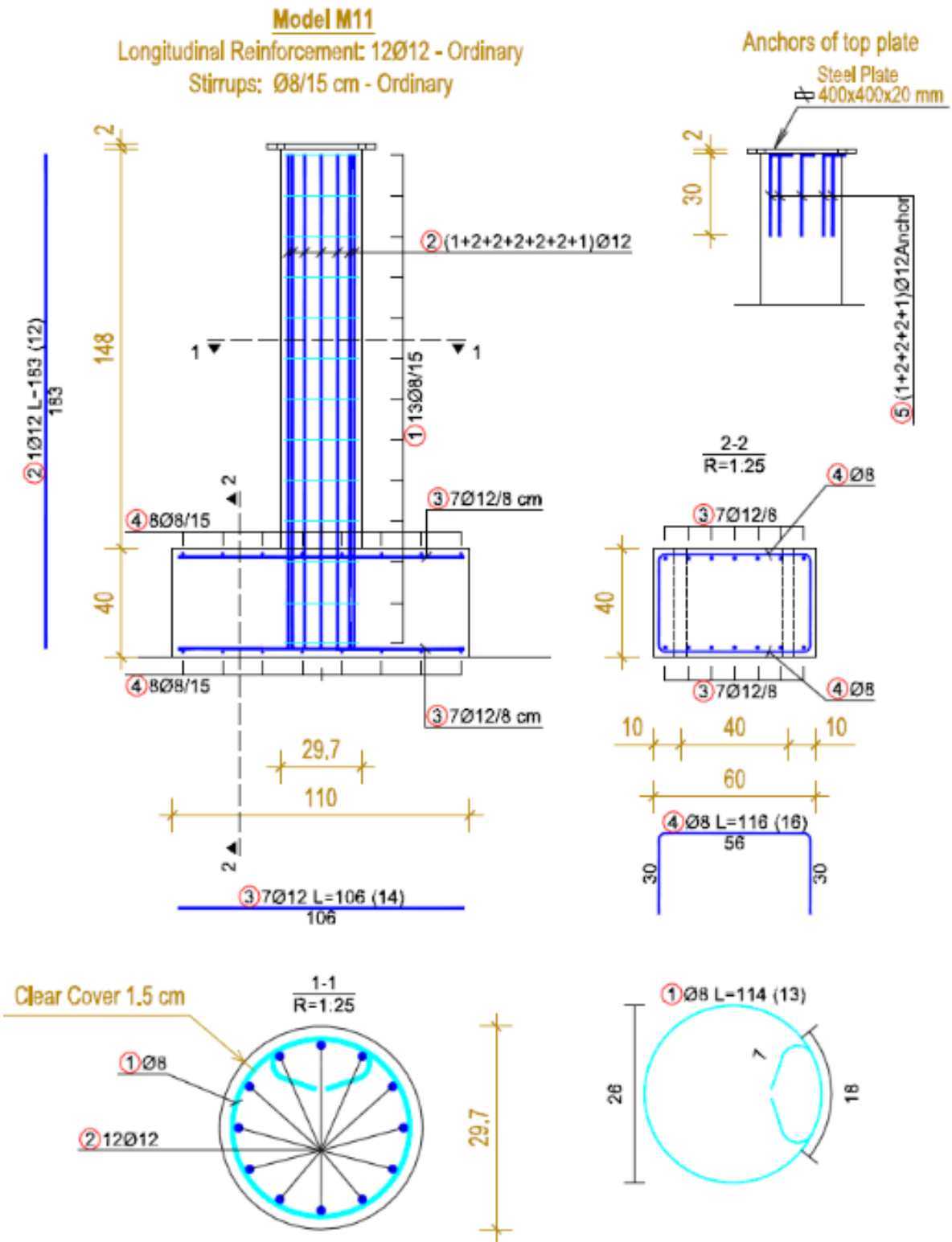


Figure 2 - Geometry, dimensions and reinforcement details for Experimental Models



Figure 3 - Formwork of Columns and Reinforcement of Columns



Figure 4 - Reinforcement of Columns – Longitudinal Rebars GFRP – Stirrups 15cm spacing



Figure 5 - Reinforcement of Columns – Longitudinal Rebars GFRP – Stirrups 7.5cm spacing



Figure 6 - Placement of Steel Pipes for fixing of anchors in foundation



Figure 7 - Top plate for application of Load



Figure 8 - Concrete columns after concreting



Figure 9 - Concrete cube specimens during and after testing in compression



$$Ft_1 = 1108.52 \text{ N/mm}^2$$
$$Ft_2 = 1110.65 \text{ N/mm}^2$$
$$Ft_3 = 1101.22 \text{ N/mm}^2$$
$$Ft_4 = 1117.20 \text{ N/mm}^2$$
$$Ft_5 = 1104.32 \text{ N/mm}^2$$
$$Ft_6 = 1107.72 \text{ N/mm}^2$$
$$Ft_{mes} = \mathbf{1100.00 \text{ N/mm}^2}$$



Figure 10 - Testing of GFRP rebars in tension

Ordinary reinforcement used in columns is B500B.

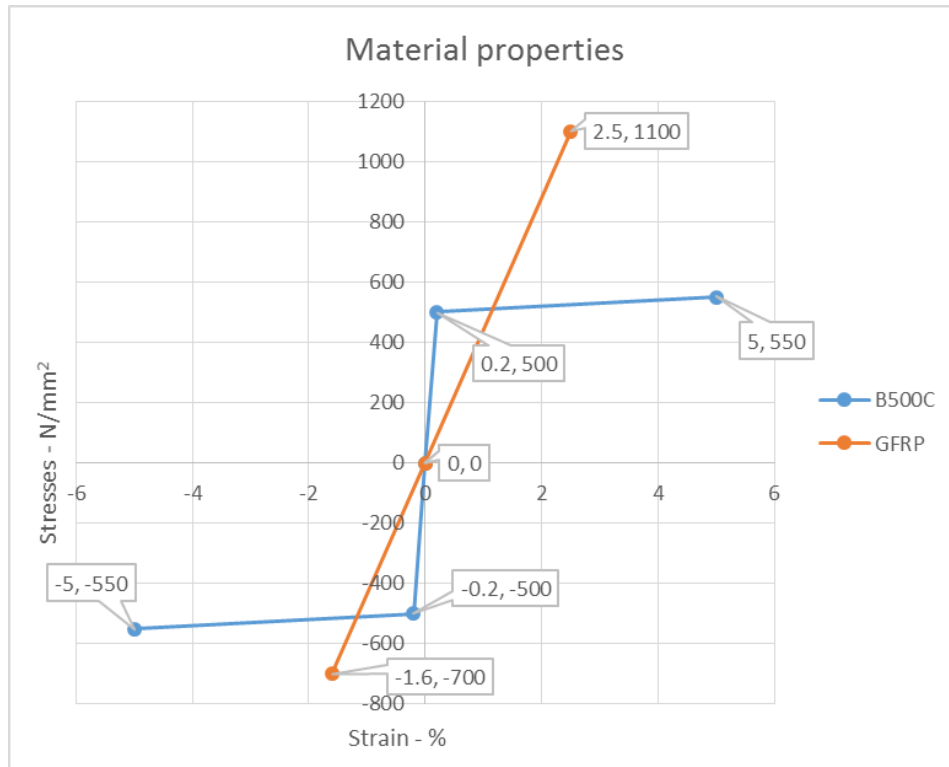


Figure 11 - Properties of used GFRP and Steel Reinforcement in tested models



Figure 12 - Testing of GFRP bars in Tension

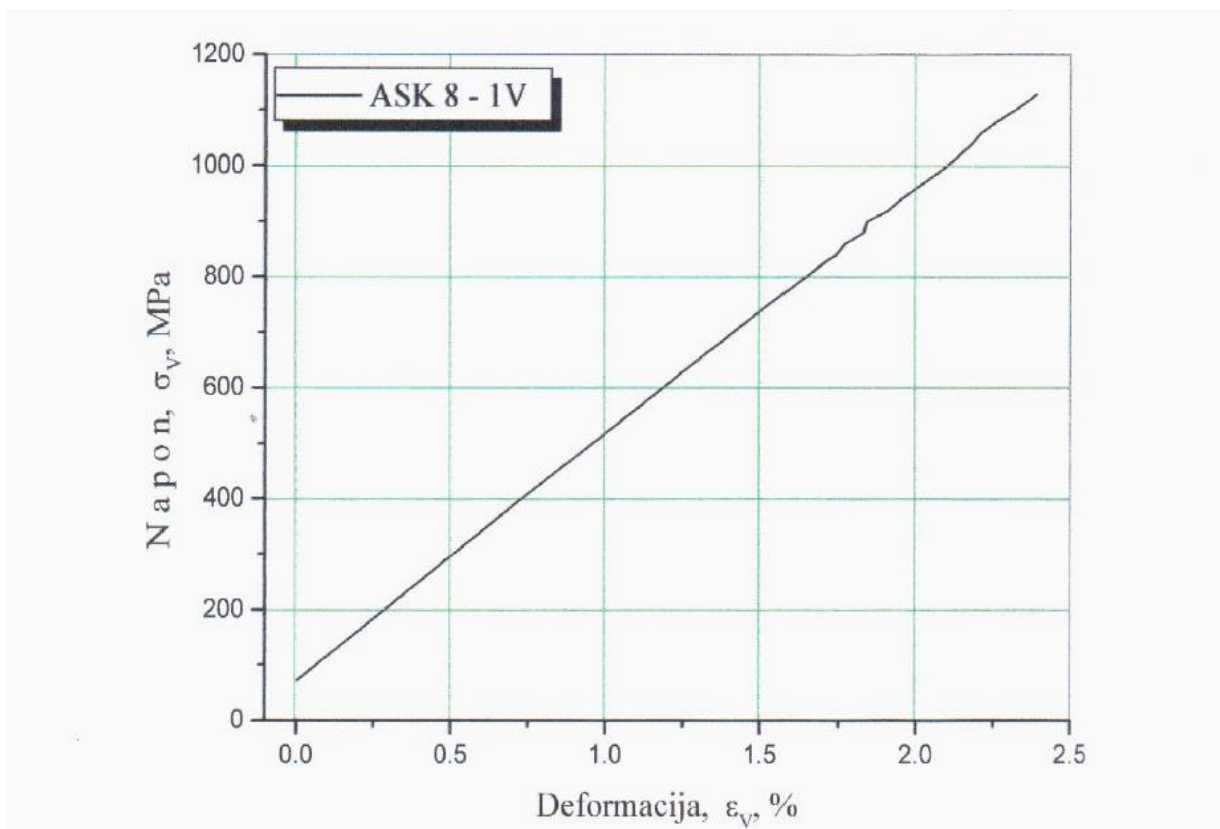


Figure 13 - Stress Strain diagram for GFRP rebar

Table 1: Results of Testing in Tension

Specimen	Diameter of Specimen, d - mm	Tensile Strength σ_v , MPa	Modul of Elasticity E_f , Gpa	Deformation, ϵ_v , %
ASK 8 - 1V		1117	53.8	2.4
ASK 8 - 2V		1087	54.1	2.2
ASK 8 - 3V	8	1163	53.1	2.5
ASK 8 - 4V		1072	52.9	2.4
ASK 8 - 5V		1102	54.5	2.2
Average Value		1108.2	53.7	2.34

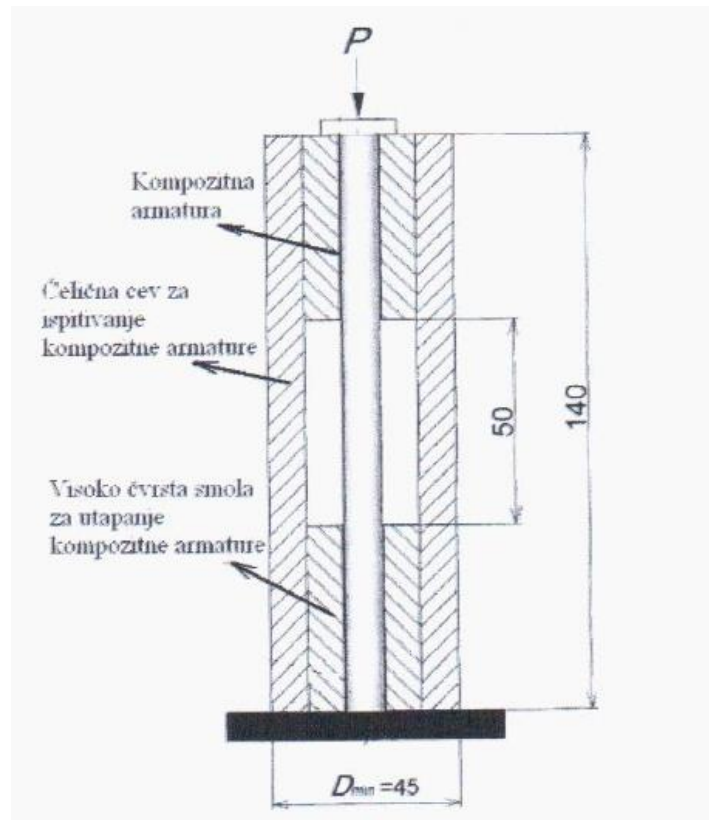


Figure 14 - Testing of GFRP Rebars in Compression

$$\sigma_{VS} = \frac{P_{\max}}{A} = \frac{4P_{\max}}{\pi d^2}$$

σ_{VS} - Compressive Strength, MPa

P_{\max} - Maximal Compressive Force, kN

$A = \frac{\pi d^2}{4}$ - Cross section of GFRP rebar, mm²

Table 2: Results of Testing in Compression

Specimen	Diameter of Specimen, d - mm	Tensile Strength σ_v , MPa
ASK 8 - 1VS	8	715
ASK 8 - 2VS		746
ASK 8 - 3VS		759
ASK 8 - 4VS		726
ASK 8 - 5VS		707
Average Value		730.6

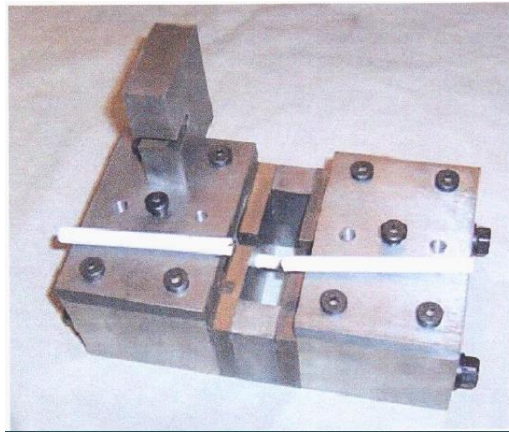


Figure 15 - Devices for shear testing of GFRP rebar

$$\tau_{sh} = \frac{P_{max}}{2A} = \frac{2P_{max}}{\pi d^2}$$

τ_{sh} - shear strength of GFRP rebars

P_{max} - Maximal Compressive Force, kN

$A = \frac{\pi d^2}{4}$ - Cross section of GFRP rebar, mm²

Specimen	Diameter of Specimen, d - mm	Shear Strength τ_{sh} , MPa
ASK 8 - 1Vsh		325
ASK 8 - 2Vsh		299
ASK 8 - 3Vsh	8	334
ASK 8 - 4Vsh		287
ASK 8 - 5Vsh		341
Average Value		317.2

Figure 16 - Results of Shear testing of GFRP rebars

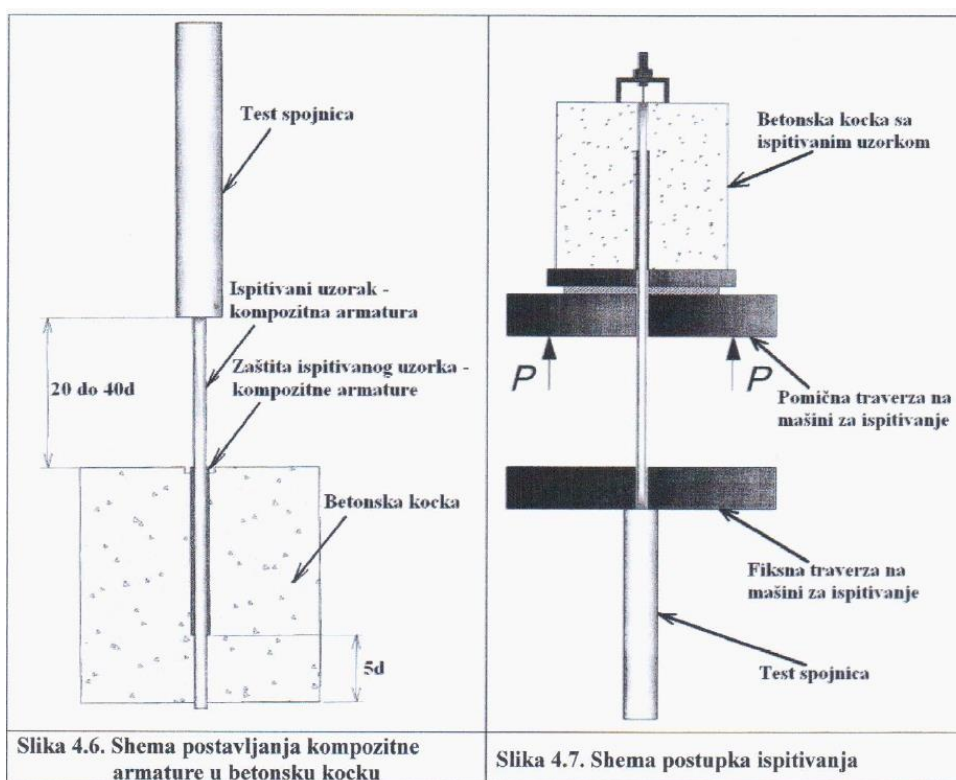


Figure 17 - Pull Out testing of GFRP used rebars

$$\tau_r = \frac{P_{\max}}{cL_{fb}}$$

τ_r - bond stresses between GFRP rebar and concrete

P_{\max} - Maximal Compressive Force, kN

$c = \pi d$ - Perimeter of cross section of bar - mm

L_{fb} - length of bonded part of bar in concrete – mm

Table 3: Results of Pull Out testing

Specimen	Diameter of Specimen, d - mm	Bond Stresses τ_r , MPa
ASK 8 - 1r	8	18.5
ASK 8 - 2r		22.3
ASK 8 - 3r		16.9
ASK 8 - 4r		20.5
ASK 8 - 5r		19.3
Average Value		19.5



Figure 18 - Specimens for testing of GFRP and Steel rebars – Pull-Out test



Figure 19 - Specimens for testing of GFRP and Steel rebar – Isolation of Bars



Figure 20 - Process of Pull out Testing

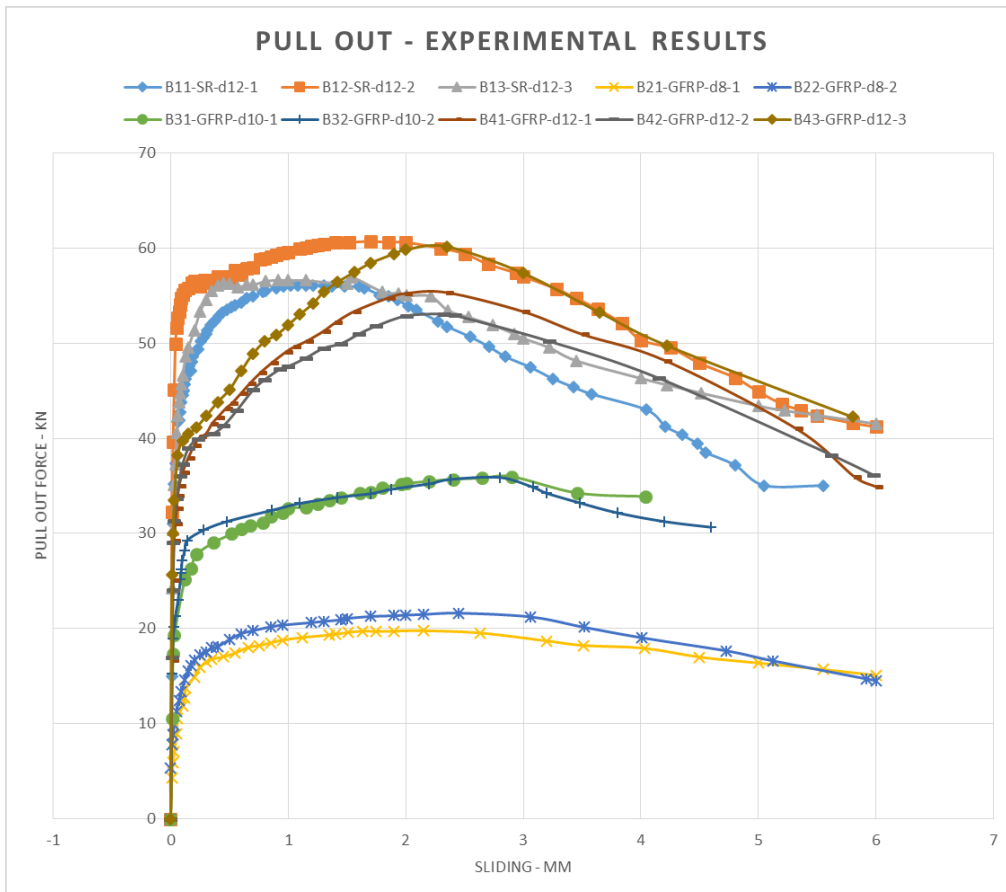


Figure 21 - Pull Out experimental results – Force – Sliding



Figure 22 – Damage on surface of GFRP rebar after pullout testing

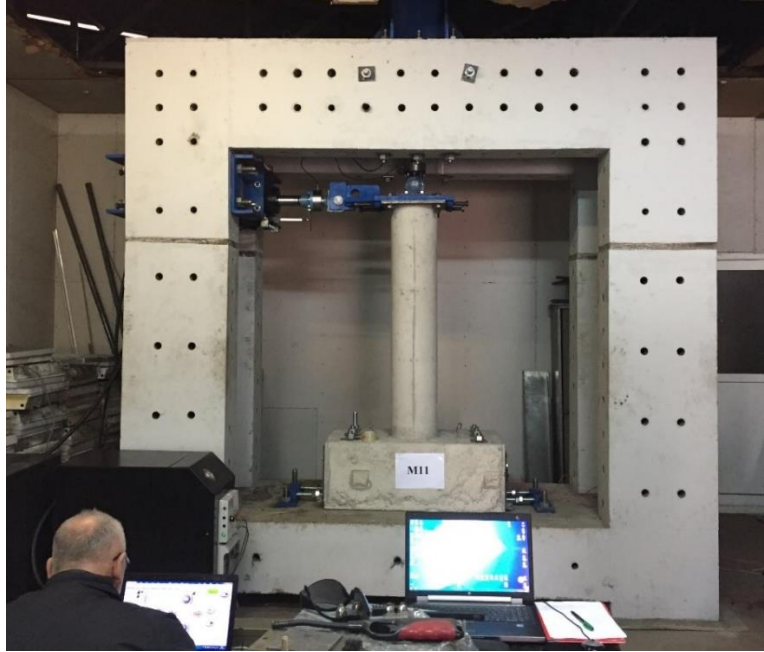


Figure 23 - Testing frame with installed column and instrumentation

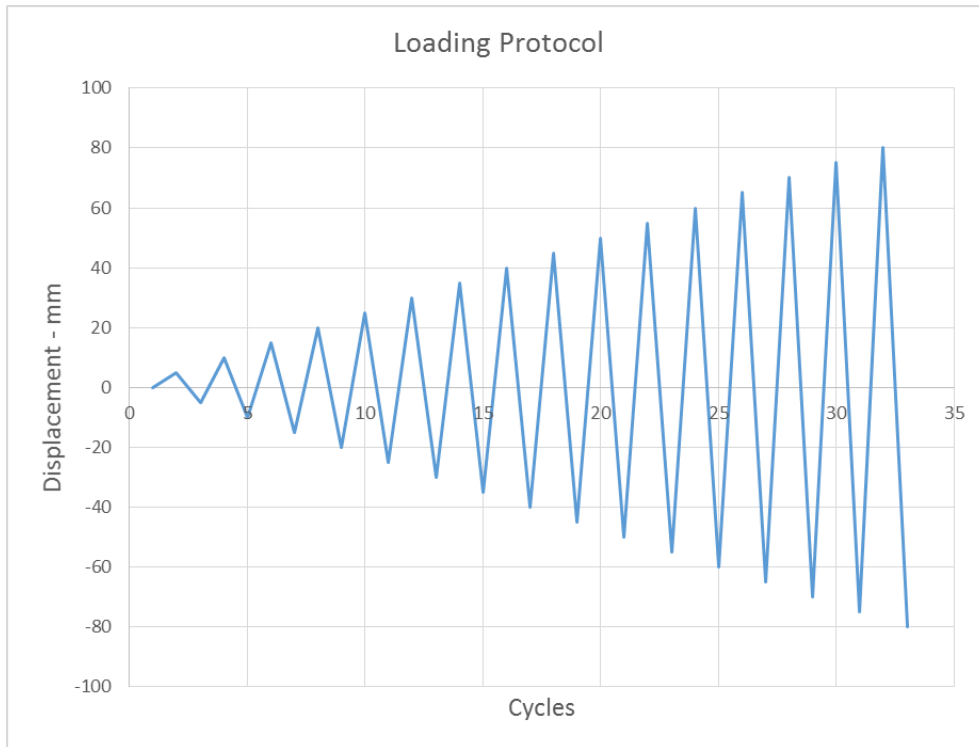


Figure 24 - Loading protocol

Page is intentionally left blank

4 CHAPTER 4 ORIGINAL RESULTS OBTAINED FROM NONLINEAR EXPERIMENTAL TESTS OF BRIDGE COLUMN MODELS WITH STEEL AND GFRP REINFORCEMENT

4.1 Introduction

The main objective of conducting the present research involving experimental testing of concrete column models reinforced with GFRP and steel reinforcement included a specifically directed original study to demonstrate that they are able to achieve an acceptable deformability and strength characteristics which will lead to their wide practical implementation.

The present research is directed toward development of new types of reinforced concrete elements by using the new composite material composed of glass fibers as a reinforcement.

Numerous earthquakes that have occurred for the last decades have caused severe damages to old and also modern structures. Seismic behavior of GFRP reinforced concrete elements and especially bridge columns has still not been investigated into all specific details in our region and even on the world scale.

From these reasons, these investigations are very topical and important for further development of the use of new reinforced concrete elements in which new composite materials play the role of reinforcement.

Comparison of the obtained results in terms of hysteretic relations, bond behavior, buckling of compressed rebars and many other important related factors is highly valuable in the process of nonlinear behavior evaluation of the bridge columns reinforced with ordinary steel-reinforcement and with composite GFRP reinforcement.

Having in mind the above clear statements, further in this chapter, i.e., in item 4.2, the results obtained from the tests conducted on steel reinforced bridge column models are first of all presented. Further, in item 4.3, the original experimental results obtained from the conducted cyclic tests on GFRP-reinforced concrete models with different reinforcement options are presented.

Finally, item 4.4 contains a summary of the most important concluding remarks arising from the performed ample original experimental investigations.

4.2 Results From Cyclic Tests of Steel-Reinforced Bridge Column Models

As previously stated, within the frames of the first experimental programme, experimental testing of two experimental prototype models, model M1 and model M2, of bridge piers reinforced with ordinary steel reinforcement has been performed.

Both experimental models have been reinforced with identical longitudinal reinforcement ($12\phi 12$), i.e, with 12 steel bars with a diameter of 12 mm. In the case of the first experimental model, the round hoops have been placed at a distance of $t = 15.0$ cm, while in the second experimental model, the hoops have been placed more densely, i.e., at a distance of $t = 7.5$ cm. In this way, conditions have been created for exploration of the effect of the transverse reinforcement upon the nonlinear hysteretic behavior of the experimental models up to deep nonlinearity.

The required conditions have been enabled since, in both cases, identical loading conditions have been applied. In both cases, a constant vertical (axial) compressive force of $N = 250.0$ kN has been applied. With this force, in column section a total initial compressive stress of $\sigma_0 = 0.396$ kN/cm² has been obtained, corresponding to the usual level of stress of bridge structures under the effect of dead loads.

Also, in both cases, an identical loading programme with a horizontal cyclic force has been applied since the experiments have been conducted with the prescribed cyclic displacements up to the defined ultimate value of $U_{limit} = UL = 60.0$ mm. Using the installed acquisition system, ample numerical results have successfully been stored in special files for further processing. By using the experimentally recorded numerical results on the time histories of forces and displacements, the obtained original hysteretic relationships from the experimental tests on model M11 and model M12 have been plotted and these are presented in a graphic form in Fig. 36 and Fig. 37, respectively.

4.2.1 Experimental Hysteretic Curve of Model-M11: Steel Reinforcement Level SRL=1 (12XD12) and Confinement Level CL=1 ($t=15.0$ cm)

The hysteretic relationship obtained from testing of model M11 is shown in Fig. 36. It is evident that the hysteretic relationship is very stable and regular, which points to the expected good nonlinear behavior of the tested prototype model M11 of a bridge pier.

In accordance with the obtained experimental results, there has been developed a corresponding envelope relationship defined by the following four points: (1) point 0 – coordinate origin; (2) point Y – yielding point; (3) point U – point of recorded maximum force and (4) point L – referring to limit deformation, i.e., maximum applied deformation.

In this case, for model M11, the defined points on the envelope curve have been of the following values:

- 1) Point Y: $DY = 4.5 \text{ mm}$; $FY = 24.0 \text{ kN}$
- 2) Point U: $DU = 39.0 \text{ mm}$; $FU = 65.0 \text{ kN}$
- 3) Point L: $DL = 60.0 \text{ mm}$; $FL = 57.0 \text{ kN}$.

In addition, using the recorded data from the envelope curve, there have been recorded other three indicative parameters as follows: (1) initial stiffness of the model – K_0 ; (2) second stiffness of the model – K_1 and (3) negative stiffness of the model – K_2 .

For the tested model M11, the following values of these parameters have been obtained:

- 1) $K_0 = 5.33 \text{ kN/mm}$
- 2) $K_1 = 1.18 \text{ kN/mm}$
- 3) $K_2 = -0.38 \text{ kN/mm}$

4.2.2 Experimental Hysteretic Curve of Model-M12: Steel Reinforcement Level SRL=1 (12XD12) and Confinement Level CL=2 ($t=7.5 \text{ cm}$)

The obtained original hysteretic relationship from testing of model M12 is shown in Fig. 37. It is also evident that the hysteretic relationship is very stable and regular, showing the expected good nonlinear behavior of the tested prototype model M12 of a bridge pier with better confinement due to the more densely placed hoops. For the tested model M12, there have been obtained the following numerical values by which the corresponding points on the envelope curve have been defined:

- 1) Point-Y: $DY = 3.5 \text{ mm}$; $FY = 29.5 \text{ kN}$
- 2) Point-U: $DU = 31.0 \text{ mm}$; $FU = 75.0 \text{ kN}$
- 3) Point-L: $DL = 60.0 \text{ mm}$; $FL = 62.8 \text{ kN}$

Using the points defined on the envelope curve, there have also been obtained the following parameters that characterize the nonlinear hysteretic behavior of the tested bridge prototype model M12:

- 1) $K_0 = 8.42 \text{ kN/mm}$ – initial stiffness of the model
- 2) $K_1 = 1.63 \text{ kN/mm}$ – second stiffness of the model
- 3) $K_2 = -0.42 \text{ kN/mm}$ – negative stiffness of the model

These parameters are of a great importance for evaluation of the successfulness and suitability of the formulated nonlinear analytical models for practical use.

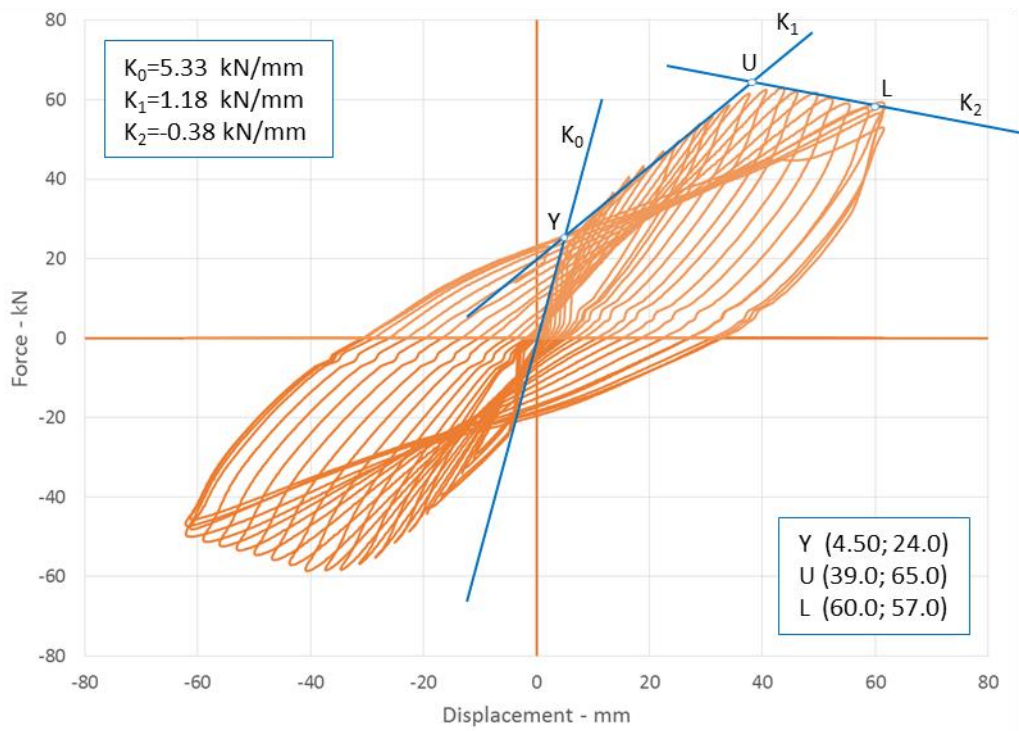


Figure 1 - Experimental hysteresis of M11 Column

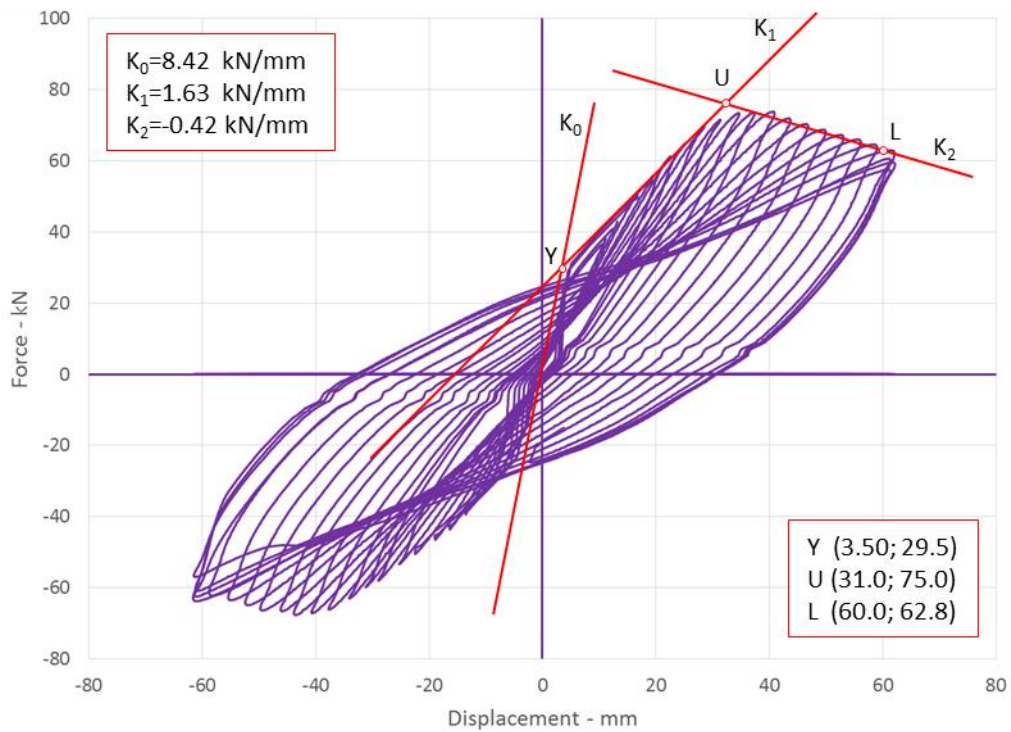


Figure 2 - Experimental hysteresis of M12 Column

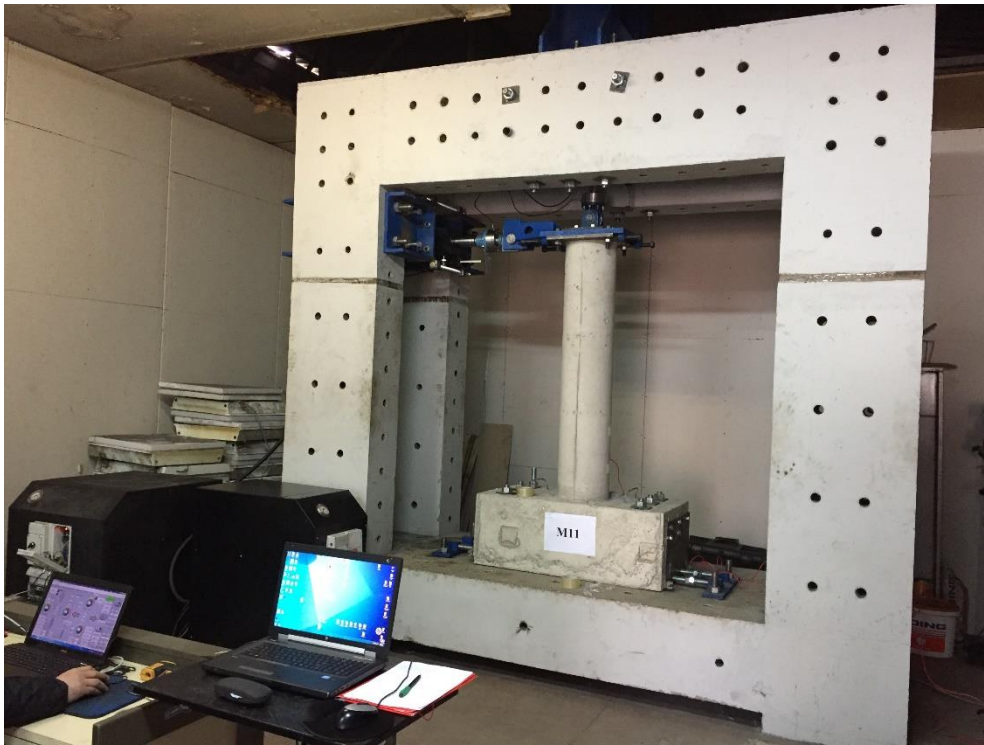


Figure 3 - Testing of Column M11



Figure 4 - Column M11 - Cracking at different stages of loading



Figure 5 - Column M11 – Spalling of Cover and Buckling of Longitudinal Rebar



Figure 6 - Testing of Column M12



Figure 7 - Column M12 - Cracking at different stages of loading



Figure 8 - Column M12 – Cover spalling

4.3 Results From Cyclic Tests of GFRP-Reinforced Bridge Column Models

Within the frames of the second phase of the experimental programme, experimental testing on four experimental prototype models of bridge piers reinforced with composite GFRP – reinforcing bars has been performed.

- The first two experimental models, M21 and M22, have been reinforced with identical longitudinal reinforcement, $(12\phi 10)$, i.e., with 12 GFRP – reinforcing bars with a diameter of 10 mm. In the first experimental model, the round hoops have been placed at distance $t = 15.0$ cm, while in the second experimental model, the hoops have been placed at a denser distance, namely at $t = 7.5$ cm.

In this way, conditions have been created for exploration of the effect of the transverse reinforcement on the nonlinear hysteretic behavior of the experimental models with GFRP reinforcement up to deep nonlinearity.

The necessary conditions for comparison have also been provided in this case since in both cases, the same constant axial compressive force of $N = 250$ kN, i.e., an initial stress of $\sigma_0 = 0.396$ kN/cm² has been applied.

Using the experimentally recorded numerical results on the time histories of forces and displacements, the original hysteretic relationships obtained from the experimental tests on model M21 and model M22 have been plotted. These are presented in a graphic form in Fig. 44 and Fig. 45.

- The second two experimental models, M31 and M32, have been reinforced with identical longitudinal reinforcement, $(12\phi 8)$, i.e., by 12 GFRP-reinforcing bars with a diameter of 8 mm.

In the first experimental model, the round hoops have been placed at a distance of $t = 15.0$ cm, while in the second experimental model, the hoops have been placed more densely, i.e., at a distance of $t = 7.5$ cm.

In this way, conditions have once again been created to explore the effect of transverse reinforcement upon the nonlinear hysteretic behavior of the second pair of experimental models with GFRP reinforcement up to deep nonlinearity.

Also, in this case, the necessary conditions for comparison have been provided since in both cases, the same constant axial compressive force of $N = 250.0$ kN has been applied. Using the experimentally recorded numerical results on the time histories of forces and displacements, the obtained original hysteretic relationships from the experimental tests on model M31 and model M32 have been plotted. These are presented graphically in Fig. 46 and Fig. 47.

Presented further is a brief review of the main parameters by which the nonlinear behavior of each tested individual experimental model is characterized.

4.3.1 Experimental Hysteretic Curve of Model-M21: GFRP Reinforcement Level GFRP-RL=1 (12XD10) and Confinement Level CL=1 ($t=15.0$ cm)

The original hysteretic relationship obtained from testing of model M21 is presented in Fig. 44. It is evident that the hysteretic relationship shows a very stable and regular form. However, a considerably expressed “pinching” effect, i.e., its narrowing under reverse deformations is present.

For the tested model M21 reinforced with GFRP reinforcement as the main reinforcement and with a lower level of confinement with transverse reinforcement, the following numerical values defining the corresponding points on the envelope curve have been obtained:

- 1) Point – Y: $DY = 7.5$ mm; $FY = 30.0$ kN
- 2) Point – U: $DU = 30.0$ mm; $FU = 33.0$ kN
- 3) Point – L: $DL = 80.0$ mm; $FL = 17.5$ kN

Using the defined points on the envelope curve, the following parameters characterizing the nonlinear hysteretic behavior of the tested model of the prototype bridge pier M21 have been obtained:

- 1) $K_0 = 4.0$ kN/mm – initial stiffness of the model
- 2) $K_1 = 0.13$ kN/mm – second stiffness of the model
- 3) $K_2 = -0.31$ kN/mm – negative stiffness of the model

These parameters enable adequate comparison with the results obtained for the next tested model of a bridge prototype pier M22.

4.3.2 Experimental Hysteretic Curve of Model-M22: GFRP Reinforcement Level GFRP-RL=1 (12XD10) and Confinement Level CL=2 (t=7.5 cm)

The obtained original hysteretic relationship from the performed testing of model M22 is shown in Fig. 45. It is also evident in this case that the hysteretic relationship is of a very stable and regular form. However, in this case, it can also be seen that there is a considerably expressed “pinching” effect, i.e., its narrowing during reverse deformations.

For the tested model M22 reinforced with GFRP reinforcement as the main reinforcement, with a greater level of confinement with transverse reinforcement, the following numerical values defining the representative points on the envelope curve have been obtained:

- 1) Point – Y: $DY = 7.5 \text{ mm}$; $FY = 32.0 \text{ kN}$
- 2) Point – U: $DU = 30.0 \text{ mm}$; $FU = 38.0 \text{ kN}$
- 3) Point – L: $DL = 80.0 \text{ mm}$; $FL = 18.0 \text{ kN}$

Using the defined points on the envelope curve, the following parameters characterizing the nonlinear hysteretic behavior of the tested model of prototype bridge pier M22 have been obtained:

- 1) $K_0 = 4.26 \text{ kN/mm}$ – initial stiffness of the model
- 2) $K_1 = 0.27 \text{ kN/mm}$ – second stiffness of the model
- 3) $K_2 = -0.40 \text{ kN/mm}$ – negative stiffness of the model

The stated parameters are of an extraordinary importance for verification of the formulated analytical model for simulation of the nonlinear behavior of the tested model of the prototype bridge pier M22.

4.3.3 Experimental Hysteretic Curve of Model-M31: GFRP Reinforcement Level GFRP-RL=2 (12XD8) and Confinement Level CL=1 (t=15.0 cm)

The obtained original hysteretic relationship from testing of model M31 is shown in Fig. 46. It is evident that the hysteretic relationship is quite stable and of a regular form. However, also in this case, it can be concluded that there is a quite expressed “pinching” effect, i.e., its narrowing under reverse deformations.

For the tested model M31 reinforced with GFRP reinforcement as the main reinforcement, with a lower level of confinement with transverse reinforcement, the following numerical values defining the corresponding points on the envelope curve have been obtained:

- 1) Point – Y: $DY = 6.5 \text{ mm}$; $FY = 22.0 \text{ kN}$
- 2) Point – U: $DU = 20.0 \text{ mm}$; $FU = 26.0 \text{ kN}$
- 3) Point – L: $DL = 80.0 \text{ mm}$; $FL = 6.5 \text{ kN}$

Using the defined points on the envelope curve, the following parameters characterizing the nonlinear hysteretic behavior of the tested model of prototype bridge pier M31 have been obtained:

- 1) $K_0 = 3.38 \text{ kN/mm}$ – initial stiffness of the model
- 2) $K_1 = 0.29 \text{ kN/mm}$ – second stiffness of the model
- 3) $K_2 = -0.36 \text{ kN/mm}$ – negative stiffness of the model

These parameters enable very successful verification of the formulated nonlinear analytical model for simulation of the hysteretic behavior of the tested experimental model M31.

4.3.4 Experimental Hysteretic Curve of Model-M32: GFRP Reinforcement Level GFRP-RL=2 (12XD8) and Confinement Level CL=2 ($t=7.5 \text{ cm}$)

The obtained original hysteretic relationship from the performed testing of model M32 is presented in Fig. 47. Also, in this case, it is evident that the hysteretic relationship is of a very stable and regular form. However, also in this case, an expressive “pinching” effect, i.e., its narrowing under reverse deformations is manifested.

For the tested model M32 reinforced with GFRP reinforcement as the main reinforcement, with a larger level of confinement with transverse reinforcement, the following numerical values defining the representative points on the envelope curve have been obtained:

- 1) Point – Y: $DY = 6.5 \text{ mm}$; $FY = 22.0 \text{ kN}$
- 2) Point – U: $DU = 20.0 \text{ mm}$; $FU = 28.0 \text{ kN}$
- 3) Point – L: $DL = 80.0 \text{ mm}$; $FL = 12.5 \text{ kN}$

Using the defined points on the envelope curve, there have been obtained the following parameters that characterize the nonlinear hysteretic behavior of the tested model of the prototype bridge pier M32.

- 1) $K_0 = 3.38 \text{ kN/mm}$ – initial stiffness of the model
- 2) $K_1 = 0.61 \text{ kN/mm}$ – second stiffness of the model
- 3) $K_2 = -0.29 \text{ kN/mm}$ – negative stiffness of the model

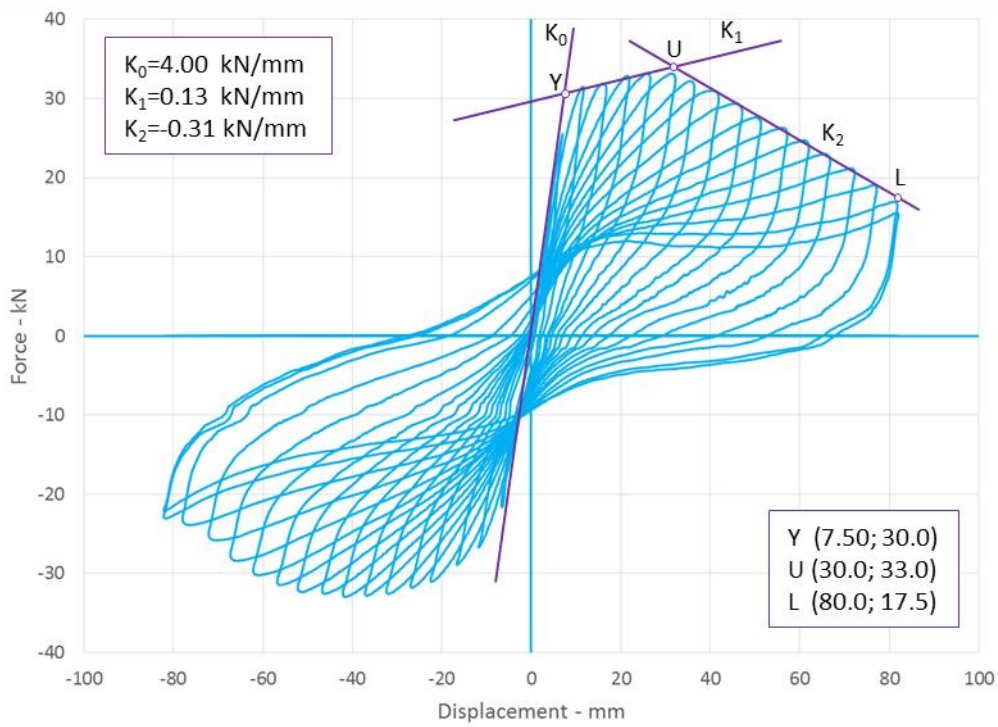


Figure 9 - Experimental hysteresis of M21 Column

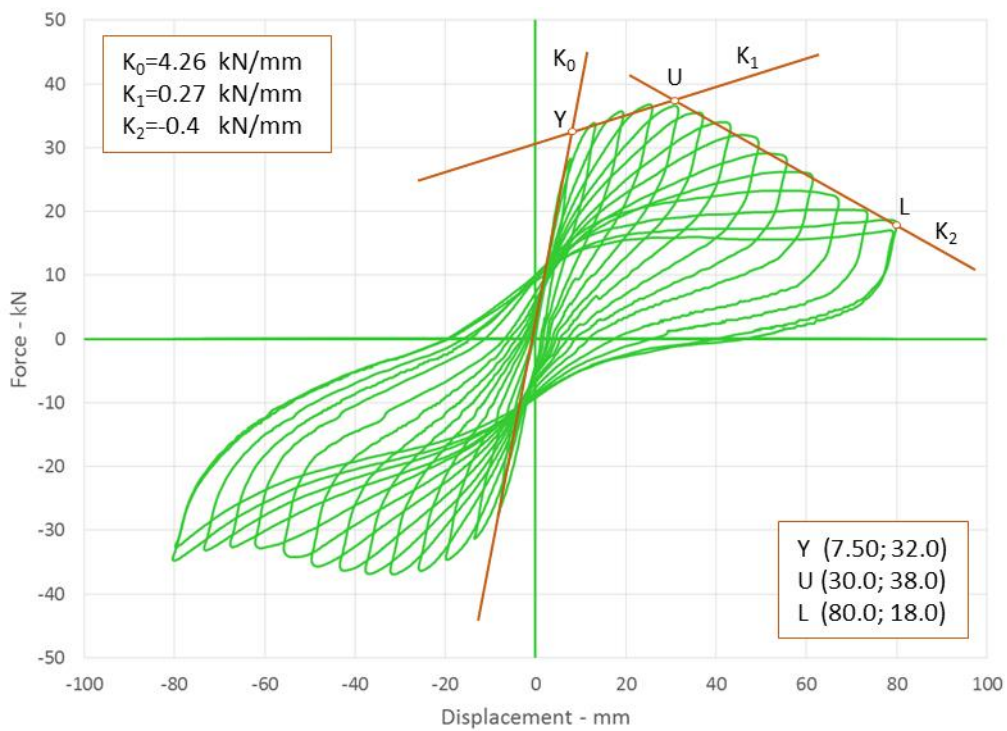


Figure 10 - Experimental hysteresis of M22 Column

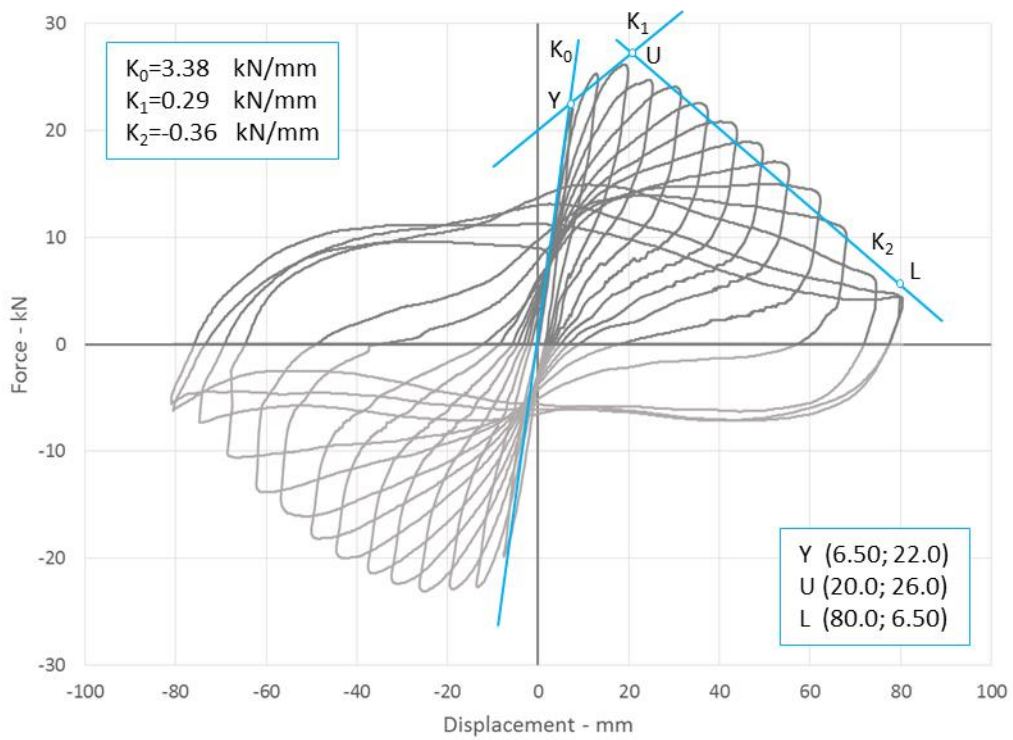


Figure 11 - Experimental hysteresis of M31 Column

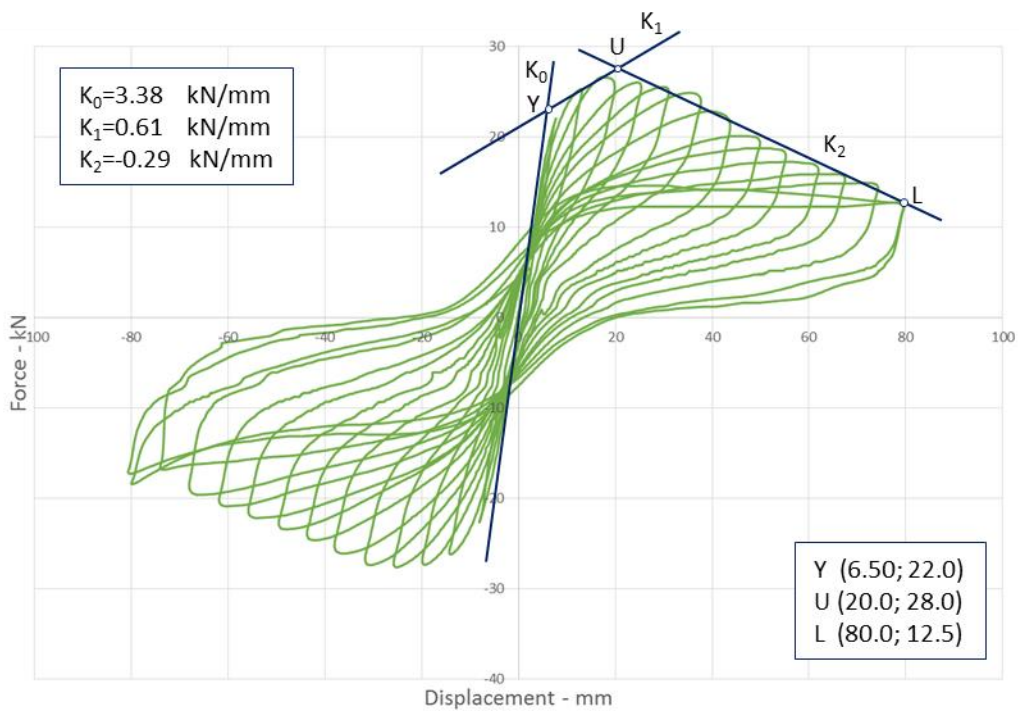


Figure 12 - Experimental hysteresis of M32 Column

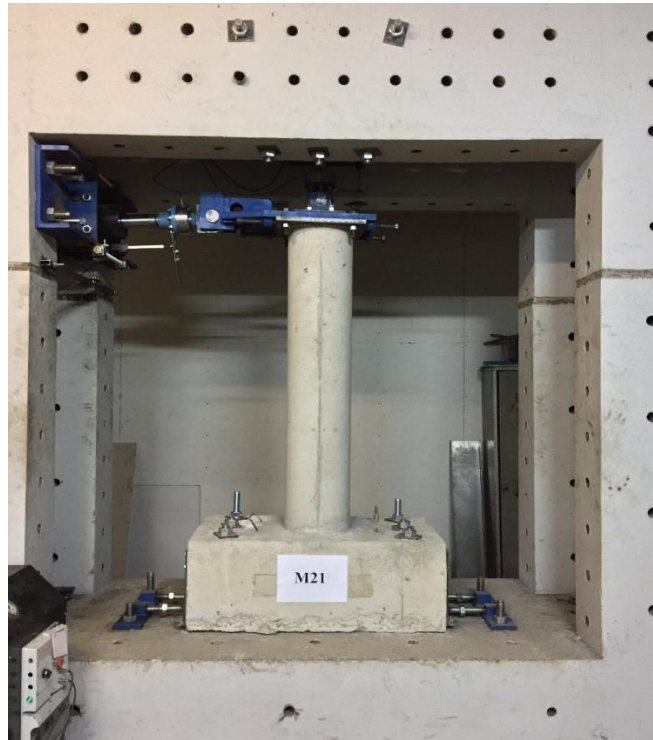


Figure 13 - Testing of Column M21



Figure 14 - Column M21 - Cracking at different stages of loading



Figure 15 - Column M21 – Max displacement of column and cover spalling

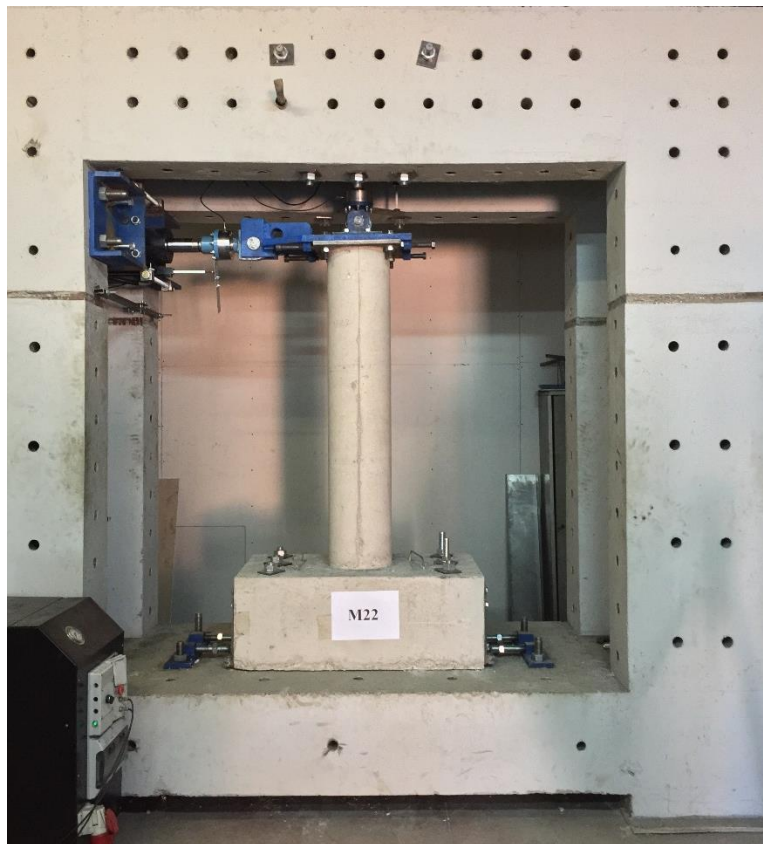


Figure 16 - Testing of Column M22



Figure 17 - Column M22 - Cracking at different stages of loading and displacements



Figure 18 - Column M22 – Cover Spalling and maximum displacement

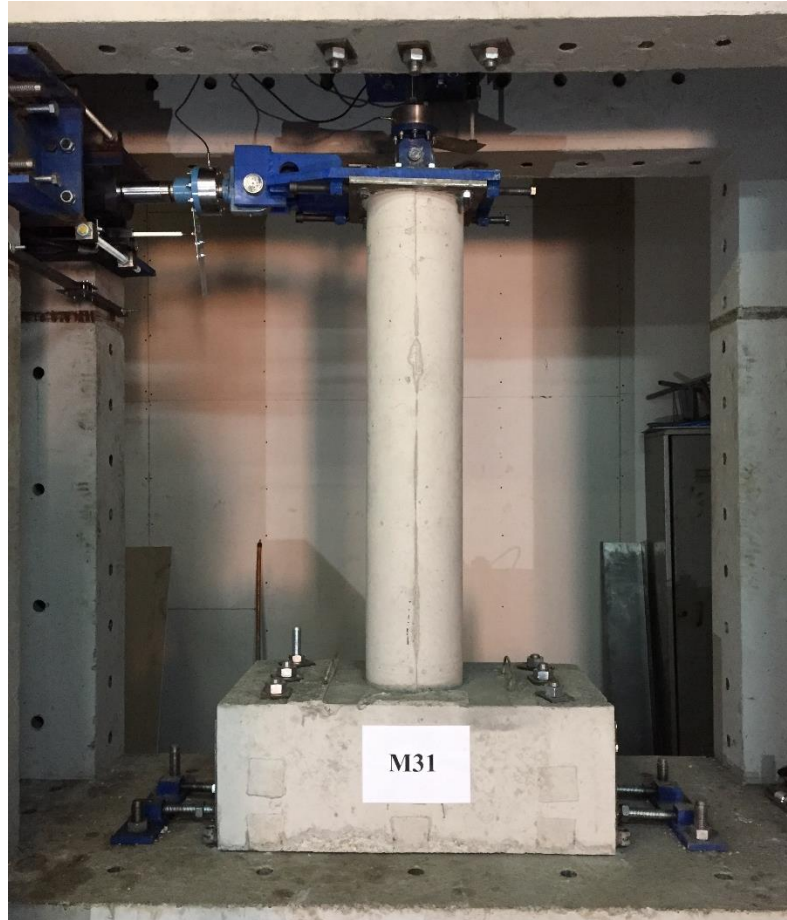


Figure 19 - Testing of Column M31



Figure 20 - Column M31 - Cracking at different stages of loading



Figure 21 - Column M31 – Longitudinal Bar buckling and Bond Failure of GFRP rebar



Figure 22 - Column M31 – Different cover in left and right side of column



Figure 23 - Testing of Column M32



Figure 24 - Column M32 - Cracking at different stages of loading



Figure 25 - Column M32 – Concrete spalling and maximum displaced column

4.4 Concluding Remarks

Considering that the performed ample experimental investigations involve realized experimental tests on models of prototype bridge piers reinforced with ordinary steel reinforcement and with composite GFRP – reinforcing bars, it is possible to summarize specific concluding remarks for both performed original test cases.

a) Steel Reinforced Bridge Column Models

Based on the presented experimental results obtained for the tested steel-reinforced bridge column models, the following observations can be summarized:

- (1) **Shape of the recorded hysteretic response.** The recorded shape of the hysteretic curves, Fig. 36 and Fig. 37, shows excellent nonlinear behavior characteristics under repeated earthquake-like cyclic loads.
- (2) **Load bearing capacity and recorded envelope curves.** The load bearing capacity of the two tested models, model M11 and Model M12 shows a very common regular form which can be very well represented by a tri-linear envelope curve. The implemented improved confinement level (CL=2) contributed to recording of an increased load bearing capacity. Specifically, the yielding force F_Y was increased for 22.9%, the ultimate force F_U was increased for 15.4% and the recorded limit force F_L was increased for 10.2%, in respect to the tested model with the lower confinement level (CL=1). In addition, the improved confinement level contributed to the increasing of the initial stiffness K_0 of the tested model for 57.9%, as well as increasing of the second stiffness for 38.1%. These results indicate the importance of improving the confinement of bridge columns exposed to expected cyclic earthquake loads.
- (3) **Pinching effect.** In the present case of the tested steel-reinforced columns, no pinching effect was observed, which demonstrates that the tested models possess large energy absorption capacity.
- (4) **Crack and damage propagation.** For both tested steel-reinforced column models, development of initial cracks and further gradual damage propagation and damage increasing appeared, as expected, in regular sequences. This is evident from Fig. 38,

Fig. 39 and Fig. 40, for the tested column model M11, and from Fig. 41, Fig. 42 and Fig. 43 for the tested column model M12.

- (5) **Stiffness deterioration.** The observed stiffness deterioration from the tested steel-reinforced bridge column models showed a very stable regularity and it appeared in full correlation with the actually induced initial cracks and damage propagation patterns.
- (6) **Confinement level effect.** The conducted experimental tests of steel-reinforced bridge column models clearly demonstrated the importance of application of an improved confinement level. The improved confinement level, $CL = 2 > CL = 1$, contributed to the tested model increased initial and second stiffness, increased load bearing capacity and recording of evidently improved hysteretic behavior characteristics, specifically under cyclic, earthquake-like loading conditions.

b) GFRP – Reinforced Bridge Column Models

Based on the presented experimental results obtained for the tested GFRP – reinforced bridge column models, the following important conclusions can be summarized:

- (1) **Shape of the recorded hysteretic response.** The recorded shapes of hysteretic curves, Fig. 44, Fig. 45, Fig. 46 and Fig. 47 appeared as considerably specific, but all of them showed very regular and stable form. It is clear that all recorded hysteretic curves of the tested bridge column models reinforced with composite GFRP – reinforcing bars exhibit a stable nonlinear response under repeated cyclic loads. Generally, the test results indicate that the composite GFRP – reinforcing bars can be very efficiently used in real practice, including their advanced application in all seismic regions exposed to expected strong earthquakes.
- (2) **Load bearing capacity and recorded envelope curves.** The load bearing capacity of the two pairs of tested models, column models M21 and M22, and column models M31 and M32, shows a stable regular form, which can also be very well represented by tri-linear envelope curves. The implemented improved confinement level ($C2=2$) in both cases contributed to recording an increased load bearing capacity.

Comparing model M22 with model M21, it was obtained that, in the case of model M22, the yield force F_Y was increased for 6.6%, the ultimate force was increased for 15.1% and the limit force was increased for 2.8%. Also, the initial stiffness K_0 was increased for 6.5% and the second stiffness was increased for 107%. Comparing model M32 with model M31, it can be concluded that, in the case of model M32, the yield force F_Y was not increased, but the ultimate force F_U was increased for 7.6% and the limit force was largely increased for 92.3%. Also, the initial stiffness was not increased, but the second stiffness was increased for 110.3%.

These results also indicate the importance of improving the confinement level of bridge columns reinforced with GFRP-bars if they are exposed to cyclic earthquake-like loading conditions.

- (3) **Pinching effect.** Following the present tests of GFRP-reinforced column models, M21, M22, M31 and M32, observed is a significantly expressed pinching effect, Fig. 44, Fig. 45, Fig. 46 and Fig. 47. This phenomenon is present and it is a real challenge to be taken into account in the process of development of an advanced refined 3D nonlinear analytical model. Most probably, this effect is imposed due to the observed continuous pure linear behavior of the GFRP – reinforcing bars. However, further specifically directed research in this complex nonlinear response domain is required.
- (4) **Crack and damage propagation.** For both tested pairs of GFRP-reinforced column models, models M21, M22 and models M31, M32, development of initial cracks and further gradual damage propagation and damage increasing appeared as expected during regular, consequently increased cyclic loading. For models M21 and M22, this is evident from Fig. 48, Fig. 49, Fig. 50, Fig. 51, Fig. 52 and Fig. 53. For models M31 and M32, this is evident from Fig. 54, Fig. 55, Fig. 56, Fig. 57, Fig. 58, Fig. 59 and Fig. 60. Specific studies directed to analytical modeling of full and complex damage patterns is yet highly needed and is a challenging research area.
- (5) **Stiffness deterioration.** The observed stiffness deterioration from the tested GFRP – reinforced bridge column models appeared as regular and stable process and it was in full correlation with the initial cracks and further damage propagation patterns.
- (6) **Confinement level effect.** The conducted experimental tests on GFRP – reinforced bridge column models in this case also clearly demonstrated the importance of

application of the improved confinement level. For both tested model pairs, M21, M22 and M31, M32, the improved confinement level, $CL = 2 > CL = 1$ contributed to getting an increased load bearing capacity as well as ductility capacity. Generally, the improved confinement contributed to improvement of the hysteretic behavior characteristics of the GFRP reinforced bridge column models.

5 CHAPTER 5 ADVANCED REFINED NONLINEAR BEHAVIOUR SIMULATION MODEL OF BRIDGE COLUMN MODELS WITH STEEL AND GFRP REINFORCEMENT

5.1 General Remarks

Considering the obtained original experimental results from the completed laboratory tests of the constructed large scale bridge column models, it has been possible to further conduct a specific and complex analytical study focused on advanced, analytical modeling of the same specimens under the same simulated simultaneous loading conditions up to deep nonlinear model behavior stages.

The particular advantage of this analytical study resulted directly from the previous, well designed, experimental study programme, providing conditions for conducting of the following two highly important analytical study phases:

- (1) Analytical study devoted to advanced refined nonlinear behavior simulation of the tested bridge column models reinforced with ordinary steel reinforcement, and
- (2) Analytical study devoted to advanced refined nonlinear behavior simulation of the tested bridge column models reinforced with composite GFRP-reinforcing bars.

Regarding the originally applied complex loading conditions during the experimental tests on bridge column prototype models, considering simultaneous loading with constant vertical and reverse cyclic horizontal load, facing the development and/or formulation of a successful analytical model was a very complex research task.

In item 5.2, the implemented refined concept of the advanced 3D analytical modeling of all tested bridge column models with their implemented specific reinforcing conditions, is briefly presented.

The next item 5.3 provides a brief presentation of the results from the conducted initial specific study devoted to: (1) refined modeling of axial force – moment interaction curves; (2) refined modeling of push-over force – deformation curves and (3) refined modeling of moment- curvature relations.

The subsequent two items, namely item 5.4 and item 5.5 show respectively the results from the conducted refined 3D modeling of steel-reinforced bridge column models and refined 3D modeling of GFRP-reinforced bridge column models. Both, very complex

studies, have been realized by application of two selected advanced software packages, i.e., SOFISTIK and SEISMOSOFT, providing solution to the problem based on application of quite general refined 3D nonlinear modeling concept.

The last item 5.6 provides a summary of the most important observations resulting from this specific analytical modeling study of the tested, specifically reinforced bridge column models with ordinary and GFRP-reinforcement.

5.2 Concept of Advanced Refined 3D Analytical Modelling

For nonlinear analysis of structures and their components, different techniques of modeling of nonlinear behavior of elements and materials are used. There are different models of components based on the way in which plasticity is distributed along the elements [9], [10], [21], [26], [28]. Generally, five idealized models for modeling of the inelastic behavior of elements are used. Many of the structural elements like columns, beams, flexural walls can be modeled by use of one of the models presented in Figure 61.

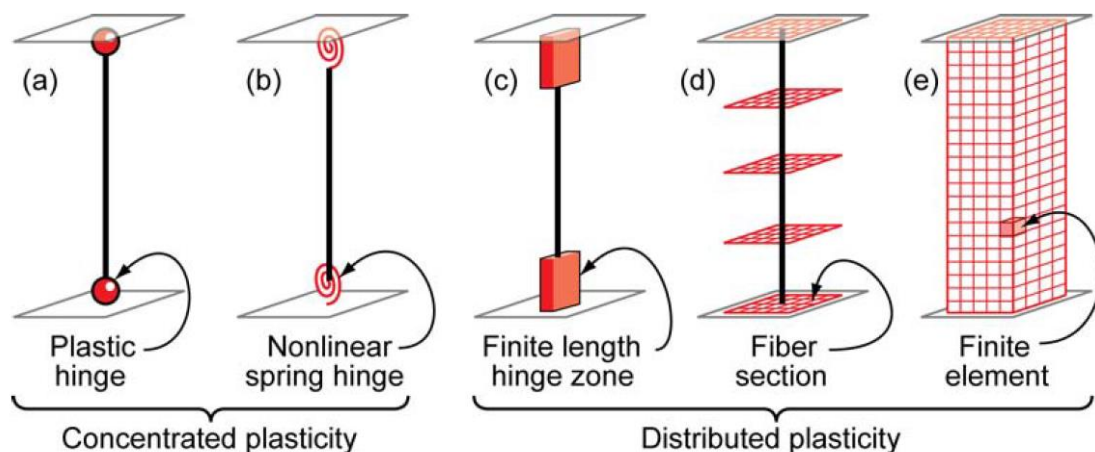


Figure 1 - Inelastic models for beams, columns, flexural walls

The simplest models for modeling of the inelastic behavior of elements are the so called zero-length rigid plastic hinges, Figure 61 - a) and b) that concentrate inelasticity into the end of elements through a plastic hinge or nonlinear link with hysteresis properties. These elements are usually formulated based on moment-rotation or force-displacement parameters.

The distributed plasticity model such as finite length hinge model and fiber section model are formulated by use of a nonlinear moment-curvature relationship or fiber section integration by using the Bernoulli assumption that sections remain plane after deformations.

Using the fiber section concept, a cross section is discretized into fibers, in which case, a uniaxial stress-strain relationship is defined for each fiber. Stresses in a section are obtained by integration of nonlinear stress-strain response for each fiber, taken separately. The use of such approach is simple because there is no need for curvature analysis and definition of hysteretic behavior of elements. Nonlinear behavior of an element is incorporated directly by section discretization into fibers and by defining material constitutive models. The concept of fiber discretization of elements is presented in Figure 62.

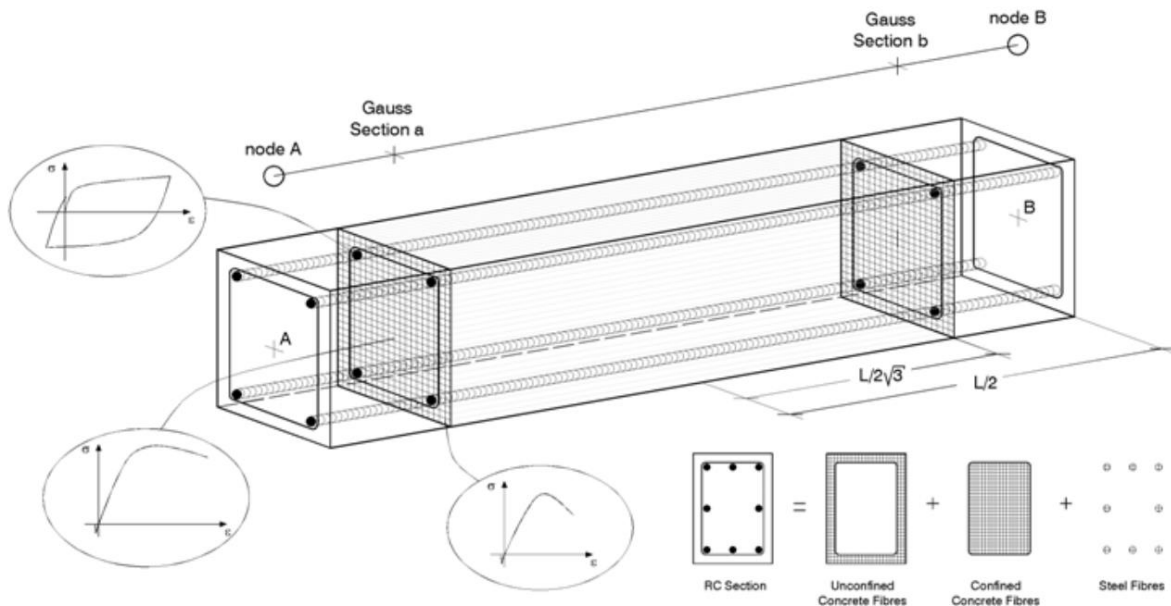


Figure 2 - Fiber section discretization concept.

One of the most complex models for modeling of nonlinear behavior of elements is the discretization of a continuum into small 3D micro volume elements along length and cross-section. Micro volume elements formulate nonlinear constitutive models in three axial states. The modeling of longitudinal reinforcement and stirrups is also possible by using truss elements and connection of the truss elements with volume concrete elements can be modelled taking into account a bond slip or a perfect connection (no bond). (Figure 61 - e and Figure 63).

Models using concentrated plasticity can take into account the axial force only by defining the P-M interaction surface. Fiber section and finite length hinge can capture the axial force effects directly, but degradation due to bar buckling and fracture cannot be captured without any sophisticated formulated model. The bond slip behavior cannot be captured by any of the models mentioned above with the exception of the model with 3D micro volume elements and truss bars.

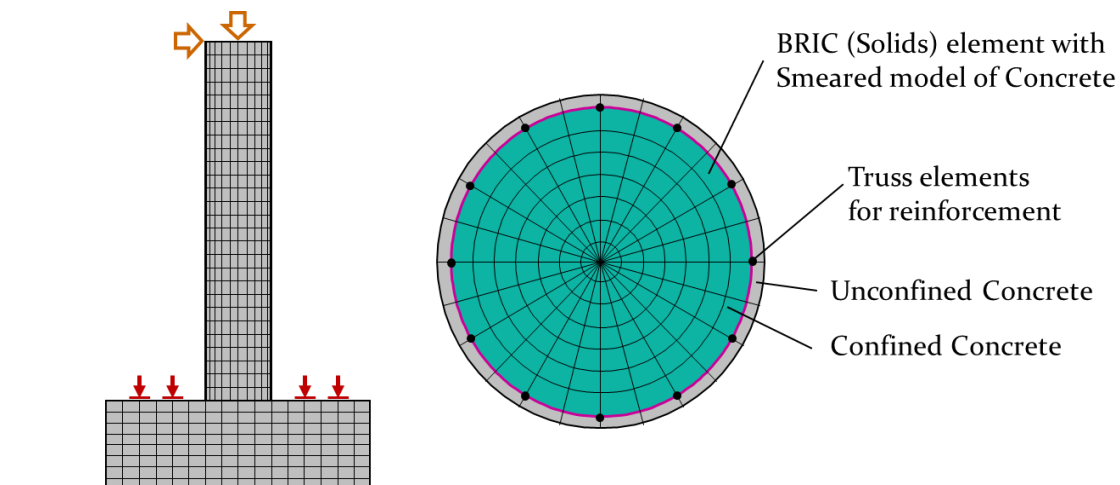


Figure 3 - 3D volume element modeling.

5.3 Refined Modelling of Axial Force-Moment Curves, Push-Over Curves and Moment-Curvature Relations of Tested Bridge Column Models

Detailed nonlinear finite element models have been analyzed by use of the Fiber Section concept in Seismostruct software [30]. Two formulations of fibers are available. Displacement based DB fiber section where displacements are imposed by linear variation of the curvature along the element and force based FB fiber section where equilibrium is strictly satisfied, in which case, linear moment variation along the element is applied. In the case of linear behavior of material, both approaches give the same results, while in the case of nonlinear behavior of material, the imposed displacements do not capture the real deformed shape because the curvature can be highly nonlinear.

Incorporation of large displacements (P-Delta effect) is done by the total co-rotational formulation concept based on description of kinematic transformations of displacement and rotations. Based on that, the element deformations, the forces and the effect of geometrical

nonlinearities on the stiffness matrix of a structure are included. Six displacement degrees of freedom $\theta_{2(A)}, \theta_{3(A)}, \theta_{2(B)}, \theta_{3(B)}, \Delta, \theta_T$, and corresponding element internal forces $M_{2(A)}, M_{3(A)}, M_{2(B)}, M_{3(B)}, F, M_T$ are defined in Figure 64.

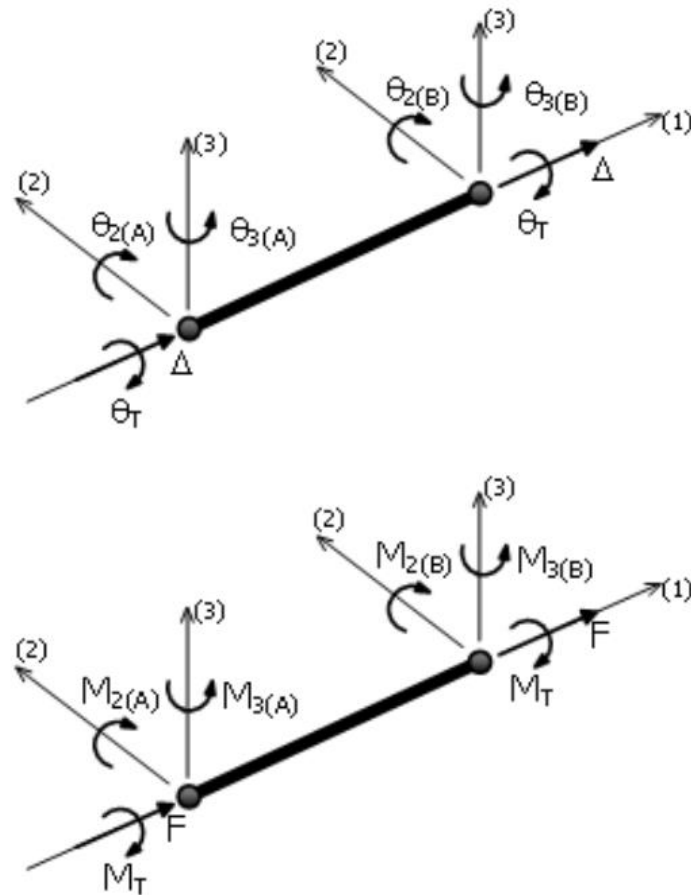


Figure 4 - Degrees of freedom and internal forces.

For concrete modeling, the brick element (volume elements) of concrete is used as confined and unconfined. For modeling of reinforcement, a truss model with nonlinear properties of ordinary reinforcement and FRP reinforcement is used. The assumption of a full bond between reinforcement and concrete is adopted.

For modeling of the nonlinear behavior of concrete, the Chang and Mander [9] model of concrete is used. The part of concrete in tension is modelled as cyclic like in compression. The parameters for definition of the stress-strain relationship for concrete based on this model are given below and in Fig. 65.

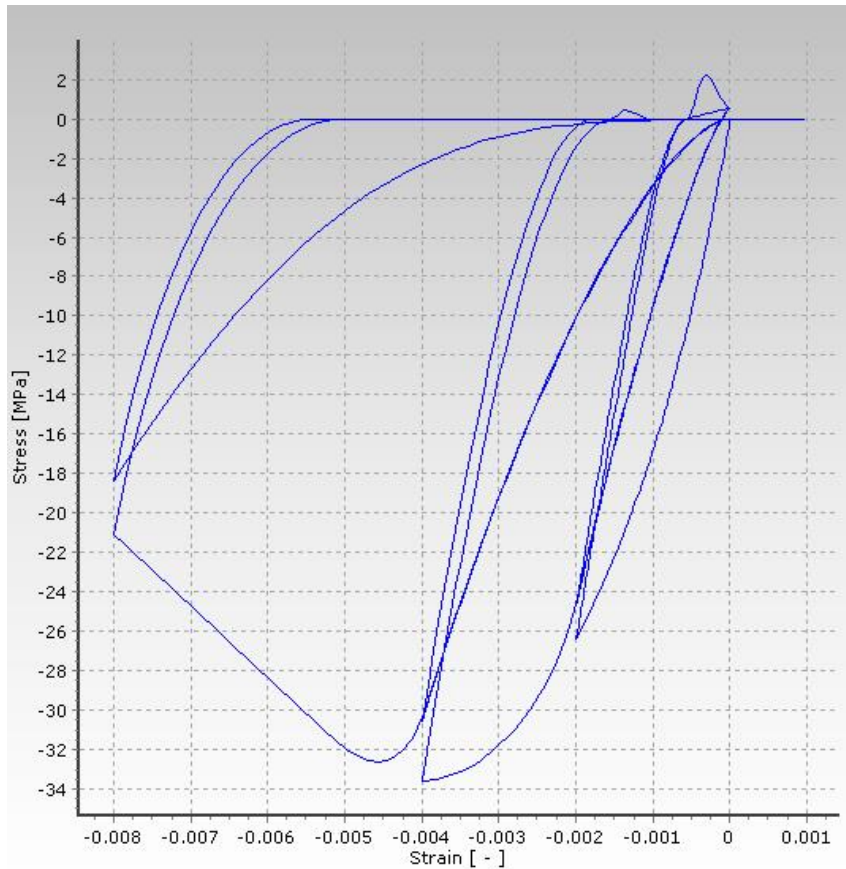


Figure 5 - Uniaxial stress-strain relationship for concrete.

1. Mean compressive strength 28000 kPa,
2. Mean tensile strength 2200 kPa,
3. Modulus of elasticity 22960000 kPa,
4. Strain at peak compressive stress (m/m) 0.002,
5. Strain at peak tensile stresses (m/m) 0.0002,
6. Nondimensional critical compressive strain 1.3
7. Nondimensional critical tensile strain 3.0
8. Specific weight 24.0 kN/m³

The non-dimensional critical compressive strain and the non-dimensional critical tensile strain coefficients determine the shape of the descending branch of the curve, respectively.

For modeling of the nonlinear behavior of steel reinforcement, the Menegoto-Pinto [26] steel model is used. The parameters for definition of stress strain relationship for steel reinforcement based on this model are given below and in Fig. 66.

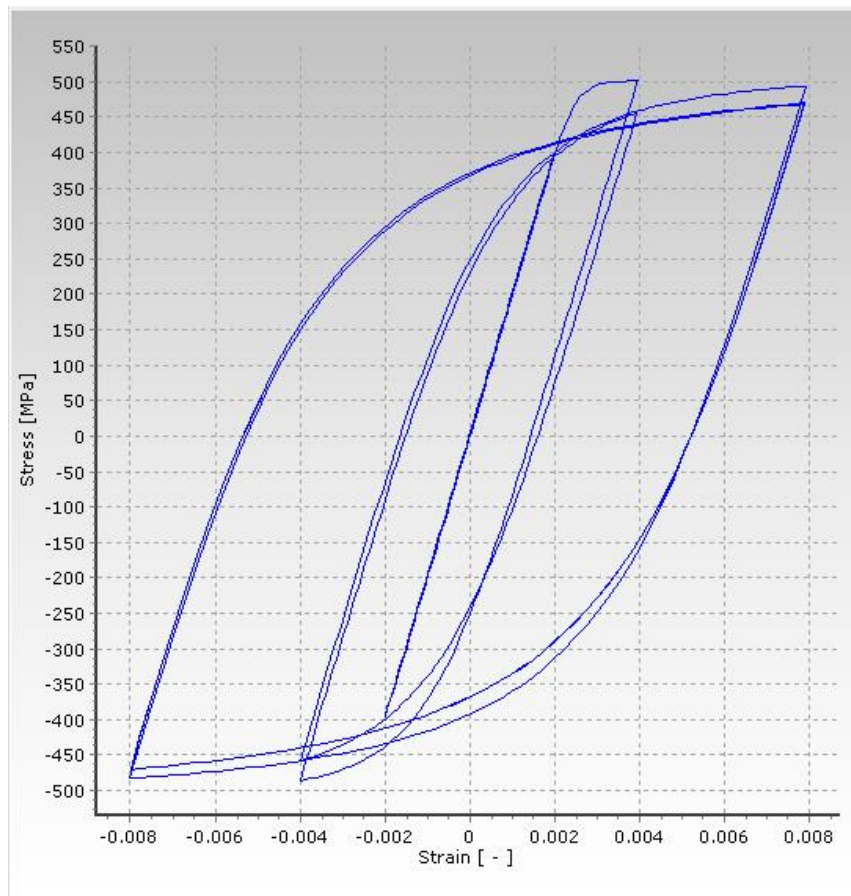


Figure 6 - Uniaxial Stress-Strain relationship for Steel Reinforcement.

1. Modulus of elasticity 2.0000E+008 kPa
2. Yield strength 500000.00 kPa
3. Strain hardening parameter 0.005
4. Transition curve initial shape parameter 20.00
5. Transition curve shape calibrating coeff. A1 18.50
6. Transition curve shape calibrating coeff. A2 0.15
7. Isotropic hardening calibrating coeff. A3 0.00
8. Isotropic hardening calibrating coeff. A4 1.00
9. Fracture/buckling strain 0.1
10. Specific weight 78.0 kN/m³

The strain hardening parameter is the ratio between the post yield stiffness and the initial stiffness. The post yield stiffness is defined by:

$$E_{sp} = (f_{ult} - f_y) / (\varepsilon_{ult} - f_y / E_s)$$

Where, f_{ult} is the ultimate stress of the material, ε_{ult} is the ultimate strain of the material, E_s is the modulus of elasticity of the material.

The transition curve initial shape parameter is the parameter that controls the shape of the transition curve from initial to post yield stiffness in the first loading cycle. This parameter is also used to control the Baushinger effect and the pinching effect of the hysteresis.

Transition curve shape calibrating coefficients A1 and A2 are coefficients that are used to calibrate the changes of the transition curve initial shape parameter in order to update the transition curve from initial to post yield stiffness.

Isotropic hardening calibrating coefficients A3 and A4 are parameters that define the level at which isoperimetric hardening is included in the stress strain cyclic behavior of a material.

Fracture/buckling strain is the strain value that specifies when fracture or buckling occurs.

For modeling the linear behavior of GFRP reinforcement, the elastic material model is used. The parameters for definition of the stress strain relationship for the GFRP reinforcement based on this model are given below.

1. Modulus of elasticity 5.0000E+007 kPa
2. Tensile strength 1100000 kPa
3. Compressive strength 700000 kPa
4. Specific weight 50.00 kN/m³

Detailed nonlinear finite element models have been analyzed by using 3D solid finite elements included in the SOFiSTiK software. For concrete modeling, the brick element (volume elements) of concrete has been used as confined and unconfined. For modeling of reinforcement, a truss model with nonlinear properties of ordinary reinforcement and FRP reinforcement has been used. A full bond assumption between reinforcement and concrete

has been adopted. For nonlinear analysis of columns with the SOFiSTiK software, an elasto-plastic material according to the LADE Model with non-associated flow rule for concrete, has been used.

Calibration of the parameters of the LADE model cannot be obvious at first sight, because these parameters are of a non-physical nature. The uniaxial tensile and compressive strength of concrete should be known in order to calibrate the parameters. Section of three-dimensional yield surface is used Kupfer approach.

Young's modulus	E	34080	[N/mm ²]	Safetyfactor	1.50	[-]
Poisson's ratio	μ	0.20	[-]	Strength	f _c	35.00 [MPa]
Shear modulus	G	14200	[N/mm ²]	Nominal strength	f _{ck}	35.00 [MPa]
Compression modulus	K	18930	[N/mm ²]	Tensile strength	f _{ctm}	3.21 [MPa]
Weight	γ	25.0	[kN/m ³]	Tensile strength	f _{ctk,05}	2.25 [MPa]
Density	ρ	2400.00	[kg/m ³]	Tensile strength	f _{ctk,95}	4.17 [MPa]
Elongation coefficient	α	1.00E-05	[1/K]	Bond strength	f _{bd}	3.37 [MPa]
				Service strength	f _{cm}	43.00 [MPa]
				Fatigue strength	f _{cd,fat}	20.07 [MPa]
				Tensile strength	f _{ctd}	1.50 [MPa]
				Tensile failure energy	G _f	0.14 [N/mm]

Stress-Strain for serviceability	ε[o/oo]	σ-m[MPa]	E-t[N/mm ²]
Is only valid within the defined stress range	0.000	0.00	35781
	-1.123	-31.50	19765
	-2.246	-43.00	0
	-3.500	-26.18	-28065
	Safetyfactor 1.50		

Stress-Strain for ultimate load	ε[o/oo]	σ-u[MPa]	E-t[N/mm ²]
Is only valid within the defined stress range	0.000	0.00	35000
	-2.000	-35.00	0
	-3.500	-35.00	0
	Safetyfactor 1.50		

Stress-Strain of calc. mean values	ε[o/oo]	σ-r[MPa]	E-t[N/mm ²]
Is only valid within the defined stress range	0.000	0.00	29818
	-1.123	-19.27	8335
	-2.246	-23.33	0
	-3.500	-20.25	-4413
	Safetyfactor (1.50)		

Figure 7 - Properties of concrete – uniaxial behaviour – SOFiSTiK.

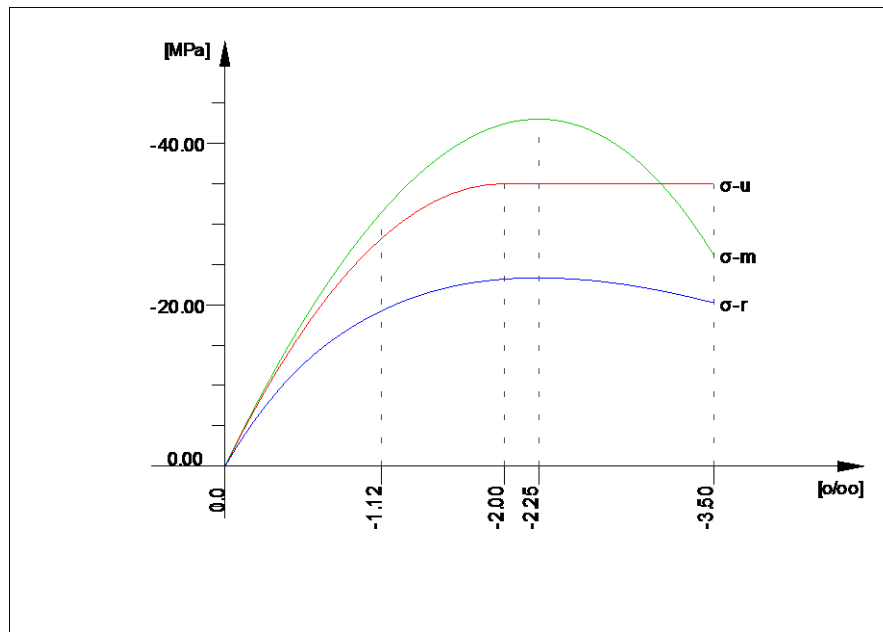


Figure 8 - Uniaxial behavior of concrete in compression – SOFiSTiK.

The model parameters and the Lade parameters are given below:

Table 1 - Parameters for the LADE model of concrete

LADE	Description	Unit	Default
P1	Parameter η_1	–	!
P2	Exponent m	–	!
P3	Uniaxial tensile strength f_t	kN/m^2	0.0
P4	Parameter η_2 for flow rule	–	P1/10
P5	Compressive strength (cap)	kN/m^2	-
P6	Tensile failure strain ε_{tu}	‰	-

$$f = I_1^3 - \left[27 + \eta_1 \cdot \left(\frac{p_a}{I_1} \right)^m \right] \cdot I_3 \leq 0$$

$$g = I_1^3 - \left[27 + \eta_2 \cdot \left(\frac{p_a}{I_1} \right)^m \right] \cdot I_3$$

with

$$p_a = 103.32 kN/m^2 \text{ atmospheric air pressure,}$$

$$I_1 = -(\sigma_1 - P_3) - (\sigma_2 - P_3) - (\sigma_3 - P_3)$$

$$I_3 = -(\sigma_1 - P_3) \cdot (\sigma_2 - P_3) \cdot (\sigma_3 - P_3)$$

Parameter m (exponent) determines the shape of the intersection curve. Parameter m affects the curvature (convexity) of the yield surface towards the hydrostatic axis - the larger

value of m generates a stronger curvature. A value of m between 1.0 and 2.0 is reasonable for most types of concrete. Using the known quantities of uniaxial tensile and compressive strength and the chosen parameter m , parameter η_1 can be determined from the condition: For the stress state corresponding to the uniaxial compressive stress limit, the yield condition must be fulfilled.

The yield function can be rewritten as:

$$\eta_1 = \left(\frac{I_1^3}{I_3} - 27 \right) \cdot \left(\frac{|I_1|}{\rho_a} \right)^m$$

The considered stress state is defined by (translated reference system):

$$\sigma_I = \sigma_{II} = -f_t$$

$$\sigma_{III} = -(f_t + f_c)$$

$$I_1 = \sigma_I + \sigma_{II} + \sigma_{III}$$

$$I_3 = \sigma_I \cdot \sigma_{II} \cdot \sigma_{III}$$

Where f_t (=P3) and f_c are the magnitudes of the uniaxial tensile and compressive strength, respectively, I_1 and I_3 are the required invariants for this stress state. Substituting it into the rewritten yield function yields the yet unknown parameter η_1 .

The following table contains exemplary parameters for the selected concrete types, derived from the procedure described above (classification according to EC2, Ultimate Limit State).

Table 2 - Model parameters based on concrete class.

Strength class	f_{cd} [kN/m ²]	P3 ($f_{ctk;0.05}$) [kN/m ²]	P2 [-]	P1 [-]
C20/25	13333	1500	1.0	24669.11
			1.5	324095.87
C30/37	20000	2000	1.0	43466.02
			1.5	689515.99
C40/50	26667	2500	1.0	63426.77
			1.5	1153410.57
C50/60	33333	2900	1.0	88162.15
			1.5	1778218.62

By specification of parameter P5, the model can optionally be extended by a spherical cap (in the principal stress space) that limits the volumetric compressive stress to a maximum value. This can be meaningful, in particular, for mainly hydrostatic compression. The cap is defined by:

$$f = \sqrt{\sigma_1^2 + \sigma_2^2 + \sigma_3^2} - \sqrt{P_5^2 + P_5^2 + P_5^2} \leq 0$$

The optional parameter P6 defines a linear decay of the material's tensile capacity after the initial tensile strength f_t has been exceeded, such that $f_t(\varepsilon_{tu}) = 0$. If not specified, the behavior is ideally plastic and the tensile strength remains at the initial value f_t (tension cut-off). The tension model is suitable for monotonic loading, only.

Reinforcement can be modeled as a discrete and smeared element. Discrete reinforcement is in the form of reinforcing bars and is modeled by use of truss elements. It can be connected to concrete elements at nodes and can be embedded in solid elements. In analysis of columns by use of the SOFiSTiK software, the reinforcement is modeled as a discrete truss element connected with the same nodes of the concrete finite elements. The bilinear law of elastic-plastic behavior is assumed for the behavior of the steel reinforcement.

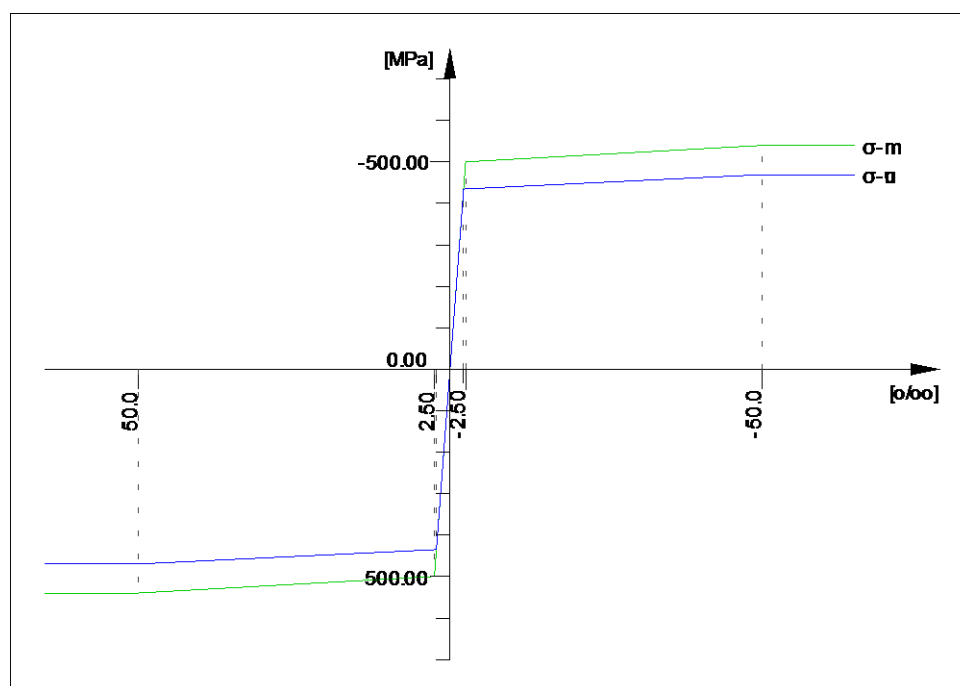


Figure 9 - Stress - strain relationship for steel reinforcement.

Mat 2 B 500 B (EN 1992)

Young's modulus	E	200000	[N/mm ²]	Safetyfactor		1.15	[-]
Poisson's ratio	μ	0.30	[-]	Yield stress	fy	500.00	[MPa]
Shear modulus	G	76923	[N/mm ²]	Compressive yield	fyc	500.00	[MPa]
Compression modulus	K	166667	[N/mm ²]	Tensile strength	ft	540.00	[MPa]
Weight	γ	78.5	[kN/m ³]	Compressive strength	fc	540.00	[MPa]
Density	ρ	7850.00	[kg/m ³]	Ultimate strain		50.00	[o/oo]
Elongation coefficient	α	1.20E-05	[1/K]	relative bond coeff.		1.00	[-]
max. thickness	t-max	32.00	[mm]	EN 1992 bond coeff.	k1	0.80	[-]
				Hardening modulus	Eh	0.00	[MPa]
				Proportional limit	fp	500.00	[MPa]
				Dynamic allowance	σ-dyn	152.17	[MPa]

Stress-Strain for serviceability	ε[o/oo]	σ-m[MPa]	E-t[N/mm²]
Is also extended beyond the	1000.000	540.00	0
defined stress range	50.000	540.00	0
	2.500	500.00	842
	0.000	0.00	200000
	-2.500	-500.00	842
	-50.000	-540.00	0
	-1000.000	-540.00	0
	Safetyfactor 1.15		

Stress-Strain for ultimate load	ε[o/oo]	σ-u[MPa]	E-t[N/mm²]
Is also extended beyond the	1000.000	469.57	0
defined stress range	50.000	469.57	0
	2.174	434.78	727
	0.000	0.00	200000
	-2.174	-434.78	727
	-50.000	-469.57	0
	-1000.000	-469.57	0
	Safetyfactor (1.15)		

Stress-Strain of calc. mean values	ε[o/oo]	σ-r[MPa]	E-t[N/mm²]
Is also extended beyond the	1000.000	469.57	0
defined stress range	50.000	469.57	0
	2.174	434.78	727
	0.000	0.00	200000
	-2.174	-434.78	727
	-50.000	-469.57	0
	-1000.000	-469.57	0
	Safetyfactor (1.15)		

Figure 10 - Properties of steel reinforcement material.

The numerical results are extracted in terms of force-displacement capacity, moment curvature or rotation and interaction surfaces N-M for the models. Vertical load N=250kN is continuously applied and horizontal loads are increased gradually up to failure of the column.

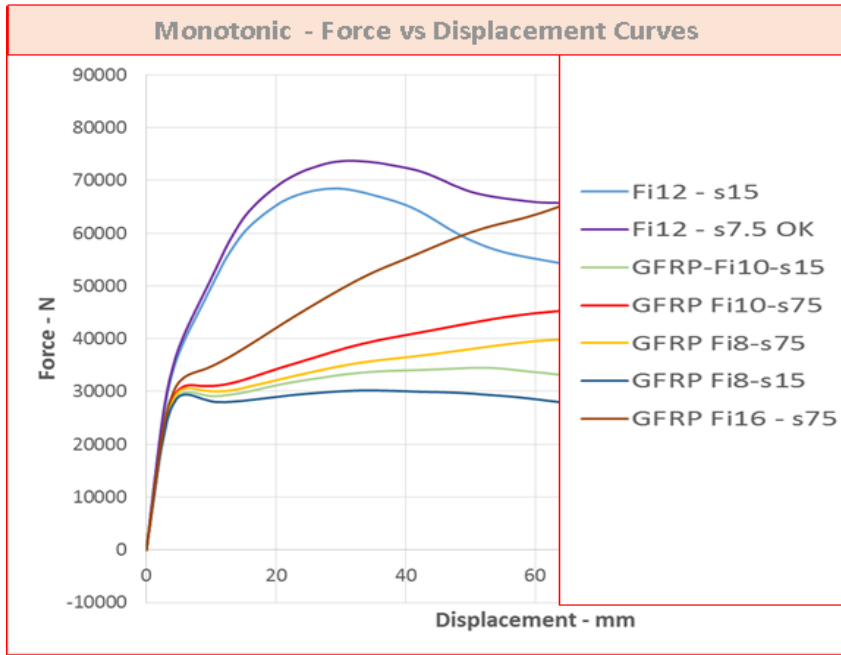


Figure 11 - Monotonic force - displacement curves.

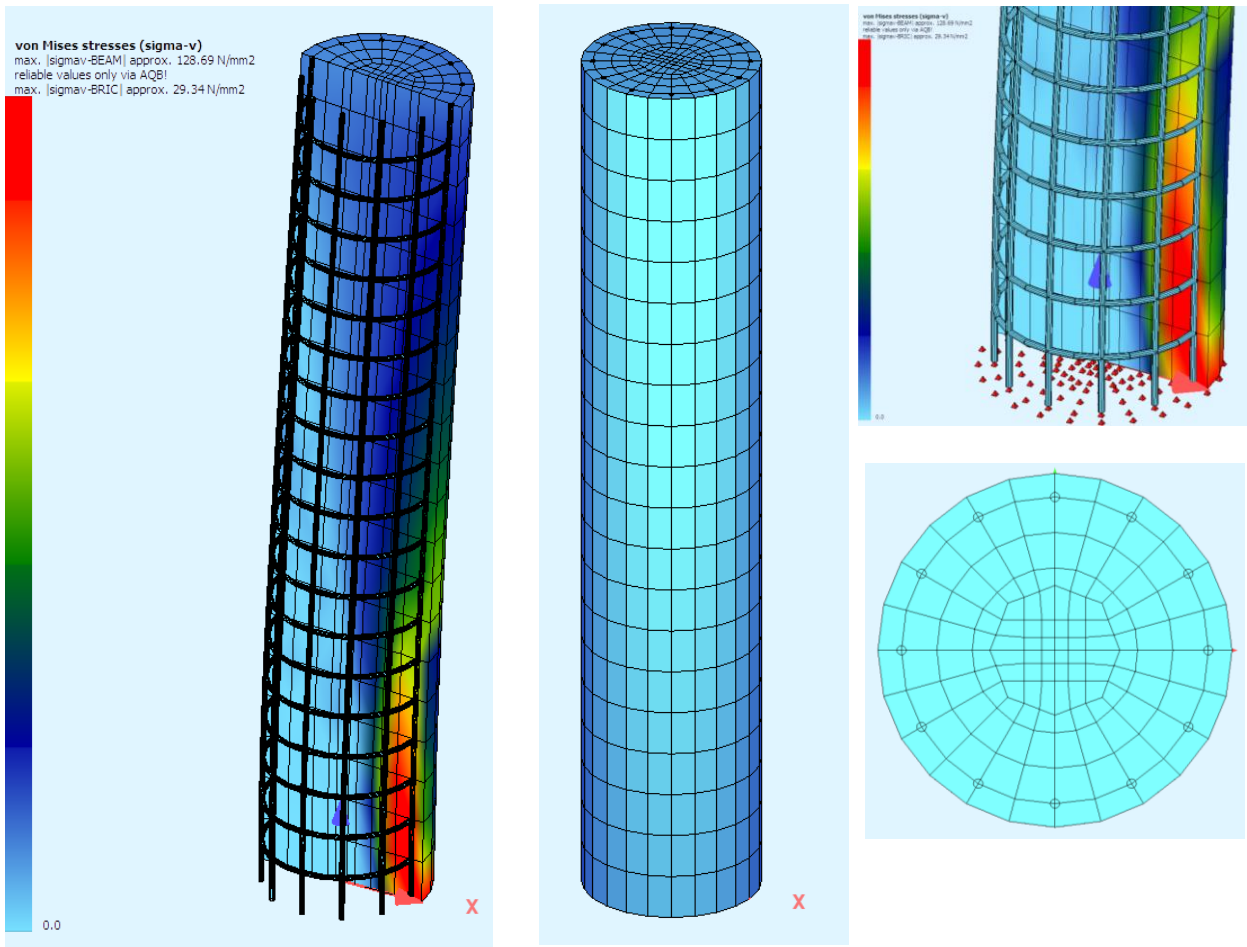


Figure 12 - FEM model for a column. Iteration factor of ultimate loads.

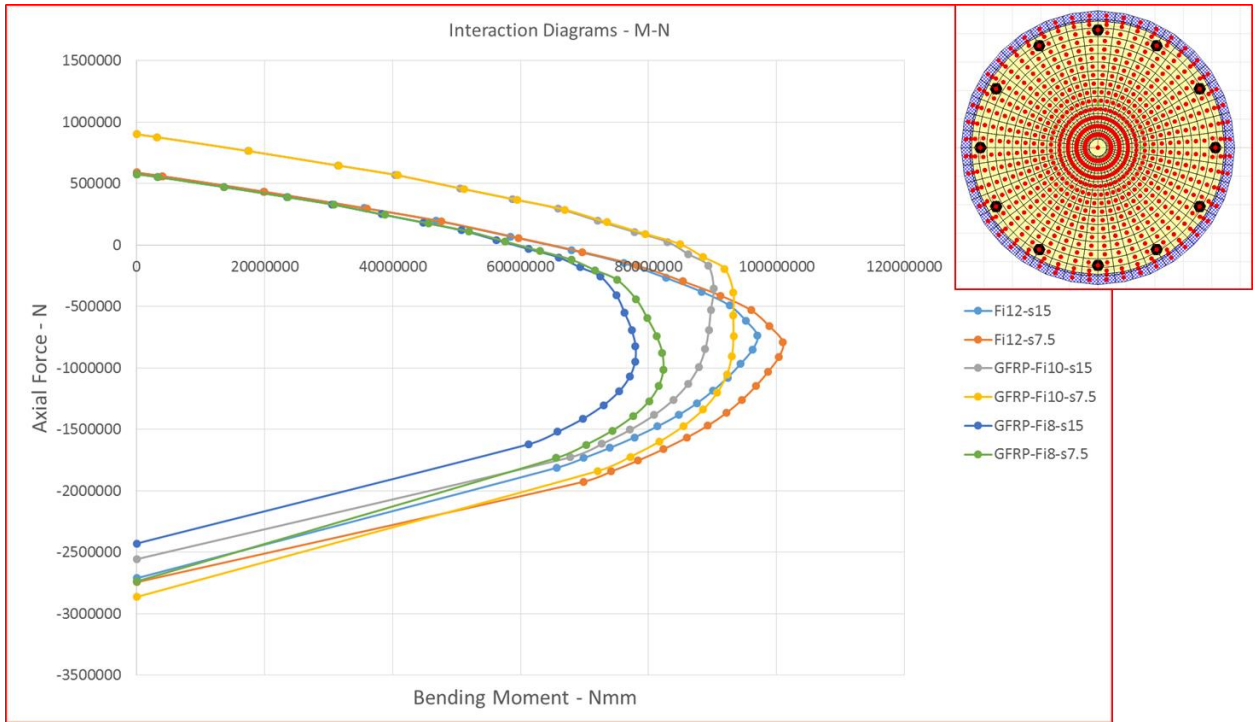


Figure 13 - Fiber model for calculations and interaction surface for columns.

5.4. Refined 3D Modelling of Steel-Reinforced Bridge Column Models

Based on the obtained and presented analytical results from the conducted refined 3D modeling of steel – reinforced bridge column models, the following observations can be summarized:

(1) **Shape of the analytically defined hysteretic response.** The shape of the analytically defined hysteretic responses from the conducted analytical nonlinear behavior study of the tested bridge column model M11 by use of the formulated, refined 3D analytical model, is presented in a graphic form in Fig. 74. The next Fig. 75 shows jointly the experimental and theoretical hysteretic relations by direct overlapping based on the used different colors of the respective plots.

In a similar way, the obtained, analytical nonlinear hysteretic response of the tested bridge column model M12 is presented in Fig. 76. Similarly, the next Fig. 77, provides a joint presentation of the experimental and theoretical hysteretic relations by direct overlapping of the respective plots presented in different colours. The computed and presented analytical results have been obtained considering the same reinforcing conditions as well as the same simultaneous loading conditions as those used for the constructed and laboratory tested models with steel reinforcement. Based on the presented, most representative study results, it is evident that the formulated refined 3D nonlinear analytical model provided a high degree of correlation with the experimental test results, defined for complex simultaneous loading conditions up to deep nonlinearity.

(2) **Load bearing capacity and computed envelope curve.** From the plotted results, it is evident that the load bearing capacity curves show a high degree of agreement. For example, in the case of bridge pier model M11, the theoretically defined maximum value of shear force is $\max F_{U_{th}} = 61.5$ kN. Actually, it is only -5.38% smaller than the experimentally defined value of $\max F_{U_{exp}} = 39.0$ kN. Similarly, for the same point U, the computed theoretical displacement is $DU_{th} = 37.0$ mm, which appears to be only -5.12% smaller than the experimentally defined value $DU_{exp} = 39.0$ mm.

In the case of the bridge pier model M12, very high level of agreement has also been observed. The theoretical shear force of $\max F_u = 72.0$ kN is only -4.0% smaller than

the experimental value of $\max F_U = 75.0$ kN. Similarly, the theoretical displacement for the same point $D_{U_{th}} = 32.0$ mm is only +3.2% larger than the experimental value $D_{U_{exp}} = 31.0$ mm.

- (3) **Pinching effect.** In the computed theoretical hysteretic relations as well as in the experimentally recorded hysteretic relations, the pinching effect is not present. A high agreement between the theoretical and experimental results has been observed in the case of both tested bridge column models reinforced with ordinary steel reinforcement.
- (4) **Crack and damage propagation.** The theoretically simulated crack and damage propagation appears respectively correct because a very good agreement of both resulting hysteretic relations has evidently been achieved.
- (5) **Stiffness deterioration.** The stiffness deterioration pattern has been very successfully simulated. This is also a direct consequence of the achieved very good agreement of the theoretical and experimental hysteretic relations.
- (6) **Confinement level effect.** The implemented refined 2D nonlinear analytical model provided the capability for theoretical simulation of the implemented actual confinement considering the real spacing of the circular hoops.

The achieved very good accuracy of the general nonlinear hysteretic relations actually represents the best confirmation that the effect of the actual confinement level is very successfully simulated with the formulated refined 3D analytical model.

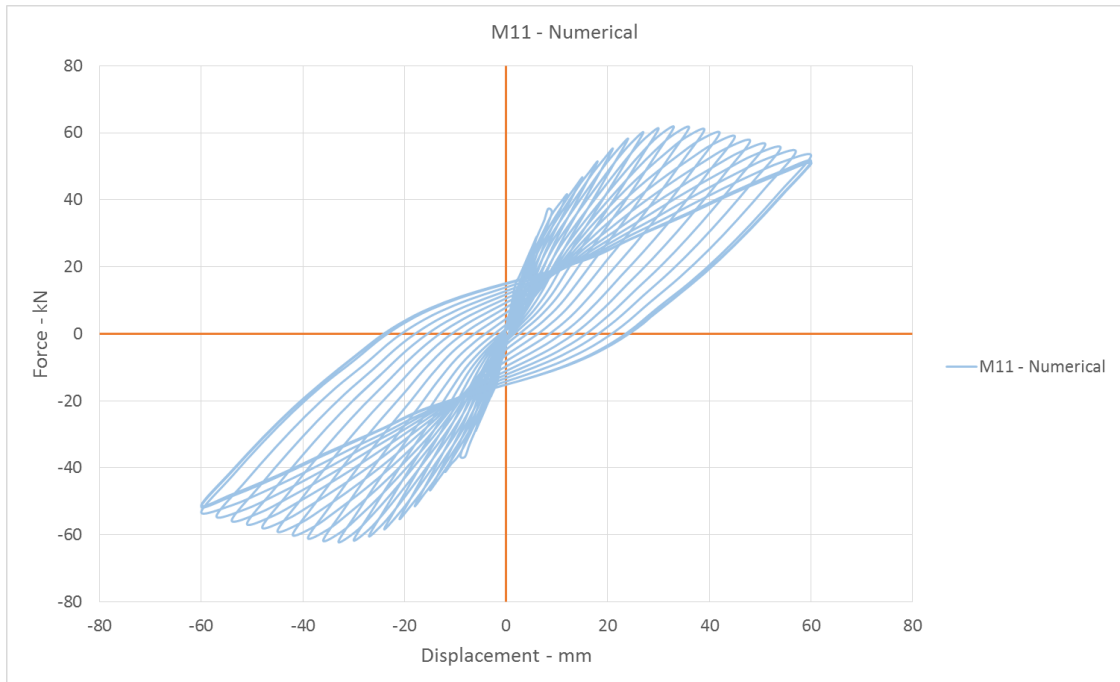


Figure 14 - M11 – Numerical analysis – hysteresis force – displacement.

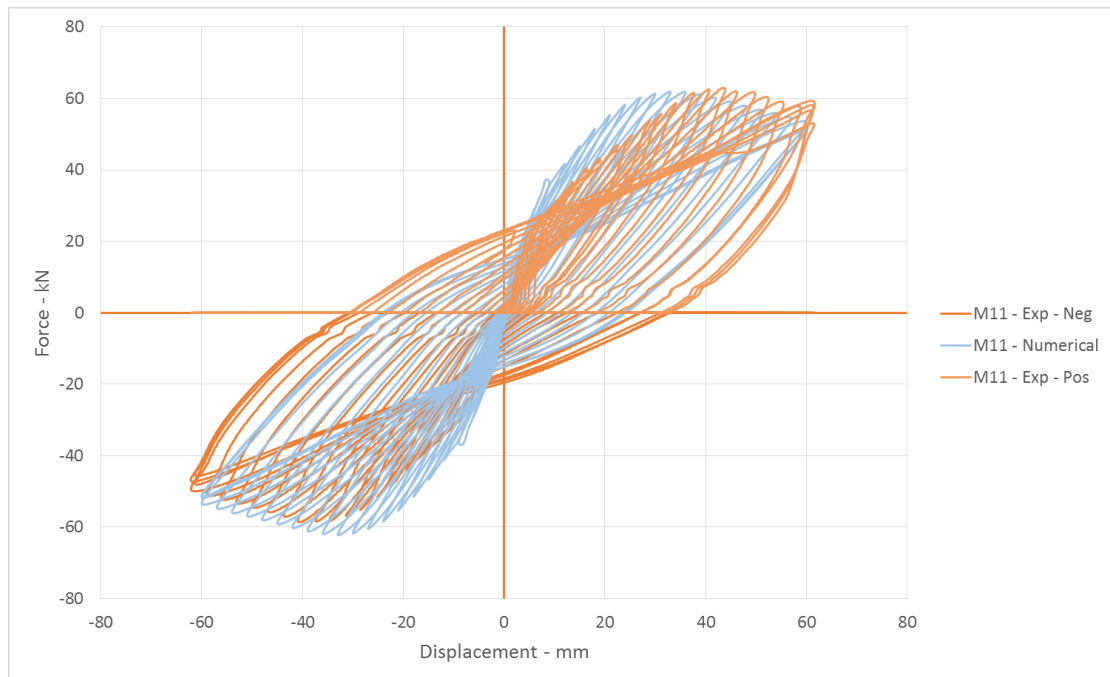


Figure 15 - M11 – numerical vs experimental analysis – hysteresis F-D.

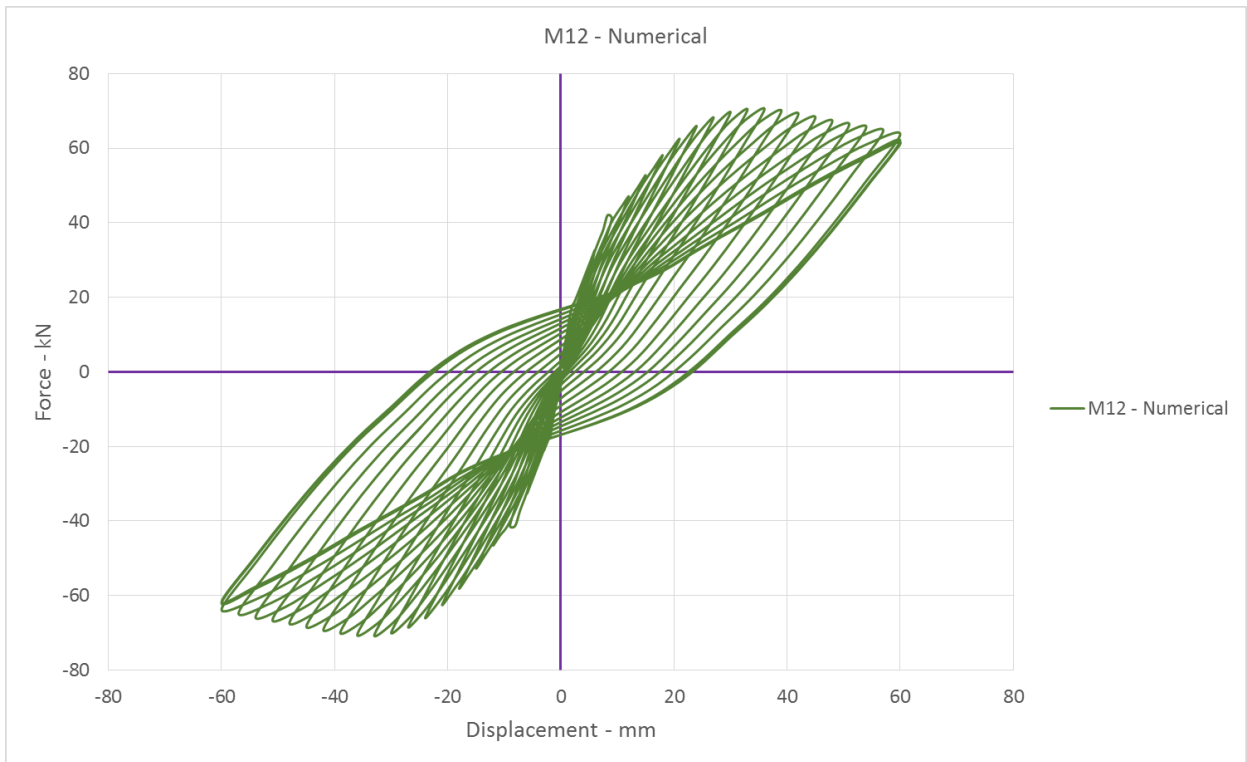


Figure 16 - M12 – Numerical analysis – hysteresis force – displacement.

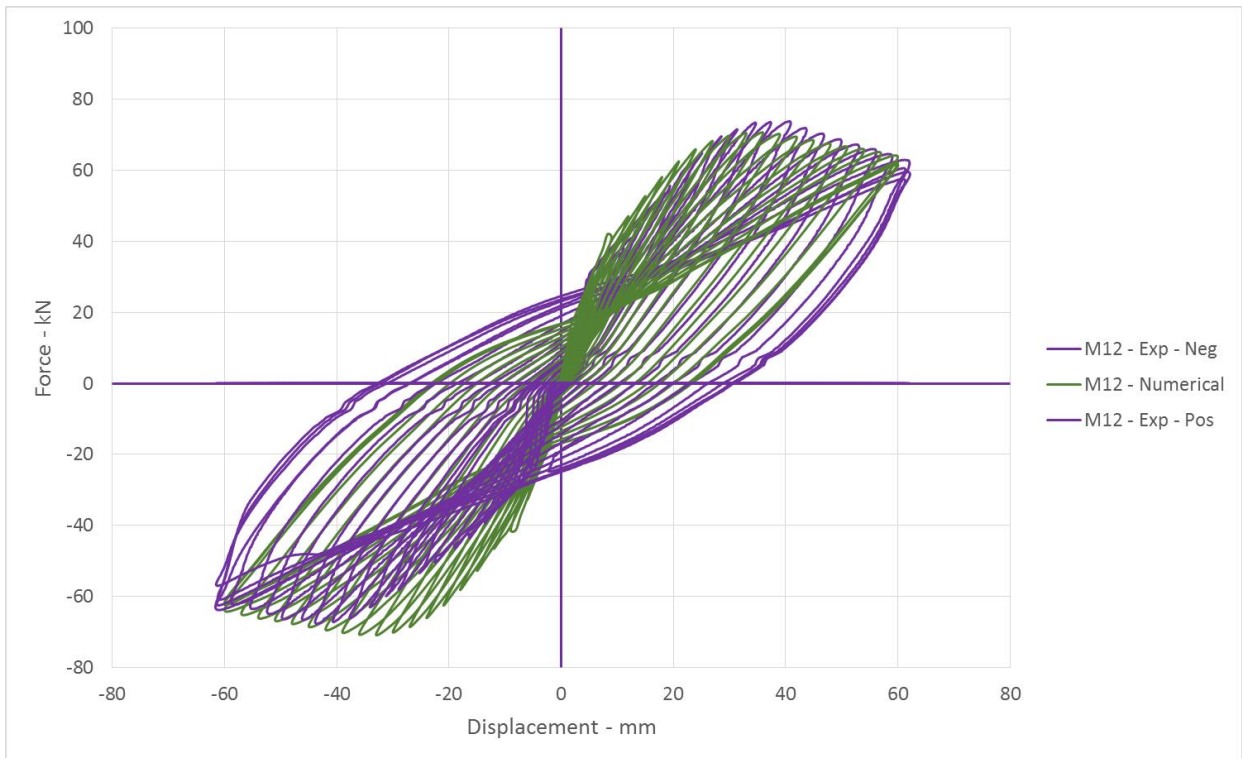


Figure 17 - M12 – Numerical vs experimental analysis – hysteresis F-D.

5.5. Refined 3D Modelling of GFRP-Reinforced Bridge Column Models

Similarly, based on the obtained and presented analytical results from the conducted refined 3D modeling of GFRP-reinforced bridge column models, the following observations can be summarized:

(1) **Shape of the analytically defined hysteretic response.** The shapes of the analytically defined hysteretic responses from the conducted analytical nonlinear behavior study of the tested bridge column models with GFRP-reinforcement, M21, M22, M31 and M32, are presented in the respective figures, Fig. 78, Fig. 80, Fig. 82 and Fig. 84. To obtain a more clear insight into the integral results from both theoretical studies and experimental tests, the respective hysteretic relations are presented in the same figures by use of different colours. For all four tested GFRP-reinforced bridge column models, M21, M22, M31 and M32, the overlapped theoretical and experimental hysteretic responses are presented in the respective figures, Fig. 79, Fig. 81, Fig. 83 and Fig. 85.

From the given comparative plots of the theoretical and experimental hysteretic relations, the following important observations can be made: (1) the shapes of both envelope curves for all tested bridge column models are in a very good agreement; (2) the main controlling parameters related to the specimen initial stiffness, the second stiffness and the related cyclic patterns are also in a very good agreement.

However, in the theoretical hysteretic relations, a significant “pinching” effect is evident in the unloading curves.

The expressed “pinching” effect in the theoretical hysteretic responses generally resulted from the fact that possible bond slip between the GFRP-rebars and concrete was ignored in the defined nonlinear analytical model. The GFRP-rebars behavior is basically linear, but the bond behavior may play a significant role in the domain of unloading patterns. In future studies, modeling of a specified bond behavior can be a highly important research topic.

(2) **Load bearing capacity and computed envelope curves.** From the plotted results, it is evident that the load bearing capacity curves for all tested GFRP-reinforced bridge column models show a high degree of agreement.

For example, the comparative experimental and theoretical results related to point U defining the maximum load bearing capacity (max FU) and the respective displacement (DU) for all four tested GFRP-reinforced bridge column models are in very good agreement as follows:

- 1) Bridge column model – M21
 - Max $FU_{exp} = 30.0$ kN
 - Max $FU_{th} = 34.0$ kN (Difference: + 3.03%)
 - $DU_{exp} = 30.0$ mm
 - $DU_{th} = 31.0$ mm (Difference: + 3.33%)
- 2) Bridge column Model – M22
 - Max $FU_{exp} = 38.0$ kN
 - Max $FU_{th} = 36.0$ kN (Difference: -5.26%)
 - $DU_{exp} = 30.0$ mm
 - $DU_{th} = 29.0$ mm (Difference: -3.33%)
- 3) Bridge column model – M31
 - Max $FU_{exp} = 26.0$ kN
 - Max $FU_{th} = 25.0$ kN (Difference: - 3.84%)
 - $DU_{exp} = 20.0$ mm
 - $DU_{th} = 20.0$ mm (Difference: 0.0%)
- 4) Bridge column model – M32
 - Max $FU_{exp} = 28.0$ kN
 - Max $FU_{th} = 27.5$ kN (Difference: -1.8%)
 - $DU_{exp} = 20.0$ mm
 - $DU_{th} = 21.0$ mm (Difference: +5.0%)

(3) **Pinching effect.** In the theoretically obtained hysteretic relations of the tested GFRP-reinforced bridge pier models, the “pinching” effect is significantly expressed due to the evident deviations of the unloading patterns. This observation shows that the bond behaviour of the GFRP-reinforcing bars should

be included in the defined refined analytical models, especially if a model is used to simulate nonlinear behavior of GFRP-reinforced members under cyclic loads and up to their deep nonlinear response.

- (4) **Crack and damage propagation.** The theoretically simulated crack and damage propagation in GFRP- reinforced bridge column models also appears to be generally correct because of the evident very good agreement of the envelope curves recorded from the experiments and those obtained from the conducted analytical studies.
- (5) **Stiffness deterioration.** The stiffness deterioration patterns were simulated very successfully. This was also a direct consequence of the achieved very good agreement in both experimental and theoretical hysteretic relations. The differences present in the unloading patterns can be improved by including of the real bond behavior in the formulated refined analytical models.
- (6) **Confinement level effect.** The formulated refined 3D nonlinear analytical model provided the capability for theoretical simulation of the real confinement level by consideration of the real spacing of the circular hoops in the analytical model. The achieved very good agreement between the experimental and the theoretical envelope curves for all tested GFRP-reinforced bridge column models is the best confirmation of the correct modeling of the actual confinement levels.

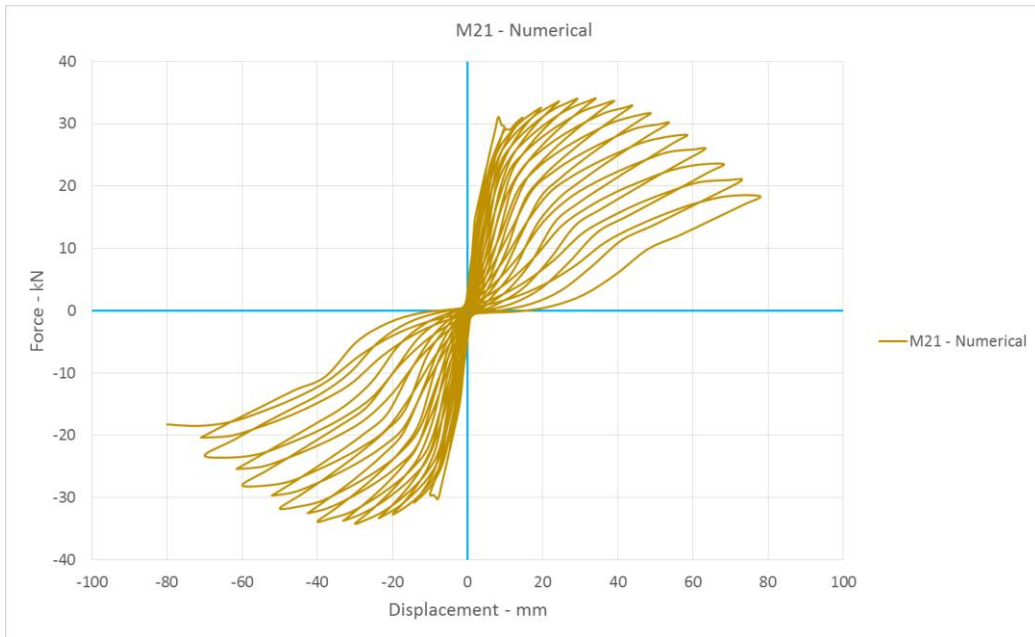


Figure 18 - M21 – Numerical analysis – hysteresis force – displacement.

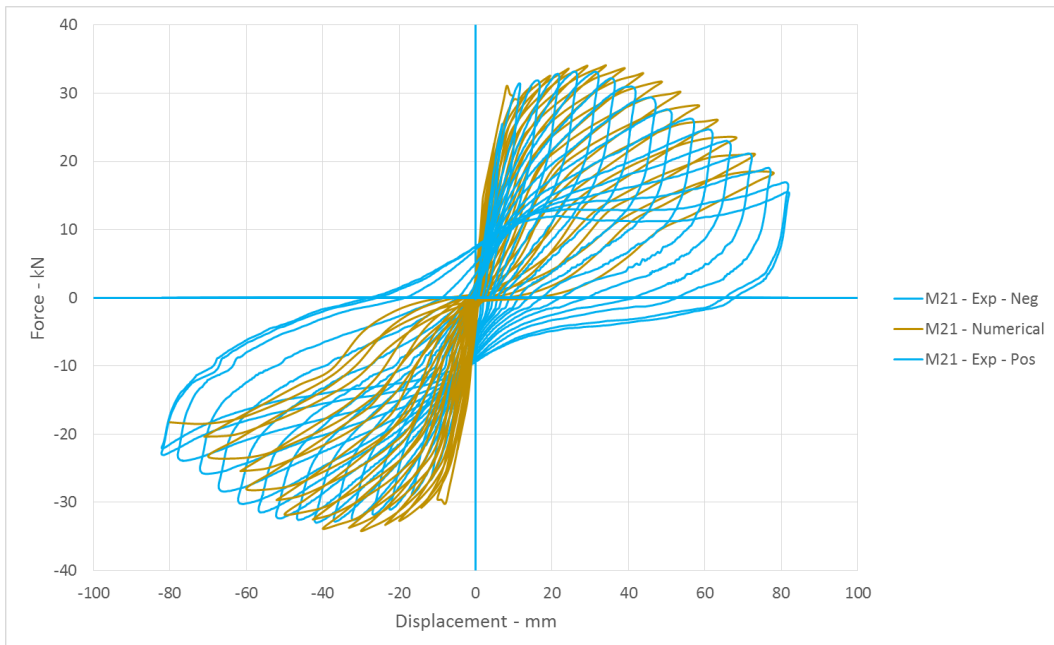


Figure 19 - M21 – Numerical vs experimental analysis – hysteresis F-D.

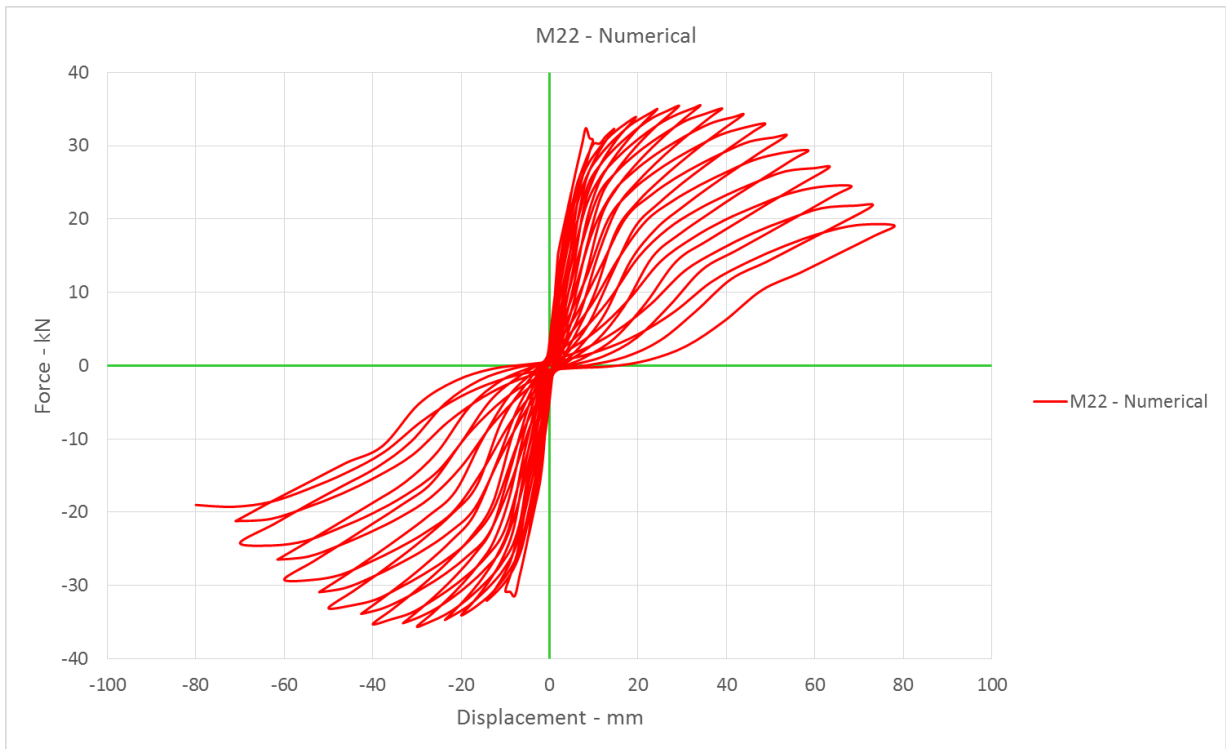


Figure 20 - M22 – Numerical analysis – hysteresis force – displacement.

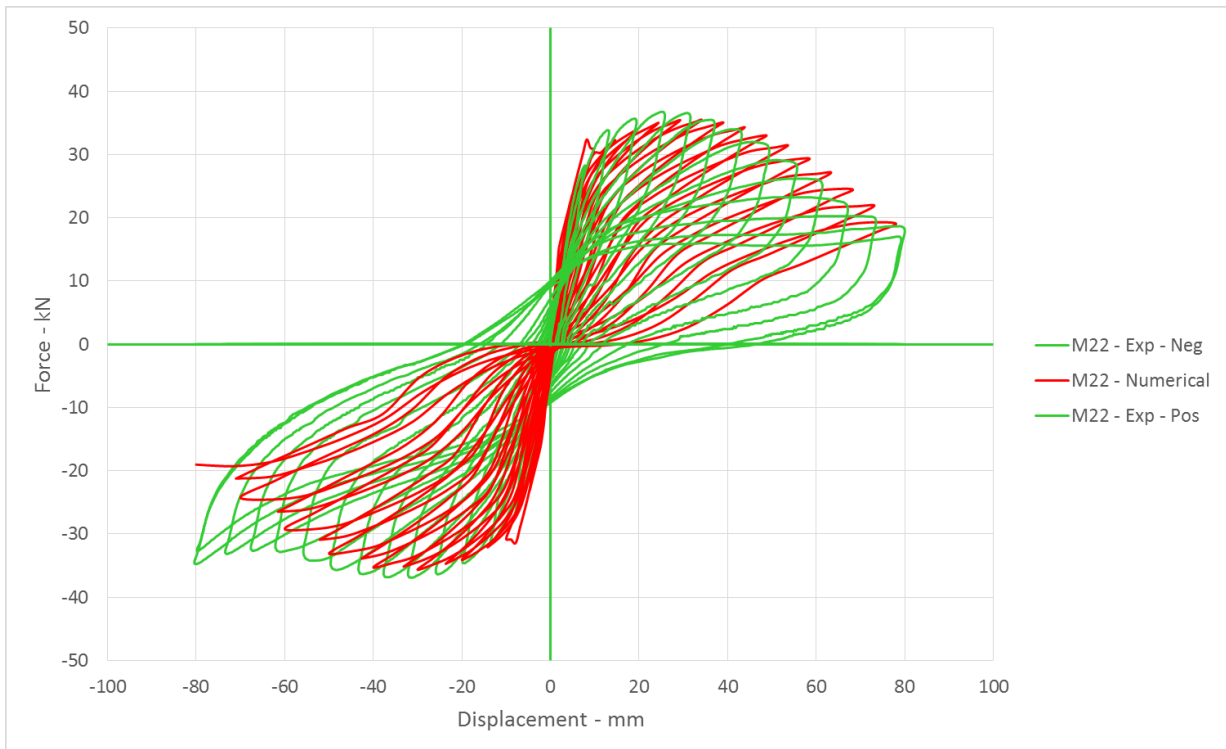


Figure 21 - M22 – Numerical vs experimental analysis – hysteresis F-D.

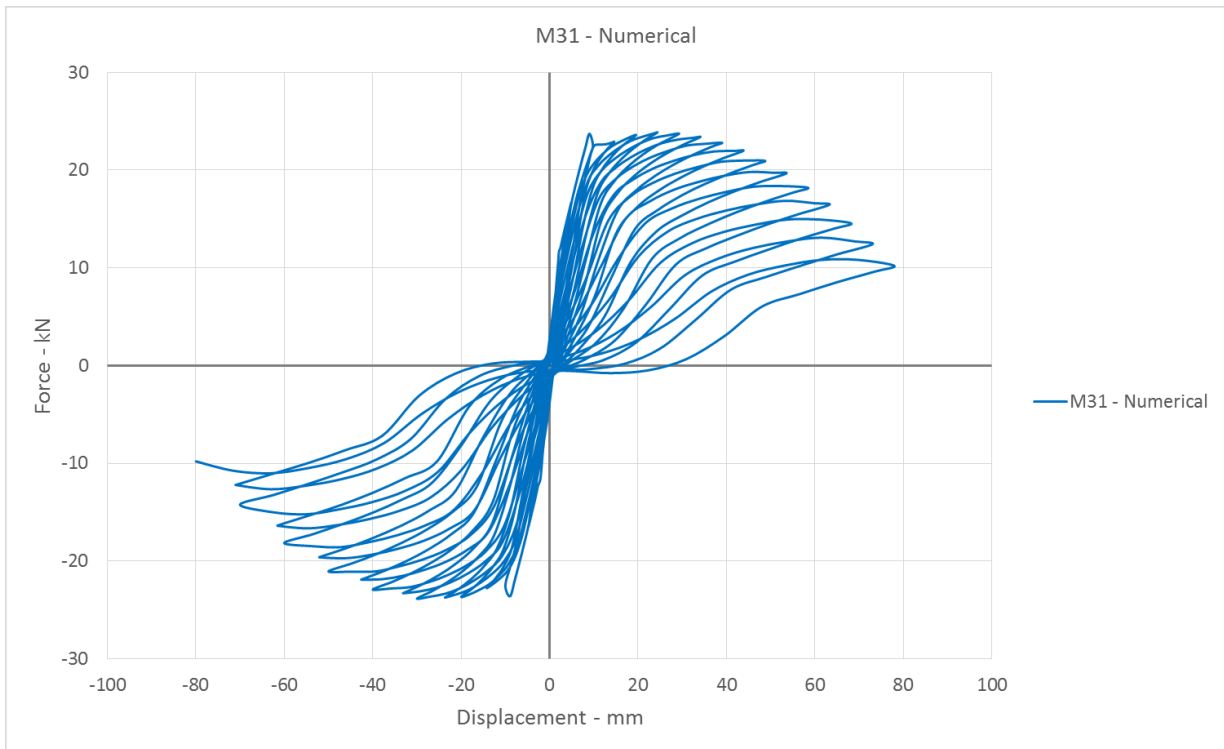


Figure 22 - M31 – Numerical analysis – hysteresis force – displacement.

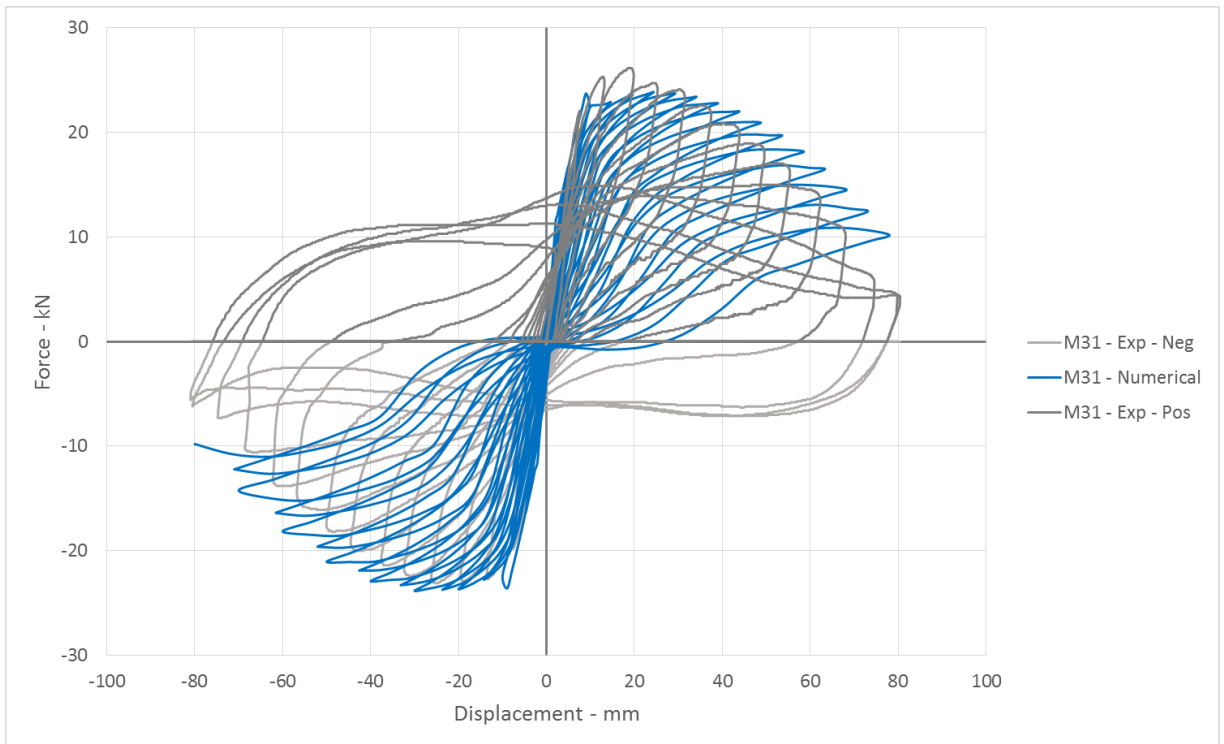


Figure 23 – M31 – Numerical vs experimental analysis – hysteresis F-D.

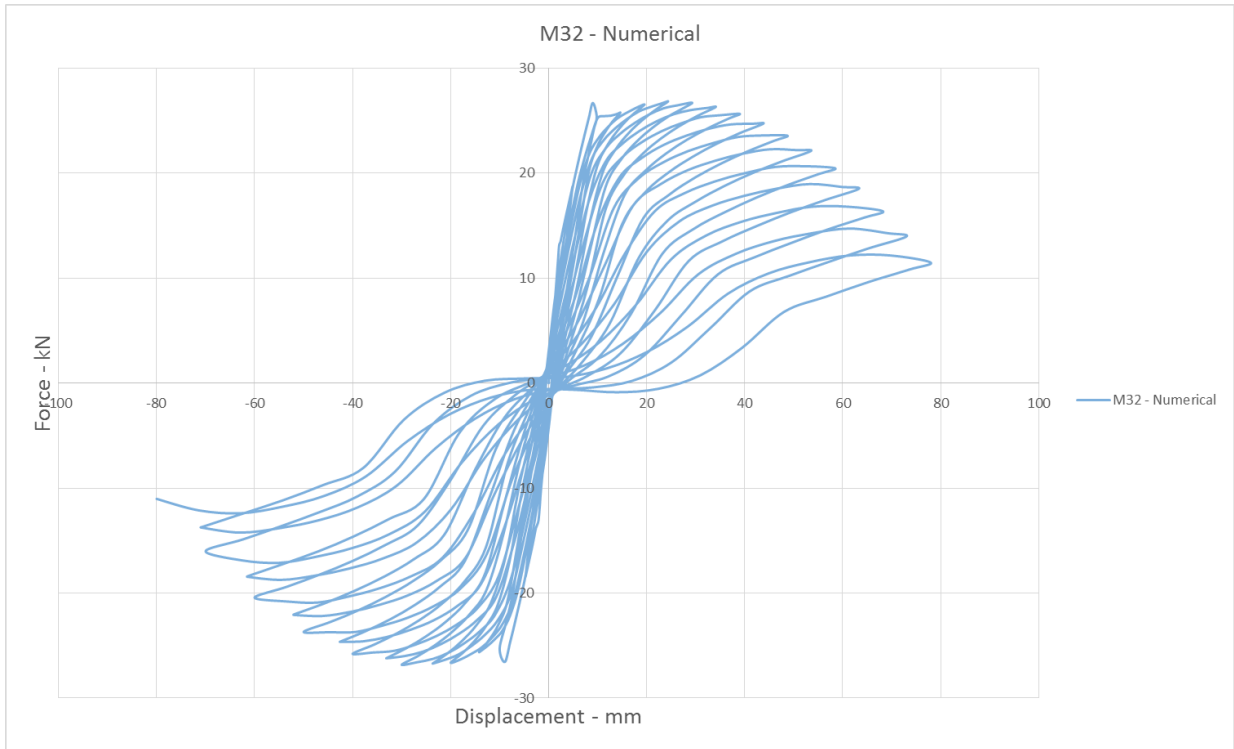


Figure 24 - M32 – Numerical analysis – hysteresis force – displacement.

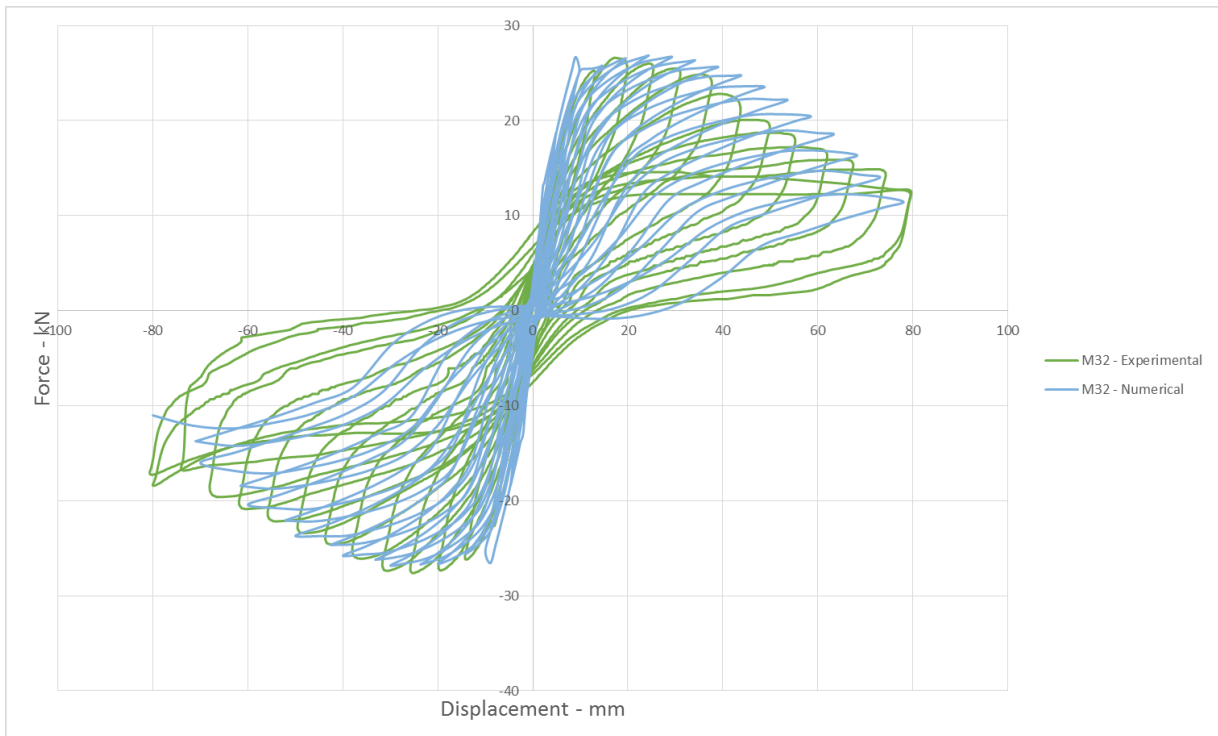


Figure 25 - M32 – Numerical vs experimental analysis – hysteresis F-D.

5.6 Concluding Remarks

From the obtained results from the conducted extensive analytical study devoted to refined 3D nonlinear behavior modeling of steel-reinforced and GFRP-reinforced bridge column models, the following concluding remarks can be summarized:

- (1) The defined shapes of the envelope curves for both steel-reinforced and GFRP-reinforced bridge column models show very good agreement with the experimental results. The shape of the unloading patterns should be improved by consideration of the actual bond behavior of the GFRP-bars.
- (2) The predicted load bearing capacity of all tested bridge column models with the implemented refined 3D nonlinear model shows a very good agreement with the recorded experimental results. This is fully confirmed by the presented actual differences for the defined ultimate point – U, where the actual differences in the respective force and deformation parameters are less than 5%.
- (3) The “pinching” effect is more expressed in the modeled GFRP-reinforced bridge column models. This shows the need for consideration of the real bond behavior of the GFRP-bars in the formulated refined 3D nonlinear analytical model.
- (4) The crack and damage propagation as well as the stiffness deterioration were very well simulated by the presented refined analytical model.
- (5) Finally, the real confinement level effect can be very well included because the implemented concept based on an advanced refined modeling approach provides the best conditions for realistic behavior simulation of all embedded reinforcing bars by modeling of their real behavior properties.
- (6) To improve modeling of the unloading patterns, the real bond behavior of GFRP-reinforcing bars has to be included in the formulated analytical model. The implemented advanced refined modeling concept provides the best conditions for such specific modeling improvements.

Page is intentionally left blank

6 CHAPTER 6 APPLICATION OF REFINED 3D MODELLING CONCEPT FOR NONLINEAR EARTHQUAKE RESPONSE ANALYSIS OF REAL BRIDGE WITH COLUMNS REINFORCED WITH STEEL AND GFRP REINFORCEMENT

6.1 Introduction

Chapter 6 provides presentation of selected representative results obtained from the realized extensive and specific analytical study devoted to investigation of the real possibility for practical application of the implemented refined 3D modeling concept for modeling and nonlinear detailed earthquake response analysis of the selected bridge prototype structure with columns reinforced with ordinary steel reinforcement in the first case, and then, reinforced with three different specified amounts of GFRP reinforcement in the second case.

This extensive analytical study has clearly shown the full capability and full advantages of application of the refined nonlinear modeling concept, if detailed seismic response phenomena have to be analyzed and evaluated.

Item 6.2 briefly shows the most general procedure implemented in nonlinear dynamic or nonlinear earthquake response analysis of the considered real bridge prototype structure.

The next item 6.3 contains a brief description of the considered real bridge prototype structure used for computation of the nonlinear earthquake response based on application of formulated refined nonlinear models of bridge piers reinforced, first of all, with steel reinforcement and then, with three specified GFRP reinforcement options.

Presented in the subsequent two items, item 6.4 and item 6.5, are selected results on the computed nonlinear earthquake responses for the defined four calculation cases (four variants of bridge column reinforcement), under the real earthquake records of Petrovac and El-Centro earthquake scaled to a strong intensity level with $PGA = 0.45g$.

Comparative presentation of the selected analysis results is given to demonstrate various response characteristics and differences in responses.

Item 6.6 includes a comparison of the computed monotonic push-over curves and hysteretic curves of columns obtained from the computed nonlinear earthquake responses.

The last item 6.7 includes some important concluding remarks derived on the basis of the results from the performed integral analytical study.

6.2 Refined 3D Modelling Concept Applied for Nonlinear Earthquake Response Analysis of Real Structures

Nonlinear time history analysis is a step-by-step analysis of dynamic response of a structure for a specified loading that can be arbitrary that is varying by time. The dynamic equilibrium equations to be solved are given by this form:

$$M\ddot{u}(t) + C\dot{u}(t) + Ku(t) = R(t)$$

K is the stiffness matrix; **C** is damping matrix, **M** is diagonal mass matrix of structure; u, \dot{u}, \ddot{u} are displacements, velocities, accelerations of structure, **R** is applied load in the structure. If the load is a ground acceleration, displacements, velocities and accelerations are relative to this ground motion.

Nonlinear time history analysis requires an iterative solution of the equations of motions and can be performed in many options like Modal, Direct Integration. The stiffness, damping and load depend upon the displacement, velocities and time. Nonlinearity in structure can be material nonlinearity and geometric nonlinearity. Material nonlinearity in structure can be modelled as a concentrated plasticity in for of plastic hinges or fiber sections approach. Using the geometrical nonlinearity P-delta effects and large displacement effects can be incorporated.

For the integration of equations there are few methods:

Newmark's β method

Hughes α method

Wilson θ

Modified Wilson θ

Hughes α Method with $\alpha = 0$ reduces to Newmark's β Method. Modified Wilson θ Method is an extension of Wilson θ Method.

The governing equations for dynamic analysis are as follows:

Hughes α method:

$$\mathbf{M}\ddot{\bar{u}}^{t+\Delta t} + \mathbf{C}\left((1+\alpha)\dot{\bar{u}}^{t+\Delta t} - \alpha\dot{\bar{u}}^t\right) + \mathbf{K}\left((1+\alpha)\bar{u}^{t+\Delta t} - \alpha\bar{u}^t\right) = (1+\alpha)\bar{R}^{t+\Delta t} - \alpha\cdot\bar{R}^t$$

Newmark β method:

$$\mathbf{M}\ddot{\bar{u}}^{t+\Delta t} + \mathbf{C}\dot{\bar{u}}^{t+\Delta t} + \mathbf{K}\bar{u}^{t+\Delta t} = \bar{R}^{t+\Delta t}$$

(Modified) Wilson θ method:

$$\mathbf{M}\ddot{\bar{u}}^{t+\theta\Delta t} + \mathbf{C}\dot{\bar{u}}^{t+\theta\Delta t} + \mathbf{K}\bar{u}^{t+\theta\Delta t} = \bar{R}^{t+\theta\Delta t}$$

The displacement, acceleration and velocity at time $t + \Delta t$ is calculated as functions of

(already known) $\ddot{\bar{u}}^t, \dot{\bar{u}}^t, \bar{u}^t$ and displacement increments $\Delta\bar{u}^{t+\Delta t} + \Delta u$

Hughes α method:

Newmark β method:

$$\bar{u}^{t+\Delta t} = \bar{u}^t + \Delta\bar{u}^{t+\Delta t} + \Delta\bar{u}$$

$$\dot{\bar{u}}^{t+\Delta t} = \left(\frac{1}{2} \frac{(2\beta\Delta t^2 - \Delta t^2)\gamma}{\Delta t\beta} + \Delta t(1-\gamma) \right) \dot{\bar{u}}^t + \frac{1}{2} \frac{(-2\gamma - \Delta t + 2\Delta\bar{u} + 2\Delta\bar{u}^{t+\Delta t})\gamma}{\Delta t\beta} + \dot{\bar{u}}^t$$

$$\ddot{\bar{u}}^{t+\Delta t} = \frac{1}{2} \frac{2\ddot{\bar{u}}^{t+\Delta t}\beta\Delta t^2 - \ddot{\bar{u}}^{t+\Delta t}\Delta t^2 - 2\dot{\bar{u}}^t\Delta t + 2\Delta\bar{u} + 2\Delta\bar{u}^{t+\Delta t}}{\Delta t^2\beta}$$

Modified Wilson θ method:

Wilson θ method:

$$\bar{u}^{t+\Delta t} = \bar{u}^t + \Delta\bar{u}^{t+\Delta t} + \Delta u$$

$$\dot{\bar{u}}^{t+\Delta t} = -\frac{3\bar{u}^t}{\Delta t} - 2\dot{\bar{u}}^t - \frac{1}{2}\ddot{\bar{u}}^t\Delta t + \frac{3(\bar{u}^t + \Delta\bar{u}^{t+\Delta t} + \Delta\bar{u})}{\Delta t}$$

$$\ddot{\bar{u}}^{t+\Delta t} = -\frac{6\bar{u}^t}{\Delta t^2} - \frac{6\dot{\bar{u}}^t}{\Delta t} - 2\ddot{\bar{u}}^t + \frac{6(\bar{u}^t + \Delta\bar{u}^{t+\Delta t} + \Delta\bar{u})}{\Delta t^2}$$

$$\Delta\bar{u} = \mathbf{K}_{eff}^{inv} \bar{R}_{eff} \quad \mathbf{C} = \delta_M \mathbf{M} + \delta_K \mathbf{K}$$

$$\mathbf{K}_{eff} = \mathbf{M}\bar{\zeta}_M + \mathbf{K}\bar{\zeta}_K$$

$$\bar{R}_{eff} = \mathbf{M}(\bar{\zeta}_M^1 + \bar{\zeta}_M^2) + \mathbf{K}(\bar{\zeta}_K^1 + \bar{\zeta}_K^2) + \bar{\zeta}_0$$

The coefficients above are calculated using the following express

Hughes α method:

$$\begin{aligned} \bar{\zeta}_M &= \left(\left(\frac{\left(\frac{1}{2}\alpha + \frac{1}{2} \right) \delta_M \gamma}{\beta} + (-\alpha - 1) \delta_M \right) \Delta t - 1 + \frac{1}{2\beta} \right) \ddot{u}^t + \left(\frac{(1+\alpha) \delta_M \gamma}{\beta} - \delta_M + \frac{1}{\Delta t \beta} \right) \dot{u}^t - \\ &\quad \frac{\Delta \bar{u}^{t+\Delta t}}{\Delta t^2 \beta} + \frac{(-\alpha \Delta \bar{u}^{t+\Delta t} - \Delta \bar{u}^{t+\Delta t}) \gamma \delta_M}{\beta \Delta t} \\ \bar{\zeta}_K &= \left(\frac{\left(\frac{1}{2}\alpha + \frac{1}{2} \right) \delta_K \gamma}{\beta} + (-\alpha - 1) \delta_K \right) \Delta t \ddot{u}^t + \left(\frac{(1+\alpha) \delta_K \gamma}{\beta} - \delta_K \right) \dot{u}^t + \frac{(-\alpha \Delta \bar{u}^{t+\Delta t} - \Delta \bar{u}^{t+\Delta t}) \gamma \delta_K}{\beta \Delta t} \\ \bar{\zeta}_M^{[1]} &= \left(\left(\frac{\left(\frac{1}{2}\alpha + \frac{1}{2} \right) \delta_M \gamma}{\beta} + (-\alpha - 1) \delta_M \right) \Delta t - 1 + \frac{1}{2\beta} \right) \ddot{u}^t + \left(\frac{(1+\alpha) \delta_M \gamma}{\beta} - \delta_M + \frac{1}{\Delta t \beta} \right) \dot{u}^t \\ \bar{\zeta}_M^{[2]} &= -\frac{\Delta \bar{u}^{t+\Delta t} (\alpha \gamma \Delta t \delta_M + \gamma \Delta t \delta_M + 1)}{\Delta t^2 \beta} \\ \bar{\zeta}_K^{[1]} &= \left(\frac{\left(\frac{1}{2}\alpha + \frac{1}{2} \right) \delta_K \gamma}{\beta} + (-\alpha - 1) \delta_K \right) \Delta t \ddot{u}^t + \left(\frac{(1+\alpha) \delta_K \gamma}{\beta} - \delta_K \right) \dot{u}^t \\ \bar{\zeta}_K^{[2]} &= -\frac{\Delta \bar{u}^{t+\Delta t} (1+\alpha) \gamma \delta_K}{\beta \Delta t} \\ \bar{\zeta}_0 &= \bar{R}^{t+\Delta t} (1+\alpha) - \bar{R}^t \alpha - \bar{F}^{t+\Delta t} (1+\alpha) + \bar{F}^t \alpha \end{aligned}$$

Newmark β method:

$$\bar{\zeta}_M = \left(\left(\frac{\delta_M \gamma}{2\beta} - \delta_M \right) \Delta t - 1 + \frac{1}{2\beta} \right) \ddot{u}^t + \left(\frac{\delta_M \gamma}{\beta} - \delta_M + \frac{1}{\Delta t \beta} \right) \dot{u}^t - \frac{\Delta \bar{u}^{t+\Delta t}}{\Delta t^2 \beta} + \frac{(-\Delta \bar{u}^{t+\Delta t}) \gamma \delta_M}{\beta \Delta t}$$

$$\bar{\zeta}_K = \left(\frac{\delta_K \gamma}{2\beta} - \delta_K \right) \Delta t \ddot{u}^t + \left(\frac{\delta_K \gamma}{\beta} - \delta_K \right) \dot{u}^t + \frac{(-\Delta \bar{u}^{t+\Delta t}) \gamma \delta_K}{\beta \Delta t}$$

$$\bar{\zeta}_M^1 = \left(\left(\frac{\delta_M \gamma}{2\beta} - \delta_M \right) \Delta t - 1 + \frac{1}{2\beta} \right) \ddot{u}^t + \left(\frac{\delta_M \gamma}{\beta} - \delta_M + \frac{1}{\Delta t \beta} \right) \dot{u}^t$$

$$\bar{\zeta}_M^2 = -\frac{\Delta \bar{u}^{t+\Delta t} (\gamma \Delta t \delta_M + 1)}{\Delta t^2 \beta}$$

$$\bar{\zeta}_K^1 = \left(\frac{\delta_K \gamma}{2\beta} - \delta_K \right) \Delta t \ddot{u}^t + \left(\frac{\delta_K \gamma}{\beta} - \delta_K \right) \dot{u}^t$$

$$\bar{\zeta}_K^2 = -\frac{\Delta \bar{u}^{t+\Delta t} \gamma \delta_K}{\beta \Delta t}$$

$$\bar{\zeta}_0 = \bar{R}^{t+\Delta t} - \bar{F}^{t+\Delta t}$$

Wilson θ method and Modified Wilson θ method:

$$\bar{\zeta}_M = \frac{3\delta_M}{\theta\Delta t} + \frac{6}{\theta^2\Delta t^2}$$

$$\bar{\zeta}_K = 1 + \frac{3\delta_K}{\theta\Delta t}$$

$$\bar{\zeta}_M^1 = \left(\frac{1}{2} \frac{6\theta - 2}{\theta^3} + \frac{1}{2} \frac{(3\theta^2 - 2\theta)\Delta t\delta_M}{\theta^3} \right) \ddot{u}^t + \left(\frac{6}{\theta^2\Delta t} + \frac{1}{2} \frac{(6\theta^2 - 2)\delta_M}{\theta^3} \right) \dot{u}^t$$

$$\bar{\zeta}_M^2 = -\frac{3\Delta\bar{u}^{t+\Delta t}(\theta\Delta t\delta_M + 2)}{\theta^2\Delta t^2}$$

$$\bar{\zeta}_K^1 = \left(\frac{1}{2} \frac{(3\theta^2 - 2\theta)\Delta t\delta_K}{\theta^3} + \frac{1}{2} \frac{(\theta^3 - \theta^2)\Delta t^2}{\theta^3} \right) \ddot{u}^t + \left(\frac{1}{2} \frac{(6\theta^2 - 2)\delta_K}{\theta^3} + \frac{1}{2} \frac{(2\theta^3 - 2\theta)\Delta t}{\theta^3} \right) \dot{u}^t$$

$$\bar{\zeta}_K^2 = -\frac{3\Delta\bar{u}^{t+\Delta t}\delta_K}{\theta\Delta t}$$

Wilson θ method :

$$\bar{\zeta}_0 = \frac{\bar{R}^{t+\Delta t}}{\theta^2} + \left(-\frac{1}{\theta^2} + \frac{1}{\theta^3} \right) \bar{R}^t - \bar{F}^{t+\Delta t} + \left(1 - \frac{1}{\theta^3} \right) \bar{F}^t$$

Modified Wilson θ method

$$\bar{\zeta}_0 = \left(\frac{1}{\theta} - \frac{1}{\theta^3} \right) \bar{F}^t - \frac{\bar{F}^{t+\theta\Delta t}}{\theta} + \frac{\bar{R}^{t+\theta\Delta t}}{\theta^3}$$

The parameters β, γ are integration parameters used by Newmark β and Hughes α method.

Their value are essential for convergence of this time marching scheme. It can be shown that

$\gamma = \frac{1}{2}, \beta = \frac{1}{6}$ corresponds to linear acceleration within the time step. Values $\gamma = \frac{1}{2}, \beta = \frac{1}{4}$ yields constant acceleration. The integration scheme is unconditionally stable, if $\gamma \geq \frac{1}{2}, \beta \geq 0.25(\frac{1}{2} + \gamma^2)$

and it is only conditionally stable for $\gamma \geq \frac{1}{2}, \beta < 0.25(\frac{1}{2} + \gamma^2)$ provided that the stability limit is fulfilled:

$$\omega\Delta t_{crit} = \frac{\xi\left(\gamma - \frac{1}{2}\right) + \left[\frac{\gamma}{2} - \beta + \xi^2\left(\gamma - \frac{1}{2}\right)^2\right]^{\frac{1}{2}}}{\left(\frac{\gamma}{2} - \beta\right)}$$

Where: ξ is modal damping parameter.

The above defines the condition for time increment Δt for a linear conditionally stable case:

$$\frac{\Delta t}{T_n} \leq \frac{1}{\pi\sqrt{2}\sqrt{\gamma - \frac{2}{3}}} \leq 0.551$$

As for Wilson θ and Modified Wilson θ method they use θ parameter. Its value is $\theta \geq 1$ and the scheme is unconditionally stable for $\theta \geq 1.4$. It essentially specifies time, for which time we calculate the governing equations for $t + \theta\Delta t$. For $\theta = 1$ Wilson θ and Modified Wilson θ method yield the same solution expressions and equations and these are

also the same as those for Newmark and Hughes methods with $\gamma = \frac{1}{2}$, $\beta = \frac{1}{6}$, $\alpha = 0$.

Proportional damping in nonlinear time history analysis is calculated by:

$$C = \delta_M M + \delta_K K$$

Where: δ_M, δ_K are mass proportional and stiffness proportional coefficients.

In the presented nonlinear earthquake response analysis procedure, the matrix analysis approach has been considered as the most general numerical procedure for the solution of the matrix differential equation of motion of the second order.

In the present research, assembling of nonlinear stiffness matrix has been based on application of the advanced refined 3D modeling concept.

In this case, for modeling of the concrete material, very small 3D nonlinear finite elements developed on the basis of realistic nonlinear concrete stress-strain relations have been used. For modeling of the steel bars, GFRP bars, or steel hoops, nonlinear one-dimensional finite elements developed also on the basis of real non-linear stress-strain material relations have been used.

By application of such refined 3D nonlinear modeling concept, there have been provided the most general numerical analysis options with the capability to: (1) perform modeling of geometrically very complex structures; (2) obtain the required accuracy by generation of a refined finite element mesh; (3) include the real positions of the reinforcing bars in the analysis; (4) include realistic stress-strain relations of concrete materials and of the implemented reinforcing bars in the analysis.

In addition, some specific bond behavior of reinforcing bars can also be included because the implemented refined modeling concept is the most favorable analysis option for adopting specific nonlinear stress-strain based finite elements with the capability to realistically simulate the nonlinear bond behavior along the specific reinforcing bars.

6.3 Real Prototype Bridge With Columns Reinforced With Steel and Varying Levels of GFRP Reinforcement Considered For Seismic Response Analysis

To explore the applicability of the formulated refined nonlinear modeling concept for analysis of real bridge structures exposed to strong earthquake effects, the specific analytical studies have been realized. Investigations results are presented in this Chapter 6, or more precisely in item 6.4, item 6.5 and item 6.6. The investigations has been based on prototype bridge modeling and realization of the following research phases:

(1) Firstly, for the realization of the present research objectives, suitable structural system of real prototype bridge has been adopted. More concretely, the structural system of the selected prototype bridge has been adopted to possess a total of four spans and the total length of $L = 20 + 25 + 25 + 20 = 90.0$ m, Fig. 86. The substructure of the bridge is composed of two rigid abutments (supports), while the three middle piers are constructed as individual reinforced concrete elements with a circular cross-section and a diameter of $D = 60.0$ cm. The left pier (C1), the central pier (C2) and the right pier (C3) are constructed to have different height, namely $h_1 = 3.0$ m, $h_2 = 5.0$ m and $h_3 = 4.0$ m. The lower ends of the piers are fixed into constructed rigid solitary footings, while the upper end of the piers ends with transverse RC beams on which hinge supports of the bridge superstructure are formed. The bridge superstructure has been adopted to be of a simplified geometry, in the form of an RC slab with a width of $b = 6.0$ m and height $h = 1.20$ m. Such a geometry has been adopted in order to partially simplify the analytical model, but still simulate the real mass of the superstructure. Initial vibration periods of the analyzed bridge prototype model were $T_1=0.912$ s (dominant transverse direction), $T_2=0.908$ s (dominant longitudinal direction) and $T_3=0.413$ s (dominant rotation).

The main focus of the analytical model for the presented investigations was put on investigations for application of the previously experimentally verified refined modeling concept for simulation of the realistic hysteretic behavior of reinforced concrete piers with adopted different longitudinal reinforcement under the effect of simulated very strong real earthquakes, Fig. 87 and Fig. 88. The circular hoops have been adopted to be identical in all cases. More concretely, it has been adopted that these are made of ordinary steel bars $\phi = 8$ mm placed at a distance of $t = 10.0$ cm along the entire height of the piers.

To provide a more detailed insight into the results obtained from the performed nonlinear seismic analysis, variation of the longitudinal reinforcement in the central bridge piers has been adopted, whereat, for each case, a corresponding nonlinear mathematical model of the integral bridge structure has been formulated. For the present parametric analysis, there have been formulated a total of four refined nonlinear bridge models with four different column reinforcement cases (Fig. 88, Fig. 89, Fig. 90, Fig. 91). The models denoted BM1, BM2, BM3 and BM4, included the following reinforcement options:

- 1) Bridge option - 1 (BM1), representing a principal formulated refined nonlinear bridge prototype model for the case of reinforcement of the central piers with ordinary reinforcement, Fig. 89. The longitudinal reinforcement is composed of 12 ϕ 16 ordinary steel reinforcement. The performed analytical investigation for BM1 with the basic configuration of reinforcement of the middle piers is denoted as Calc 1. The remaining three bridge options refer to three different adopted configurations of reinforcement of the middle piers with composite GFRP reinforcing bars.
- 2) Bridge option - 2 (BM2), representing a formulated refined bridge prototype model for the case of reinforcement of the middle piers with a composite reinforcement of reinforcement level – 1. The longitudinal GFRP reinforcement level – 1 consisted of 12 ϕ 16 rebars. The performed analytical investigation referring to BM2 with GFRP reinforcement level – 1 is denoted as Calc 2.
- 3) Bridge option – 3 (BM3), representing the formulated refined bridge prototype model for the reinforced middle piers with GFRP reinforcement defined as reinforcement level – 2. The longitudinal GFRP reinforcement level – 2 consisted 12 ϕ 20 rebars. The performed analytical study with the considered BM3 with GFRP reinforcement level – 2 is denoted as Calc 3.
- 4) Bridge option – 4 (BM4), representing the formulated refined bridge prototype model with reinforced middle piers with GFRP reinforcement level – 3. The longitudinal GFRP reinforcement level – 3 consisted of 24 ϕ 20 rebars. The performed analytical study with the considered BM4 with GFRP reinforcement level – 3 is denoted as Calc 4.

To get a more detailed insight into the practical application of the applied refined nonlinear modeling concept, the seismic responses to simulated effect of two recorded strong real earthquakes of all four options of the prototype bridge defined as BM1, BM2, BM3 and BM4 have been analyzed. Adopted as representative in the analytical investigations have been (1) Petrovac earthquake and (2) El-Centro earthquake.

To simulate quite strong earthquake effect that will cause nonlinear behavior of the middle piers, the intensities of both earthquakes have been scaled and reduced to identical level of peak acceleration of $PGA = 0.45 g$ in both cases.

Selected characteristic results obtained from all performed analyses under the effect of Petrovac and El Centro earthquakes are presented in item 6.4 and item 6.5, respectively. The results obtained are presented in the form of comparative graphic presentations for the purpose of providing insight into the corresponding variations of the seismic response of all the analyzed options of the prototype bridge structure.

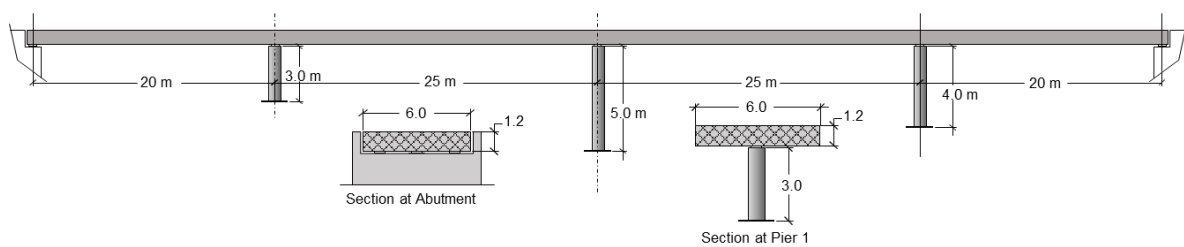


Figure 1 - Bridge Geometry

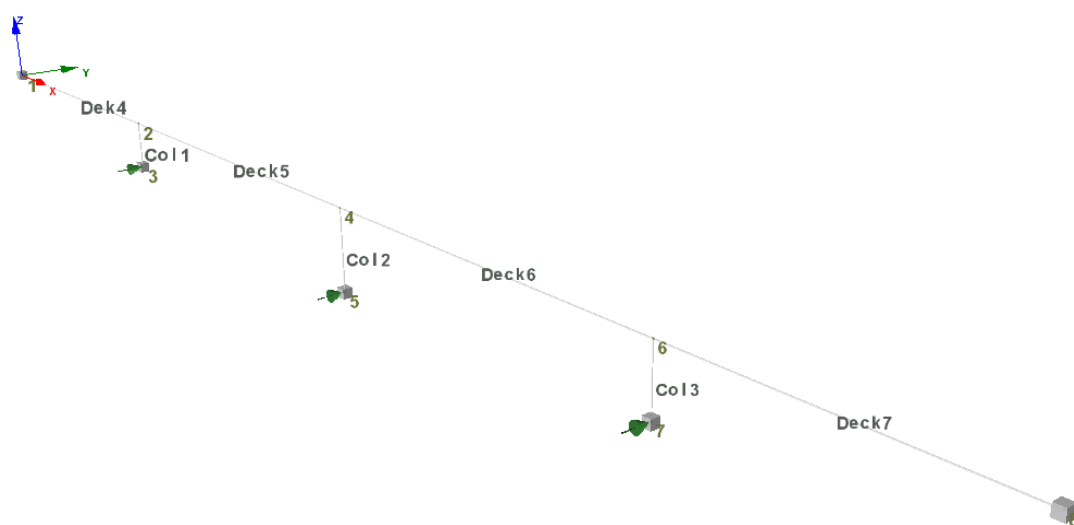


Figure 2 - Bridge Model - Node numbers and Element names

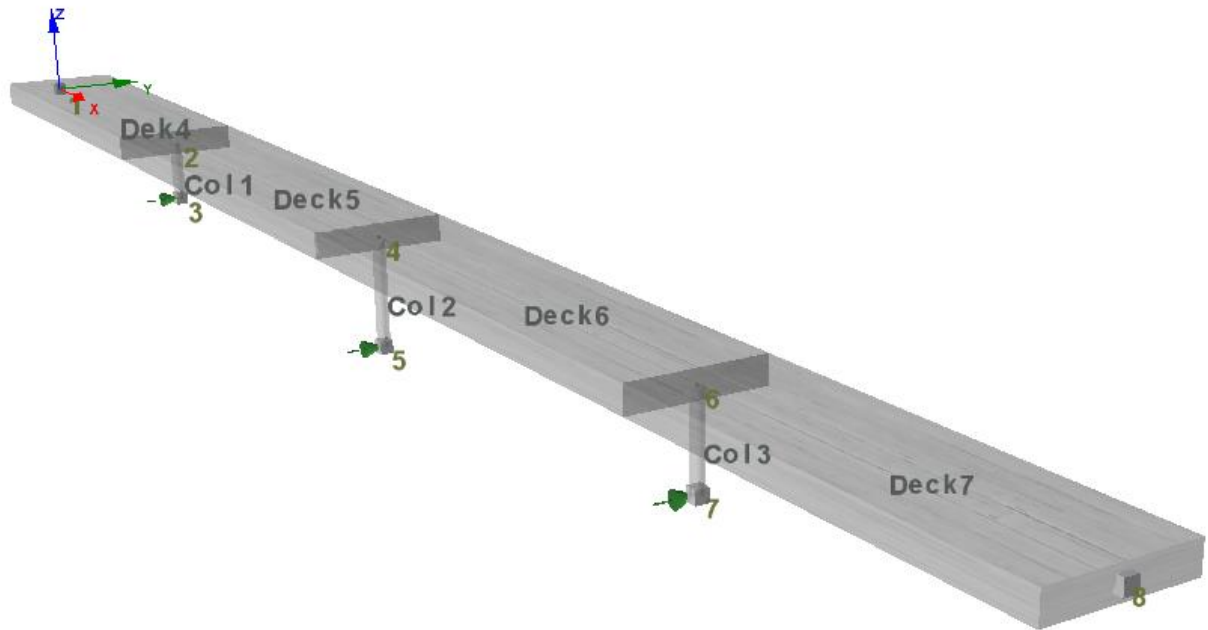


Figure 3 - Bridge Model - Visualization

Nonlinear properties for material Concrete C30/37, Reinforcing Steel S500 and Glass Fiber Reinforced Rebar GFRP are presented below.

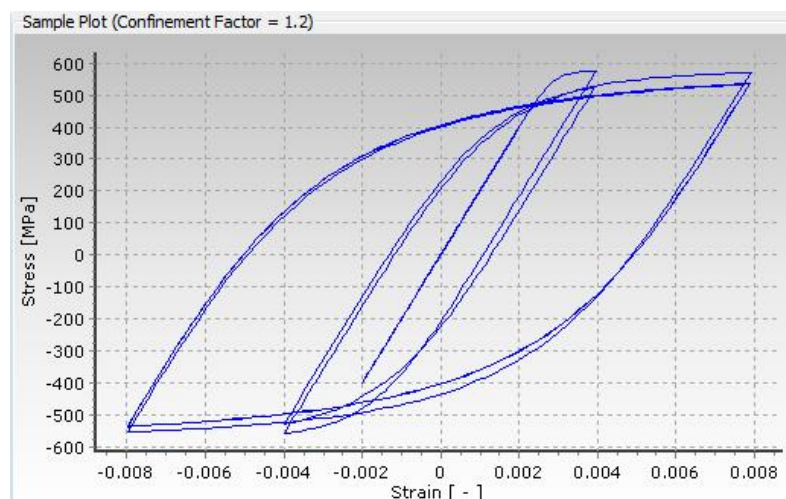


Figure 4 - Nonlinear Stress-Strain diagram for Steel Reinforcement S500

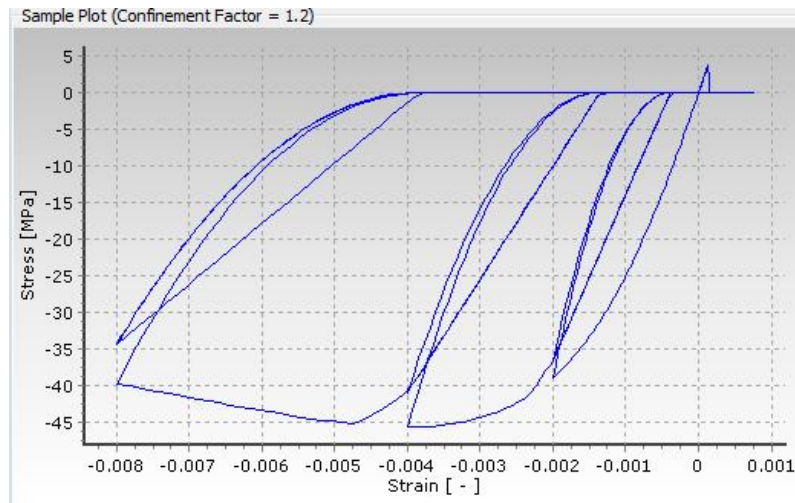


Figure 5 - Nonlinear Stress-Strain diagram for Concrete C30/37

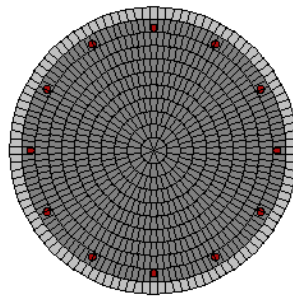


Figure 6 - Cross Section of Columns - FEM discretization in Fibers

In presently formulated refined bridge models, cross sections of bridge columns have been discretized with 800 discrete fibres. In addition, along the length of the columns, in total 5 stiffness integration sections have been selected and used.

6.4 Computed Results of Nonlinear Bridge Response For Selected Four Calculation Cases Under Real Petrovac Earthquake Scaled to PGA=0.45 g

Basically, the computed results on the nonlinear bridge responses of all four considered bridge models or bridge options defined herein as BM1 (Calc 1), BM2 (Calc 2), BM3 (Calc 3) and BM4 (Calc 4) under the simulated Petrovac earthquake (Fig. 92) scaled to PGA =0.45 g, are presented in a graphical form.

The first series of figures, from Fig. 93 to Fig. 108, shows the time history responses to the bending moments at the bottom of all columns and for all four bridge models, or calculation cases (Calc 1, Calc 2, Calc 3, Calc 4).

The second series of figures, from Fig. 109 to Fig. 120 shows the relative displacements of the top of the piers for all four calculation cases.

The third series of figures, from Fig. 121 to Fig. 129, presents the time histories of the computed absolute accelerations at the top of the piers for all four calculation cases.

Finally, the fourth series of figures, from Fig. 168 to Fig. 171 shows the calculated hysteretic responses of the shortest bridge column – 1 for the considered four characteristic bridge models or calculation cases. Included in the same figures are also the respective nonlinear push-over curves computed for all four bridge models or calculation cases.

Some of the presented results are clearly expressing the real earthquake response differences due to reinforcement variation in the middle piers of the analyzed prototype bridge.

The first four figures, Fig. 93, Fig. 94, Fig. 95 and Fig. 96 comparatively present the bending moments of all three bridge columns. The maximum value of the bending moment has generally been controlled by the height of the columns.

The subsequent figure, Fig. 97, comparatively presents the moment histories at the bottom of column – 1 of three analyzed models.

Figures 98, 99 and 100 show respectively the moment history results for Column 1 and for model M2, M3 and M4, in relation with the results obtained for model M1.

Fig. 101 provides a comparative presentation of the moment history results for the bottom of column-2, for all four analyzed models.

Fig. 102, Fig. 103 and Fig. 104 present respectively the moment history results for column – 2 and for model M2, M3 and M4, in relation with the results obtained for model M1.

Fig. 105 shows comparatively the moment history results for the bottom of column – 3, for all four analyzed models.

Fig. 106, Fig. 107 and Fig. 108 respectively display the moment history results for column – 3 and for model M2, M3 and M4, in relation with the results obtained for model M1.

Presented in the subsequent 12 figures, from Fig. 109 through Fig. 120, are the time histories of the computed relative displacements. The first set of four figures, Fig. 109 through Fig. 112, shows the results for the relative displacements of bridge column – 1, first computed for all bridge models M1, M2, M3, M4 and then comparatively for the pairs of models M1 and M2, M1 and M3 and M1 and M4. The second set of four figures, Fig. 113 through Fig. 116, presents the results for the relative displacements of bridge column – 2, including the same sets of comparative presentation as for column – 1. Displayed in the third set of four figures, Fig. 117 through Fig. 120, are the results for the relative displacements of bridge column – 3, including the same set of comparatively presented plots as for column – 1.

The last 9 figures, from Fig. 121 through Fig. 129, comparatively show the time histories of absolute accelerations for column – 1, column – 2 and column – 3. Considered for each column have been all three relevant comparisons between the results from the analyzed models M1 and M2, M1 and M3 and M1 and M4.

Due to the considered four different longitudinal reinforcements in the middle bridge piers, there have been evident respective differences in the computed nonlinear earthquake responses of the prototype bridge. The complete study and all computer results have been performed and obtained based on the formulated advanced refined fiber-based nonlinear modeling concept.

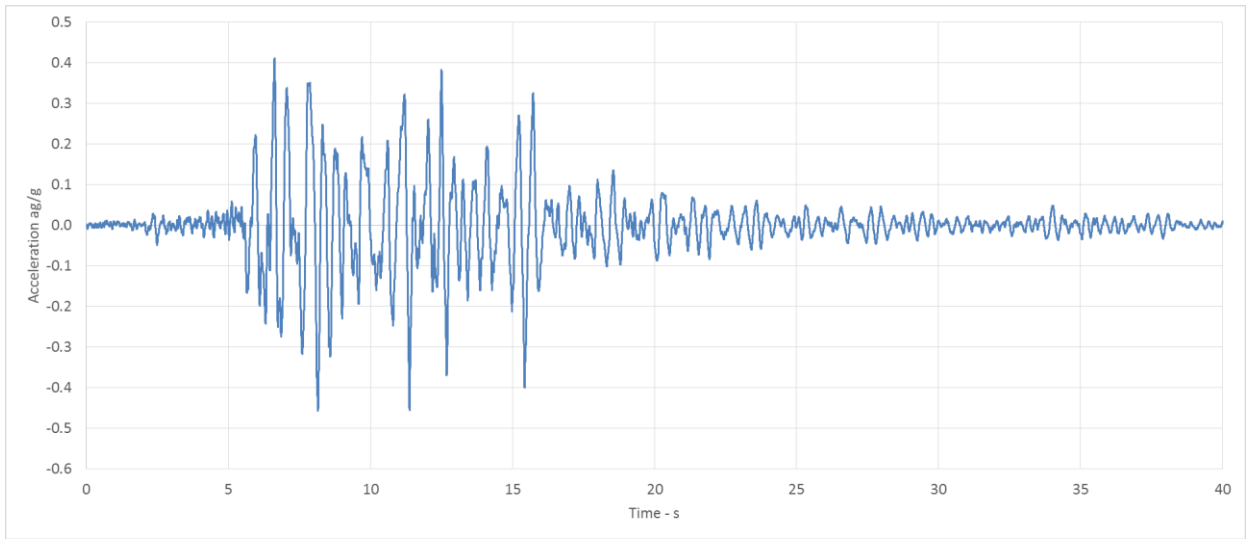


Figure 7 - Petrovac Earthquake Motion – Scaled to $a_g/g = 0.45$

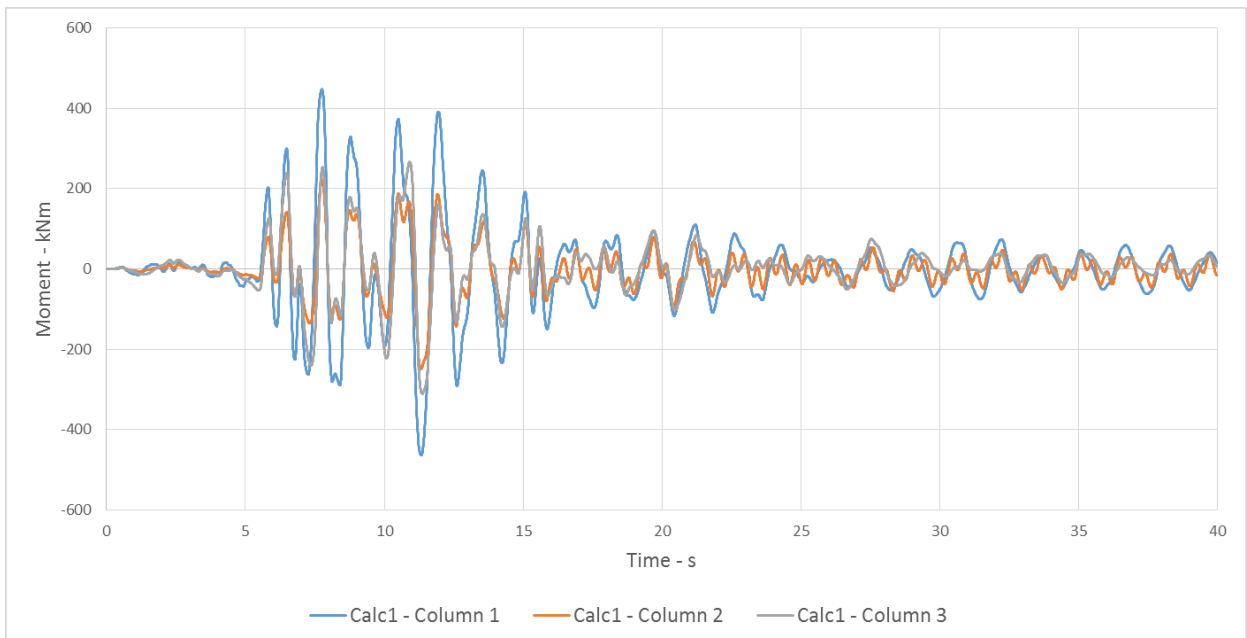


Figure 8 - Calculation 1 - Bending Moments in Bottom of Columns

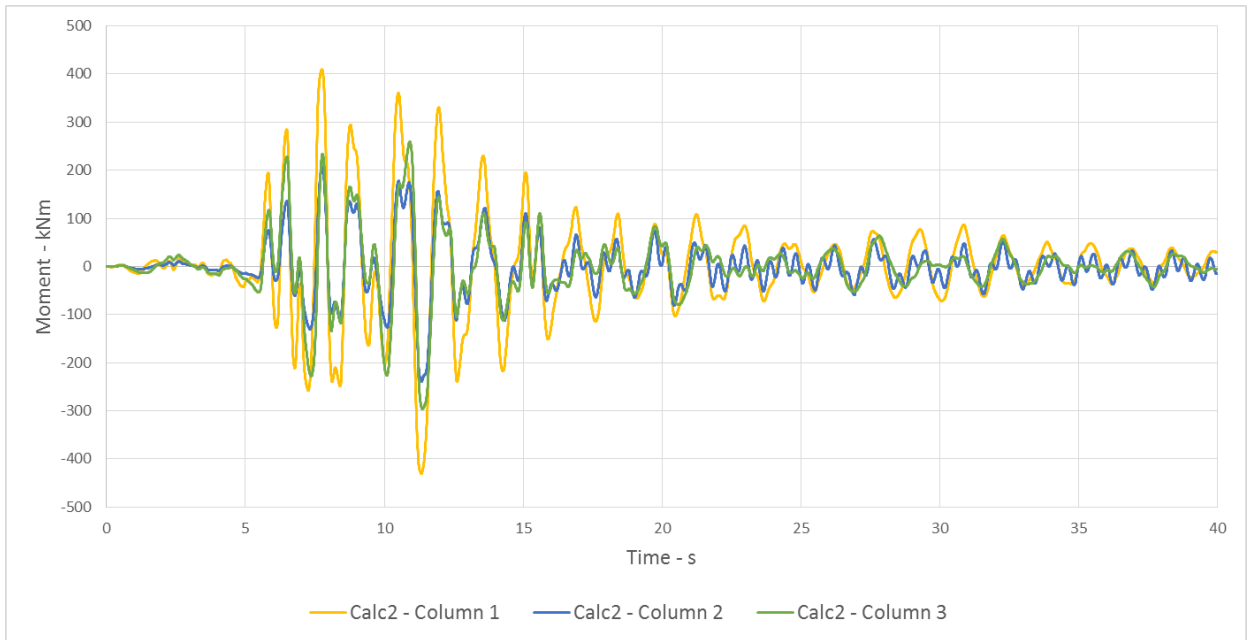


Figure 9 - Calculation 2 - Bending Moments in Bottom of Columns

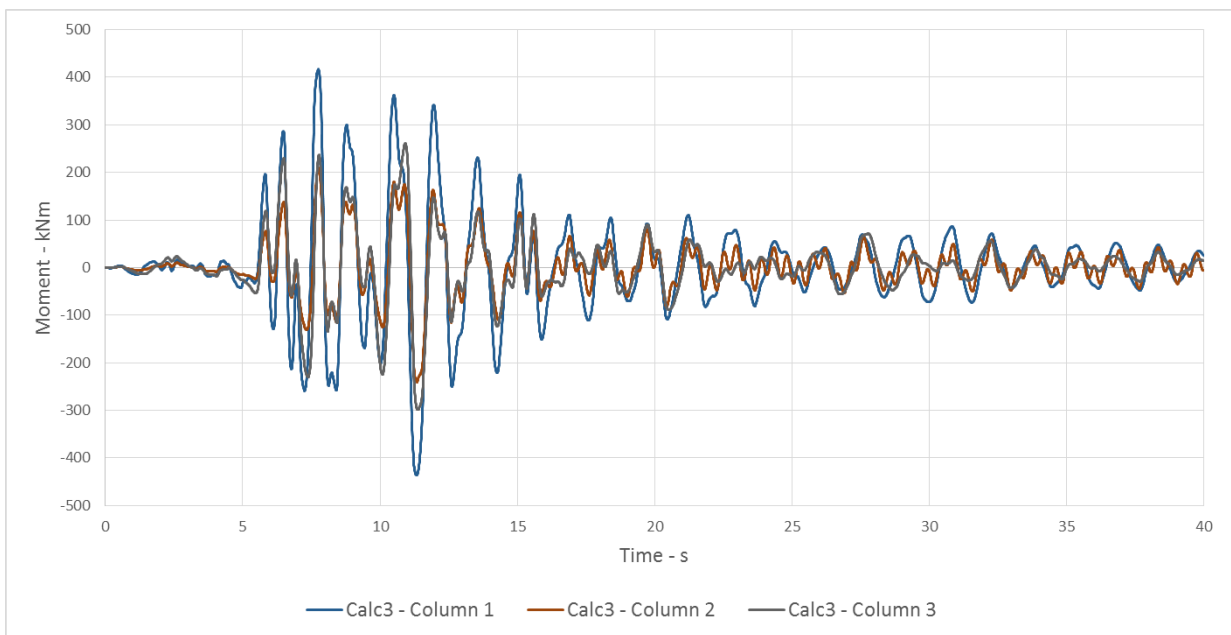


Figure 10 - Calculation 3 - Bending Moments in Bottom of Columns

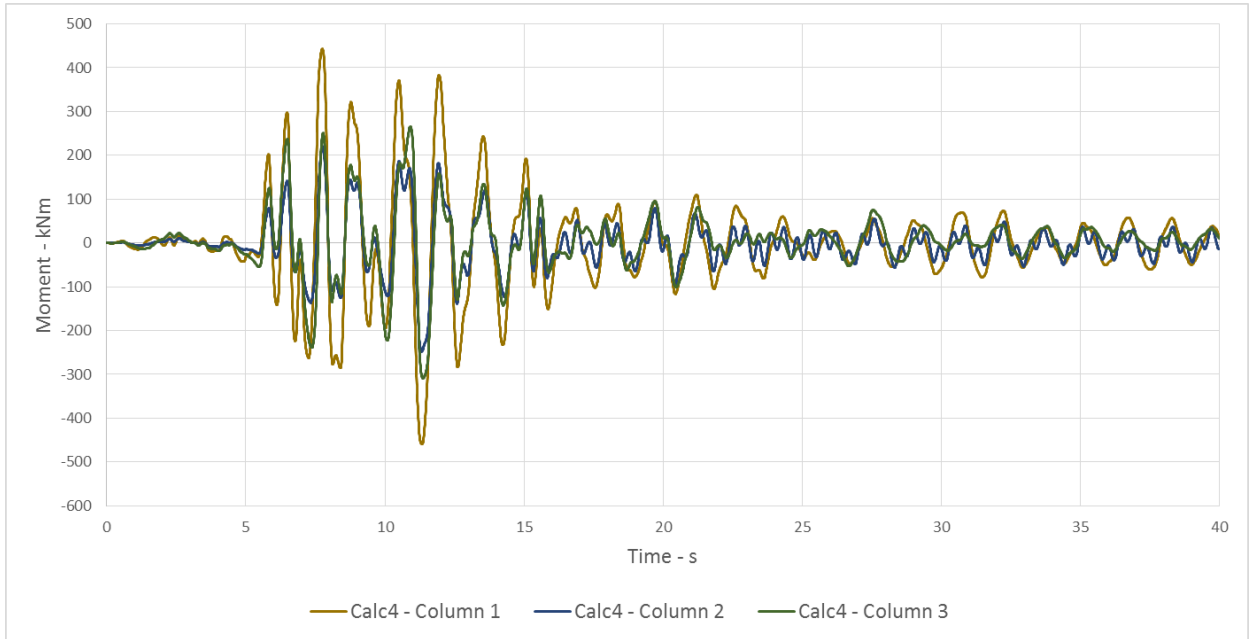


Figure 11 - Calculation 8 - Bending Moments in Bottom of Columns

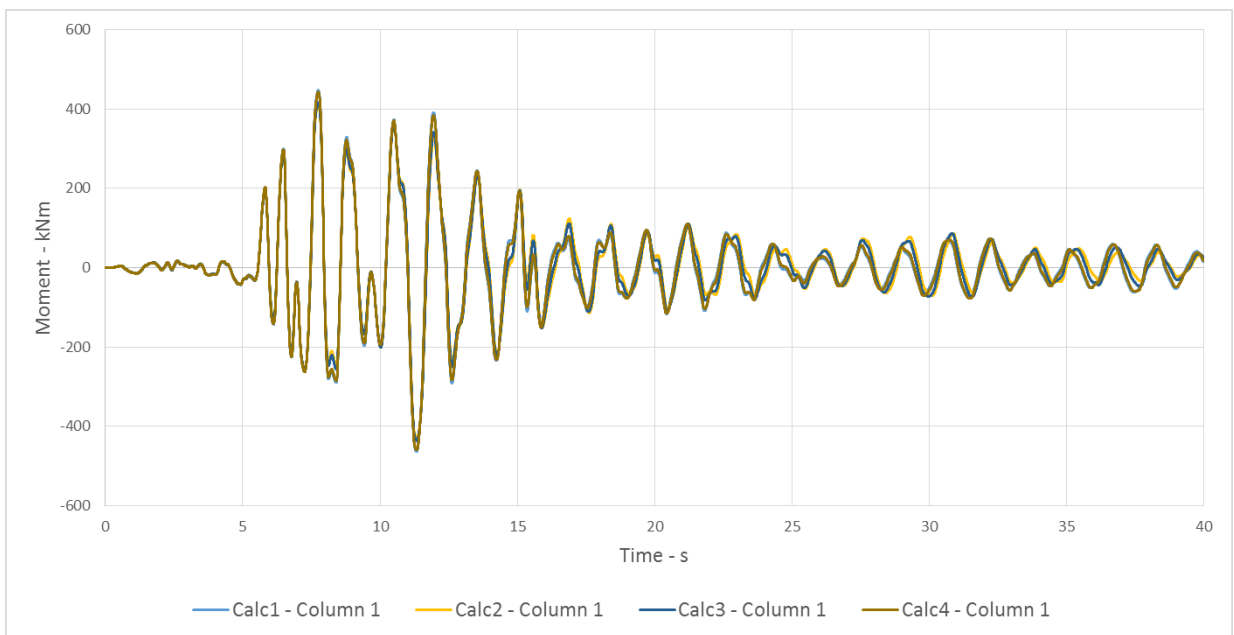


Figure 12 - Bending Moments in Bottom of Column 1 - From Calc1, 2, 3, 4

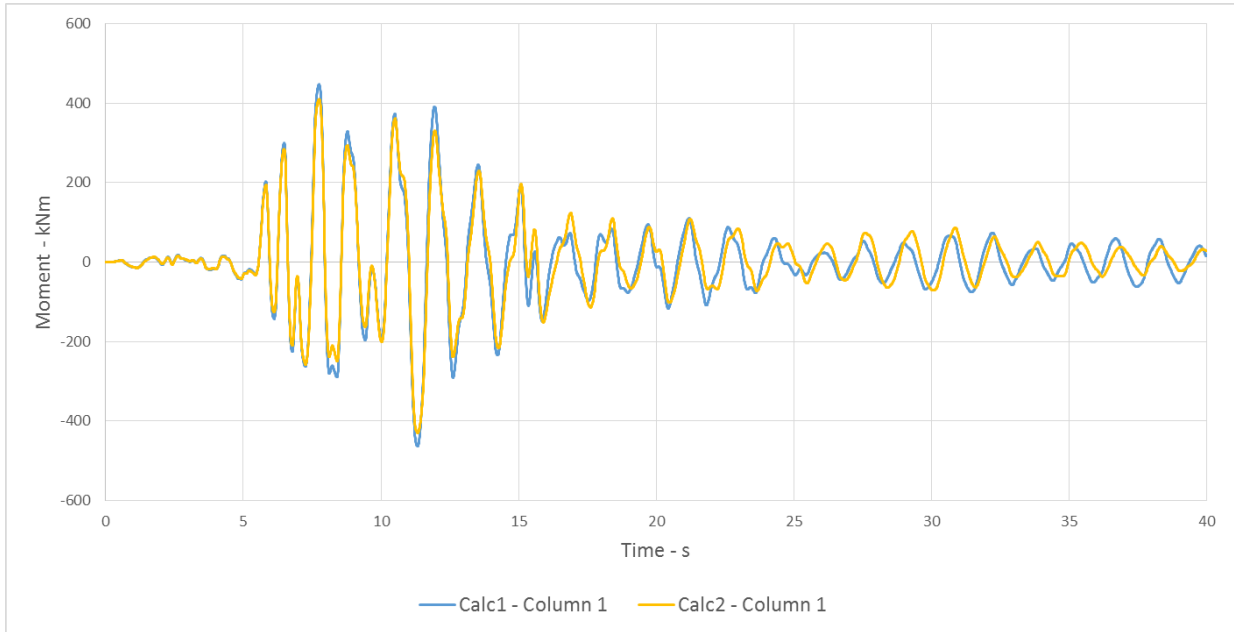


Figure 13 - Bending Moments in Bottom of Column 1 - From Calc1, 2

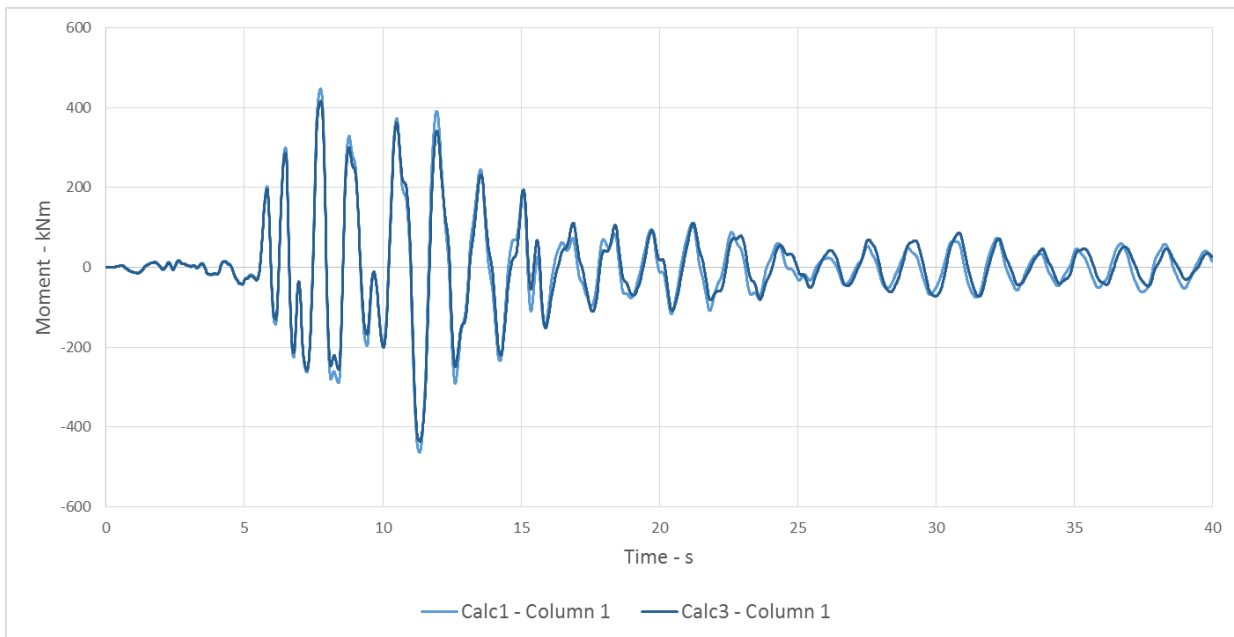


Figure 14 - Bending Moments in Bottom of Column 1 - From Calc1, 3

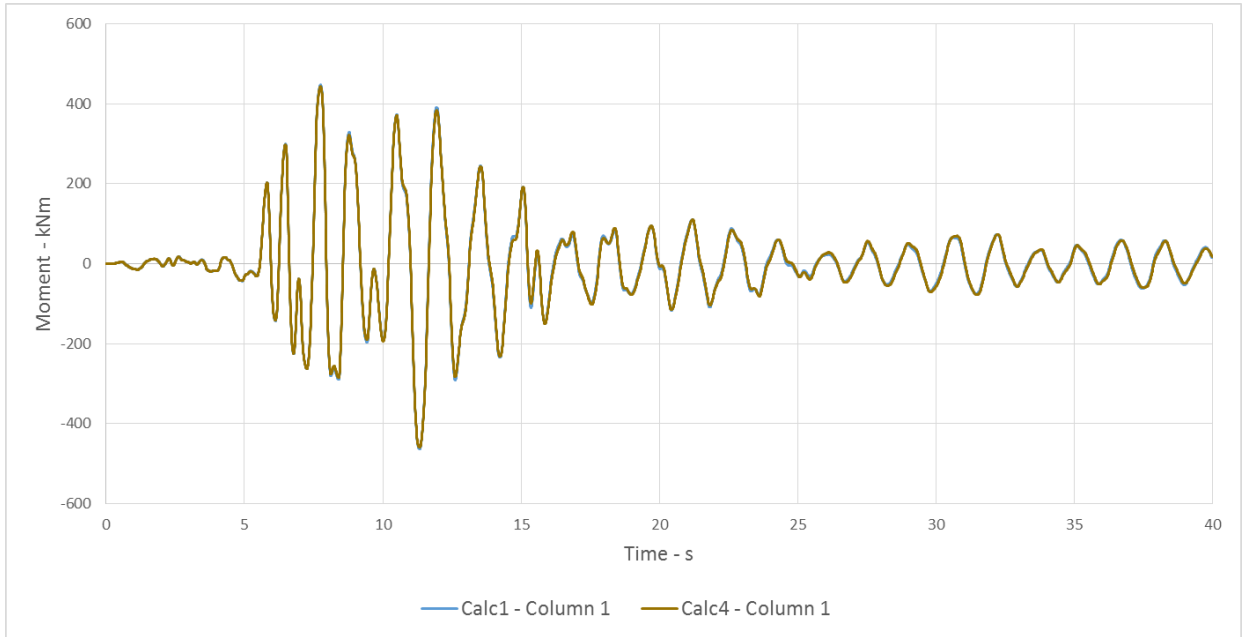


Figure 15 - Bending Moments in Bottom of Column 1 - From Calc1, 4

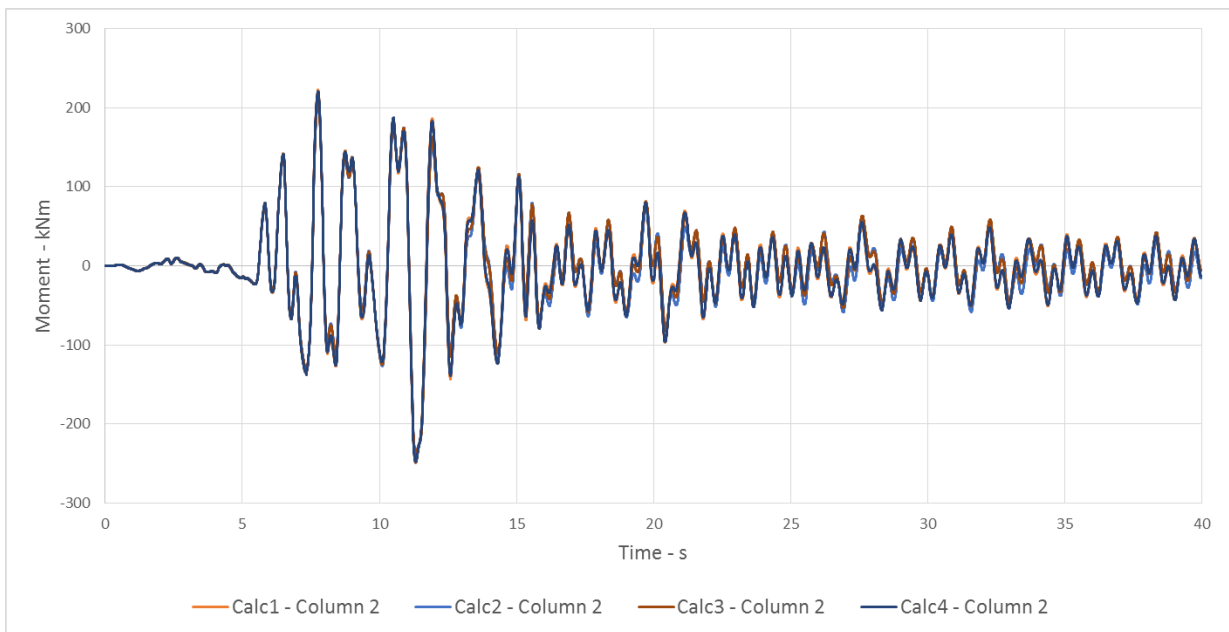


Figure 16 - Bending Moments in Bottom of Column 2 - From Calc1, 2, 3, 4

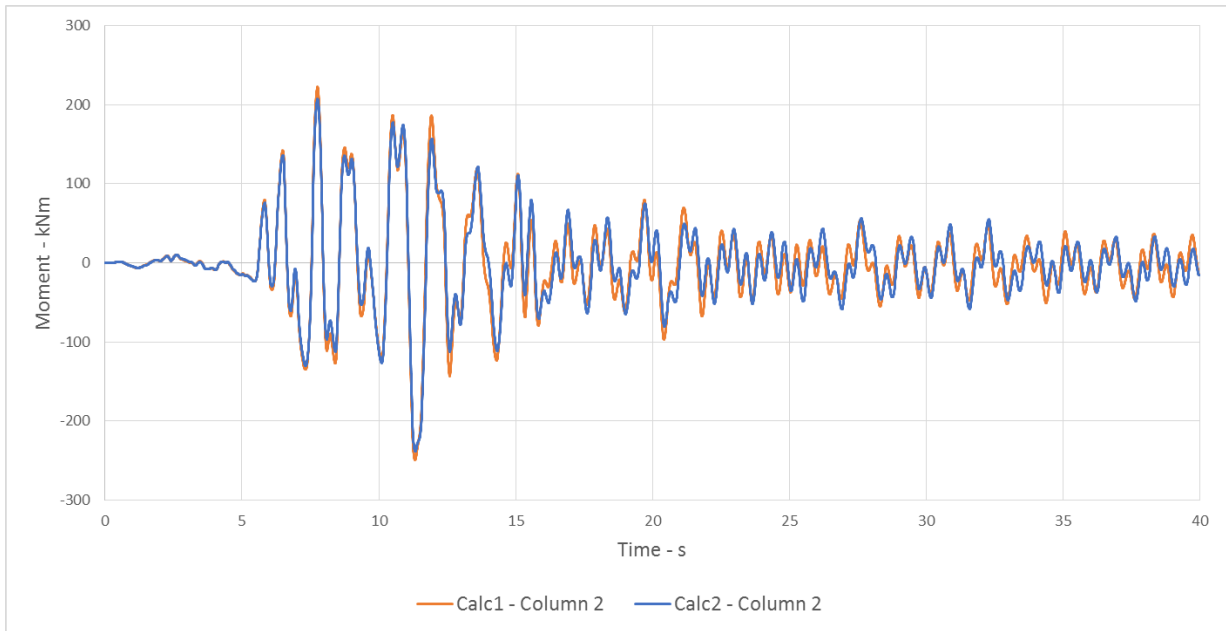


Figure 17 - Bending Moments in Bottom of Column 2 - From Calc1, 2

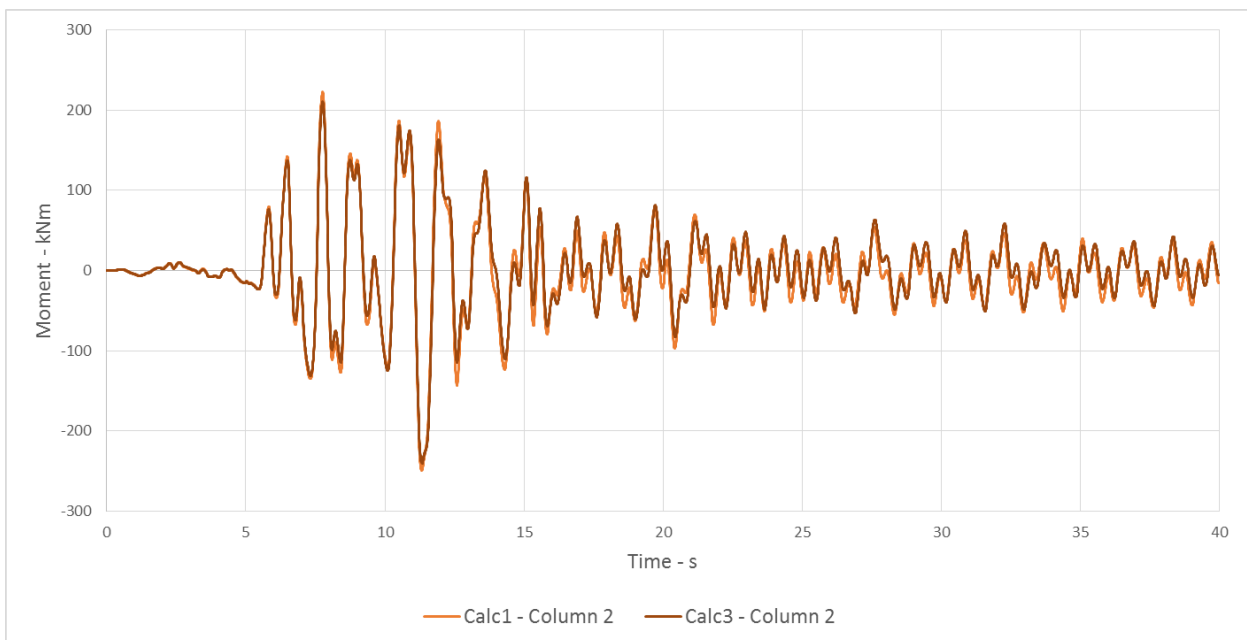


Figure 18 - Bending Moments in Bottom of Column 2 - From Calc1, 3

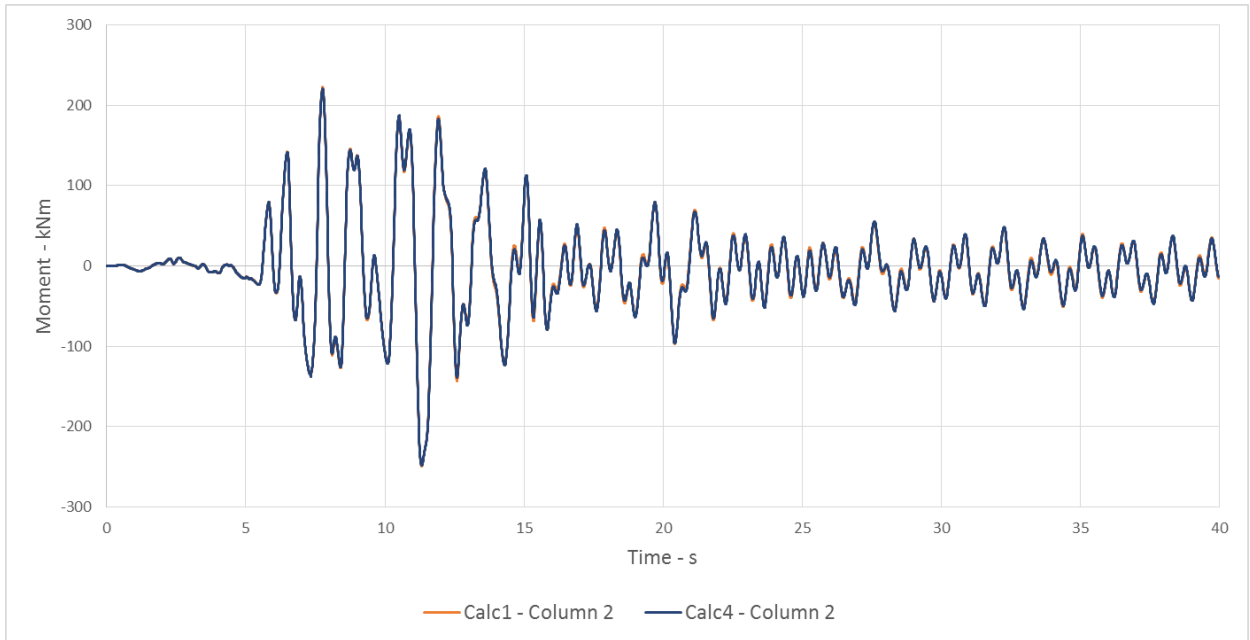


Figure 19 - Bending Moments in Bottom of Column 2 - From Calc1, 4

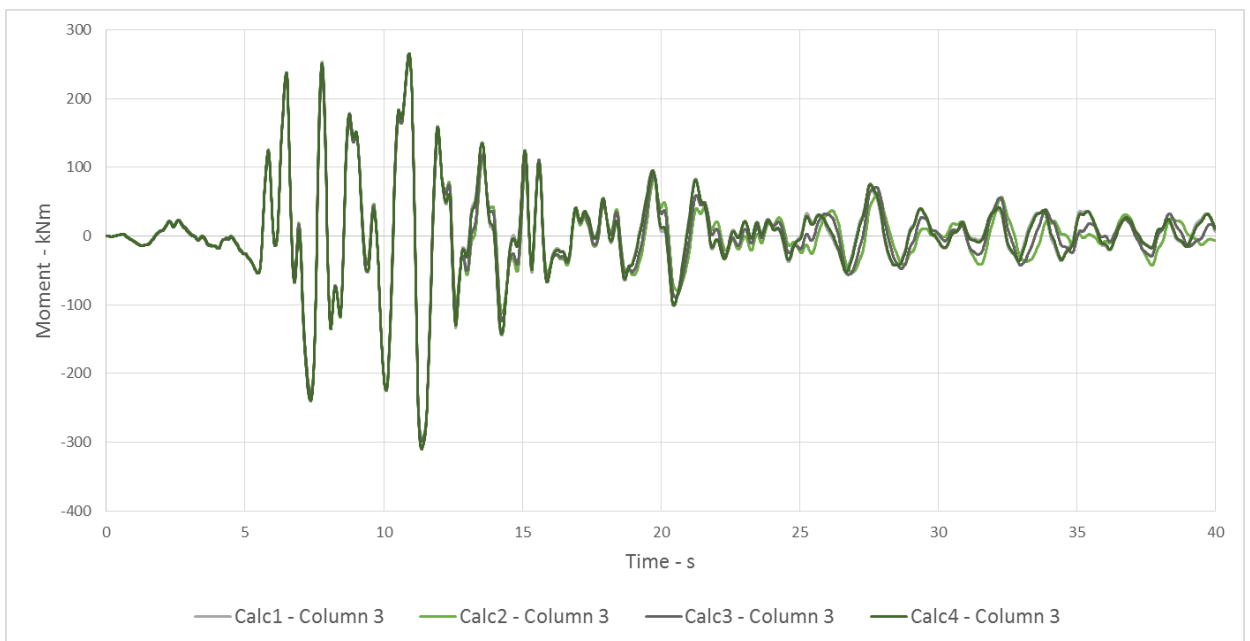


Figure 20 - Bending Moments in Bottom of Column 3 - From Calc1, 2, 3, 4

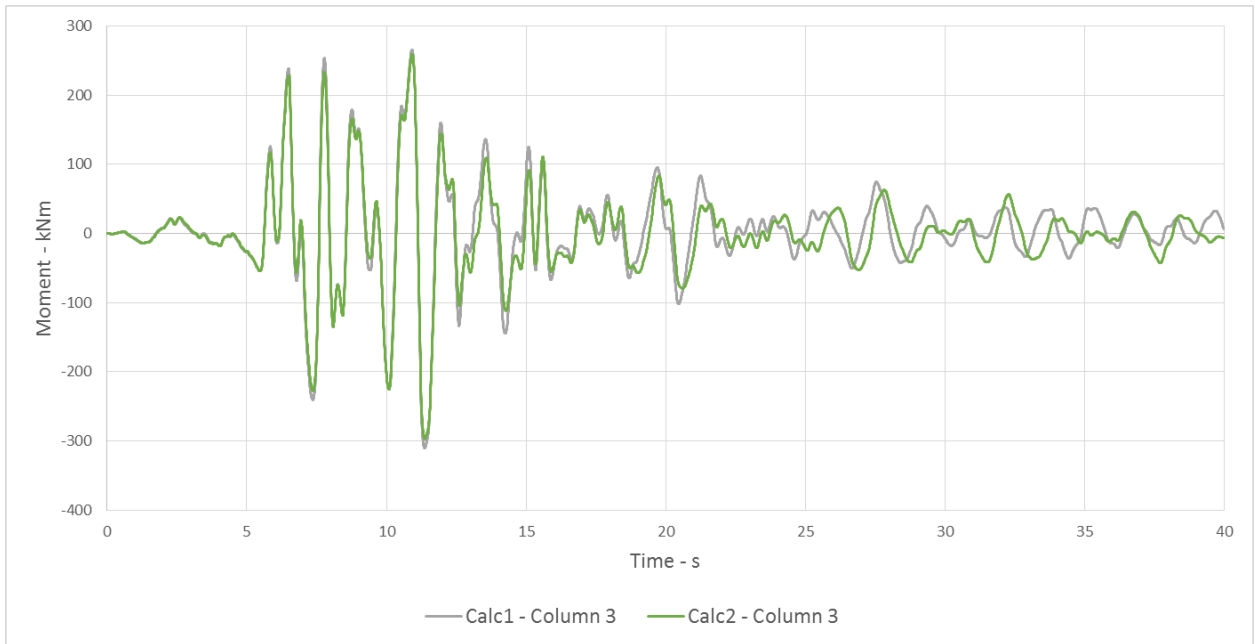


Figure 21 - Bending Moments in Bottom of Column 3 - From Calc1, 2

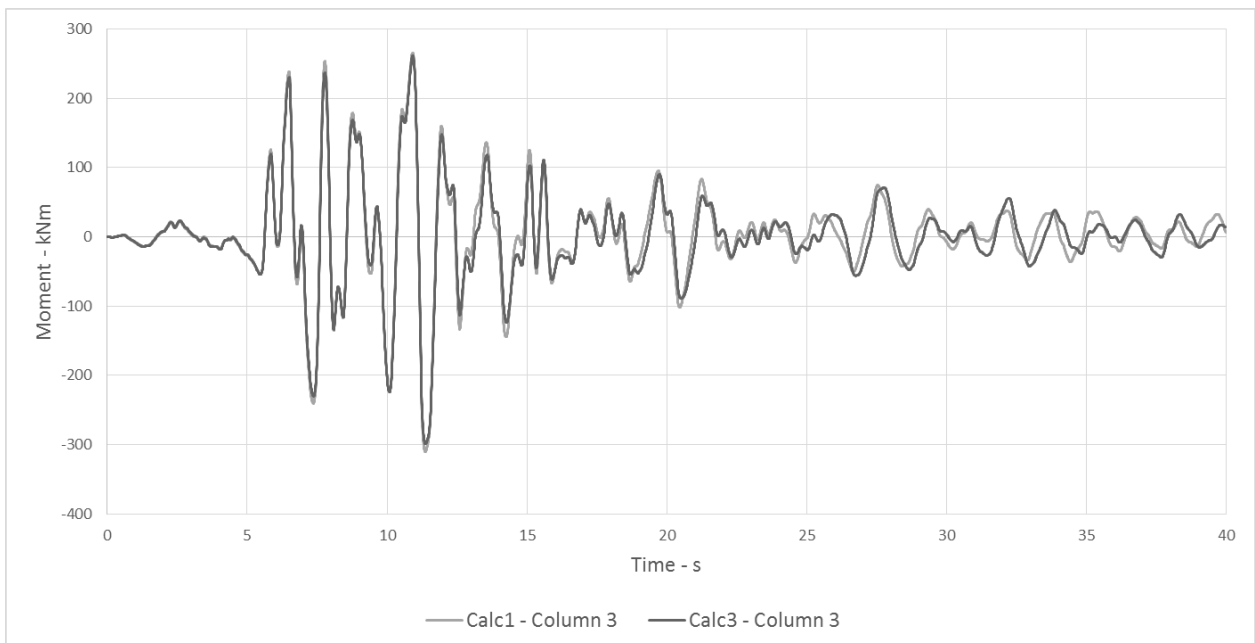


Figure 22 - Bending Moments in Bottom of Column 3 - From Calc1, 3

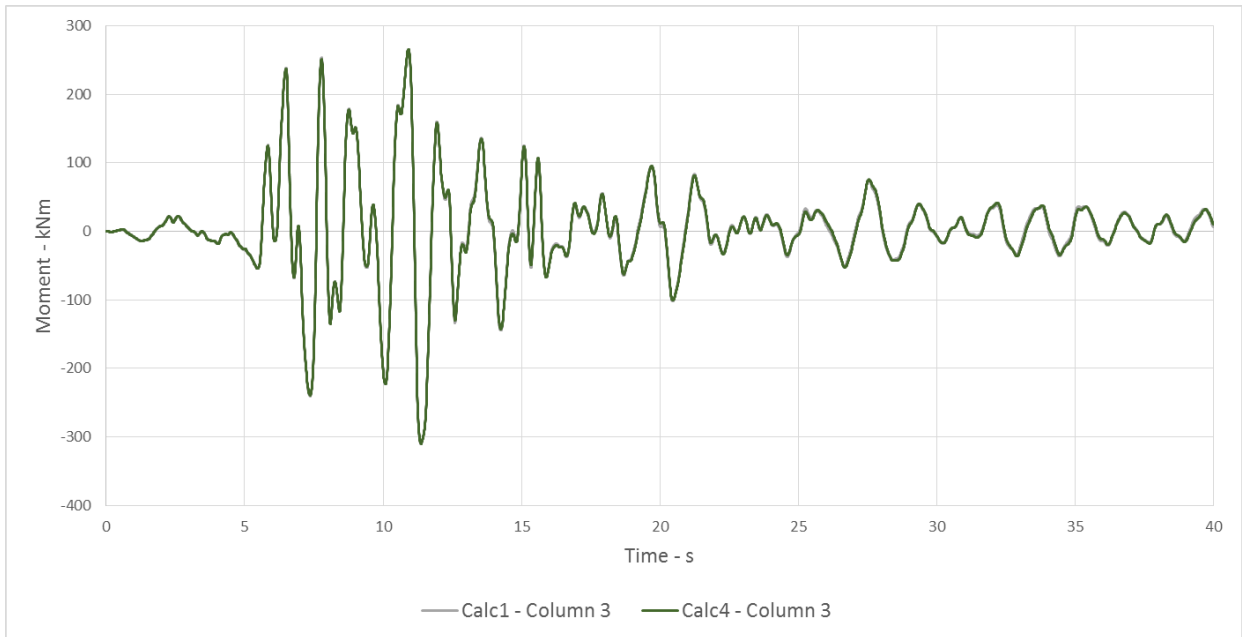


Figure 23 - Bending Moments in Bottom of Column 3 - From Calc1, 4

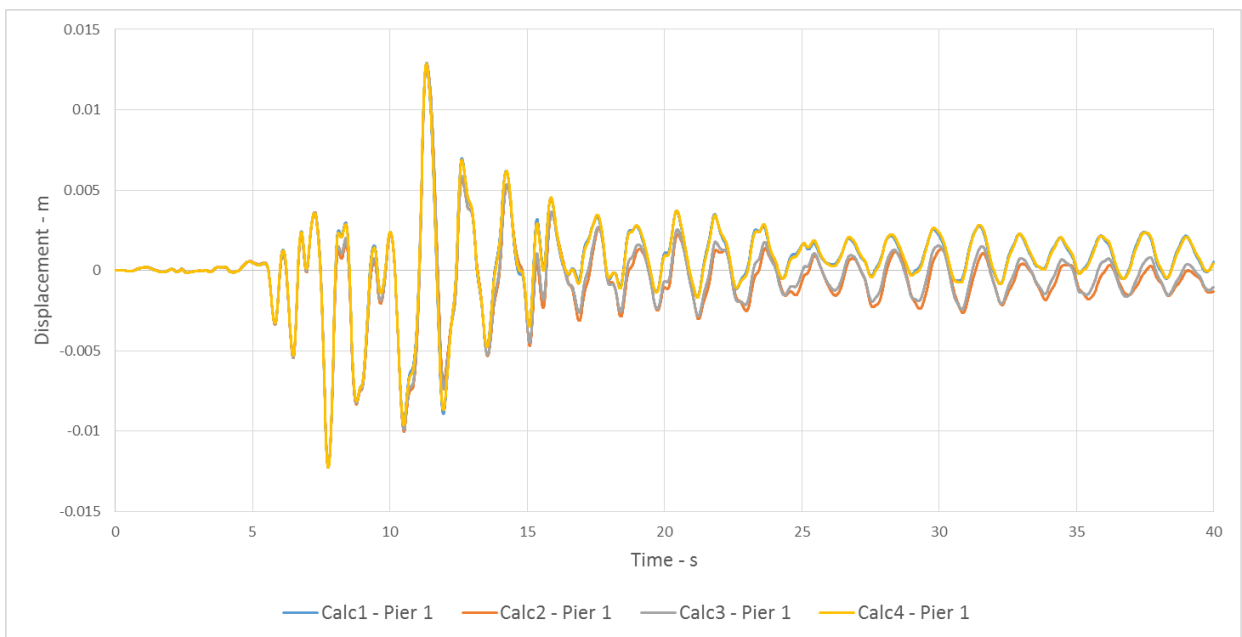


Figure 24 - Relative displacement of Pier 1 from Calc 1, 2, 3, 4

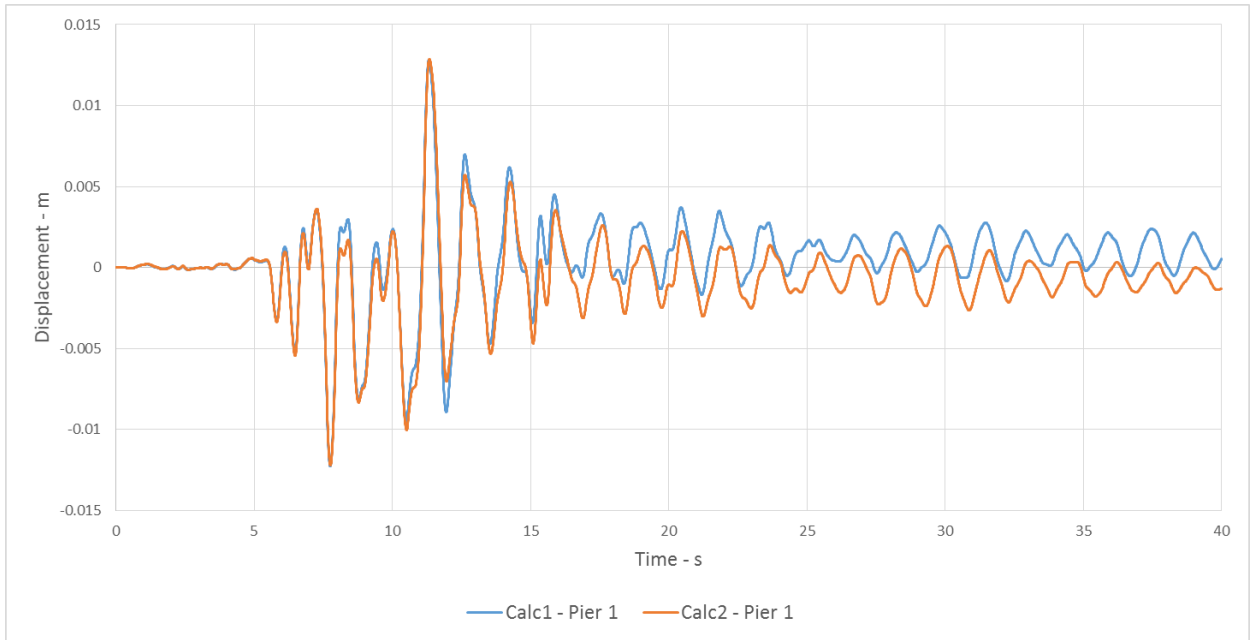


Figure 25 - Relative displacement of Pier 1 from Calc 1 and 2

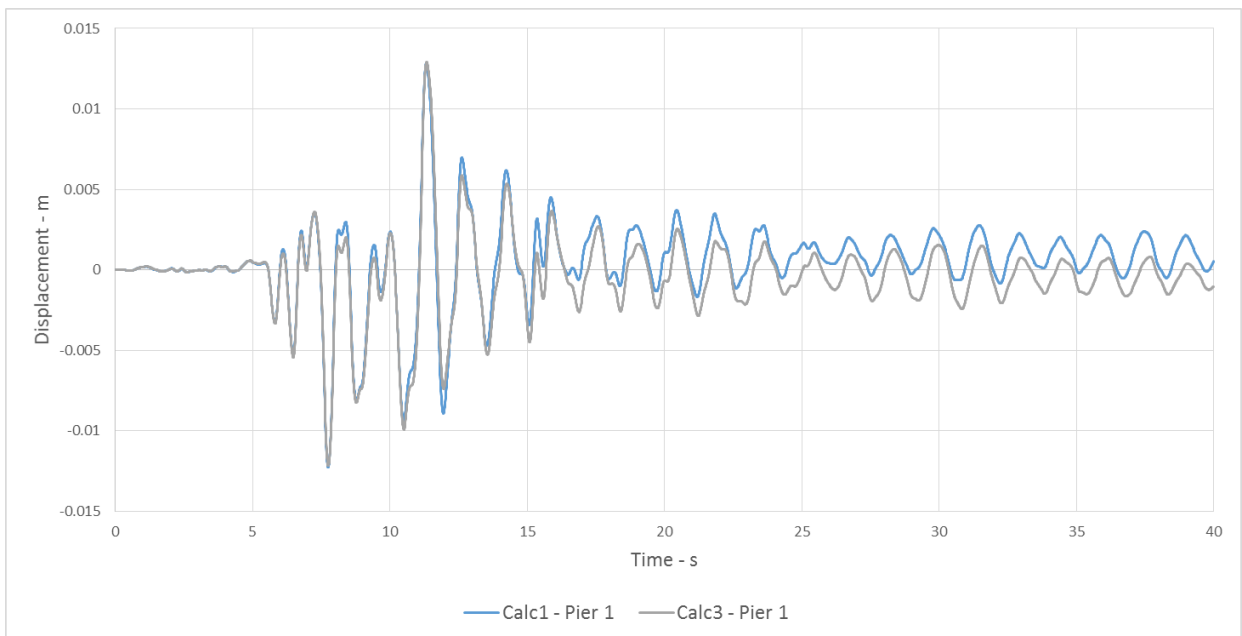


Figure 26 - Relative displacement of Pier 1 from Calc 1 and 3

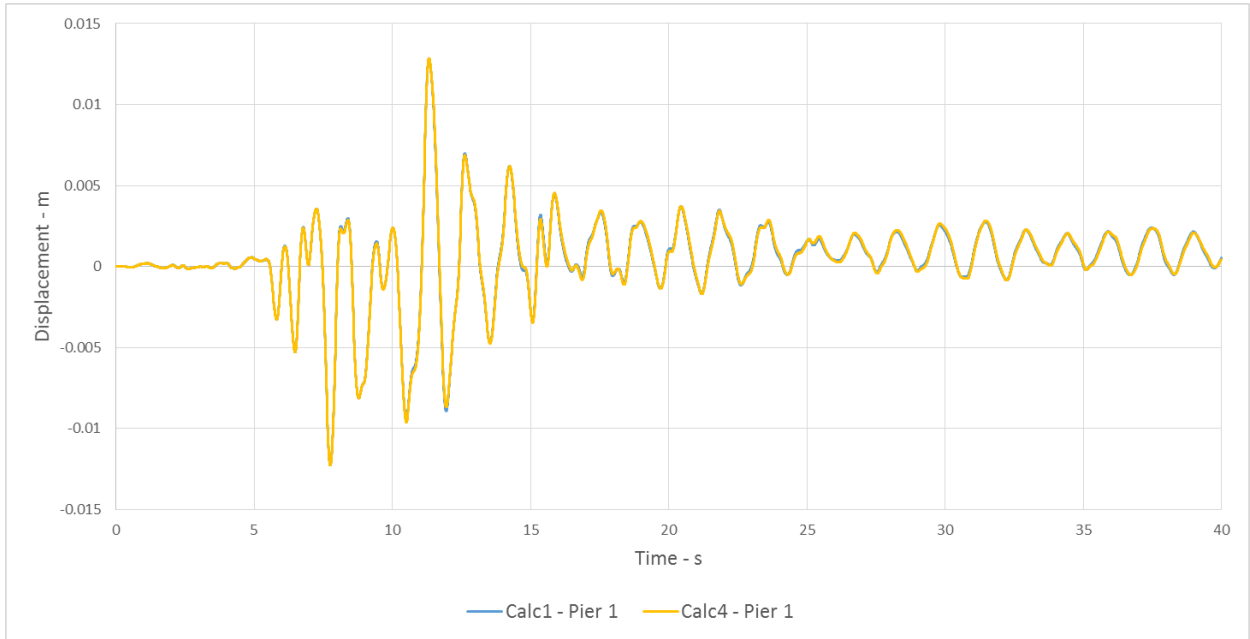


Figure 27 - Relative displacement of Pier 1 from Calc 1 and 4

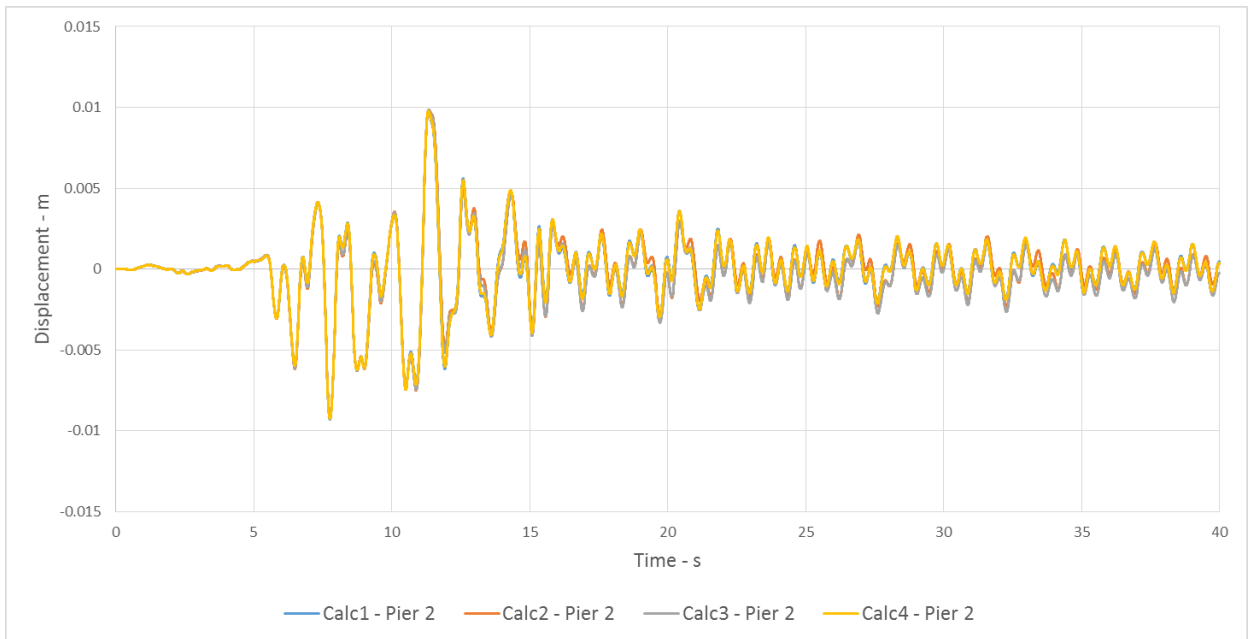


Figure 28 - Relative displacement of Pier 2 from Calc 1, 2, 3, 4

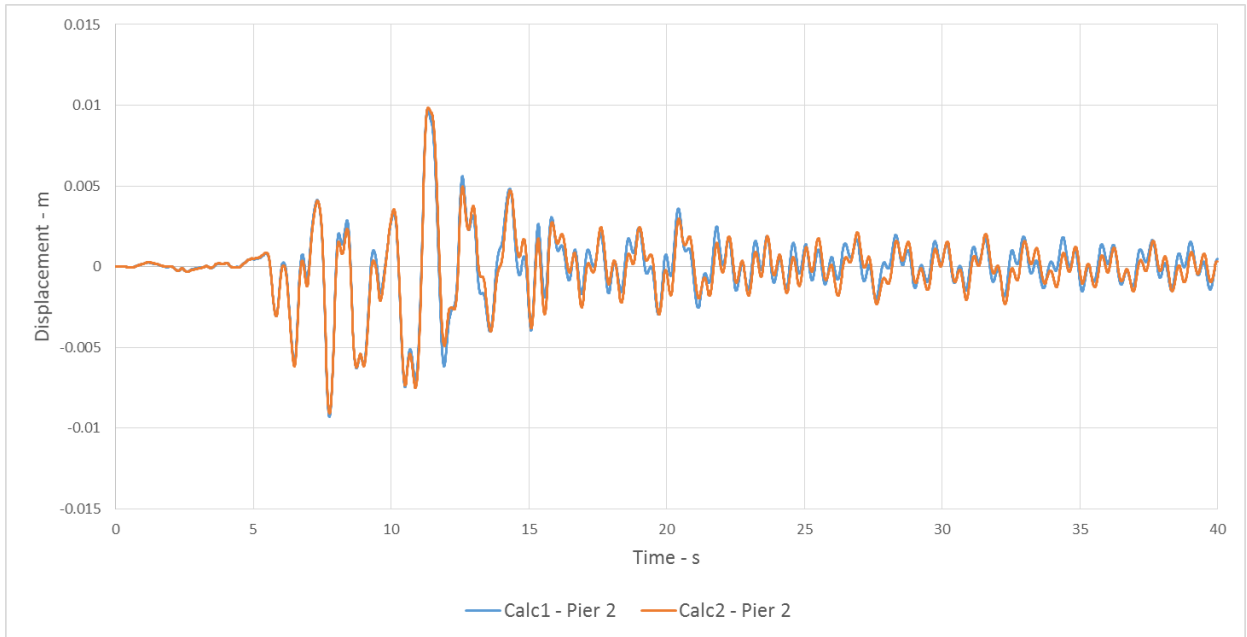


Figure 29 - Relative displacement of Pier 2 from Calc 1 and 2

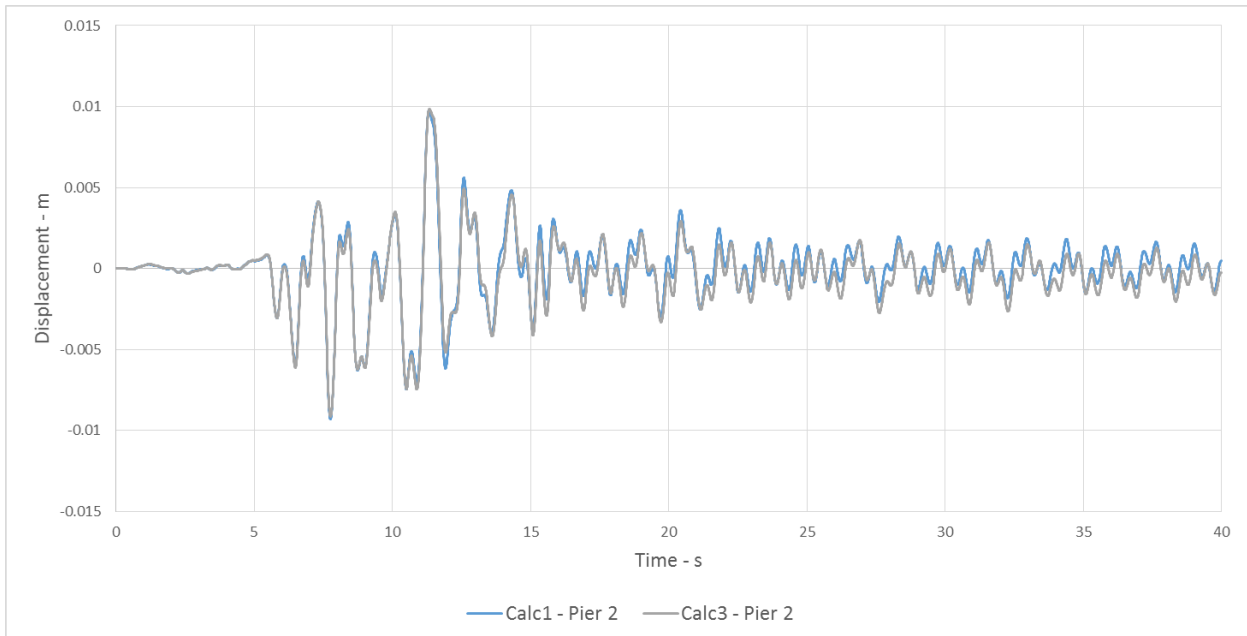


Figure 30 - Relative displacement of Pier 2 from Calc 1 and 3

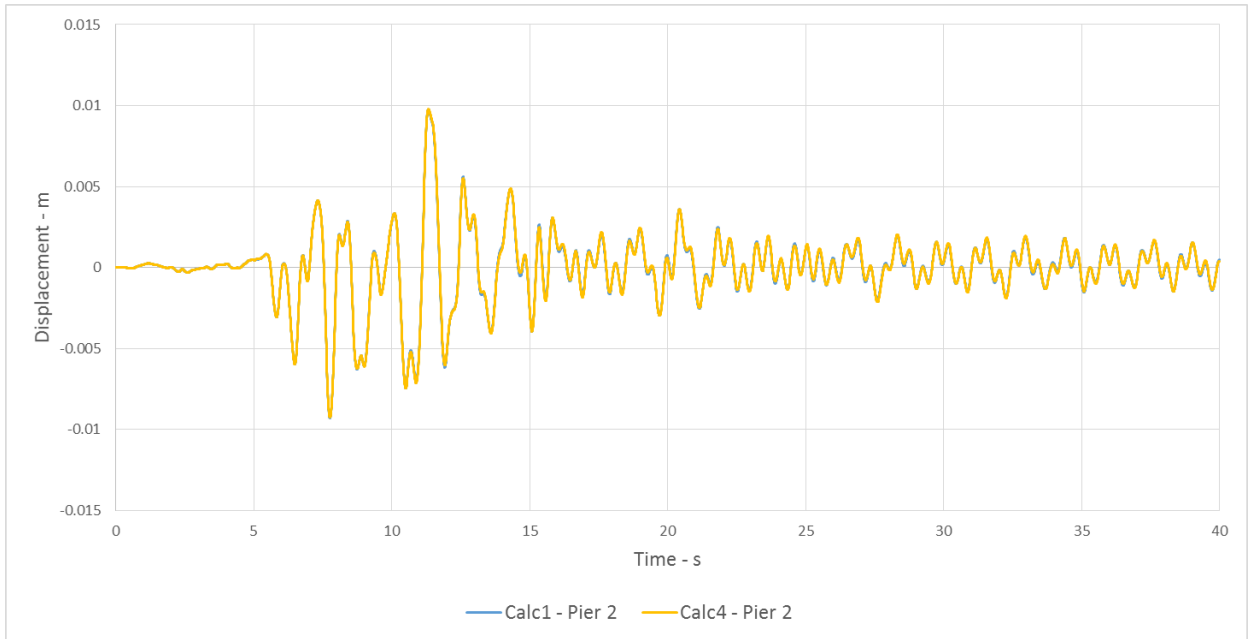


Figure 31 - Relative displacement of Pier 2 from Calc 1 and 4

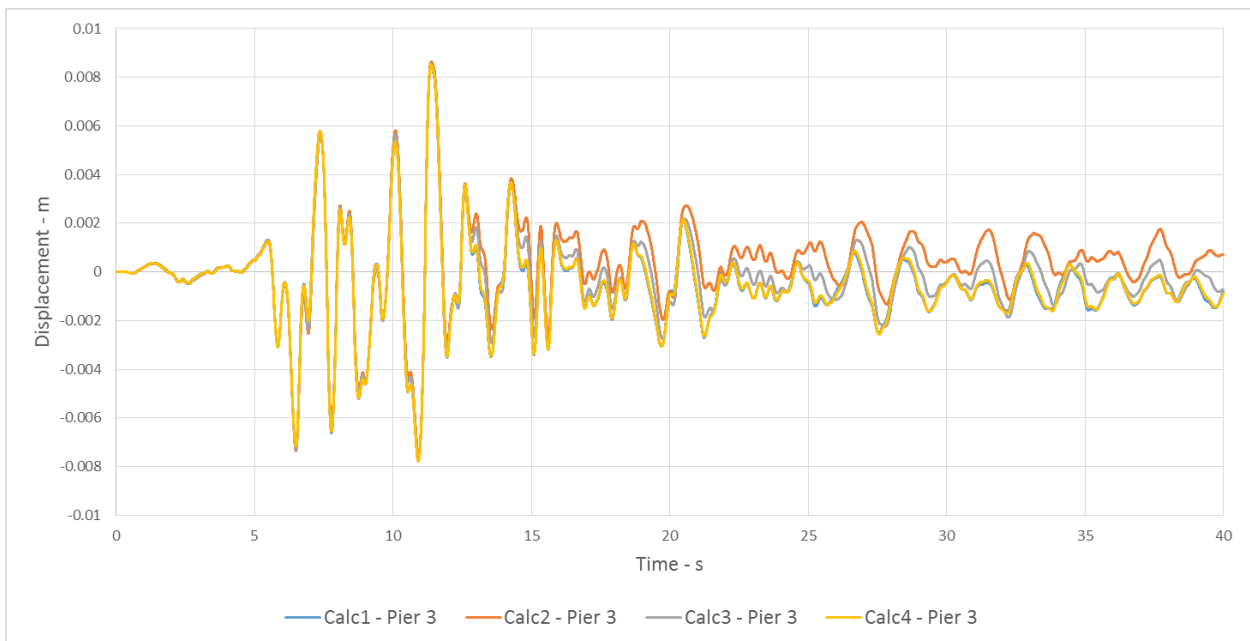


Figure 32 - Relative displacement of Pier 3 from Calc 1,2,3,4

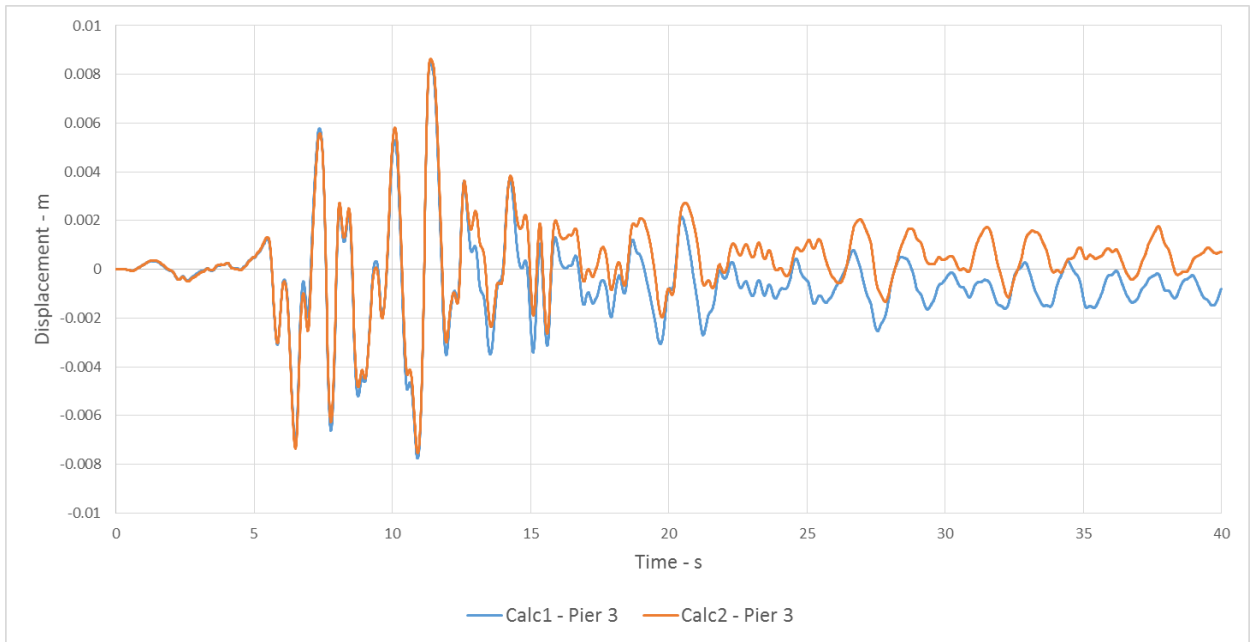


Figure 33 - Relative displacement of Pier 3 from Calc 1 and 2

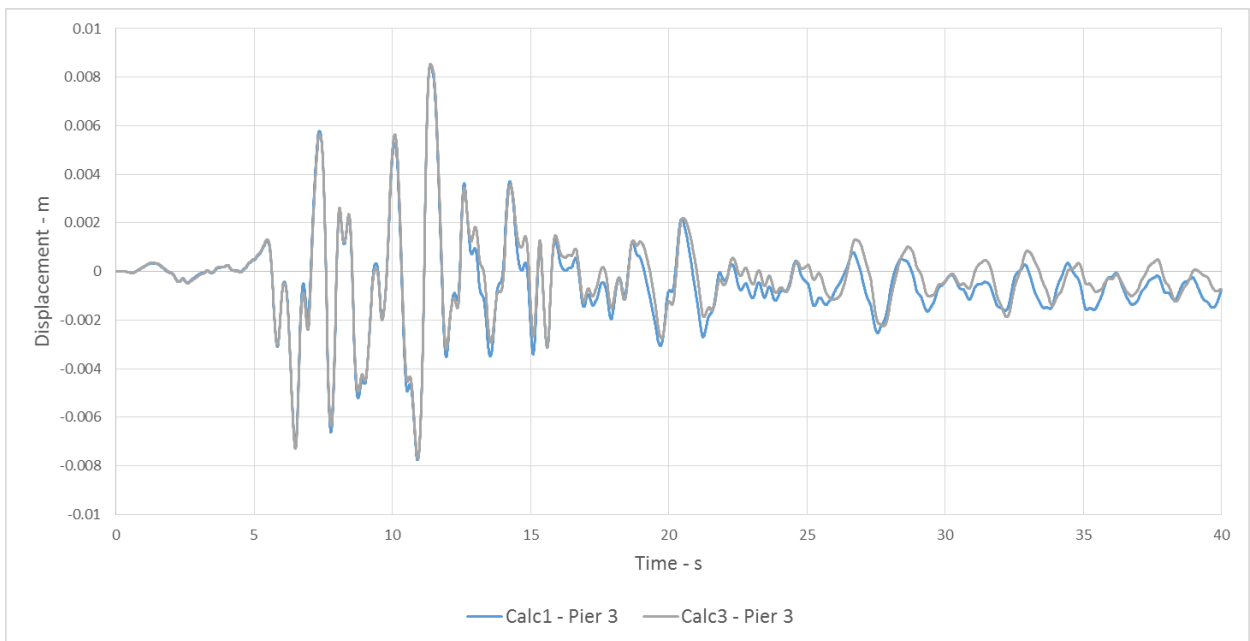


Figure 34 - Relative displacement of Pier 3 from Calc 1 and 3

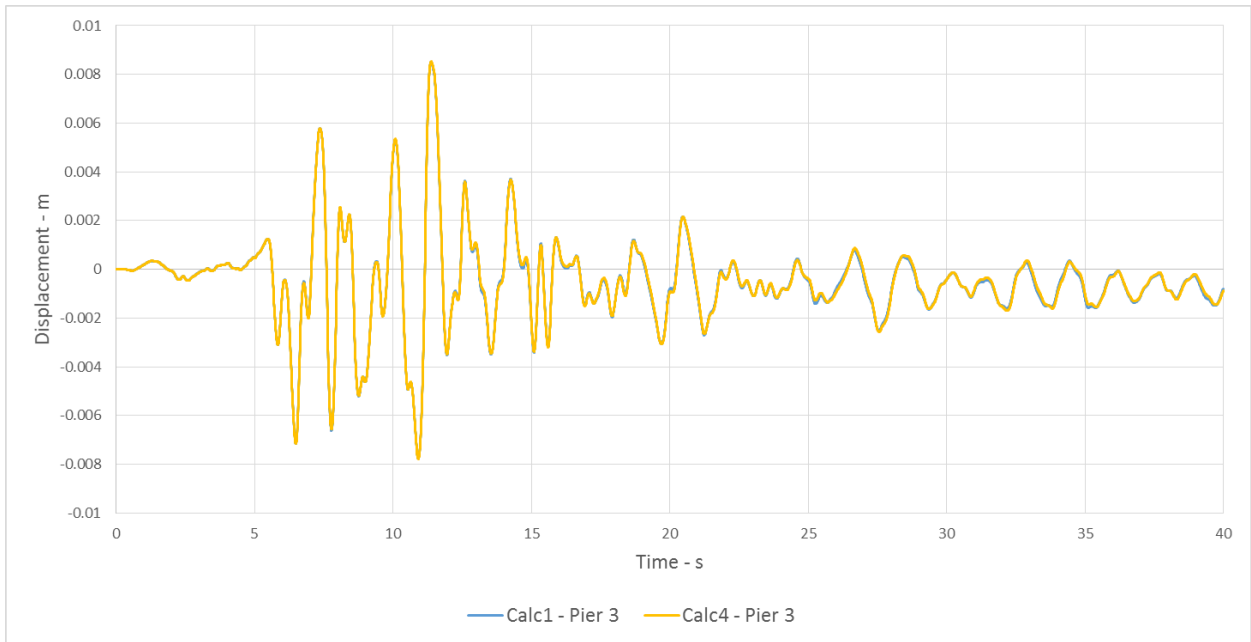


Figure 35 - Relative displacement of Pier 3 from Calc 1 and 4

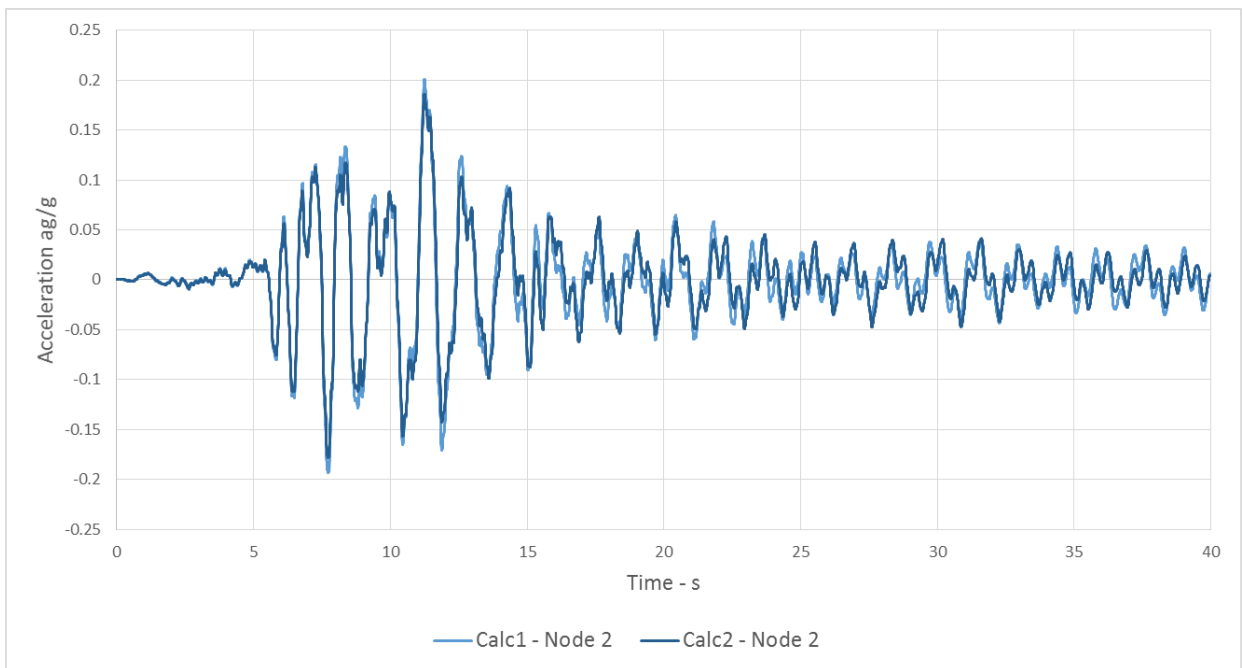


Figure 36 - Acceleration of node 2 (top of column 1) from Calculation 1 and 2

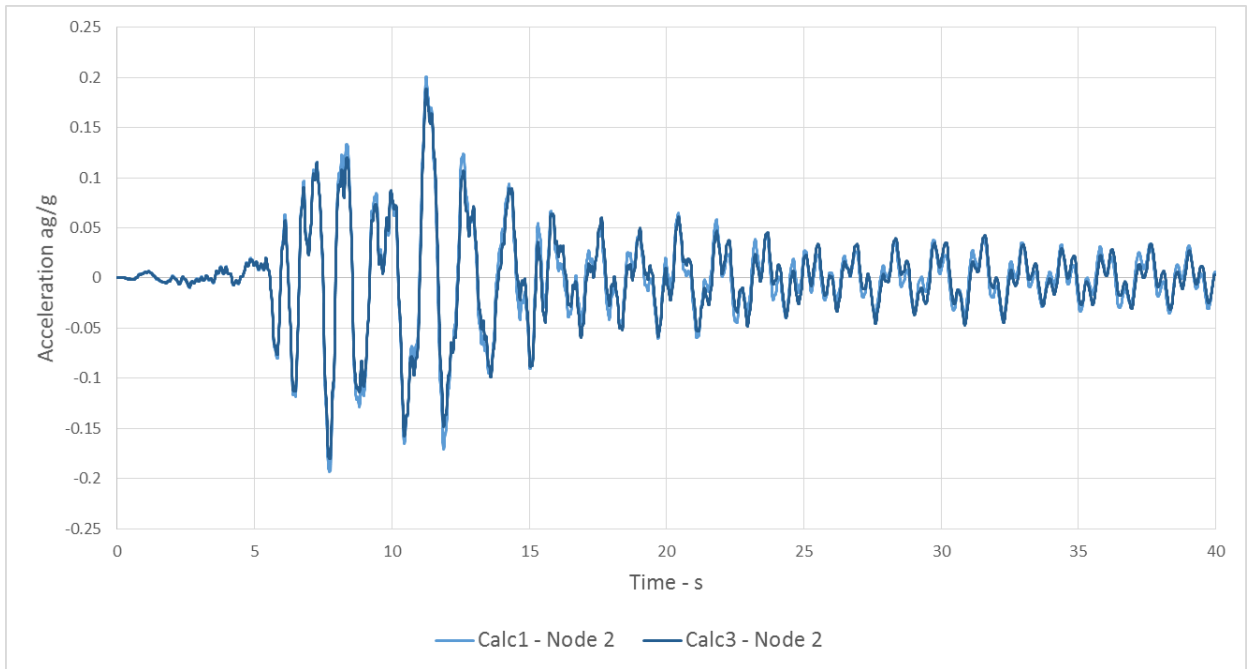


Figure 37 - Acceleration of node 2 (top of column 1) from Calculation 1 and 3

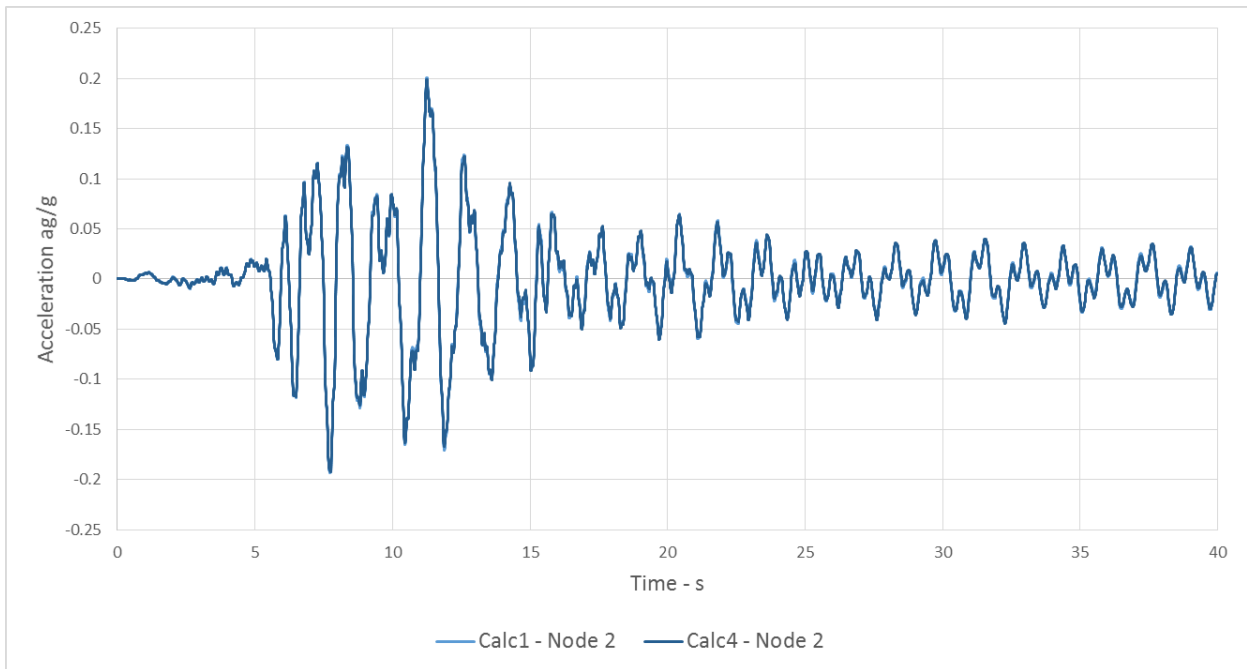


Figure 38 - Acceleration of node 2 (top of column 1) from Calculation 1 and 4

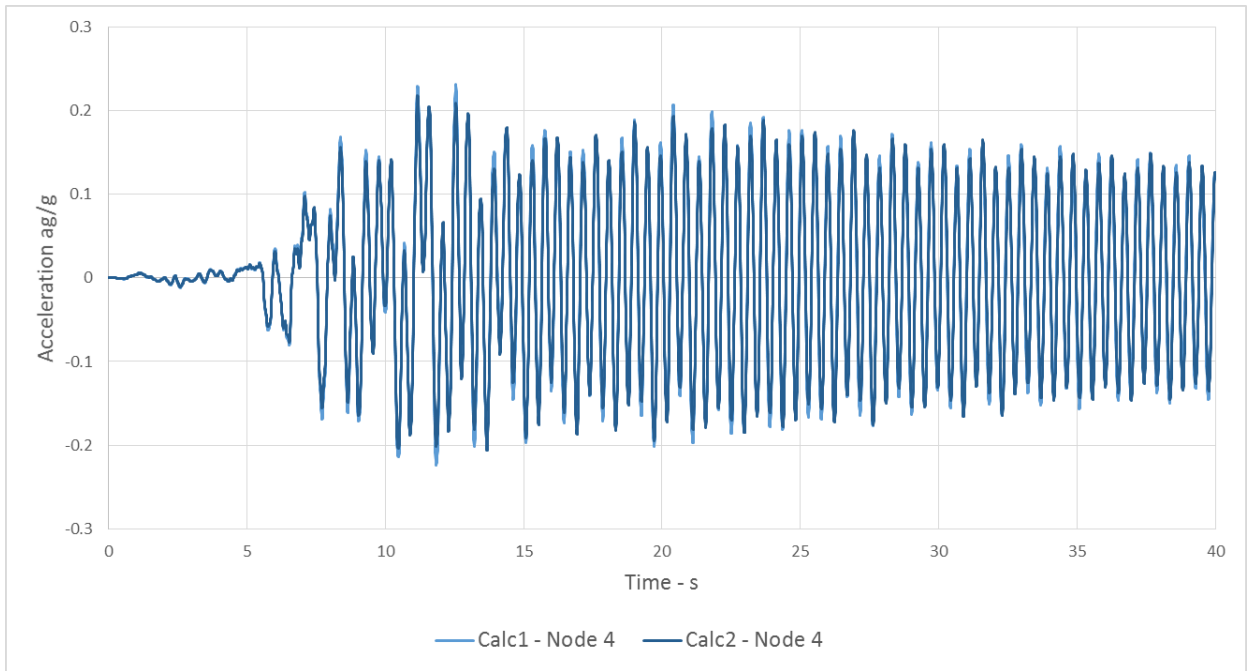


Figure 39 - Acceleration of node 4 (top of column 2) from Calculation 1 and 2

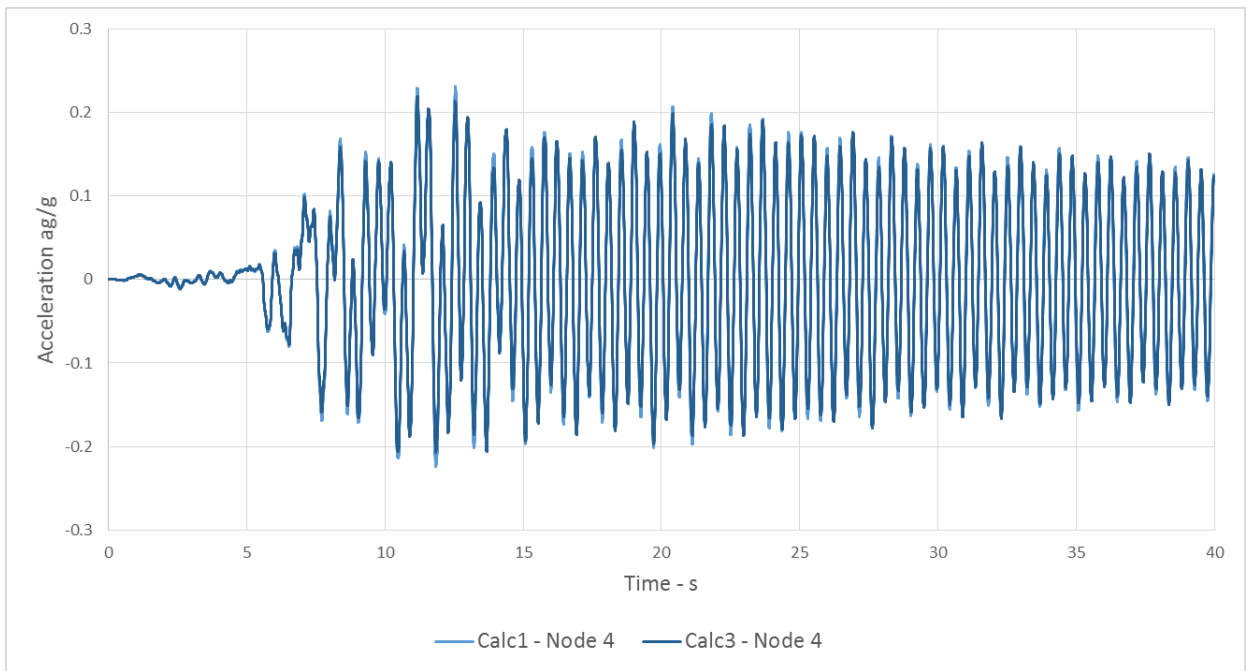


Figure 40 - Acceleration of node 4 (top of column 2) from Calculation 1 and 3

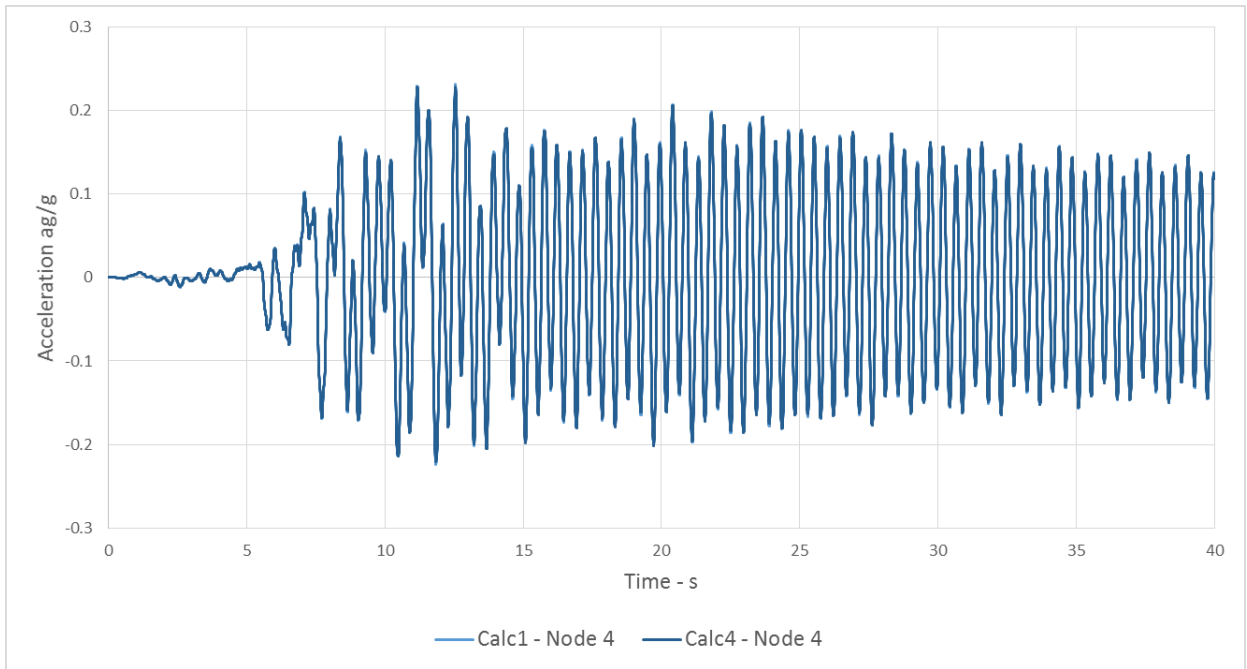


Figure 41 - Acceleration of node 4 (top of column 2) from Calculation 1 and 4

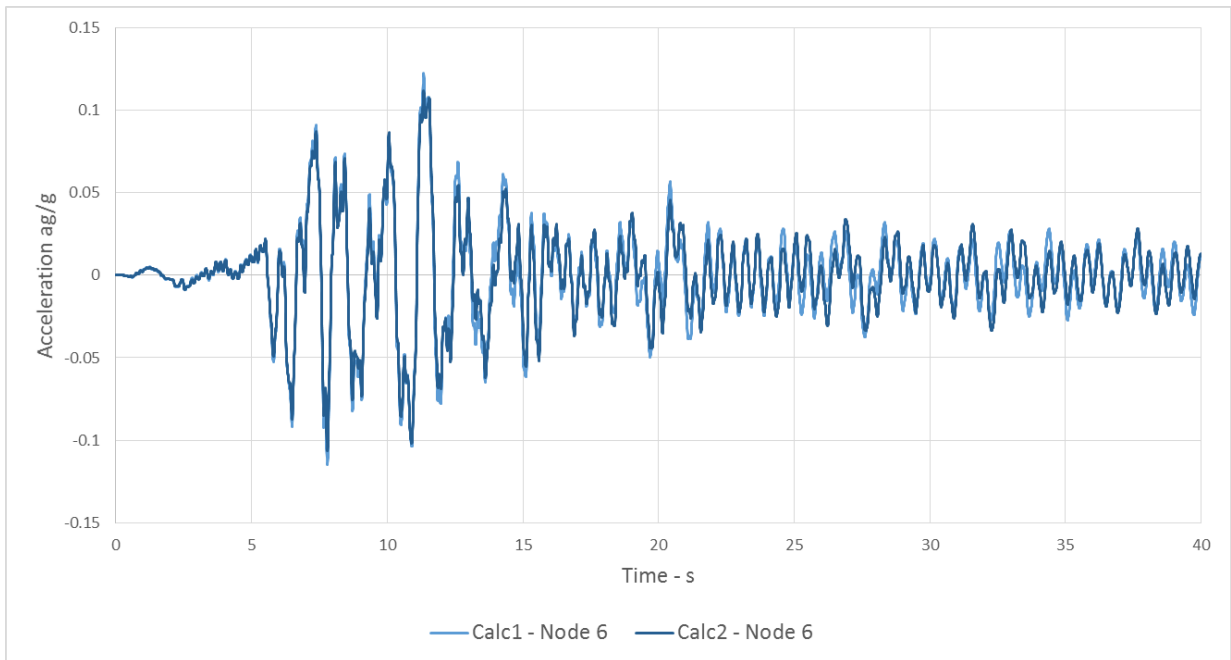


Figure 42 - Acceleration of node 6 (top of column 3) from Calculation 1 and 2

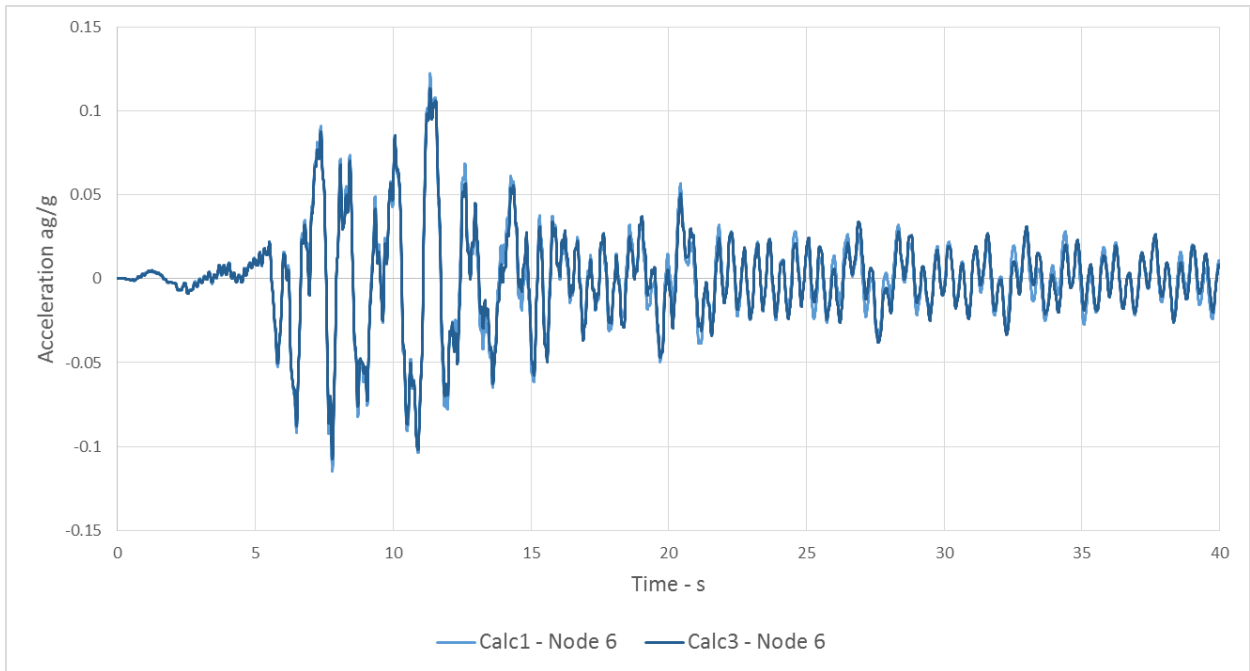


Figure 43 - Acceleration of node 6 (top of column 3) from Calculation 1 and 3

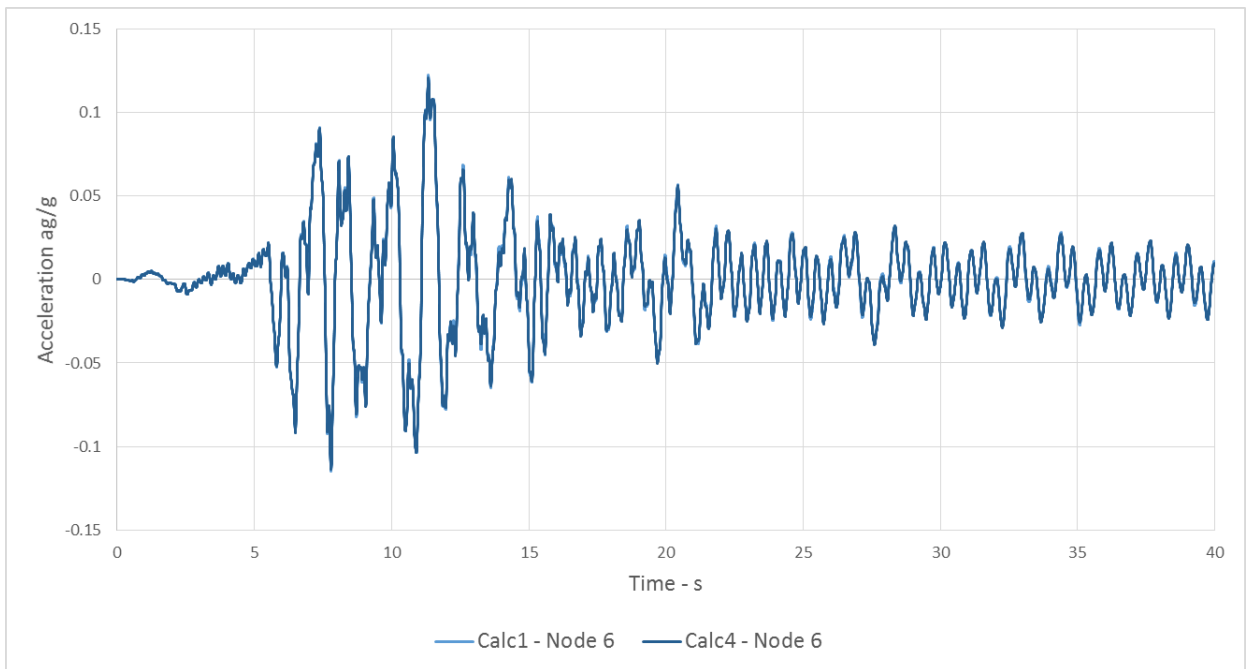


Figure 44 - Acceleration of node 6 (top of column 3) from Calculation 1 and 4

6.5 Computed Results of Nonlinear Bridge Response For Selected Four Calculation Cases Under Real El-Centro Earthquake Scaled to PGA=0.45 g

The second part of the conducted analytical study included computation of the nonlinear bridge response for the next four calculation cases (Calc 5, Calc 6, Calc 7 and Calc 8, Models M1, M2, M3 and M4), but in this case, under the real El-Centro earthquake scaled to PGA = 0.45g, Fig. 130.

The first set of four figures, Fig. 131 through Fig. 134, comparatively shows the time history responses for bending moments of all 3 columns obtained from four analytical models, namely, M1, M2, M3 and M4, defined as Calc 5, Calc 6, Calc 7 and Calc 8.

Presented in the second set of four figures, Fig. 135 through Fig. 138, are the computed comparative results for column – 1 obtained for the analyzed four different analytical models.

The third set of four figures, Fig. 139 through Fig. 142, displays the computed comparative results for column – 2 obtained for the analyzed four different analytical models.

Shown in the fourth set of four figures, Fig. 143 through Fig. 146, are the computed comparative results for column – 3 obtained for the analyzed four different analytical models.

The subsequent series of 12 figures, Fig. 147 through Fig. 158, provides a comparative presentation of the computed time history responses of relative displacements of the top of all three bridge columns and for the analyzed all four analytical models.

Comparatively presented in the last series of 9 figures, Fig. 159 through Fig. 167, are the computed time history responses of absolute accelerations of the top of all three bridge columns for the analyzed all four analytical models.

By careful observation of all the computed and presented results, considering the different formulated analytical models M1, M2, M3 and M4, respective differences in earthquake responses have been found. It is clear that the earthquake response differences directly reflect the existing differences in the reinforcement levels of the middle piers.

It is evident that the advanced refined fiber based modeling concept is the most general approach to detailed modeling and advanced analysis of real bridge structures.

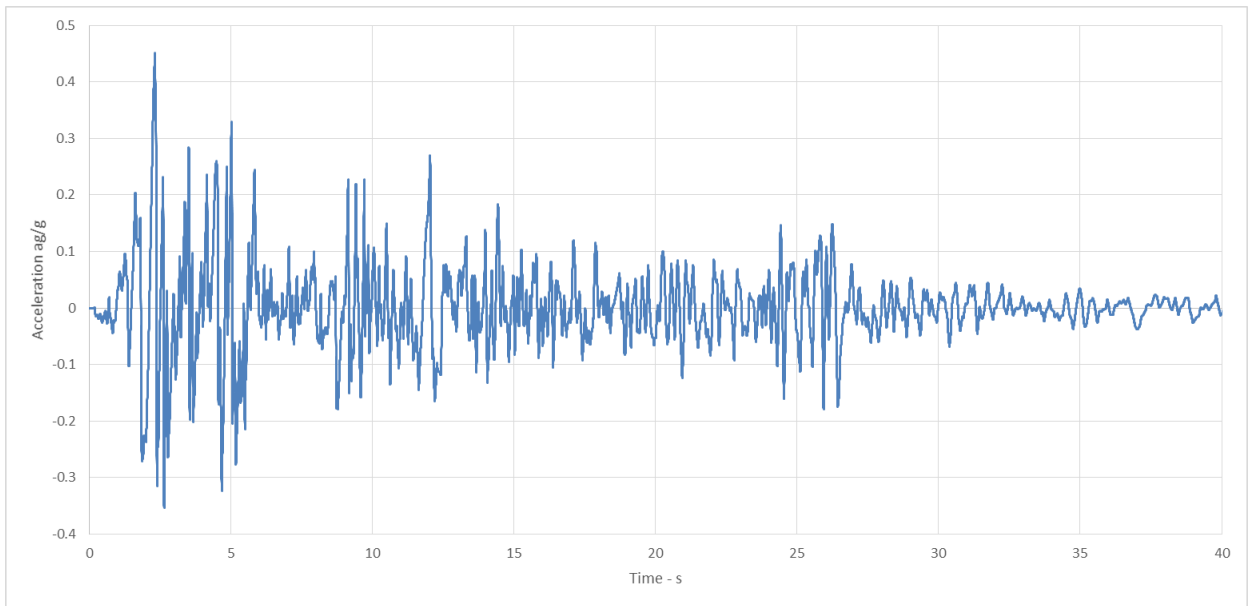


Figure 45 – Elcentro earthquake motion – Scaled to $a_g/g = 0.45$

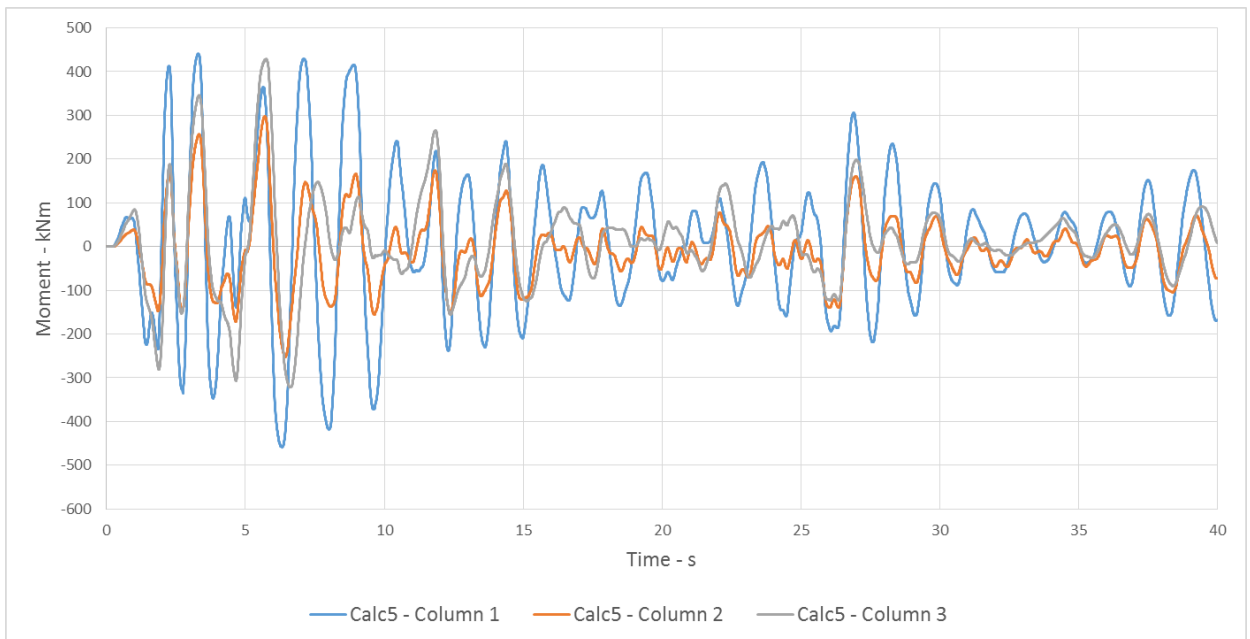


Figure 46 - Calculation 5 - Bending Moments in Bottom of Columns

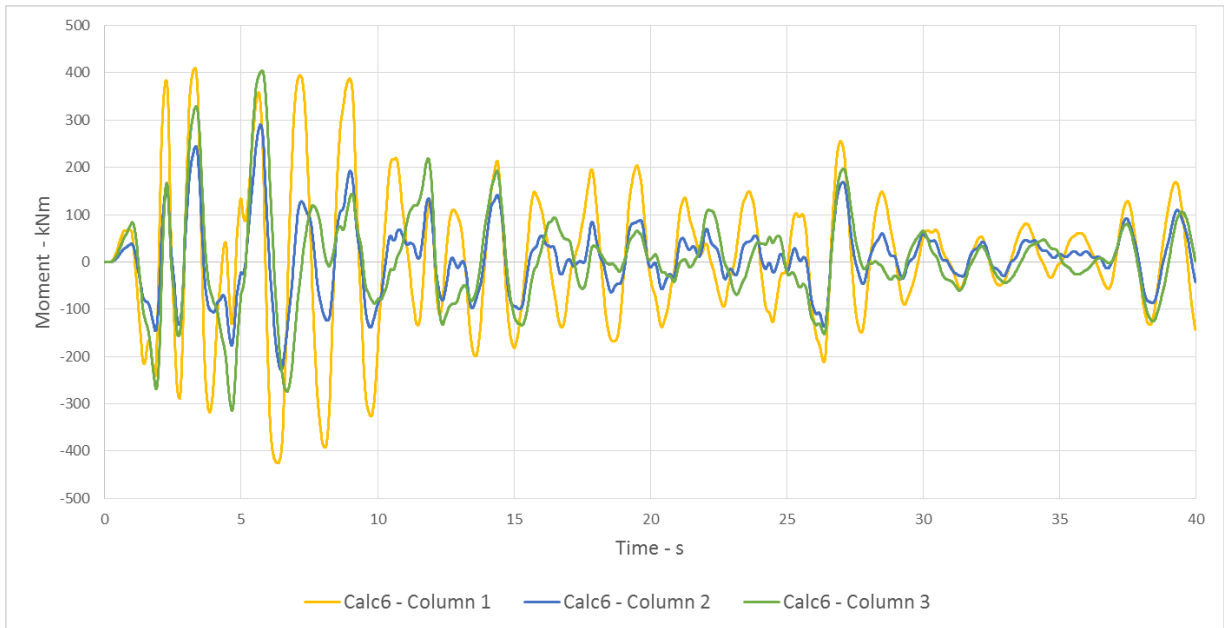


Figure 47 - Calculation 6 - Bending Moments in Bottom of Columns

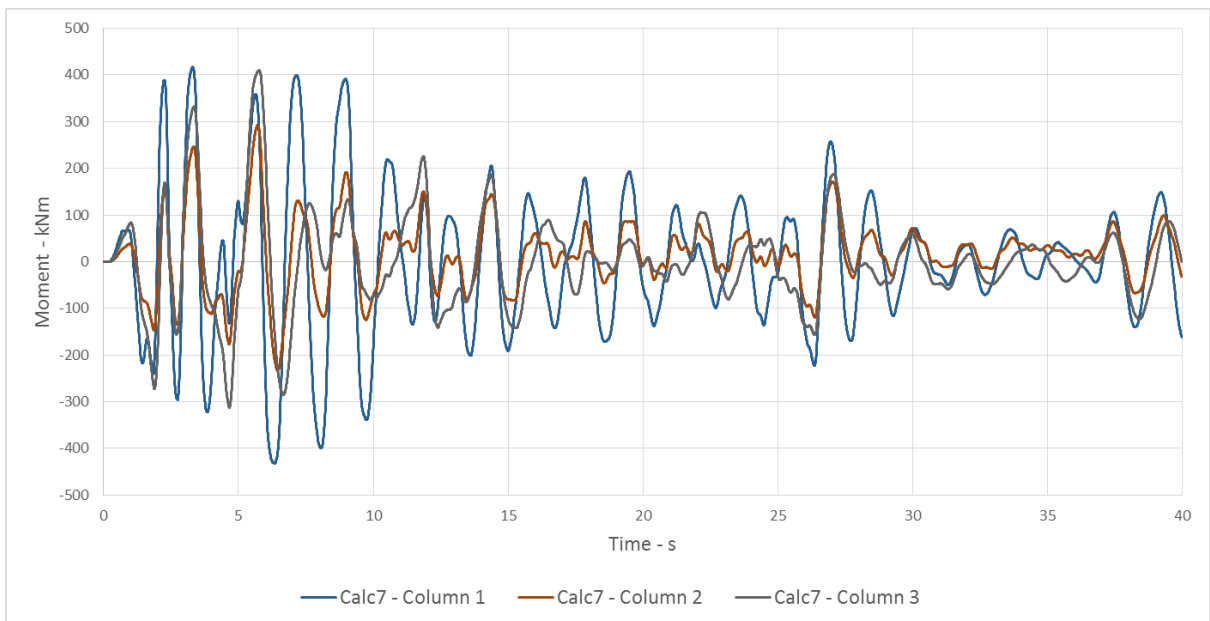


Figure 48 - Calculation 7 - Bending Moments in Bottom of Columns

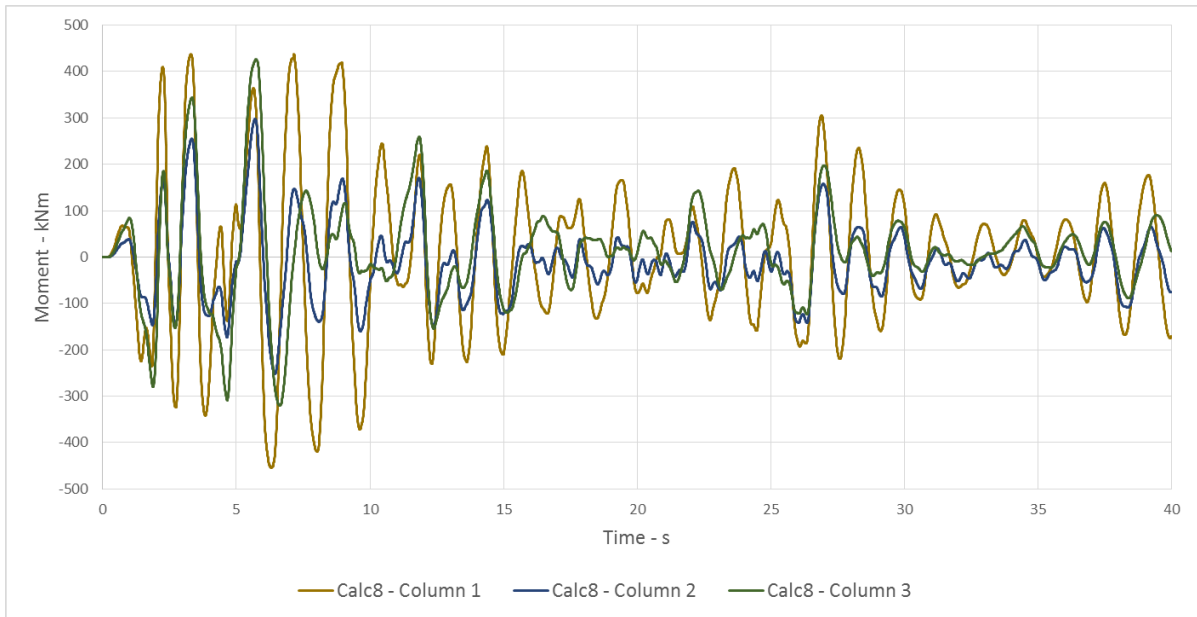


Figure 49 - Calculation 8 - Bending Moments in Bottom of Columns

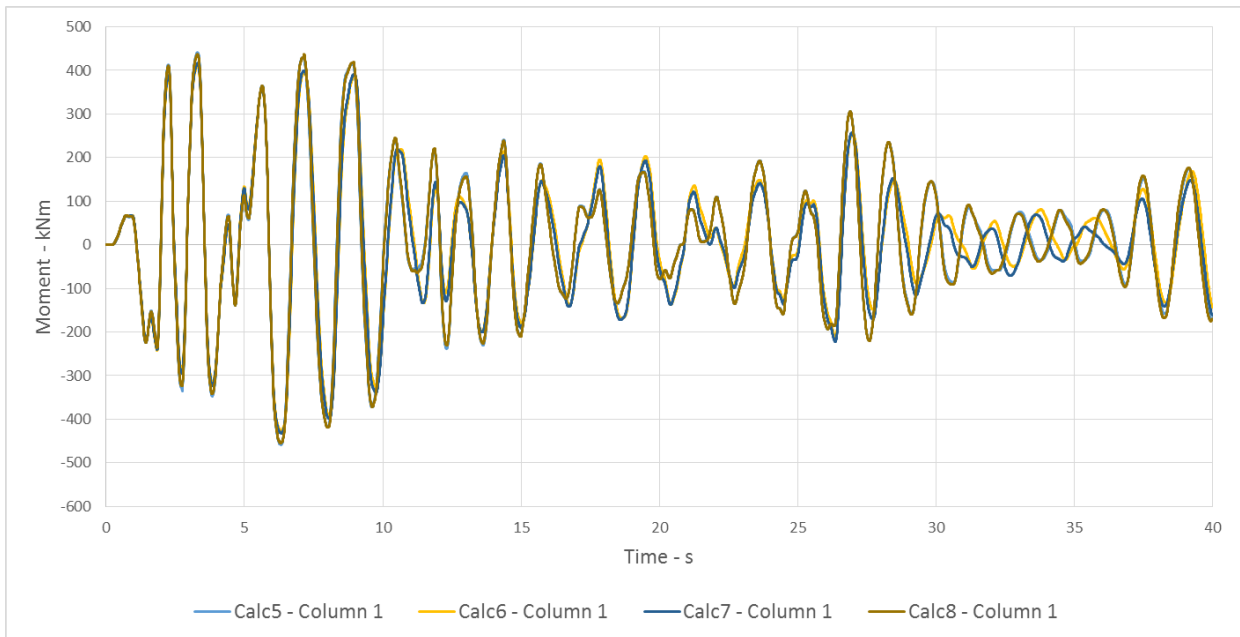


Figure 50 - Bending Moments in Bottom of Column 1 - From Calc5, 6, 7, 8

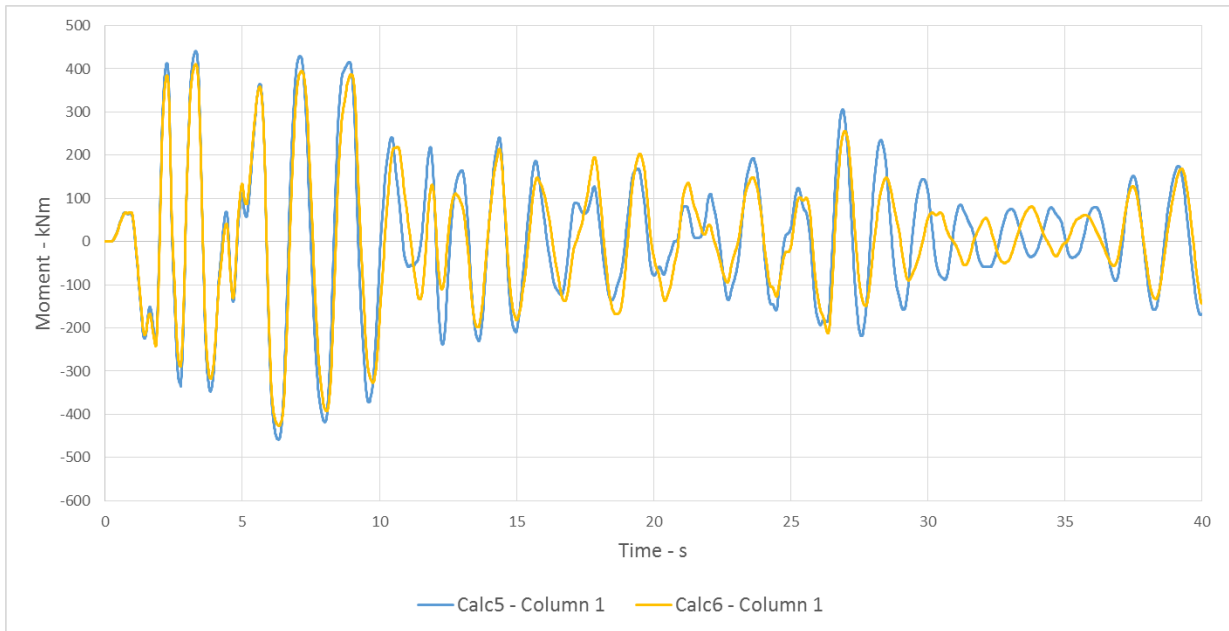


Figure 51 - Bending Moments in Bottom of Column 1 - From Calc5, 6

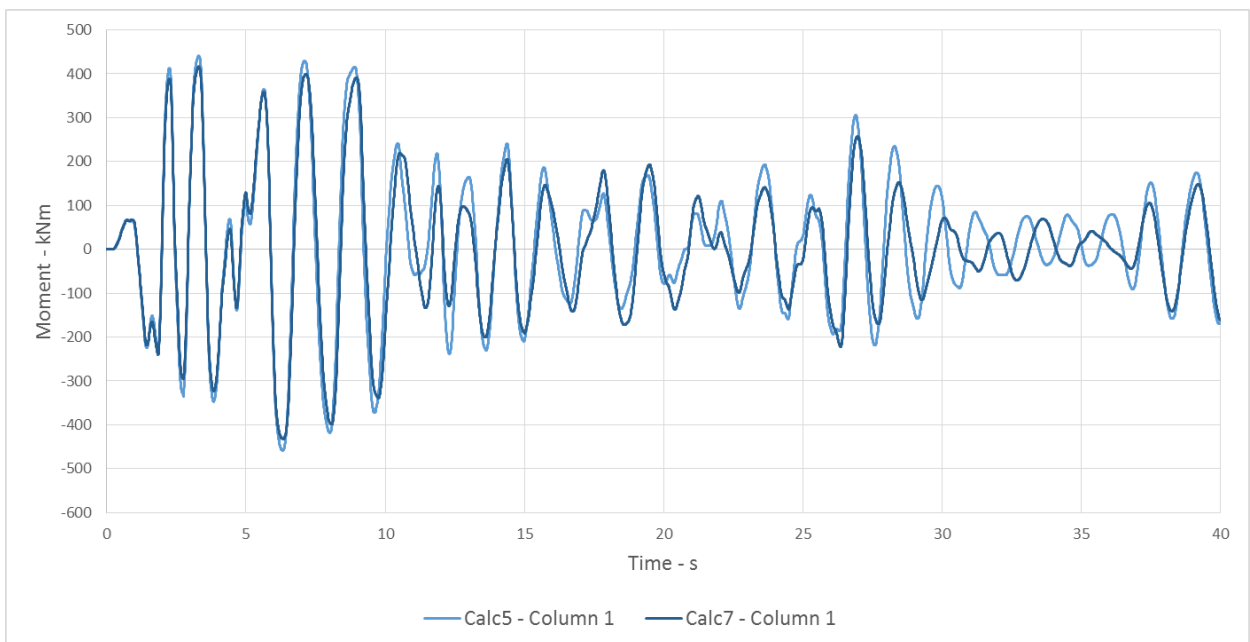


Figure 52 - Bending Moments in Bottom of Column 1 - From Calc5, 7

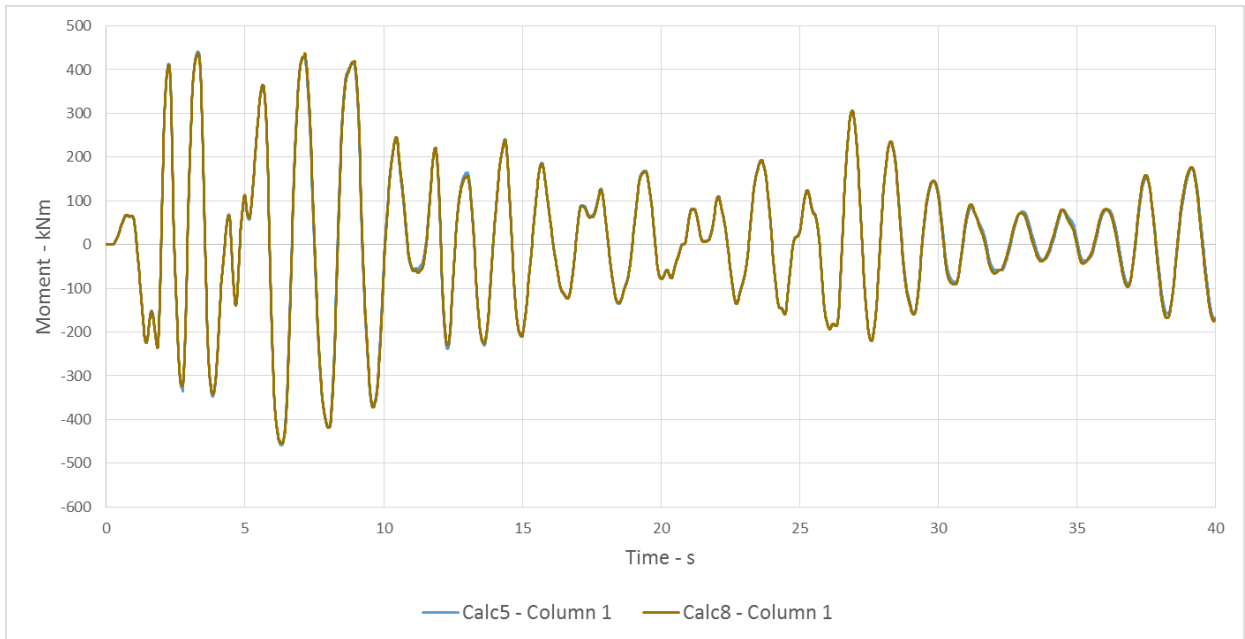


Figure 53 - Bending Moments in Bottom of Column 1 - From Calc5, 8

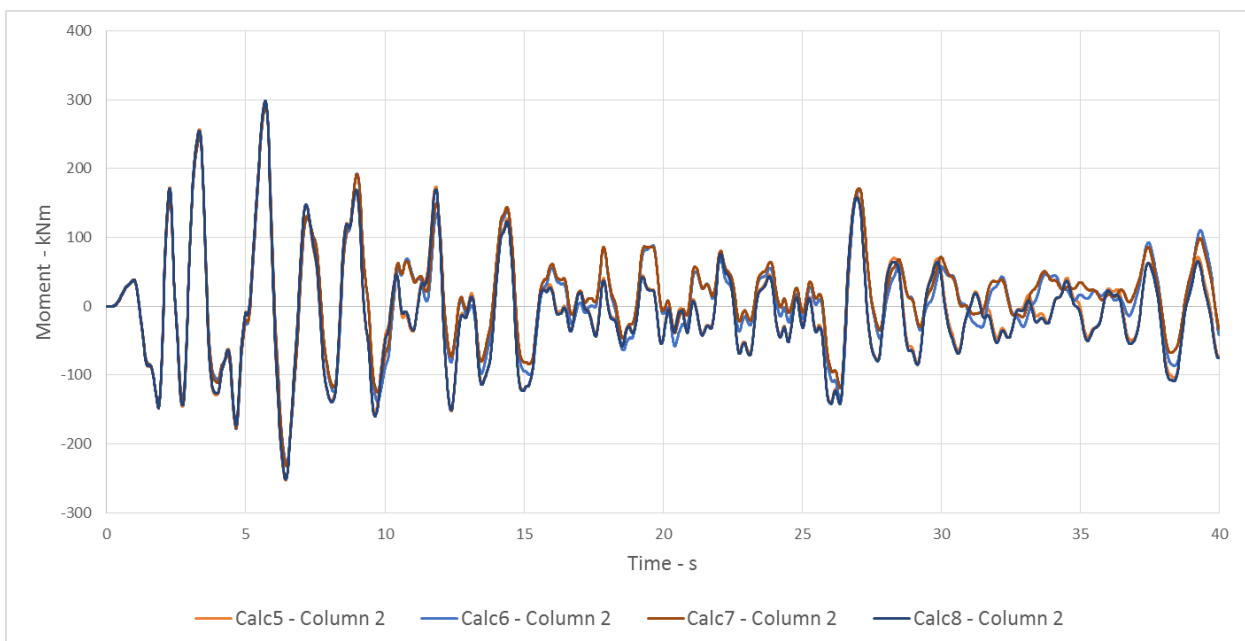


Figure 54 - Bending Moments in Bottom of Column 2 - From Calc5, 6, 7, 8

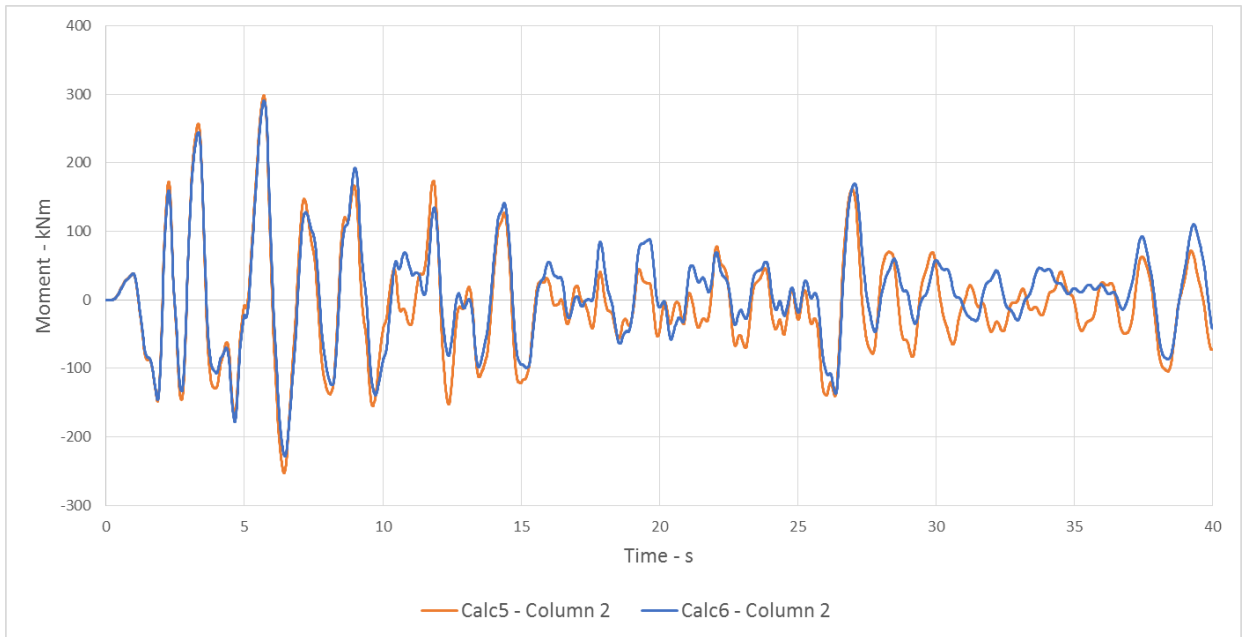


Figure 55 - Bending Moments in Bottom of Column 2 - From Calc5, 6

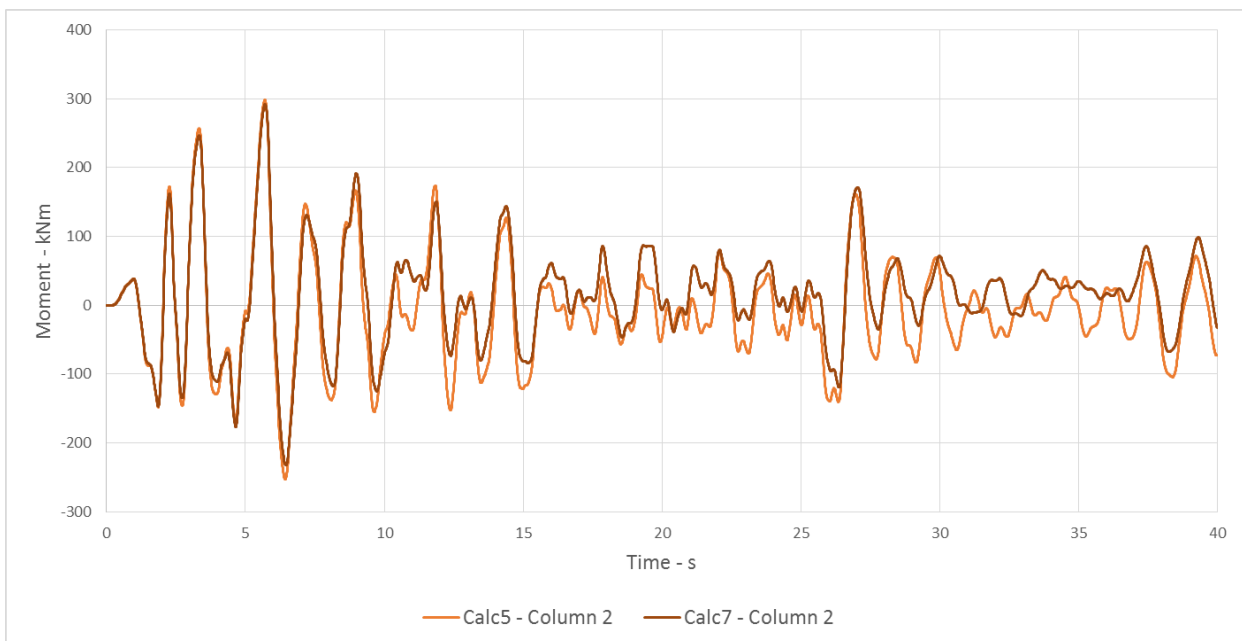


Figure 56 - Bending Moments in Bottom of Column 2 - From Calc5, 7

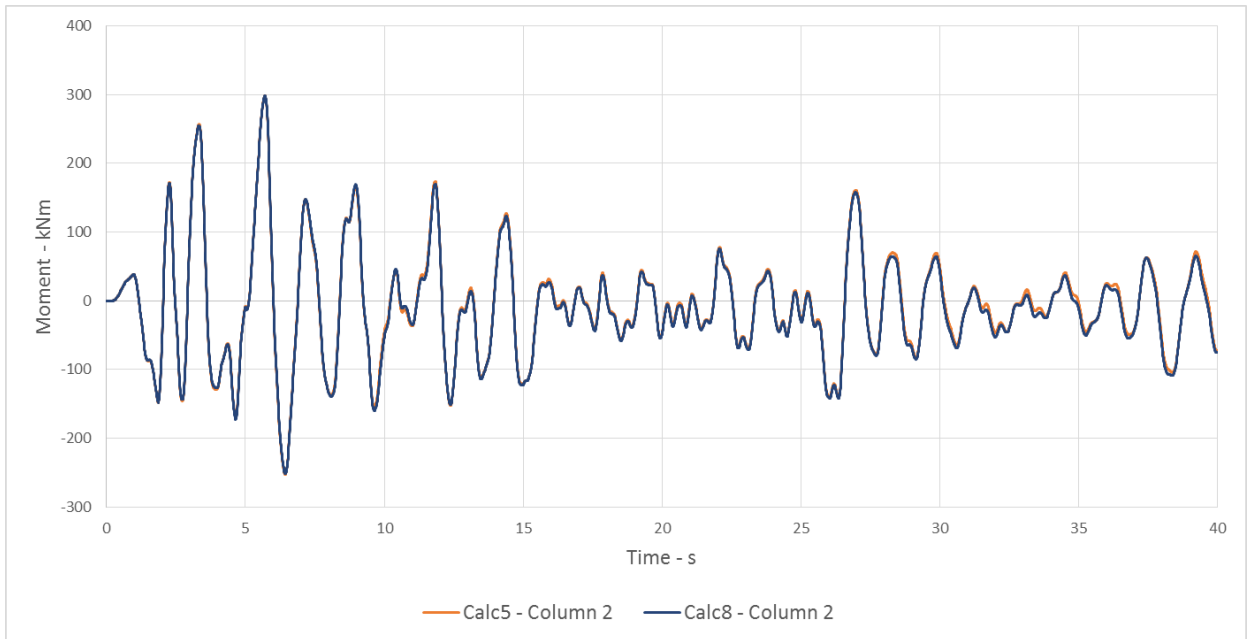


Figure 57 - Bending Moments in Bottom of Column 2 - From Calc5, 8

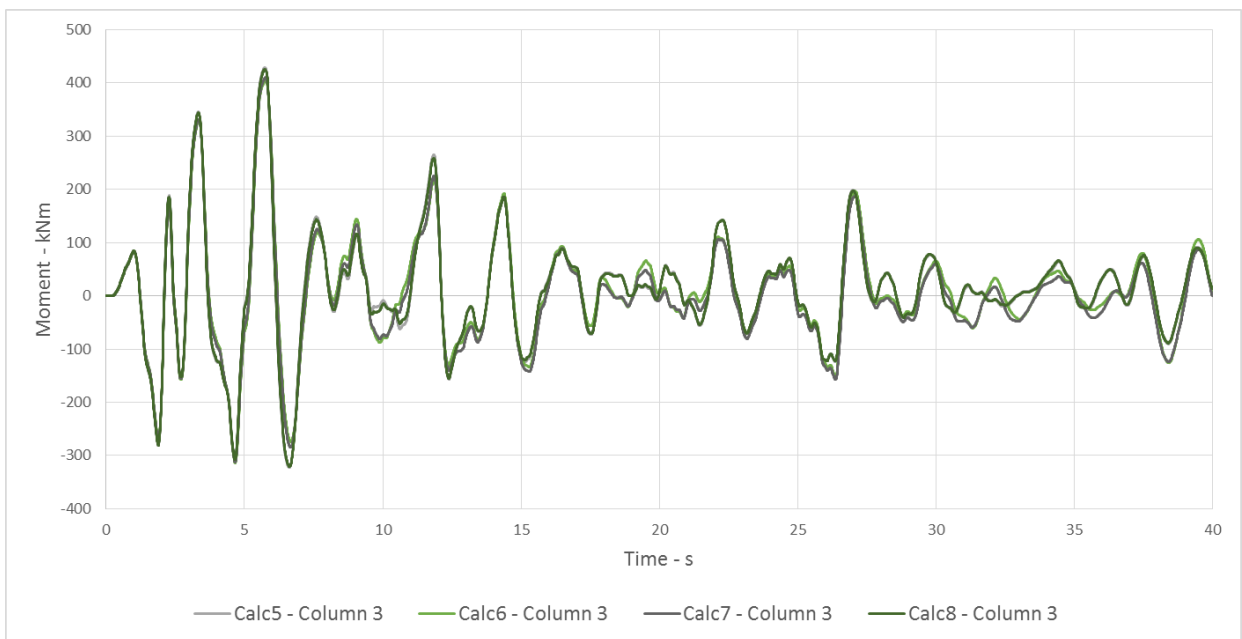


Figure 58 - Bending Moments in Bottom of Column 3 - From Calc5, 6, 7, 8

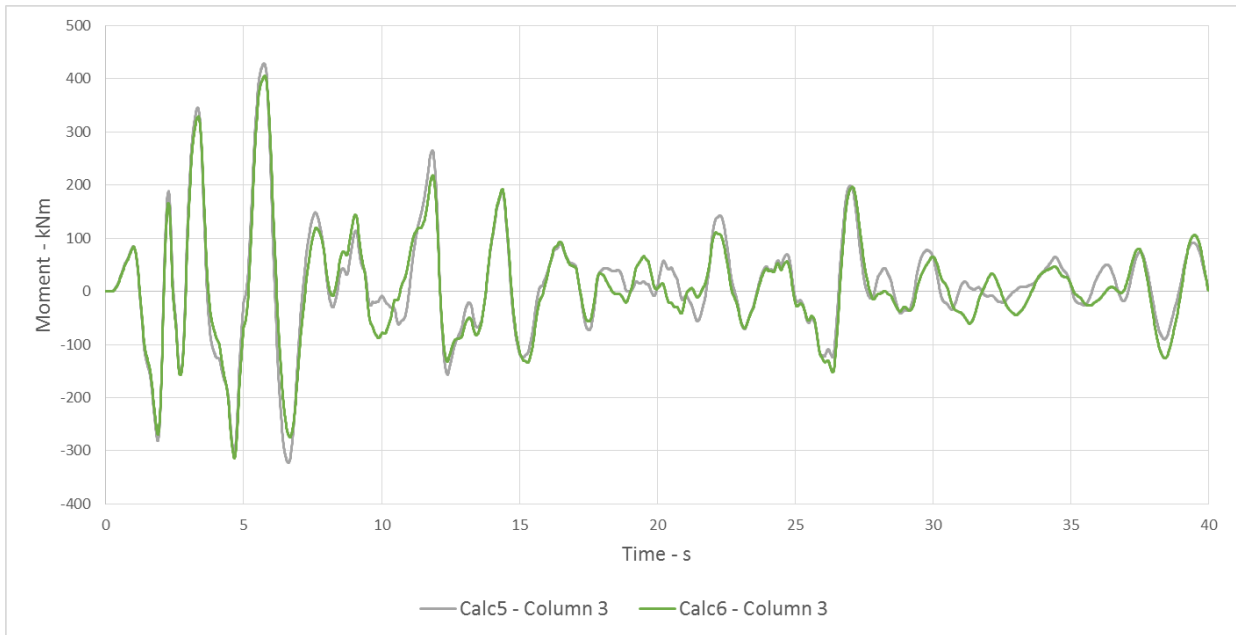


Figure 59 - Bending Moments in Bottom of Column 3 - From Calc5, 6

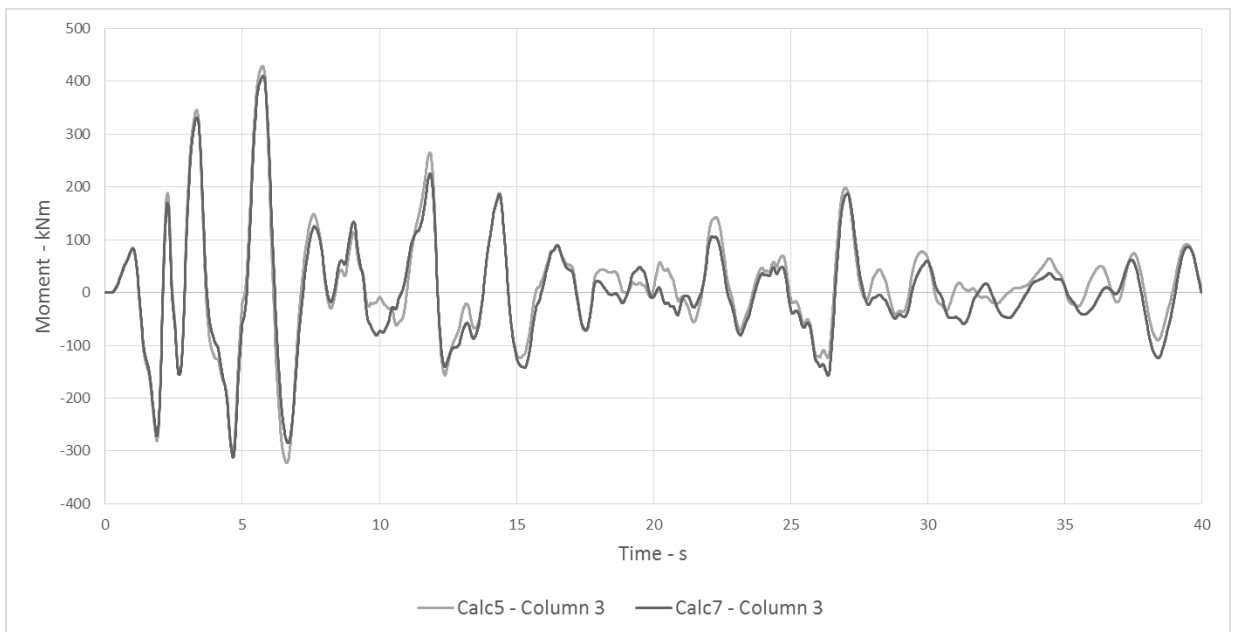


Figure 60 - Bending Moments in Bottom of Column 3 - From Calc5, 7

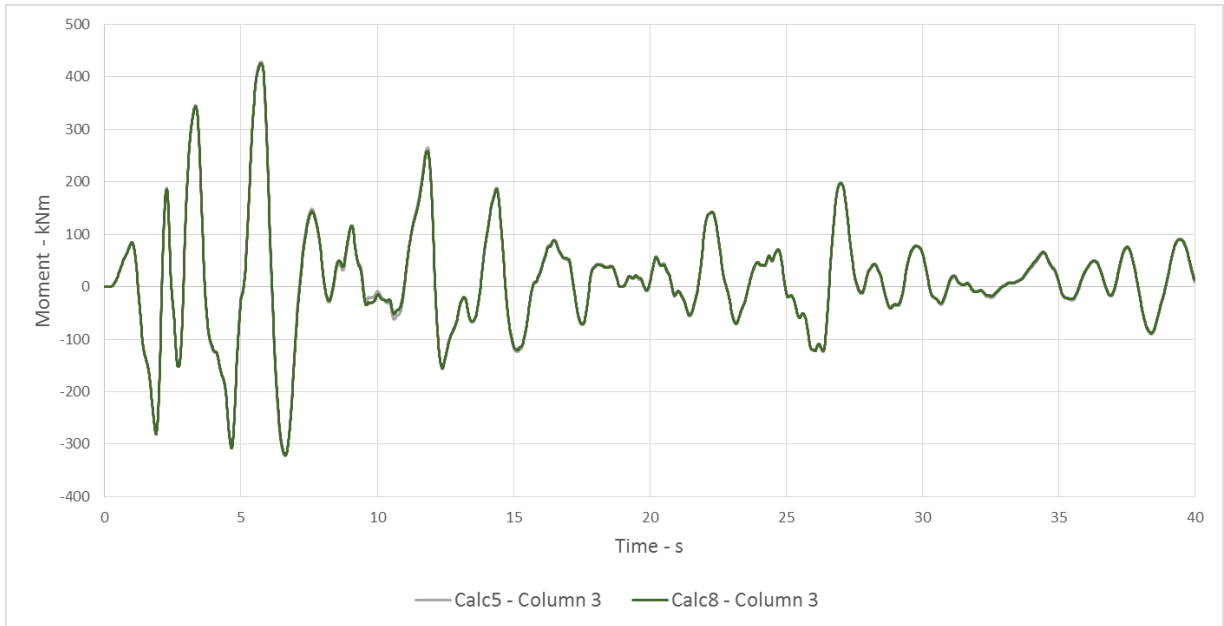


Figure 61 - Bending Moments in Bottom of Column 3 - From Calc5, 8

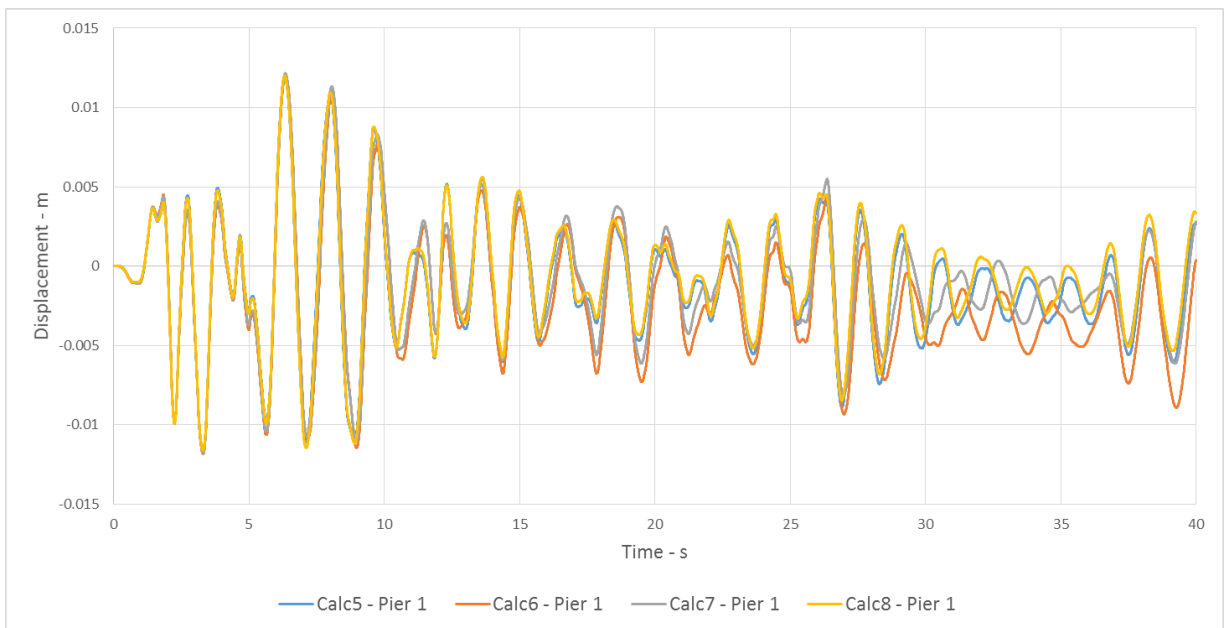


Figure 62 - Relative displacement of Pier 1 from Calc 5, 6, 7, 8

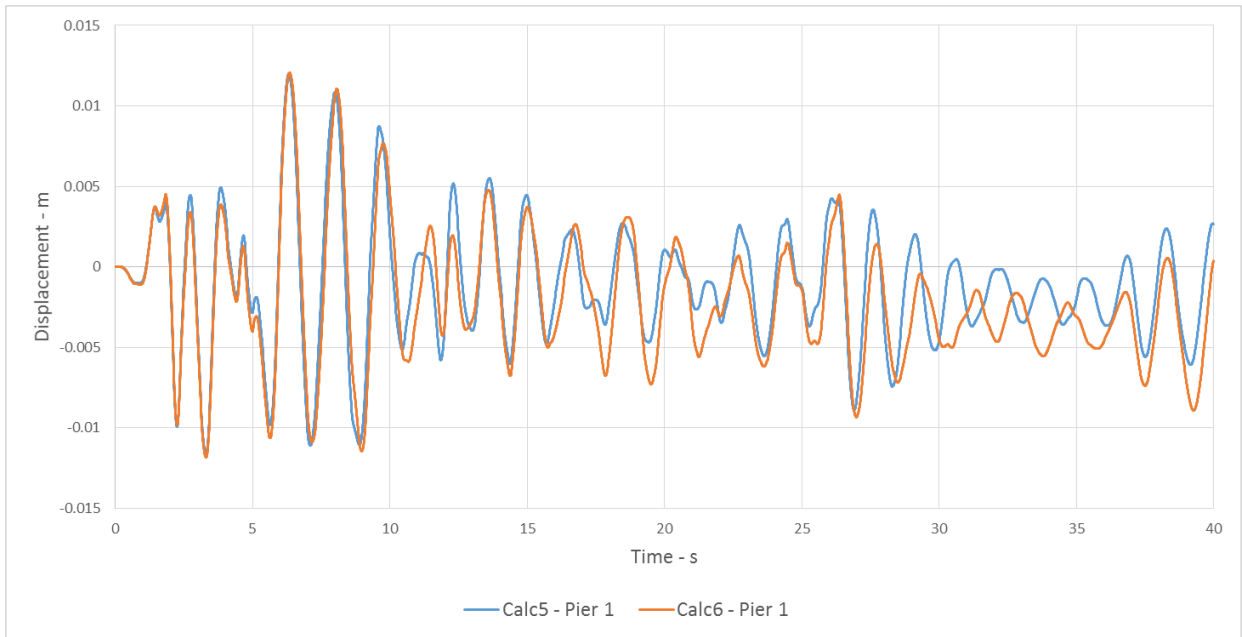


Figure 63 - Relative displacement of Pier 1 from Calc 5 and 6

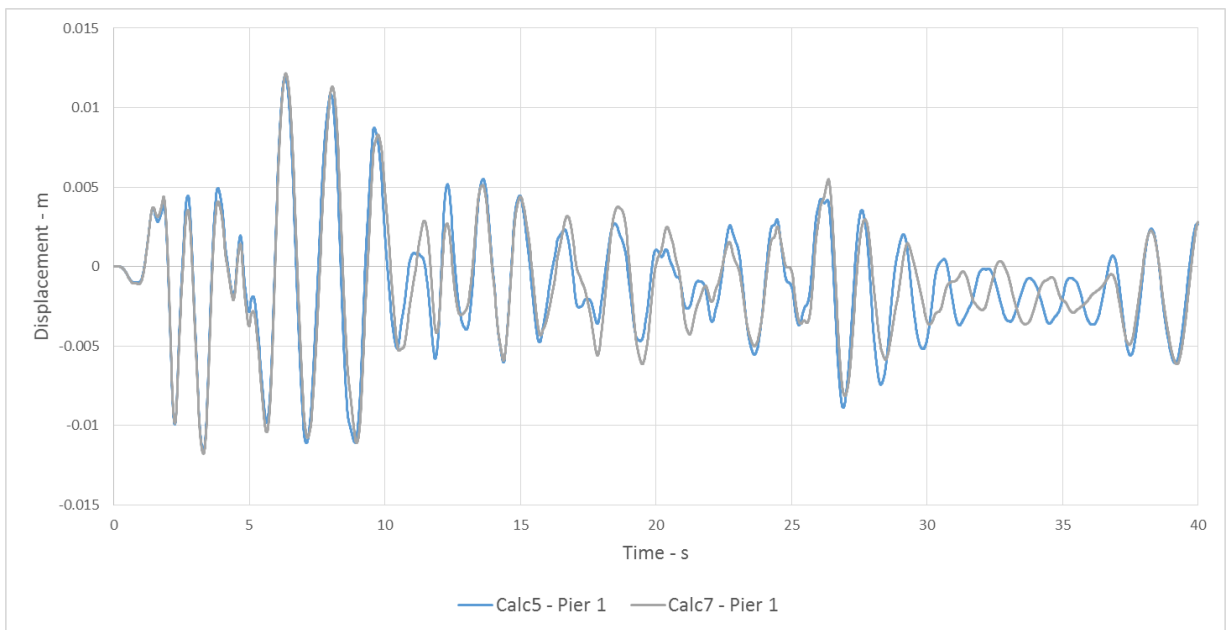


Figure 64 - Relative displacement of Pier 1 from Calc 5 and 7

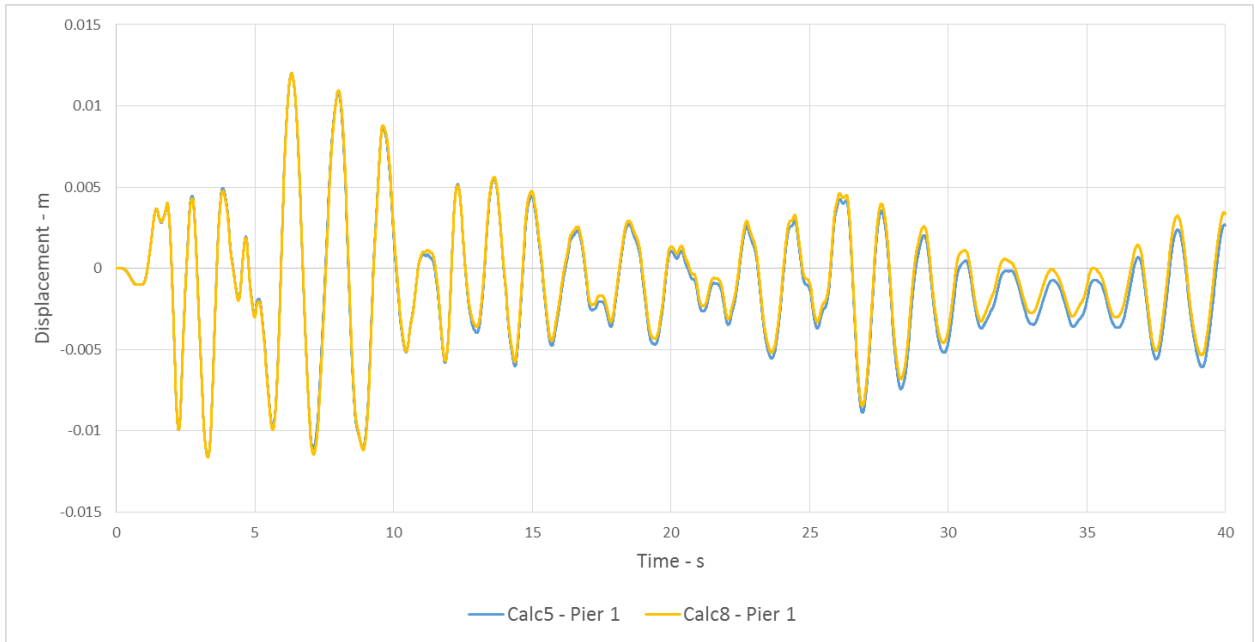


Figure 65 - Relative displacement of Pier 1 from Calc 5 and 8

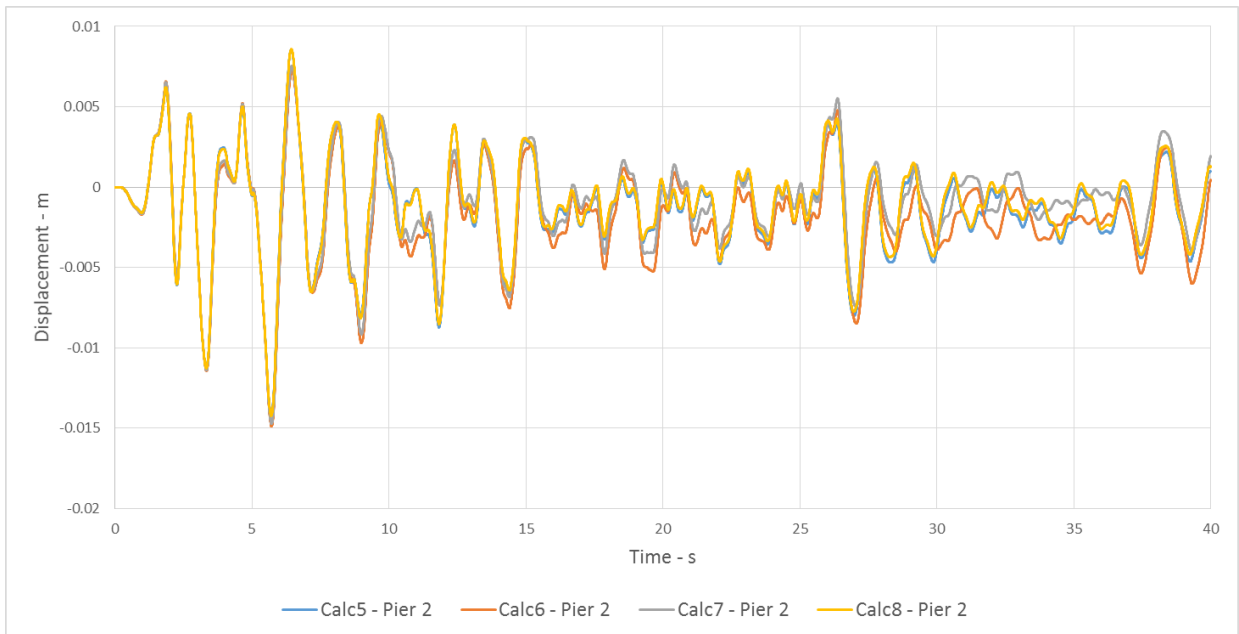


Figure 66 - Relative displacement of Pier 2 from Calc 5, 6, 7, 8

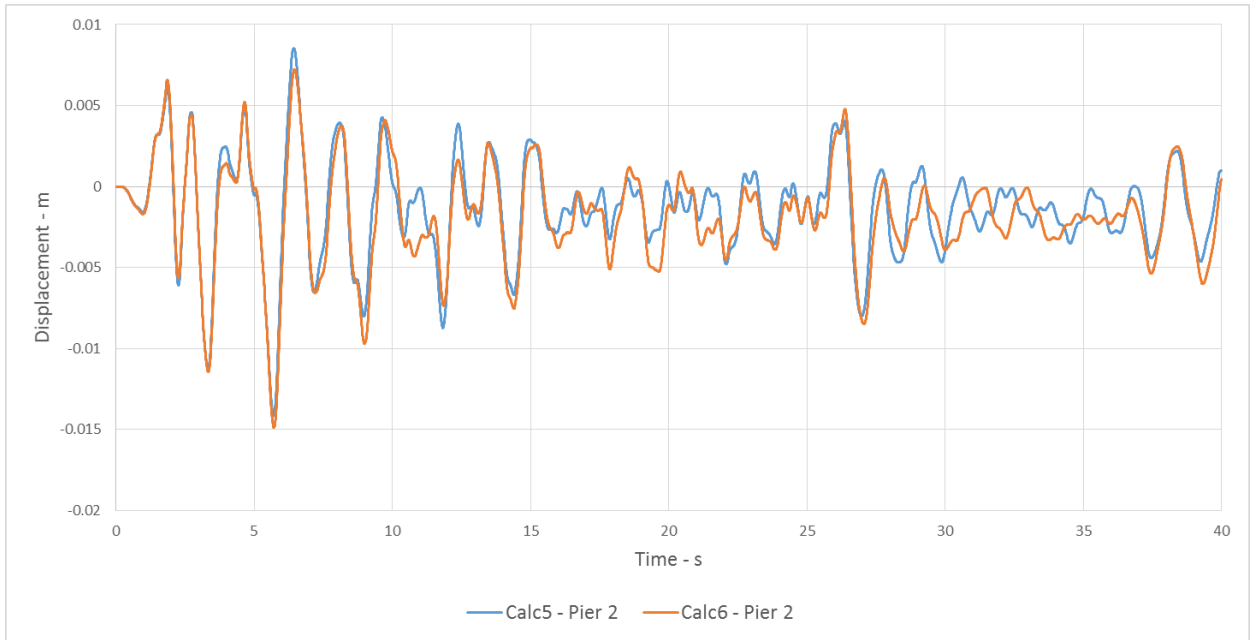


Figure 67 - Relative displacement of Pier 2 from Calc 5 and 6

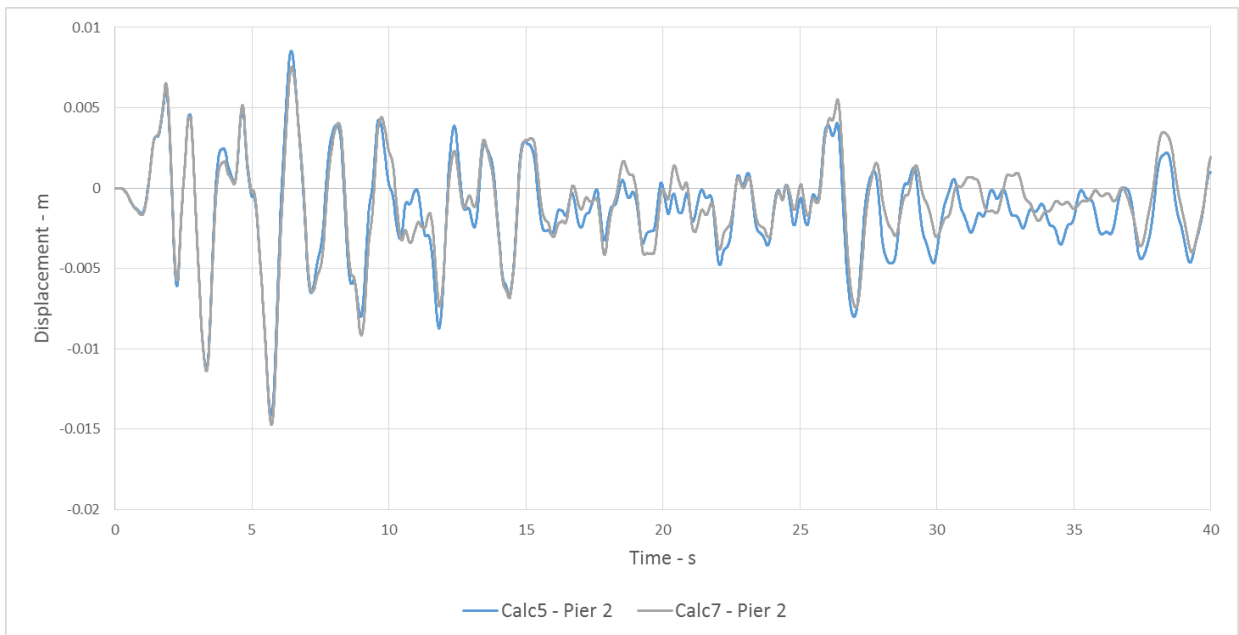


Figure 68 - Relative displacement of Pier 2 from Calc 5 and 7

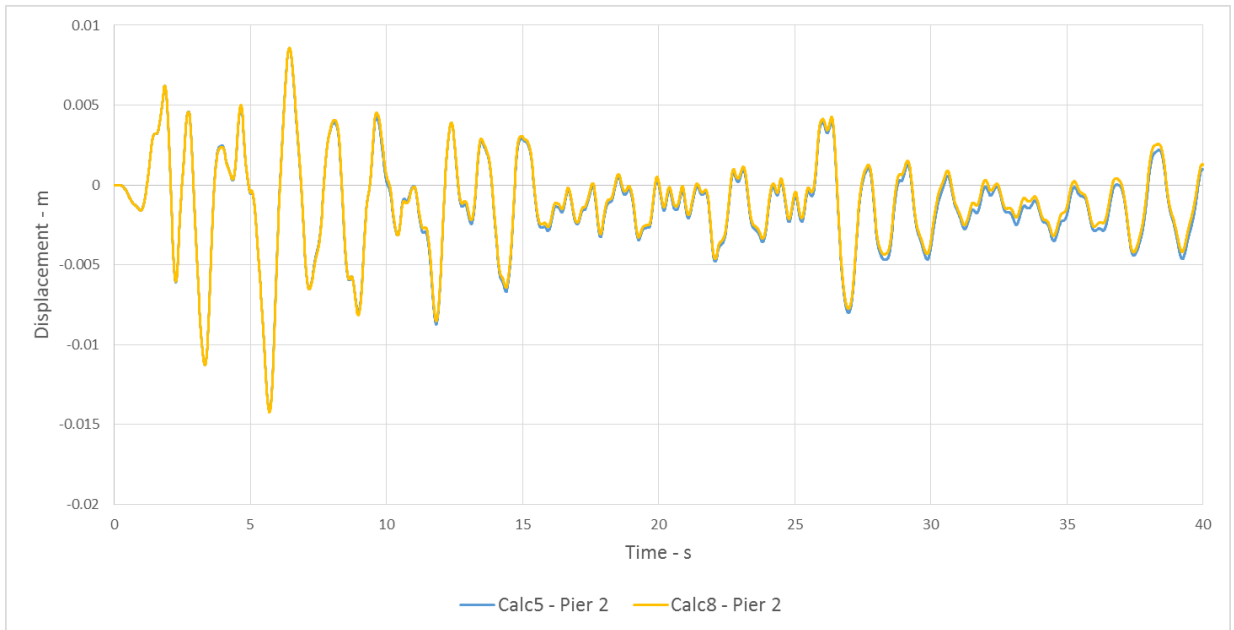


Figure 69 - Relative displacement of Pier 2 from Calc 5 and 8

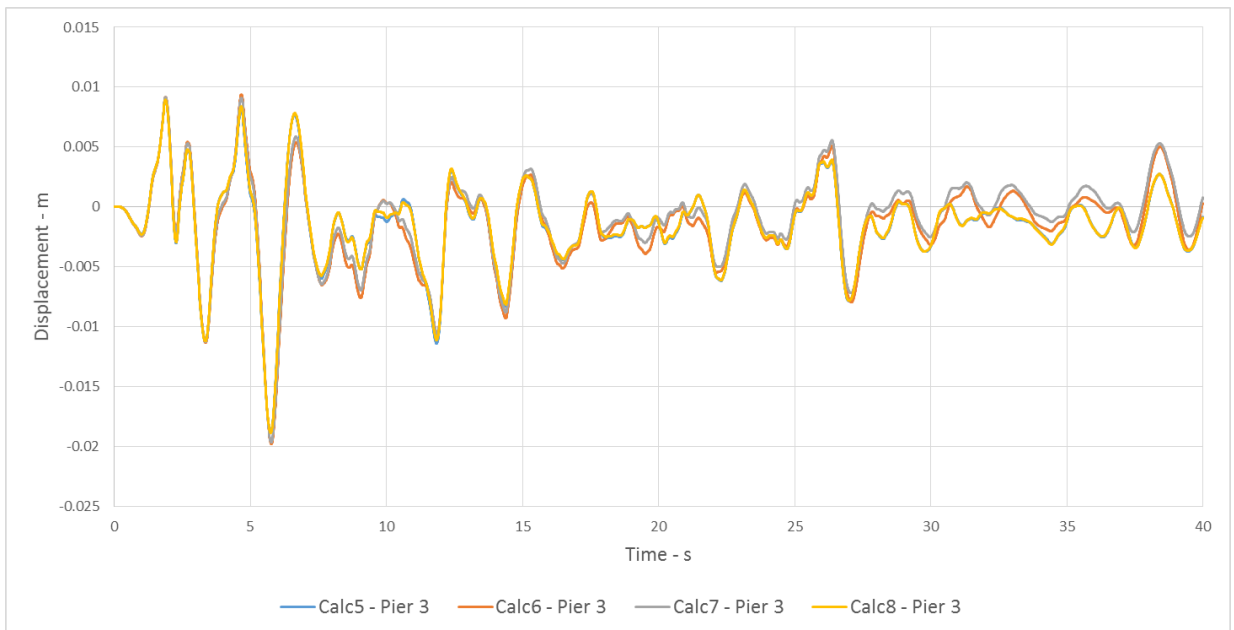


Figure 70 - Relative displacement of Pier 3 from Calc 5,6,7,8

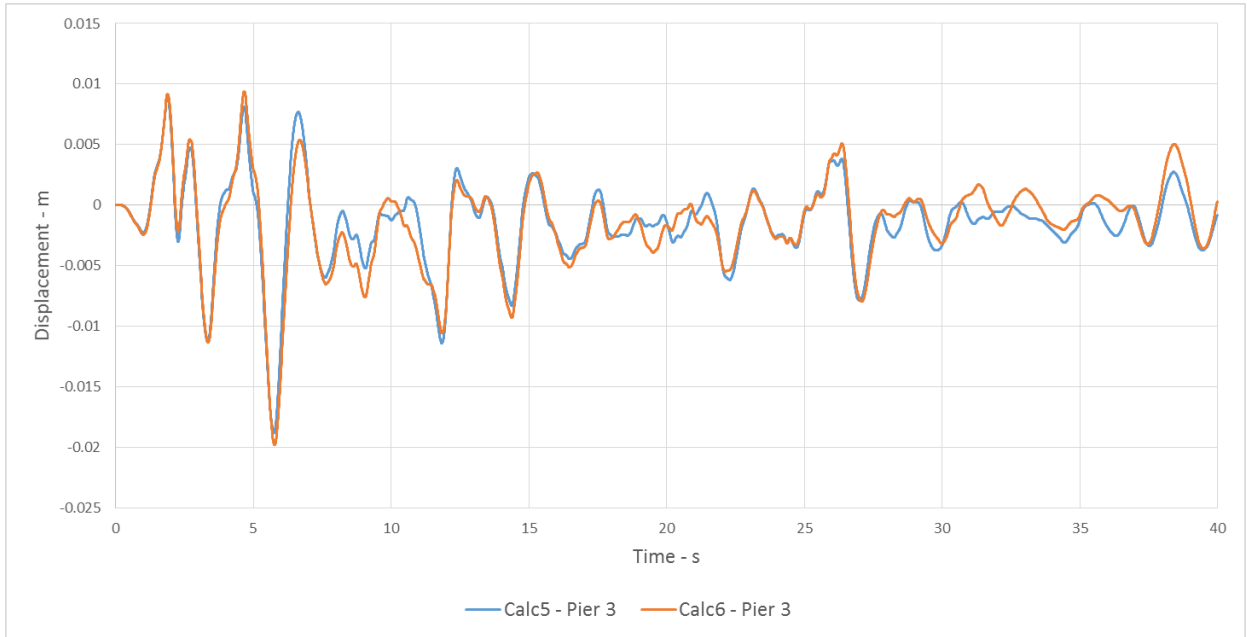


Figure 71 - Relative displacement of Pier 3 from Calc 5 and 6

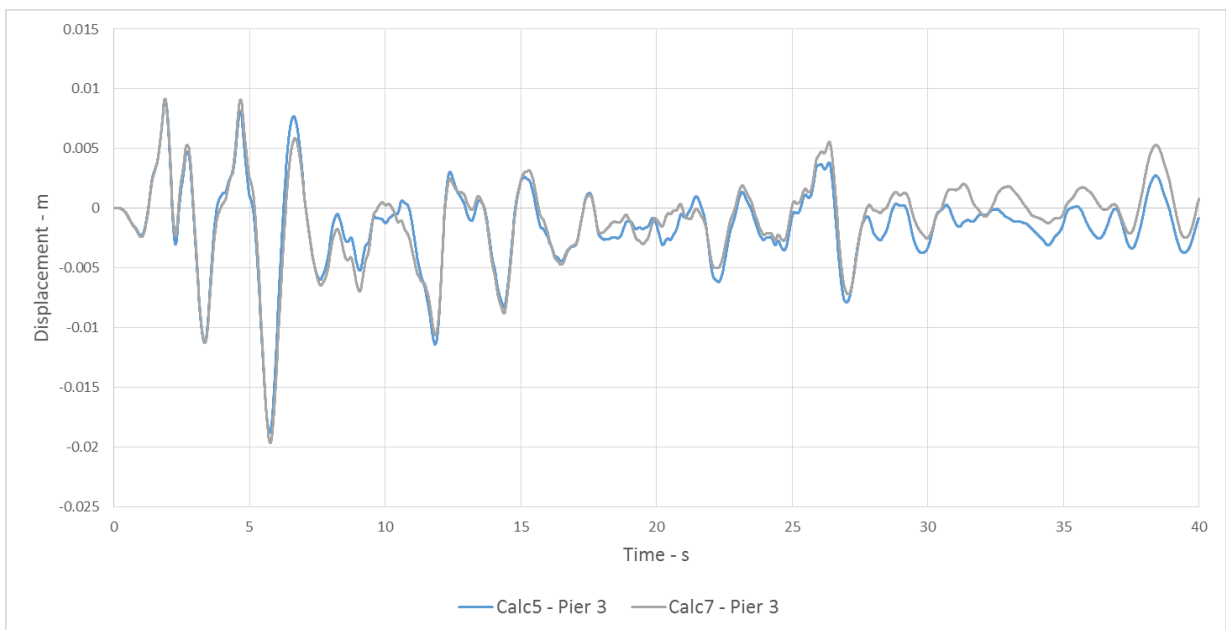


Figure 72 - Relative displacement of Pier 3 from Calc 5 and 7

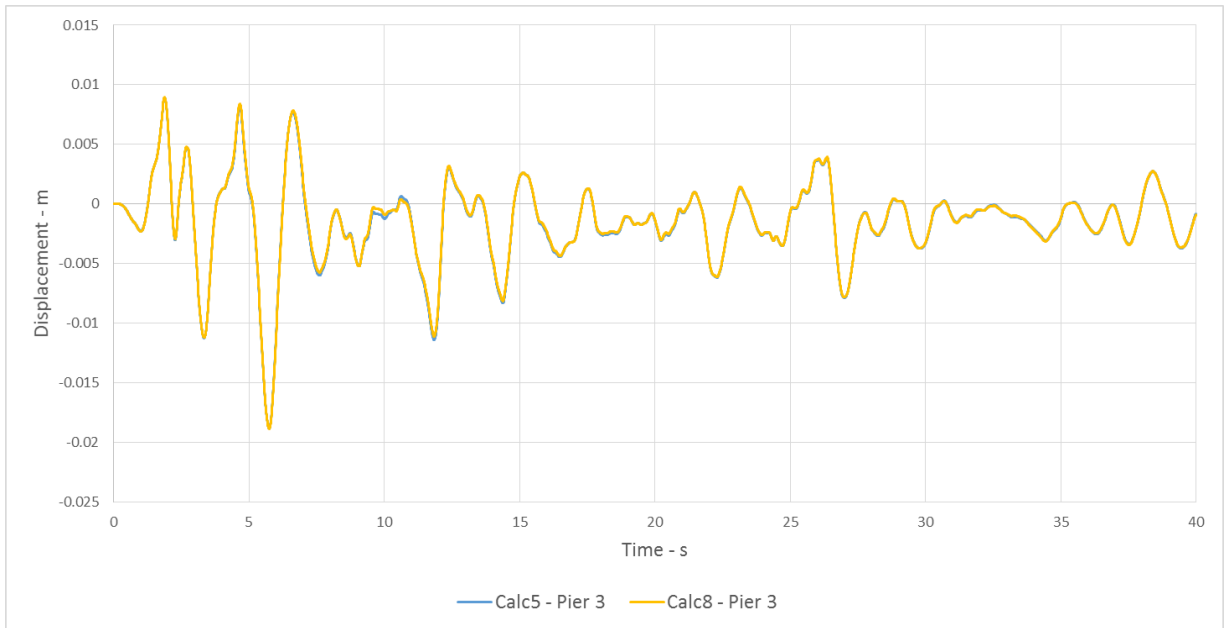


Figure 73 - Relative displacement of Pier 3 from Calc 5 and 8

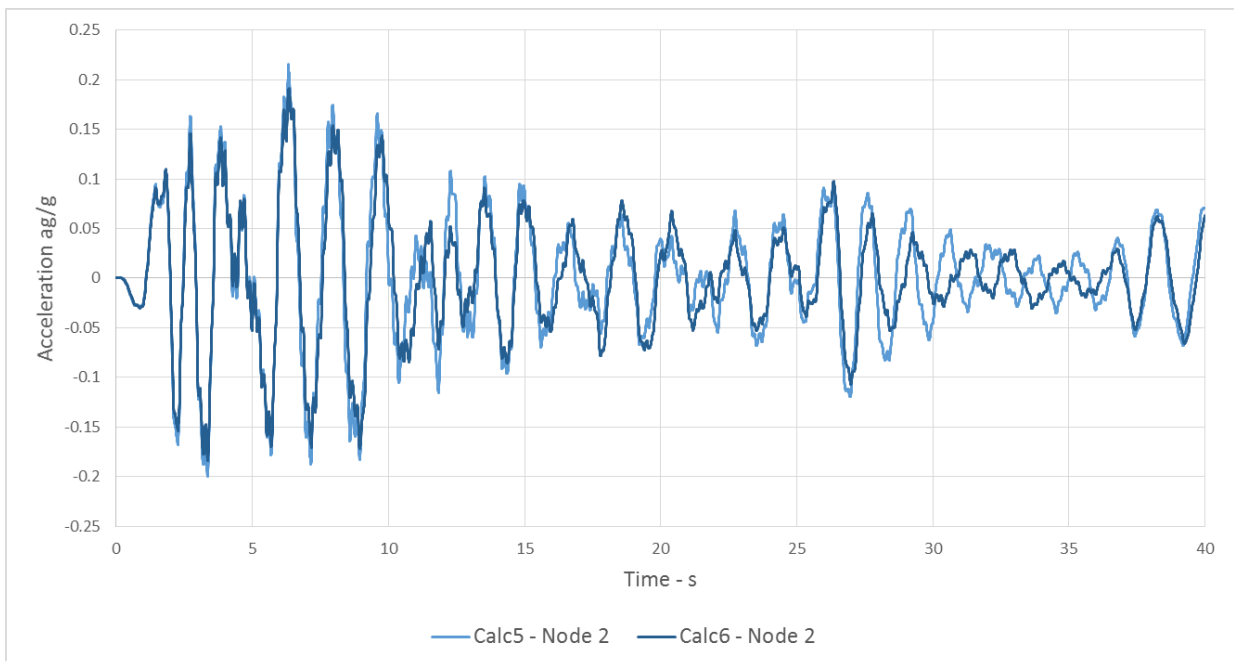


Figure 74 - Acceleration of node 2 (top of column 1) from Calculation 5 and 6

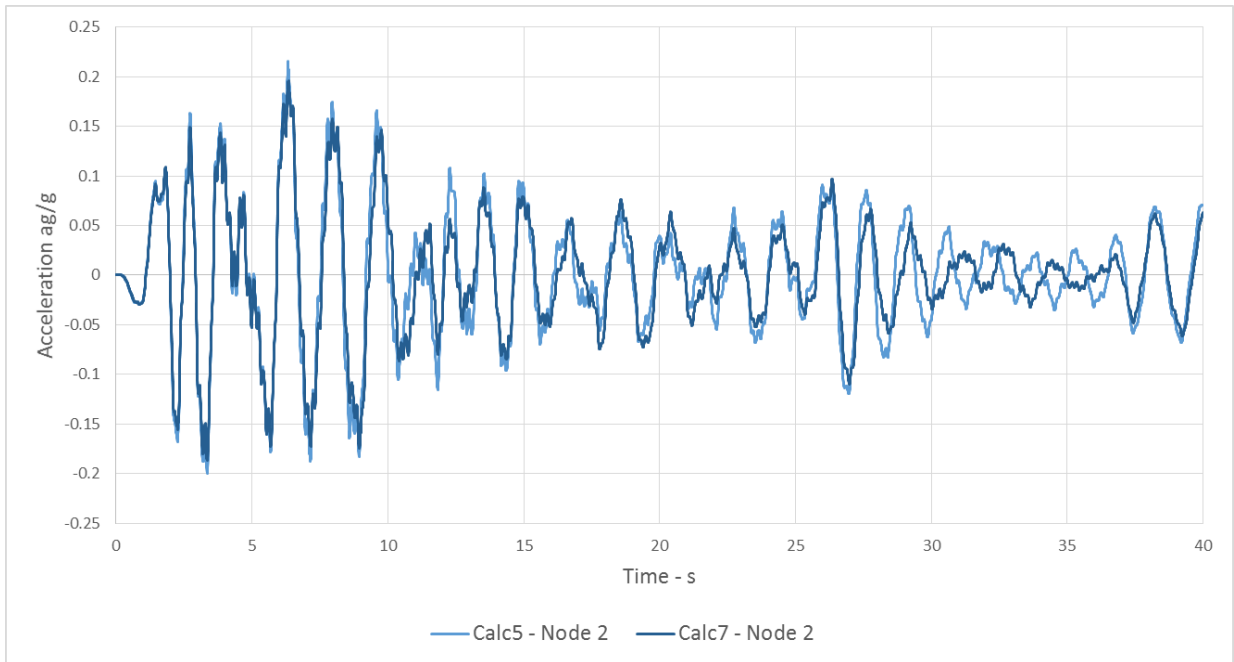


Figure 75 - Acceleration of node 2 (top of column 1) from Calculation 5 and 7

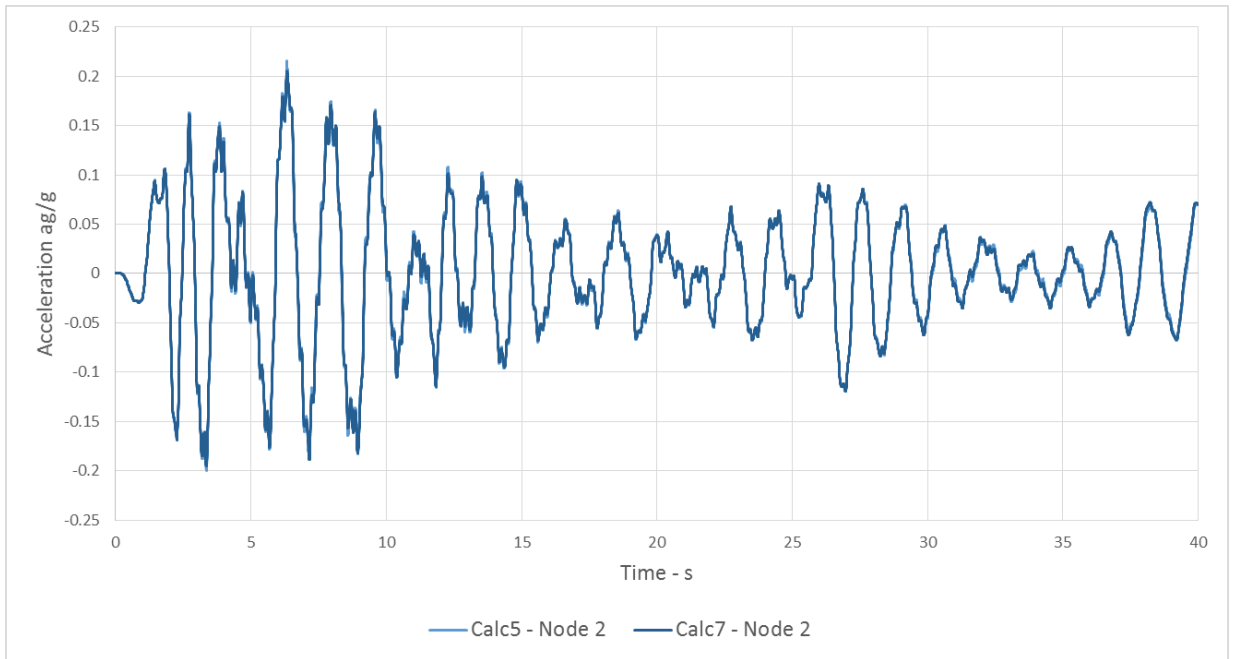


Figure 76 - Acceleration of node 2 (top of column 1) from Calculation 5 and 8

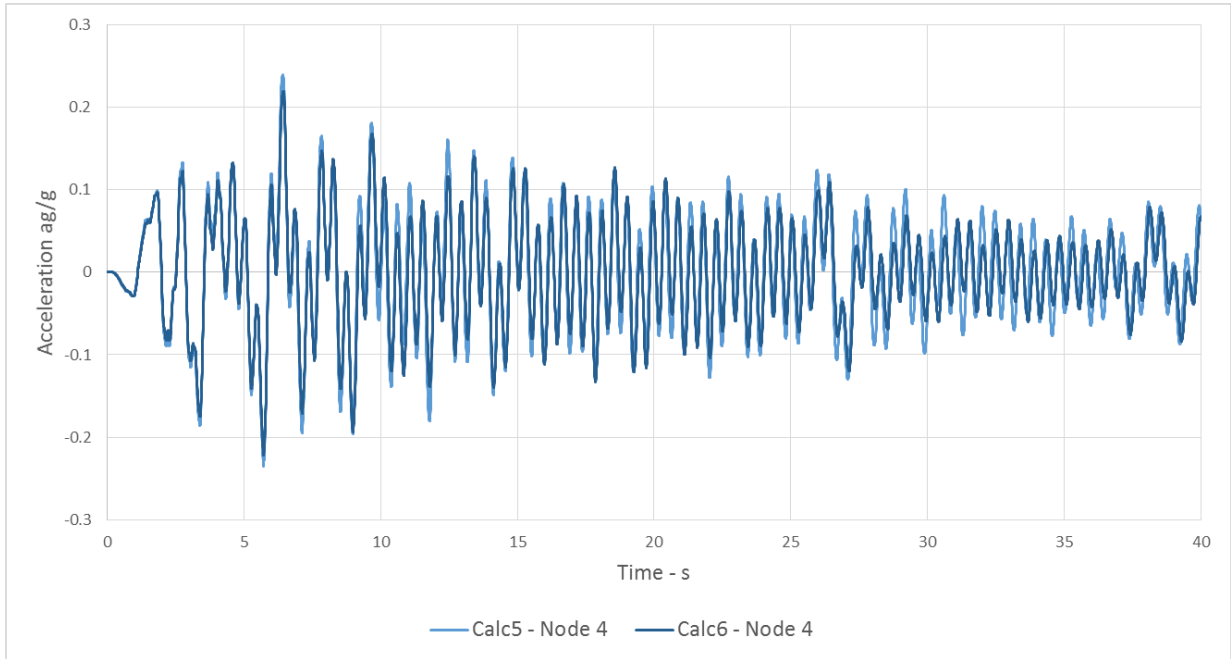


Figure 77 - Acceleration of node 4 (top of column 2) from Calculation 5 and 6

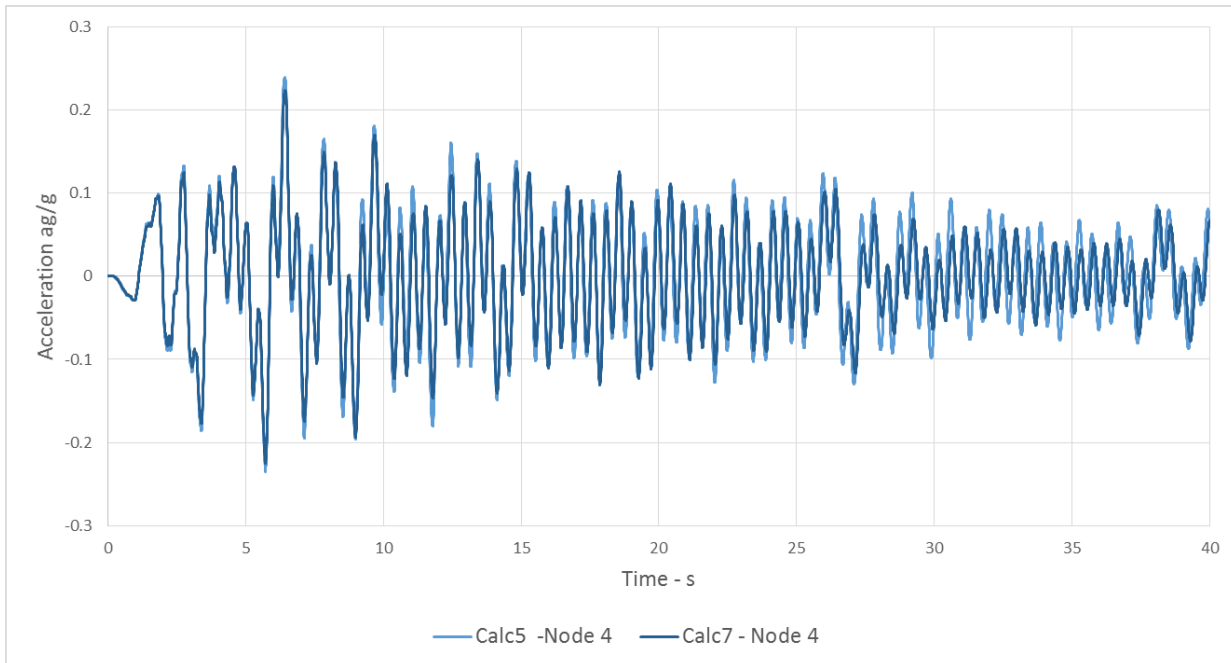


Figure 78 - Acceleration of node 4 (top of column 2) from Calculation 5 and 7

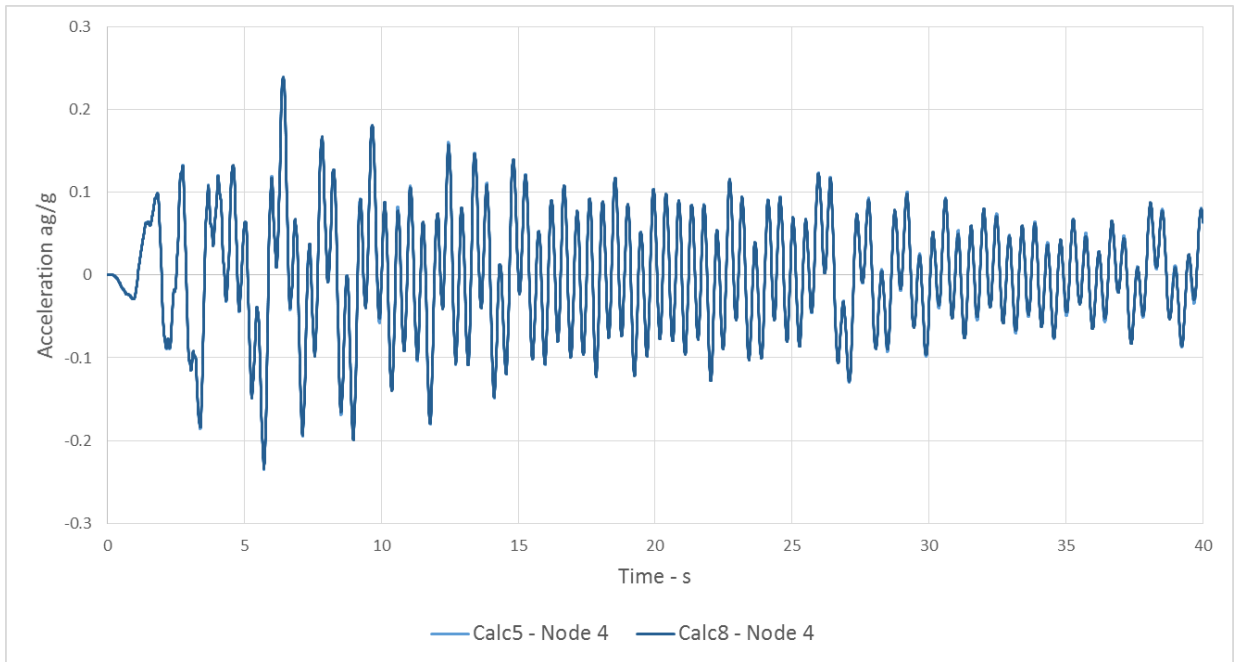


Figure 79 - Acceleration of node 4 (top of column 2) from Calculation 5 and 8

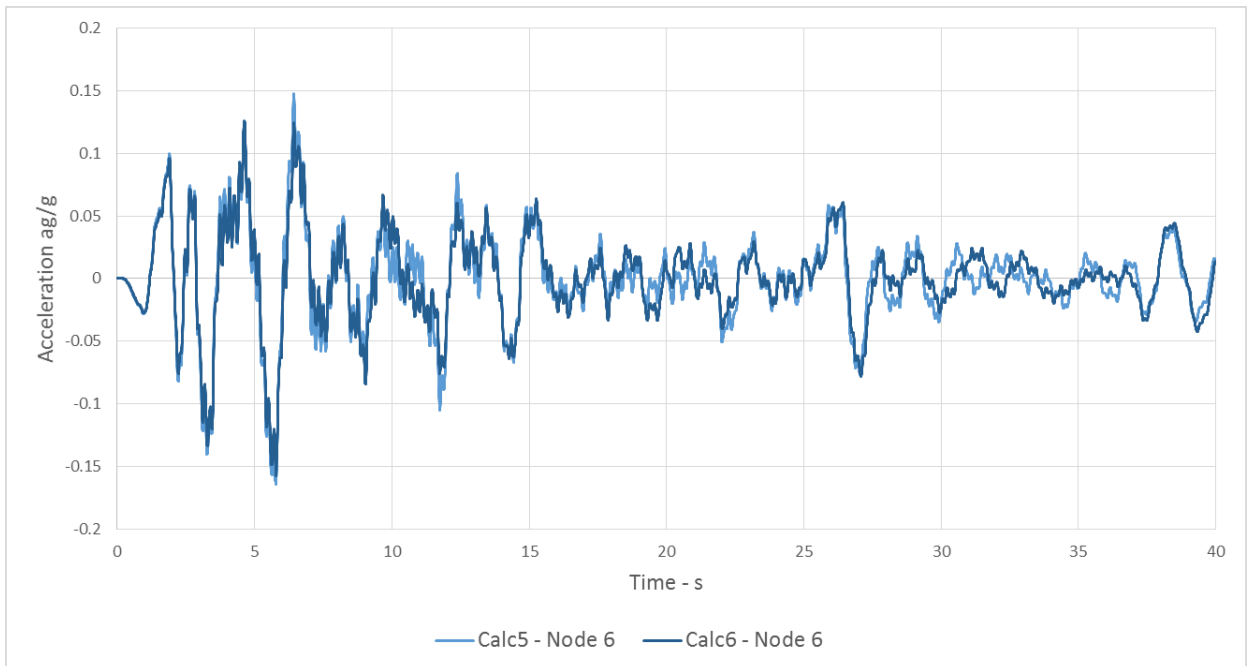


Figure 80 - Acceleration of node 6 (top of column 3) from Calculation 5 and 6

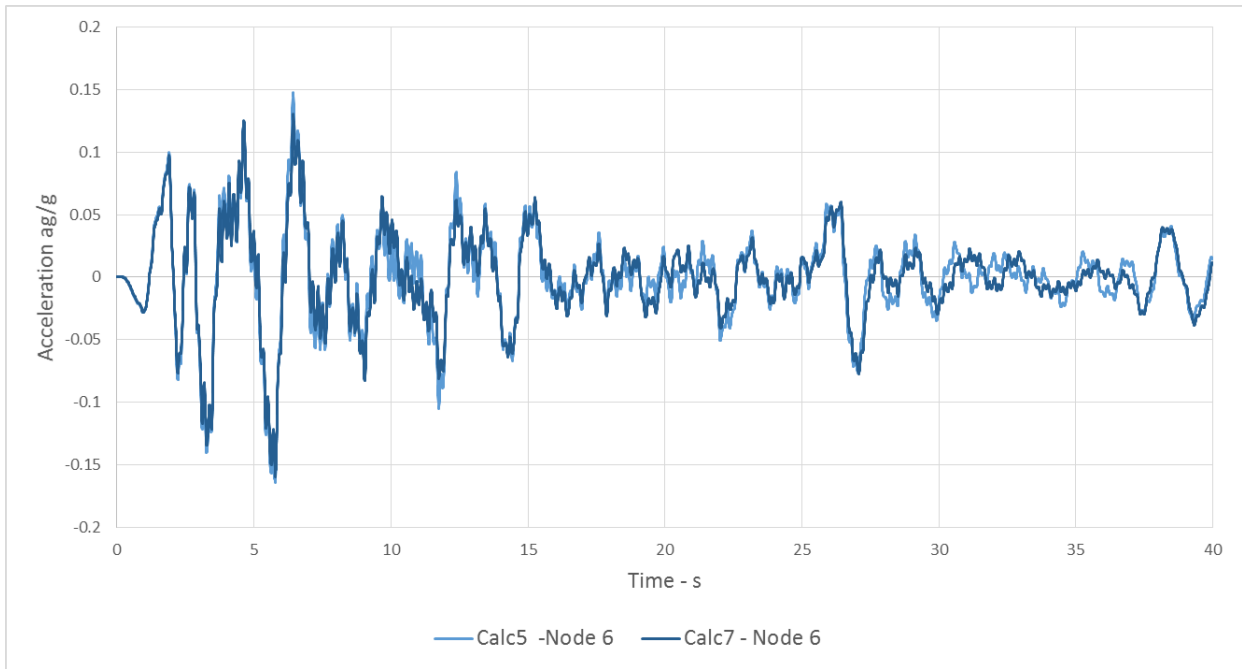


Figure 81 - Acceleration of node 6 (top of column 3) from Calculation 5 and 7

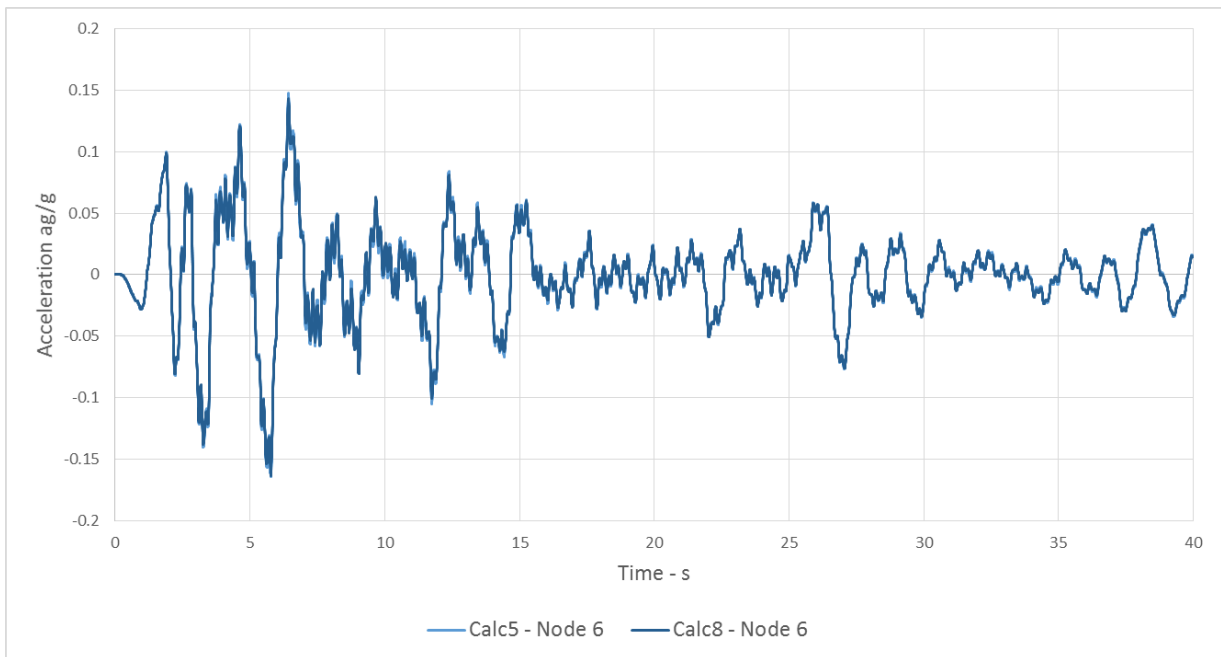


Figure 82 - Acceleration of node 6 (top of column 3) from Calculation 5 and 8

6.6 Monotonic Push-Over Curves and Hysteretic Curves of Column-1 Used In Computation of Earthquake Responses of Four Prototype Bridges

By use of the promoted advanced refined modeling concept, there have been formulated nonlinear analytical models of the real bridge column – 1 (C1) implemented in the analyzed bridge prototype models M1, M2, M3 and M4 in four different reinforcement cases.

The representative monotonic push-over curves are presented in Fig. 172. It is clear that the implemented different longitudinal reinforcement produced different push-over curves. The difference is significantly larger for the column behavior manifested in the deep nonlinear range of up to maximum displacement of $\max D = 10.0$ cm.

Fig. 168 comparatively shows the push-over curves and the hysteretic responses of the column used in the analyzed bridge model M1 and M2 (Calc 1 and Calc 2).

Fig. 169 provides a comparative presentation of the push-over curves and the hysteretic responses of the column used in the analyzed bridge model M1 and M3 (Calc 1 and Calc 3).

Fig. 178 comparatively displays the push-over curves and the hysteretic responses of the column used in the analyzed bridge model M1 and M4 (Calc 1 and Calc 4).

It is evident that the nonlinear behavior of the bridge column reinforced with ordinary steel reinforcement (bridge model M1) is characterized by regular and stable hysteretic curves. However, the hysteretic curves of the bridge column reinforced with GFRP-bars shows a significantly expressed pinching effect. The presented phenomenon confirms again that the bond behavior of the GFRP reinforcing bars should be included in the formulated refined nonlinear analytical model.

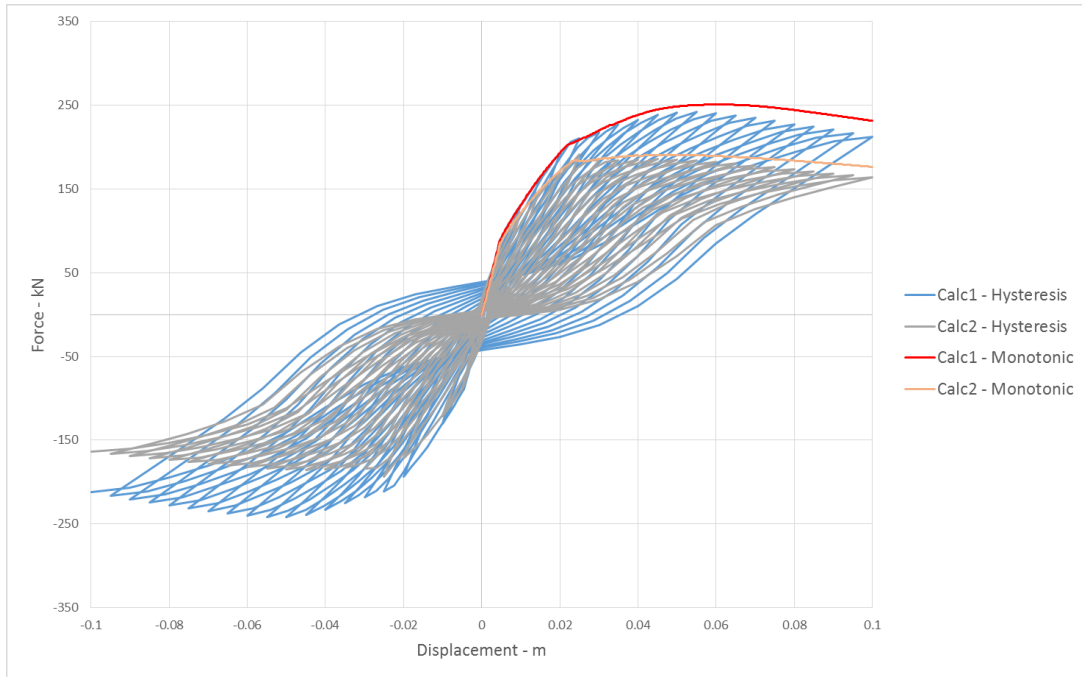


Figure 83 - Hysteresis and Monotonic Curves for Calc1 and Calc2

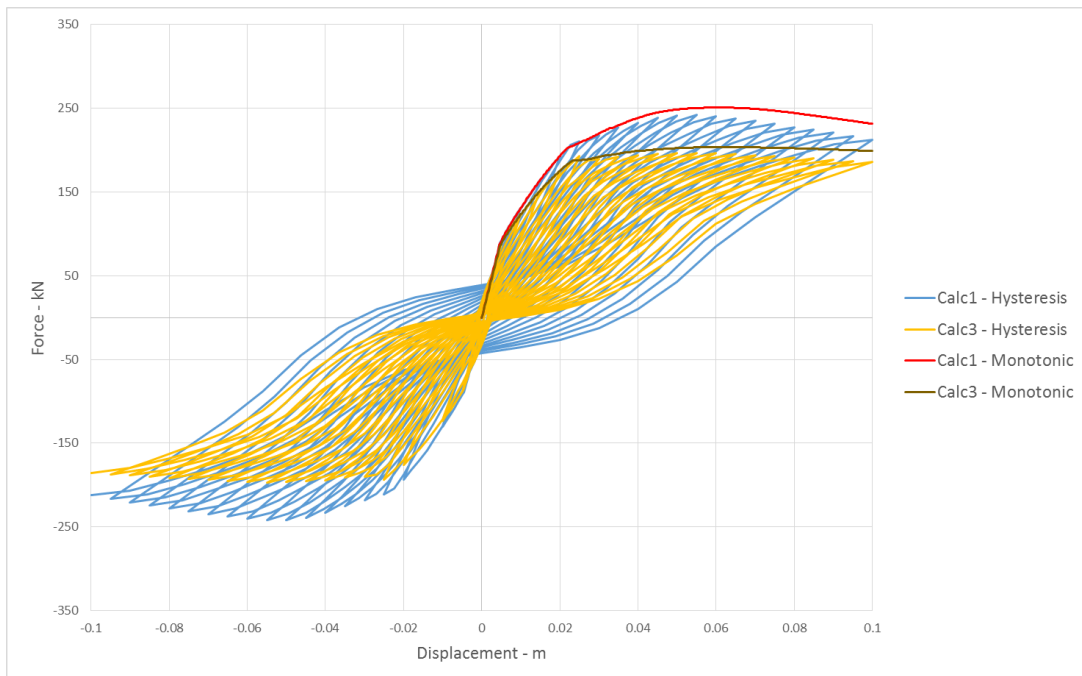


Figure 84 - Hysteresis and Monotonic Curves for Calc1 and Calc3

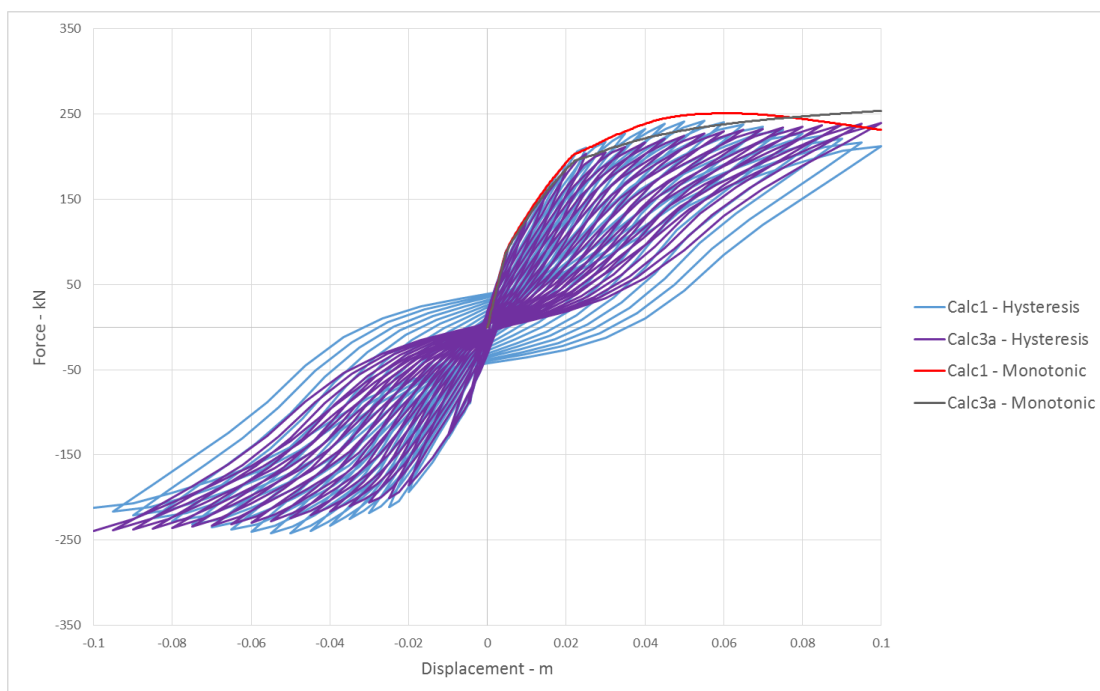


Figure 85 - Hysteresis and Monotonic Curves for Calc1 and Calc3a

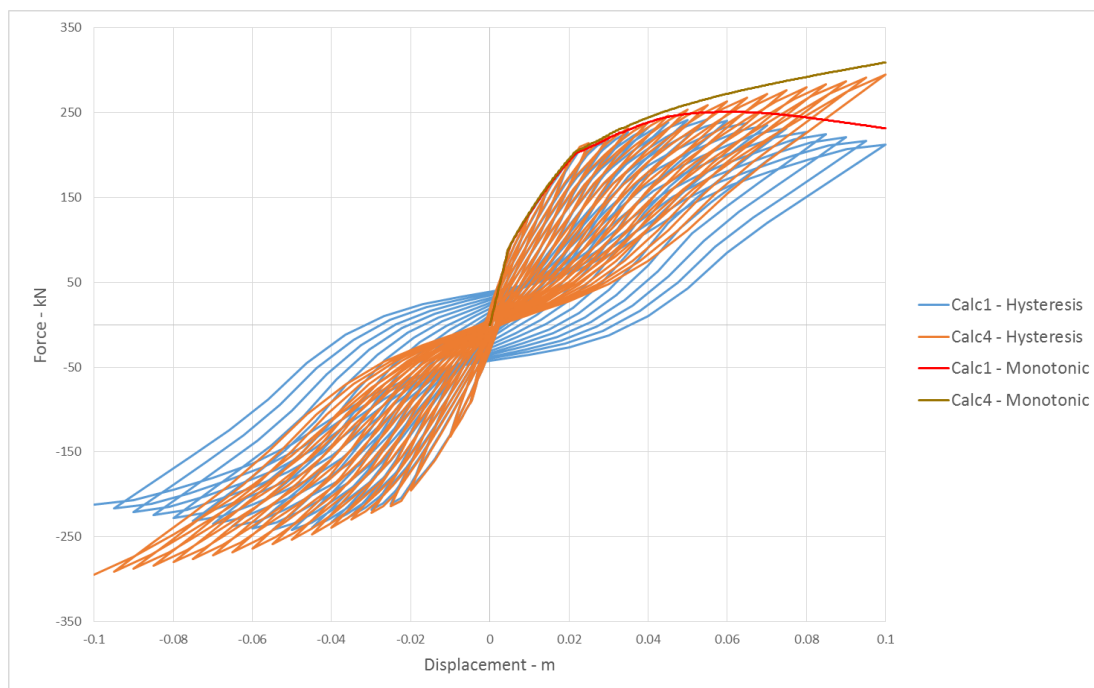


Figure 86 - Hysteresis and Monotonic Curves for Calc1 and Calc4

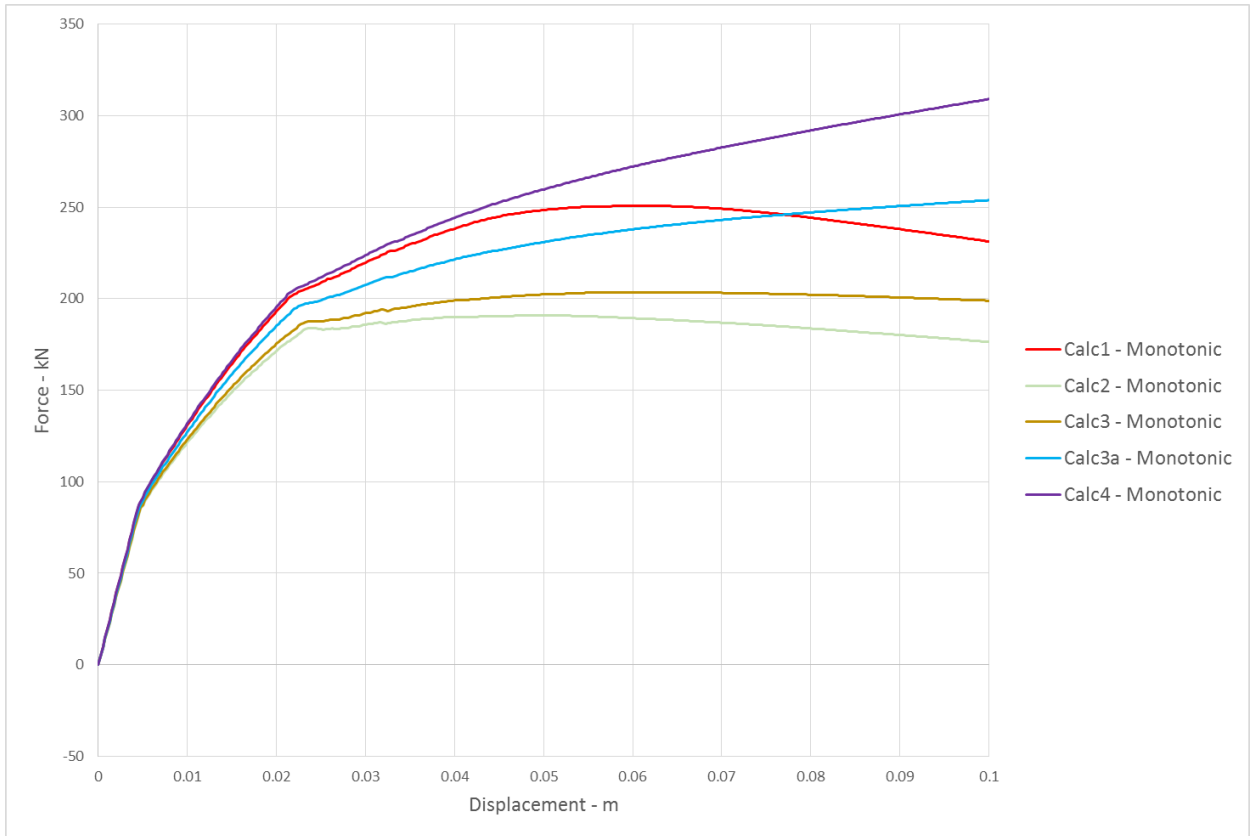


Figure 87 - Monotonic (Push Over) Curves for Calc1, 2, 3, 3a, 4

6.7 Concluding Remarks

Based on the presented results from the conducted extensive analytical study, considering four different real bridge prototypes in the analysis, the following main conclusions can be summarized:

- (1) The applied 3D refined modeling concept represents an advanced and general modeling tool for detailed earthquake response analysis of real bridges;
- (2) The implemented fiber-based nonlinear modeling concept is very convenient for realistic simulation of the actual reinforcement in all bridge columns;
- (3) Bridge columns with ordinary steel reinforcement are characterized by correct and stable hysteretic responses under constant axial and reverse cyclic loads;
- (4) Bridge columns with GFRP-reinforcement are characterized by stable hysteretic curves, but with significantly expressed pinching effect;
- (5) To model more realistically the hysteretic behavior of GFRP-reinforced bridge piers, the actual bond behavior should be simulated in the formulated nonlinear analytical model.

Page is intentionally left blank

7 CHAPTER 7 CONCLUSIONS AND RECOMMENDATIONS

7.1 Conclusions

The representative conclusions generated on the basis of the conducted and presented extensive experimental and numerical investigation of concrete columns with FRP bars have been elaborated as specific observations in three related research segments: (1) Research segment related to the general application prospects of the structural composite reinforcement technology (CRT); (2) Research segment related to the general applicability of the implemented refined nonlinear modeling concept, and (3) Research segment related to the specific conclusions generated on the basis of the obtained original research results from the conducted original experimental and theoretical study.

- I) Prospects of structural composite reinforcement technology: (1) Structural composite reinforcement technology (CRT) represents an innovative construction option providing advanced solutions in the quite specific construction areas (aggressive environments, etc.) where ordinary reinforcement appears as a solution with severe disadvantages; (2) Behavior of composite reinforcing bars under monotonic loading is simple and generally linear up to failure; (3) Behavior of composite reinforcement installed in concrete members which are exposed to cyclic loading is favorable and contributes to obtaining a respectable load bearing capacity of the designed structural members, and (4) Today, the new Innovative composite reinforcing bars are undergoing permanent development and composite reinforcement technology in structural engineering is expected to be progressively expanded in future.
- II) Prospects regarding the applicability of the implemented refined nonlinear modeling concept: (1) In conducting specific analytical nonlinear studies in which importance is given to modeling of the position of the individual composite reinforcing bars and the position of the individual reinforcing hoops, the refined modeling concept is

- actually the only acceptable alternative; (2) The refined modeling concept provides conditions for including, in the analytical model, the real nonlinear characteristics of the used materials which can be proved or obtained based on specific material tests; (3) The refined modeling concept provides appropriate conditions for its further upgrading considering other significant and specific nonlinear behavior phenomena, and (4) With the development trend of very fast computers, the refined modeling concept is becoming a unique tool enabling modeling and development of new improved technologies for composite reinforced members.
- III) Specific conclusions generated on the basis of the original research results: (1) Based on the conducted experimental tests, the regular and stable nonlinear behavior of the GFRP reinforced column models under simultaneous effect of axial and cyclic earthquake-like shear loads has been confirmed; (2) The hysteretic behavior of the GFRP reinforced bridge column models obtained from the conducted experimental tests is characterized by advanced energy dissipation features and ductility capacity under repeated loading cycles. This observation has confirmed the created further applicability of composite reinforced structural members in seismic regions exposed to strong future earthquakes; (3) The load bearing envelope curves can be very well simulated by tri-linear envelopes, representing three distinct behavior stages. The first is a pure linear stage, the second is a generated nonlinear stage before the ultimate load bearing capacity (point U) and the third is generated nonlinear stage with reduced load bearing capacity under repeated cycles with increasing amplitudes up to limit point (point-L); (4) In the case of the GFRP reinforced bridge pier models, a significant pinching effect has been observed in the experimental hysteretic curves. This is generally the result of “pure” linear behavior of the reinforcing GFRP bars; (5) Crack and damage propagation observed during the experimental tests shows logical and expected development pattern with gradually increased effect upon structural stiffness and load bearing capacity; (6) By experimental tests, it has been confirmed that the load bearing and deformability capacity of the GFRP reinforced members can be increased accordingly. This

observation is important for improved confinement design of GFRP members in seismic areas; (7) Some improvement of analytical modeling of only unloading patterns in the applied analytical model is needed considering the created conditions by the presently implemented refined modeling concept. This improvement can successfully be made by analytical modeling of the real bond behavior of the existing GFRP reinforcing bars, and (8) Based on the conducted analytical study including original analytical modeling of four selected real bridge prototype structures with columns reinforced with ordinary steel and GFRP reinforcement bars, the subsequently presented important conclusions have been drawn. Namely, the implemented refined modeling of bridge columns represents an advanced modeling concept for detailed nonlinear earthquake response analysis of real bridges. Consequently, the conducted study has directly confirmed that GFRP reinforced real bridges can be safely and successfully implemented in all regions characterized by high seismicity. However, correct design and implementation of GFRP reinforcement in various specific structural load bearing elements should be strictly provided and sufficiently experimentally confirmed.

7.2 Recommendation for Future Research

Considering the presented results obtained from the completed extensive theoretical and experimental study, some important recommendations for required future research can be created and particularly pointed out. Future research should be directed integrally to three different research fields:

- I. Conducting of specific experimental studies: The application of composite FRP bars is relatively a new technological step in the structural engineering domain of civil engineering. Continuous development and application of technologically new products of FRP bars requires continuation of experimental tests in several areas: (1) Experimental tests to define the actual behavior of FRP bars under tension loads up to failure; (2) Experimental tests to define the actual behavior of FRP bars under

- compression; (2) Experimental tests to define the actual behavior of FRP bars under shear; (4) Experimental tests to define the actual bond behavior of FRP bars of different diameters, and (5) Experimental tests to define the actual bond behavior of FRP bars embedded in different concrete classes.
- II. Continuation of theoretical research: In the domain of theoretical research, it is necessary to derive advanced concepts of how to consider the real bond behavior in the formulated refined nonlinear analytical models. Improvements of refined analytical models should be based on specific and successful experimental test results.
 - III. Continuation of the research devoted to advancement of the production technology: Specific studies in this area should result in products of a higher quality. Higher quality composite rebar should have qualitatively improved and more reliable some of the important phenomena, including, for example, an improved bond behavior and/or an improved ductility of FRP reinforcing bars.

LITERATURE

- [1] ACI (2006), *ACI 440.1R-06 - Guide for the design and construction of concrete reinforced with FRP bars*, ACI Committee 440, American Concrete Institute (ACI).
- [2] Aktan, A. E., Bertero, V. V., and Sakino, K. (1985). "*Lateral Stiffness Characteristics of Reinforced Concrete Frame-Wall Structures.*" *Deflections of Concrete Structures, ACI Special Publication, SP-86, 231-262.*
- [3] Alsayed, S.H., AL-Salloum, and Almusallam. (2000). "Performance of Glass Fiber Reinforced Plastic Bars as Reinforcing Materials for Concrete Structures." *Composite Journal Composites Part B*, 31, 555-567.
- [4] "*Bond of reinforcement in concrete,*" *State of the art Bulletin 10, International Federation for Structural Concrete (fib), 2000.*
- [5] Byars, E.A., Waldron, P.W., DeJke, V. and Demis, S. (2001), *Durability of FRP in Concrete, Current Specifications and a New Approach, Proceedings of FRP Composites in Civil Engineering*, Vol. II, Elsevier, Hong Kong, December, 1497-1507.
- [6] CAN/CSA-S806-02 (2002), *Design and Construction of Building Components with Fibre Reinforced Polymers*, Canadian Standards Association, Toronto, Ontario, Canada.
- [7] Cosenza, E., Manfredi, G., Pecce, M. and Realfonzo, R. (1999), *Bond between GFRP Rebars and Concrete: an Experimental Analysis*, Proceedings of the 4th International Symposium on Fiber Reinforced Polymer for Reinforced Concrete Structures, American Concrete Institute, Detroit, 347- 358.
- [8] Crisfield M.A. [1991] *Non-linear Finite Element Analysis of Solids and Structures*, John Wiley & Sons.
- [9] Chang G.A., Mander J.B. [1994] "*Seismic Energy Based Fatigue Damage Analysis of Bridge Columns: Part 1- Evaluation of Seismic Capacity,*" NCEER Technical Report No. NCEER-94-0006, State University of New York, Buffalo, N.Y.

- [10] CHEN, W.-F., *Plasticity in Reinforced Concrete*. J. Ross Publishing, 2007.
- [11] Choo, C.C., Harik, I.E., Gesund, H., (2006). "Strength of Rectangular Concrete Columns Reinforced with Fiber-Reinforced Polymer Bars." *ACI Structural Journal*, 103(3), May-Jun. 2006, 452-459.
- [12] De Luca, A., Matta, F., and Nanni, A. (2009). "Behavior of Full-Scale Concrete Columns Internally Reinforced with Glass FRP Bars under Pure Axial Load." *COMPOSITES & POLYCON 2009*, American Composites Manufacturers Association, January 15-17, Tampa, FL USA, 1-10.
- [13] Deitz, D.H., Harik, I.E., Gesund, H. (2003). "Physical Properties of Glass Fiber Reinforced Polymer Rebars in Compression." *Journal of Composites for Construction*, 7(4), Nov. 2003, 363-366.
- [14] Duranovic, N., Pilakoutas, K. and Waldron, P. (1997a), *FRP reinforcement for concrete structures: Design Considerations*, Proceedings of Third International Symposium on Non-metallic (FRP) Reinforcement for Concrete Structures, Japan Concrete Institute, Sapporo, Japan, Vol. 2, 527-534.
- [15] Eligehausen, R., Popov, E., and Bertero, V., "Local bond stress slip relationship of deformed bars under generalized excitations," EERC Report 83-23, Earthquake Engineering Research Center (EERC), University of California, Berkeley,
- [16] Fib - 40, *FRP reinforcement in RC structures, State-of-art Report*, Bulletin 40, fib – International Federation for Structural Concrete, Lausanne
- [17] Guadagnini, M., Pilakoutas, K., and Waldron, P. (2006). "Shear Resistance of FRP RC Beams: Experimental Study." *Journal of Composites for Construction*, ASCE, 10(6), 464-473.
- [18] Hadi M, Karim H and Sheikh M (2016) Experimental investigations on circular concrete columns reinforced with GFRP bars and helices under different loading conditions. *Journal of Composites for Construction*, 20(4).

- [19] Hegger, J., Niewels, J., and Kurth, M. (2009). *"Shear Analysis of Concrete Members with Fiber Reinforced Polymers (FRP) As Internal Reinforcement."* Proceedings of the Ninth International Symposium on Non-metallic (FRP) Reinforcement for Concrete Structures (FRPRCS-9), Sydney, Australia.
- [20] JSCE (1997), *Recommendation for design and construction of concrete structures using continuous fibre reinforcing materials*, Research Committee on Continuous Fiber Reinforcing Materials, Japan Society of Civil Engineers, Tokyo, Japan.
- [21] Kotsovos, M. D., and Pavlovic, M. N. (1999), *Ultimate Limit State Design of Concrete Structures - A New Approach*, Thomas Telford, Ltd., London, UK.
- [22] Kobayashi, K., and Fujisaki, T. (1995), *"Compressive Behavior of FRP Reinforcement in Non-prestressed Concrete Members."* Proceedings of the Second International Symposium on Non-metallic (FRP) Reinforcement for Concrete Structures (FRPRCS-2), RILEM proceedings 29, Ghent, Belgium, 267-274.
- [23] Légeron, F., Paultre, P., (2000). *"Behavior of High-Strength Concrete Columns under Cyclic Flexure and Constant Axial Load."* ACI Structural Journal, 97(4), Jul.-Aug. 2000, 591-601.
- [24] Mander, J., Priestley, J., and Park, R., *"Observed stress-strain behavior of confined concrete,"* ASCE Journal of Structural Engineering, vol. 114, pp. 1827–1849, August 1988.
- [25] Mallick, P.K. (2008). *"Fiber- Reinforced Composites: Materials, Manufacturing, and Design."* Third Edition, International Slandered Book Number-13: 978-0-8493-4205-9.
- [26] Menegotto M and Pinto PE (1973) Method of analysis for cyclically loaded RC plane frames including changes in geometry and nonelastic behavior of elements under combined normal force and bending. Proceedings of the IABSE Symposium on Resistance and Ultimate Deformability of Structures Acted on by Well-Defined Repeated Loads, Lisbon, Portugal, 15-22.
- [27] Nanni A (1993) Flexural behavior and design of RC members using FRP reinforcement. Journal of Structural Engineering 119(11): 3344–3359.

- [28] Ngo, D. and Scordelis, A., *"Finite element analysis of reinforced concrete beams,"* Journal of American Concrete Institute, vol. 64,
- [29] *"Practitioners' guide to finite element modeling of reinforced concrete structures,"* State of the art Bulletin 45, federation internationale du beton (fib), 2008.
- [30] Seismosoft (2018) SeismoStruct – A computer program for static and dynamic nonlinear analysis of framed structures Seismosoft: <http://www.seismosoft.com/en/SeismoStruct.aspx>; Pavia, Italy.
- [31] Sheikh, S.A., Yau, G., (2002). *"Seismic Behavior of Concrete Columns Confined with Steel and Fiber-Reinforced Polymers."* ACI Structural Journal, 99(1), Jan.-Feb. 2002, 72-80.
- [32] Tobbi, H., Farghaly, A.S., Benmokrane, B., (2012). *"Concrete Columns Reinforced Longitudinally and Transversally with Glass Fiber-Reinforced Polymer Bars."* ACI Structural Journal, 109(4), Jul.-Aug. 2012, 551-558.
- [33] *Toutanji H and Saafi M (2000) Flexural behaviour of concrete beams reinforced with glass fiber-reinforced polymer (GFRP) bars. ACI Structural Journal 97(5): 712–719.*
- [34] Vecchio, F.J., Collins, M.P., (1986). *"The Modified Compression-Field Theory for Reinforced Concrete Elements Subjected to Shear."* ACI Structural Journal, 83(2), 219-231.
- [35] Weber, A. (2006), advanced reinforcement technology with GFRP Rebar, *Proceedings of the 2nd International fib Congress*, Naples, Italy.